DOT/FAA/AR-07/56,V1

Air Traffic Organization
NextGen & Operations Planning
Office of Research and
Technology Development
Washington, DC 20591

Assessment of Residual Stresses and Hole Quality on the Fatigue Behavior of Aircraft Structural Joints

Volume 1: Stress Analyses, Fatigue Tests, and Life Predictions

March 2009

Final Report

This document is available to the U.S. public through the National Technical Information Service (NTIS), Springfield, Virginia 22161.

U.S. Department of Transportation
Federal Aviation Administration

NOTICE

This document is disseminated under the sponsorship of the U.S. Department of Transportation in the interest of information exchange. The United States Government assumes no liability for the contents or use thereof. The United States Government does not endorse products or manufacturers. Trade or manufacturer's names appear herein solely because they are considered essential to the objective of this report. This document does not constitute FAA certification policy. Consult your local FAA aircraft certification office as to its use.

This report is available at the Federal Aviation Administration William J. Hughes Technical Center's Full-Text Technical Reports page: actlibrary.tc.faa.gov in Adobe Acrobat portable document format (PDF).

Technical Report Documentation Page

1. Report No. DOT/FAA/AR-07/56,V1	2. Government Accession No.	3. Recipient's Catalog No.
4. Title and Subtitle ASSESSMENT OF RESIDUAL STRESSES AND HOLE QUALITY ON THE FATIGUE BEHAVIOR OF AIRCRAFT STRUCTUAL JOINTS VOLUME 1: STRESS ANALYSES, FATIGUE TESTS, AND LIFE PREDICTIONS		5. Report Date March 2009 6. Performing Organization Code
7. Author(s) James C. Newman*, Jr., W. Steven Johnson**, and Wei Zhao***		8. Performing Organization Report No.
9. Performing Organization Name and Address * Mississippi State University Mississippi State, MS 39762 ** Georgia Institute of Technology Atlanta, GA 30332 ***Solid Solutions, Inc. Irmo, SC 29063		10. Work Unit No. (TRAIS) 01-C-AW-MSU Amd 003, 012, 013 11. Contract or Grant No.
12. Sponsoring Agency Name and Address U.S. Department of Transportation Federal Aviation Administration Air Traffic Organization NextGen & Operations Planning Office of Research and Technology Development Washington, DC 20491		13. Type of Report and Period Covered Final Report 14. Sponsoring Agency Code ANM-100

15. Supplementary Notes
The Federal Aviation Administration Airport and Aircraft Safety R&D Division COTR was Dr. Felix Abali.

16. Abstract

The aging aircraft research programs conducted by the Federal Aviation Administration (FAA) and the aircraft industry have identified some technology gaps in assessing widespread fatigue damage in aircraft structures. One particular gap is a lack of understanding of the initial stages of multiple-site damage crack formation and growth. This report is the result of a study on the influence of residual stresses and production-quality holes on the fatigue behavior of laboratory coupons, laboratory flat-riveted lap joint specimens, curved-riveted lap joint panels from a narrow-body retired aircraft, and data from the retired aircraft destructive evaluations. The influence of residual stresses is accounted for in the life-prediction methodology by developing stress-intensity factor solutions and codes for both two- and three-dimensional cracked bodies. The influence of the production-quality hole is accounted for in the development of equivalent initial flaw size (EIFS) values to fit the experimental test data on the coupons and riveted lap joint panels. A 2024-T3 aluminum alloy sheet material was selected because of its use in the majority of the current fleet of commercial aircraft. National Aeronautics and Space Administration Langley Research Center supplied the material for part of this study. The Lockheed-Martin Aeronautics Company and Delta Air Lines provided production-quality drilled-hole coupons, the two-rivet lap joint specimens, and guidance on the critical parameters that were studied in this investigation. Fatigue life analyses on the polished and production-quality holes and two-rivet lap joint specimens were made using the small crack theory and the usual EIFS values. An assessment on the impact of loose and tight rivets on the fatigue life of more realistic structural configurations was made using the results from the EIFS values determined from laboratory-riveted lap joint panels and previous analyses of test results from a wide-body fuselage aircraft. Studies at Delta Air Lines indicated that the right and left sides of the retired narrow-body (Boeing 727) aircraft had quite different cracking behaviors. Predictions made on the curved panel tests conducted at the FAA Full-Scale Aircraft Structural Test Evaluation and Research facility indicated that the panels on one side of the aircraft could withstand about 90,000 additional pressure cycles to failure (panel had been subjected to about 60,000 flights before testing); whereas, the data and analyses from the destructive teardown of the retired aircraft by Delta Air Lines (lap joints from the other side of the aircraft) indicated that only an additional 10,000 flights would have been required to cause failure, if the fuselage had not been retired, inspected, or repaired.

17. Key Words Fatigue, Crack growth, Residual stress, Aircraft, Joints		18. Distribution Statement This document is available to the U.S. public through the National Technical Information Service, Springfield, Virginia 22161.	
19. Security Classif. (of this report) Unclassified	20. Security Classif. (of this page) Unclassified	21. No. of Pages 157	22. Price

Form DOT F 1700.7 (8-72) Reproduction of completed page authorized

TABLE OF CONTENTS

		Page
EXECUTIVE SUMMARY		xiii
1.	INTRODUCTION	1
1.1	Purpose	1
1.2	Background	3
1.3	Research Objectives	8
2.	LABORATORY TEST SPECIMENS AND MATERIALS	9
2.1	Straight-Drilled, Single Open-Hole Specimens	9
2.2	Countersunk Two-Rivet-Row Lap Joint Specimens	11
3.	EXPERIMENTS ON THE HOLE-DRILLING PROCESS	11
3.1	Development of Hole-Drilling Metrics	16
3.2	Drilled-Hole Quality Results	19
4.	FATIGUE TESTS ON SINGLE-HOLE SPECIMENS	25
4.1	Constant-Amplitude Loading	26
4.1.1	Polished Holes	26
4.1.2	Production-Quality Holes	27
4.2	Spike Overload and Underload Tests	27
5.	THREE-DIMENSIONAL WEIGHT FUNCTION ANALYSES	28
5.1	Calibration of Weight Function	29
5.2	Comparison of K3DL With FEAs and Equations	30
5.3	Corner Crack at Hole	38
5.3.1	Remote Applied Loads	39
5.3.2	Residual-Stress Distributions	42
5.4	Surface Crack at Hole	44
6.	TWO-DIMENSIONAL GREEN'S FUNCTION ANALYSES	47
6.1	Single Crack at Open Hole Under Remote Tension	47
6.2	General Stress Distributions for Cracks at Holes	48

7. FINITE ELEMENT ANALYSIS OF SINGLE-HOLE SPECIMEN 52

7.1 Elastic and Elastic-Plastic Stress Analyses 52
7.2 Simulated Fatigue Crack Growth and Crack Closure 55

8. FATIGUE ANALYSIS OF SINGLE-HOLE SPECIMENS 59

8.1 Fatigue Analyses Based on Small-Crack Theory 59
8.2 Constant-Amplitude Loading Tests 60
8.3 Spike Overload and Underload Tests 63

9. FATIGUE ANALYSIS OF LABORATORY LAP JOINT SPECIMENS 65

9.1 Stress Analysis of Cracks at Rivet-Loaded Fastener Holes 66

9.2 Material Crack Growth Properties 66

9.3 Northwestern University Three-Rivet-Row Test Specimens 67

9.4 Georgia Institute of Technology and Delta Air Lines Two-Rivet-Row Test Specimens 71

10. FATIGUE ANALYSIS OF CURVED LAP JOINT TEST PANELS 73

11. FATIGUE ANALYSIS OF CRACKING IN B-727 TEARDOWN AIRCRAFT 75

12. SUMMARY 78

13. REFERENCES 79

APPENDICES

A—Three-Dimensional Weight Function Method and User Guide
B—Two-Dimensional Green's Function Method and User Guide
C—Improvements to FASTRAN—Fatigue Crack Growth Life-Prediction Code

LIST OF FIGURES

Figure		Page
1	Residual Stresses From Production-Quality and Cold-Worked Holes	3
2	Cracked Fastener Hole Subjected to Various Internal and External Stresses	4
3	Comparison of WFM and the Finite Element Method for Corner Crack in Semicircular Edge Notch Under Remote Tension	5
4	Inclusion and Nucleating Particle Sizes in 2024-T3 Aluminum Alloy	6
5	Measured and Calculated Fatigue Lives Using Small-Crack Theory and Extreme Inclusion Particle Sizes in 2024-T3 Aluminum Alloy $K_T = 3.15$ Specimens	7
6	Comparison of Measured Fatigue Lives on Polished and Production-Quality Holes in 2024-T3 Aluminum Alloy With AGARD Data	8
7	Single Open-Hole Specimen Configuration	9
8	Specimen Layout for Single Open-Hole Configuration in the LT Orientation	10
9	Two-Rivet-Row Lap Joint Specimen Configuration	11
10	Multiple-Hole Specimen for the Preliminary Experiments	12
11	Drill, Bits, Drill Block, and Coupons Before Drilling Holes	13
12	Sample of a Drilled-Hole Edge and Development of Burrs	14
13	Sample of Different Gouge Shapes and Sizes	14
14	Different Types of Burrs Found on the As-Drilled Holes	15
15	Roughness and Conicality Measurements	17
16	Typical Gouge Angle and Gouge Number Measurements	18
17	Summary of the Hand-Drilled Hole Rankings for the Various Metrics	21
18	Summary of the Baseline-Drilled Hole Rankings for the Various Metrics	24
19	Examples of Holes Drilled With Short and Long Bits	25
20	Comparison of Fatigue Lives for Electropolished and Chemically Polished Specimens Made of 2024-T3 Aluminum Alloy	26

21	Comparison of Fatigue Lives for Polished and Production-Quality Open-Hole Specimens Made of 2024-T3 Aluminum Alloy	27
22	Comparison of Fatigue Lives for Polished Open-Hole Specimens Subjected to an Initial Overload or Underload Made of 2024-T3 Aluminum Alloy	28
23	Definition of Crack Configuration Parameters for a Corner Crack at Open Hole	30
24	Comparisons of Boundary-Correction Factors for a/c = 0.5 With a/t = 0.1 Under Remote Tension and Remote Bending	32
25	Comparisons of Boundary-Correction Factors for a/c = 0.5 With a/t = 0.95 Under Remote Tension and Remote Bending	33
26	Comparisons of Boundary-Correction Factors for a/c = 1 With a/t = 0.1 Under Remote Tension and Remote Bending	34
27	Comparisons of Boundary-Correction Factors for a/c = 1 With a/t = 0.95 Under Remote Tension and Remote Bending	35
28	Comparisons of Boundary-Correction Factors for a/c = 2 With a/t = 0.1 Under Remote Tension and Remote Bending	36
29	Comparisons of Boundary-Correction Factors for a/c = 2 With a/t = 0.95 Under Remote Tension and Remote Bending	37
30	Comparison of Boundary-Correction Factors for Remote Tension From Various Analyses and Equations for r/t = 1 and a/c = 1	38
31	Comparison of Boundary-Correction Factors for Remote Bending From Various Analyses and Equations for r/t = 1 and a/c = 1	39
32	Normalized SIFs (F_t) Under Remote Tension for Shallow to Deep Cracks	40
33	Normalized SIFs (F_b) Under Remote Bending for Shallow to Deep Cracks	41
34	Normalized SIFs (F_w) Under Wedge Loading for Shallow to Deep Cracks	41
35	Comparison of Residual Stresses From an Overload and the Equation Chosen to fit the Results	42
36a	Residual-Stress Distributions of a Cold-Worked Hole for Three Different R_y/r Ratios	43
36b	Normalized SIFs Under Residual-Stress Distribution for $R_y/r = 1.3$	44
37	Definition for the Surface Crack Configuration Parameters	45

38	Comparison of K3DL Results and Equations for a Surface Crack Configuration	46
39	Comparison of Results for a Surface Crack Configuration Using Various Models and Equations	46
40	Single Crack at an Open Hole in an Infinite Plate Subjected to Uniform Remote Stress	47
41	Comparison of Normalized SIFs for a Single Crack at an Open Hole Subjected to Uniform Remote Stress	48
42	Single Crack at an Open Hole Subjected to Remote Stress and Residual-Stress Distribution	49
43a	Calculated Residual Stresses Around a Circular Hole From Cold Working, Reaming, and Slotting	50
43b	Residual Stresses Around a Circular Hole at Maximum and Minimum Applied Stresses	50
43c	Calculated SIFs With and Without Residual Stresses at Maximum and Minimum Applied Stresses	51
43d	Calculated Stress Ratio (K_{min}/K_{max}) With and Without Residual Stresses at Maximum and Minimum Applied Stresses	51
44	Two-Dimensional Finite Element Model of the Single-Hole Fatigue Test Specimen	53
45	Plastic Zone Shape and Size After the 1.7 Overload on the Open-Hole Specimen (One-quarter of specimen)	53
46	Nodal Average Stresses Along x Axis for 1.7 Overload, Zero Load, and Constant-Amplitude Loading Used in Fatigue Tests	54
47	Nodal Average Stresses Along x Axis at the 1.7 Underload, Zero Load, and Constant-Amplitude Loading Used in Fatigue Tests	54
48	Nodal Average Stresses Along x Axis After Overload, Underload, and Constant-Amplitude Loading Used in Fatigue Tests	55
49	Crack-Opening Stresses for Constant-Amplitude Loading for a Crack Emanating From a Circular Hole	56
50	Crack-Opening Stresses for a Single-Spike Overload Followed by Constant-Amplitude Loading for a Crack at a Hole	57
51	Crack-Opening Stresses for a Single-Spike Underload Followed by Constant-Amplitude Loading for a Crack at a Hole	57

52 Comparison of Crack-Opening Stresses From FEA for the Three Load Cases 58

53 Comparison of Crack-Opening Stresses From FASTRAN for the Three Load Cases 58

54 Comparison of Fatigue Data on the 2024-T3 Aluminum Alloy Open-Hole Specimens With FASTRAN Calculations Using Three Flaw Sizes 60

55 Stress Against Cycles for 2024-T3 Aluminum Alloy Sheet Material With a Central Hole Under $R = 0$ Conditions 61

56 Comparison of Fatigue Lives for Electropolished and Chemically Polished Specimens Made of 2024-T3 Aluminum Alloy 61

57 Comparison of Fatigue Lives for Polished and Production-Quality Open-Hole Specimens Made of 2024-T3 Aluminum Alloy 62

58 Fatigue Lives for Drilled-Hole and Baseline Specimens as a Function of Stress Level 63

59 Fatigue Lives for Polished Specimens Subjected to Overload or Underload Prior to Constant-Amplitude Loading 64

60 Comparison of Test and Predicted Fatigue Lives for Single-Hole Specimens 65

61 Crack Configuration and Loading for Rivet-Loaded Hole 66

62 Fatigue Crack Growth Rate Properties for 2024-T3 Alclad Material 67

63 Three-Rivet-Row Lap Joint Specimen Tested at Northwestern University 68

64a Initiation Sites for Cracks in Lap Joint Specimens Tested at Low-Applied Stress Levels 69

64b Initiation Sites for Cracks in Lap Joint Specimens Tested at High-Applied Stress Levels 69

65 Crack Configuration Modeled for the Eyebrow Crack 70

66a Crack Growth in Riveted Lap Joint at a Low-Applied Stress Level 70

66b Crack Growth in Riveted Lap Joint at a High-Applied Stress Level 71

67 Two-Rivet-Row Lap Joint Specimen Tested at Georgia Institute of Technology 72

68a Fatigue Lives of Lap Joint Specimens With Underdriven Rivets 72

68b Fatigue Lives of Lap Joint Specimens With Standard and Overdriven Rivets 73

69 Curved Panel (FT-2) From Narrow-Body Aircraft Tested at the FAA William J. Hughes Technical Center 74

70 Influence of Secondary Bending on Predicted Crack Growth in Narrow-Body Aircraft 74

71 Predicted Crack Growth in Narrow-Body Aircraft and Continued Testing at the FAA William J. Hughes Technical Center 75

72 Typical Rivet Configuration in Narrow-Body Aircraft 76

73 Measured and Calculated Crack Growth From Riveted Joints in Narrow-Body Aircraft 77

74 Comparison of AFGROW and FASTRAN Crack-Shape Analyses for a Typical Riveted Lap Joint 78

LIST OF TABLES

Table		Page
1	Summary of Metrics for Hand-Drilling Experiments	19
2	Summary of Metrics for Baseline Experiments	23
3	Effective Stress-Intensity Factor Against-Rate Relation for 2024-T3 (Alclad)	67

LIST OF SYMBOLS AND ACRONYMS

a	Surface or corner crack depth, mm
a_i	Initial surface or corner crack depth, mm
C_i	Crack-growth coefficient for segment i
c	Surface, corner or through crack length, mm
c_i	Initial surface, corner or through crack length, mm
da/dN	Fatigue crack growth rate in a-direction, m/cycle
dc/dN	Fatigue crack growth rate in c-direction, m/cycle
F_i	Boundary correction on stress-intensity factor for various loading
E	Modulus of elasticity, MPa
K_{Ie}	Elastic stress-intensity factor at failure, MPa√m
K_{max}	Maximum applied stress-intensity factor, MPa√m
K_{min}	Minimum applied stress-intensity factor, MPa√m
N	Number of cycles
n_i	Crack-growth power for segment i
P	Applied load, kN
P_{max}	Maximum applied load, kN
P_{min}	Minimum applied load, kN
R	Stress ratio (K_{min}/K_{max}, P_{min}/P_{max}, or S_{min}/S_{max})
S	Applied stress, MPa
S_{max}	Maximum applied stress, MPa
S_{min}	Minimum applied stress, MPa
S_{op}	Crack-opening stress, MPa
w	One-half width of specimens, mm
x	Cartesian coordinate measured along crack plane, mm
α	Constraint factor
Δc	Crack growth increment, mm
ΔK	Stress-intensity factor range, MPa√m
ΔK_{th}	Stress-intensity factor range threshold, MPa√m
ΔK_{eff}	Effective stress-intensity factor range, MPa√m
$(\Delta K_{eff})_T$	Effective stress-intensity factor range at flat-to-slant crack growth, MPa√m
σ_o	Flow stress (average of σ_{ys} and σ_u), MPa
σ_{ys}	Yield stress (0.2 % offset), MPa
σ_u	Ultimate tensile strength, MPa
AGARD	Advisory Group for Aerospace Research and Development
D/W	Diameter-to-width
DoD	Department of Defense
EDM	Electric-discharge machining
EIFS	Equivalent initial flaw size
FAA	Federal Aviation Administration
FASTER	Full-Scale Aircraft Structural Test Evaluation and Research
FEA	Finite element analysis
LI	Load identifier

LT	Longitudinal transverse
MSD	Multiple-site damage
NACA	National Advisory Committee for Aeronautics
NASA	National Aeronautics and Space Administration
SEM	Scanning electron microscope
SIF	Stress-intensity factor
TL	Transverse longitudinal
WFD	Widespread fatigue damage
WFM	Weight function method

EXECUTIVE SUMMARY

The aging aircraft research programs conducted by the Federal Aviation Administration (FAA), National Aeronautics and Space Administration (NASA), and the aircraft industry have developed methodologies to assess widespread fatigue damage (WFD) in aircraft structures. During the course of the FAA WFD evaluations, technology gaps were identified. One particular gap is a lack of understanding of the initial stages of multiple-site damage (MSD) crack formation and growth. Knowledge of MSD nucleation time and pattern, (i.e., distribution), as well as its subsequent growth, is a prerequisite for planning an acceptable program to preclude the occurrence of WFD.

As a follow-on to the FAA WFD evaluations, this report is the result of a study on the influence of residual stresses and production-quality holes on the fatigue behavior of laboratory coupons, laboratory flat-riveted lap joint specimens, curved-riveted lap joint panels from a retired narrow-body aircraft, and data from the retired aircraft destructive evaluations. The influence of residual stresses is accounted for in the life-prediction methodology by developing stress-intensity factor (SIF) solutions and codes for both two- and three-dimensional cracked bodies. The influence of the production-quality hole is accounted for in the development of equivalent initial flaw size (EIFS) values to fit the experimental test data on the coupons and riveted lap joint panels.

A 2024-T3 aluminum alloy (bare and clad) sheet material was selected because of its use in the majority of the current fleet of commercial aircraft. NASA Langley Research Center supplied the bare material for part of this study because their material has a well-documented fatigue and fatigue crack growth history. The Lockheed-Martin Aeronautics Company and Delta Air Lines, Inc., provided production-quality drilled-hole coupons, two-rivet lap joint specimens, and guidance on the critical parameters to be studied in this investigation.

Attempts to measure or to establish the magnitude and distribution of the residual stresses in the production-quality drilled fastener holes were unsuccessful. However, fatigue tests conducted on the coupons made of the 2024-T3 bare material with both production-quality and polished holes indicated that the residual stresses may be low. In contrast to previous studies, production-quality drilled holes generated compressive residual stresses that had a significant impact on the fatigue life. Additionally, the three-dimensional finite element simulations of the riveting installation process demonstrated that residual stresses were induced around the fastener hole due to the severe plastic deformations and the various riveting parameters.

Two- and three-dimensional stress analyses were developed to calculate the SIF for through, surface, and corner cracks emanating from a straight-shank fastener hole under various applied (remote tension, bending, fastener) loadings with an arbitrary residual-stress distribution. These analyses were only for straight-shank holes, i.e., the countersunk configuration was not considered. The two-dimensional SIF code was based on Green's functions, whereas the three-dimensional SIF code was based on a weight function analysis. The Green's function code (SIFK2D) and the weight function code (K3DL) are stand-alone codes, and they were used to generate SIF solutions for the FASTRAN life-prediction code.

Fatigue life analyses on the polished and production-quality, single-hole specimens and the two-rivet lap joint specimens were made using the small-crack theory and the usual EIFS values for open-hole and lap joint specimens. The predicted results on both the open-hole and two-rivet lap joint specimens agreed well with the test data. An assessment on the impact of loose and tight rivets on the fatigue life of more realistic structural configurations was made using the results from the EIFS values determined from laboratory-riveted lap joint specimens and previous analyses of test results from a wide-body fuselage aircraft. Studies at Delta Air Lines indicated that the right and left sides of the retired narrow-body (Boeing 727) aircraft had quite different cracking behaviors. Predictions made on the curved panel tests conducted at the FAA Full-Scale Aircraft Structural Test Evaluation and Research facility indicated that the panels on one side of the aircraft could withstand about 90,000 additional pressure cycles to failure (panel had been subjected to about 60,000 flights before testing); whereas, the data and analyses from the destructive teardown of the retired aircraft by Delta Air Lines (lap joints from the other side of the aircraft) indicated that only an additional 10,000 flights would have been required to cause failure, if the fuselage had not been retired, inspected or repaired.

1. INTRODUCTION.

Over the past decade, the aging aircraft research programs conducted by the Federal Aviation Administration (FAA) [1], National Aeronautics and Space Administration (NASA) [2], and the aircraft industry have developed methodologies to assess widespread fatigue damage (WFD) in aircraft structure. In a recent FAA-sponsored research project [3], The Boeing Company assessed and validated state-of-the-art fracture mechanics methods developed under previous FAA, NASA, and Department of Defense (DoD) programs. For model calibration and verification, an extensive building-block test program was conducted starting with small coupons, leading to a more complex built-up fuselage structure tested at the FAA Full-Scale Aircraft Structural Test Evaluation and Research (FASTER) facility, and a full-scale test on the aft pressure bulkhead of an actual aircraft. Emphasis of the WFD Assessment project was placed on determining the effects of multiple-site damage (MSD) on the residual strength of structural joints representative of commercial aircraft. Using the STAGS finite element code and the critical crack tip opening angle criterion, accurate predictions of the residual strength (within 5% of test results) were made on complex fuselage structure and on an aft pressure bulkhead of an actual aircraft [4]. This effort demonstrated the successful technology transfer of a robust analysis methodology for assessing the residual strength of aircraft structure with MSD.

During the course of the WFD Assessment project, technology gaps were identified. One particular gap was a lack of understanding of the initial stages of MSD formation and growth. Knowledge of MSD nucleation time and pattern (i.e., distribution), as well as its subsequent growth, is a prerequisite for planning an acceptable program to preclude the occurrence of WFD. As a building block task in the WFD Assessment project to understand MSD initiation, fatigue and small-crack growth behavior of production-quality and polished holes in 2024-T3 aluminum alloy sheet material were investigated. It was found that production-quality holes behaved quite differently from polished holes. The production-quality holes produced fatigue lives that were over a factor of 5 times longer than the polished holes. It has long been known that machining or the drilling process and fastener installation may induce compressive residual stresses at fastener holes. Typically, these production-quality holes receive minimal working to deburr the edges of the holes to prevent premature cracking from the edge. But the bore of the holes may have these machining residual stresses and/or rivet installation residual stresses present during flight operations. The application of the FASTRAN life-prediction code [5] to predict fatigue lives and small crack growth behavior on test specimens in the WFD Evaluation project was fairly successful on the polished holes, but severely underestimated the fatigue lives on the production-quality holes presumably due to residual stresses. These results highlighted the need to include residual-stress distributions in the FASTRAN life-prediction methodology. In the past, the FASTRAN life-prediction code and small-crack theory [6-8] have been quite successful in predicting the fatigue behavior in a variety of materials, especially the 2024-T3 aluminum alloy bare and clad, under both constant-amplitude and spectrum loading conditions.

1.1 PURPOSE.

The purpose of the present study was to investigate fastener hole residual stresses and hole quality and their influence on life-prediction methodology to study crack initiation and crack growth in aircraft structural joints commonly used in fuselages. This research was a joint

activity between Mississippi State University, Georgia Institute of Technology, and Solid Solutions, Inc., with extensive collaboration with Lockheed-Martin Corporation, Delta Air Lines, and NASA Langley Research Center.

The results of this project are published in three volumes. The first volume, Assessment of Residual Stresses and Hole Quality on the Fatigue Behavior of Aircraft Structural Joints (this report), contains the experimental test programs on open-hole specimens (polished and as-drilled holes) and the two-rivet-row lap joint specimens, an elastic-plastic finite element analysis of the open-hole specimens, the development of two- and three-dimensional stress-analysis codes to calculate stress-intensity factors (SIF) for through, surface, and corner cracks at a hole under arbitrary loading, and the fatigue analyses of the laboratory specimens (open hole and lap joint), the curved lap joint panels removed from a retired narrow-body aircraft [9 and 10], and the actual lap joint sections destructively examined from the retired aircraft [11 and 12]. The second volume is on the assessment of hole drilling procedures and the fatigue performance of production-quality aircraft fastener holes [13]; and the third volume is on experimental and computational investigation of the riveting mechanics in aircraft fuselage structure [14].

In addition to the above documents, the FAA has sponsored a destructive teardown of a retired commercial B-727 aircraft. This research project was conducted in parallel with the destructive teardown investigation made by Delta Air Lines.

2024-T3 aluminum alloy sheet was the material selected for the open-hole specimens. NASA Langley Research Center supplied the bare alloy and the single open-hole specimens for this study. Lockheed-Martin and Delta Air Lines produced production-quality drilled holes in many samples using different drilling methods, and produced riveted lap joint specimens using various fastener installation procedures. Attempts were made to measure or to establish the magnitude and distribution of the residual stresses in the production-quality drilled fastener holes. Fatigue tests were conducted on the single open-hole specimens made of the 2024-T3 aluminum alloy with both production-quality and polished holes to calibrate the analysis methodology. Fatigue tests were also conducted on two-rivet-row lap joint specimens prepared by Delta Air Lines.

Two- and three-dimensional stress analysis codes were developed to calculate the SIFs for through, surface, or corner cracks at a hole under a wide variety of applied loading and with an arbitrary residual-stress distribution along the crack path. The Green's function method was used for the through-crack configurations. The weight function analysis, K3DL, was developed and used to calculate SIFs for surface and corner crack at hole configurations. These SIFs were then used in the FASTRAN life-prediction code. Fatigue life analyses on polished and production-quality holes were performed using the small-crack theory. The influence of nucleating particle distributions and of manufacturing defects on calculated fatigue lives was studied using equivalent initial flaw-sizes (EIFS) to fit fatigue lives on the various specimens and structural configurations.

As a final verification of the approach developed, assessments on the impact of hole quality on more realistic structural configurations were made using the results from the retired narrow-body (Boeing-727) aircraft panels tested in the Destructive Evaluation and Extended Fatigue Test of Retired Aircraft Program, sponsored by the FAA and conducted by Delta Air Lines, and panels

tested in the FAA FASTER facility that had been removed from the retired aircraft. Fatigue analyses were also conducted on three-rivet-row lap joint specimens, which are similar to the lap joints in a retired narrow-body (B-727) aircraft. These analyses were to determine the EIFS for the fatigue analyses of the test panels removed from the retired aircraft and of the cracking observed in the actual lap joint sections of the retired aircraft.

1.2 BACKGROUND.

The machining and drilling process leaves a region of disturbed material along the edges of a drilled hole that can cause a residual-stress field, as shown in figure 1(a). It was estimated that the depth of the residual-stress field is about 20 to 100 μm. These residual stresses could affect the fatigue behavior of as-drilled open-hole specimens. However, the drilling residual-stress field would be greatly altered by the rivet installation process, which yields the rivet and adjacent material in the rivet hole. By contrast, the cold-working process (i.e., pulling a mandrel through the hole and yielding the material) produces a more significant residual-stress field (typically 0.5-5 mm [15]), as shown in figure 1(b). A literature survey was conducted on the measurement and analyses of residual stresses due to the drilling and the fastener installation process. However, no information was found on residual stresses due to the drilling process. Attempts to measure the residual stresses along the bore of the hole using X-ray diffraction were also unsuccessful. Normal hole drilling residual-stress measurement methods were impractical due to the extremely small depth of the residual-stress field. Finite element analyses (FEA) were also conducted on the fastener installation, as part of this study, but the results are given in a separate report [14].

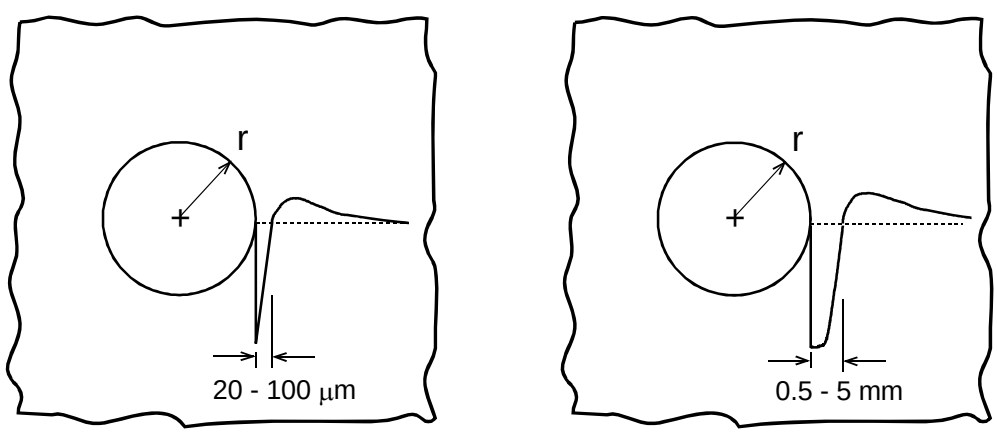

(a) Machining Residual Stresses (b) Cold-Working Residual Stresses

Figure 1. Residual Stresses From Production-Quality and Cold-Worked Holes

The SIFs for surface, corner, and through cracks emanating from a fastener-loaded hole were determined from three-dimensional FEAs [16 and 17] and weight function methods (WFM) [18-20]. These crack configurations were subjected to remote tension (S), remote bending (M), and pin loading (P), as shown in figure 2. The SIF solutions for interference **(I)** loading and various residual-stress (σ_{rs}) distributions can be obtained by using either Green's functions or weight functions for through cracks and weight functions for surface and corner cracks.

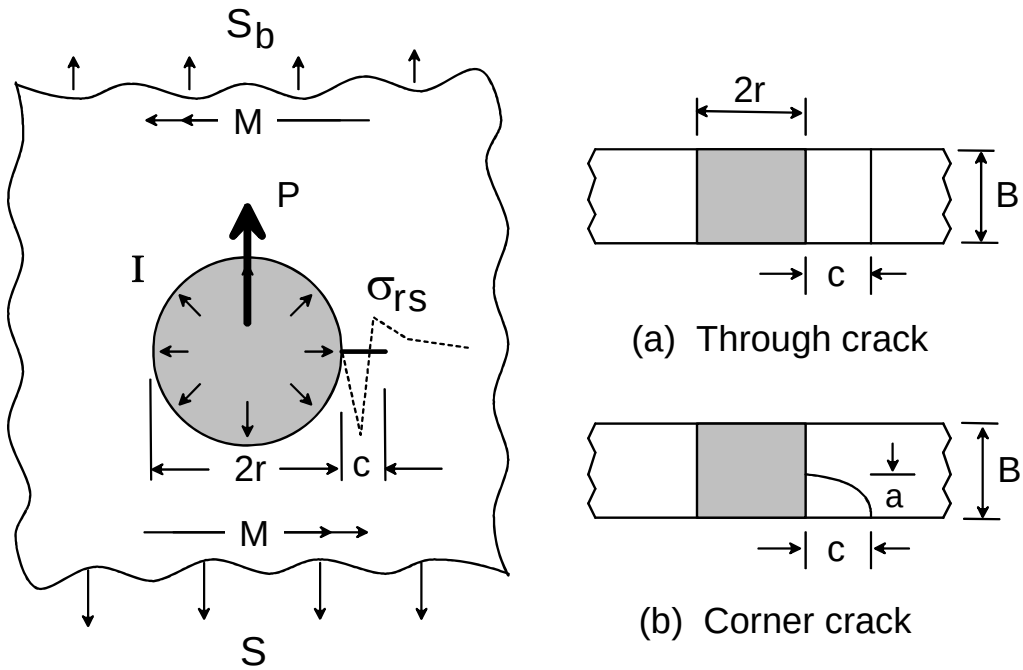

Figure 2. Cracked Fastener Hole Subjected to Various Internal and External Stresses

The current K3D (weight function analysis) code [21-23] can analyze surface and corner cracks (a/B < 0.6) at a hole in a specimen under remote tension and bending loads. Figure 3 shows a comparison of SIFs for various depth corner cracks at a semicircular edge notch using the WFM and finite element method. (Note that for a corner crack at a hole, the thickness B is equal to t; but for a surface crack at a hole, the thickness B is equal to 2t.) For the mid-range (a/t = 0.2 and 0.5), both methods agreed within 3 percent. The WFM can be applied to small-crack depths (a/t << 0.1) but not the finite element method. However, in the previous study [22 and 23], the WFM was limited to a/t < 0.6.

It was proposed to develop an option in the K3D code (K3DL) to calculate the SIFs for a surface and corner crack emanating from an open hole under an arbitrary residual-stress field (σ_{rs}) from the edge of the hole, as shown in figure 2. The K3DL analyses will also be extended to cover very deep surface and corner cracks at the hole (a/B or a/t values up to 0.99). The modification to the weight function code will use the recent results from Fawaz and Andersson [24 and 25] from high-fidelity finite element solutions.

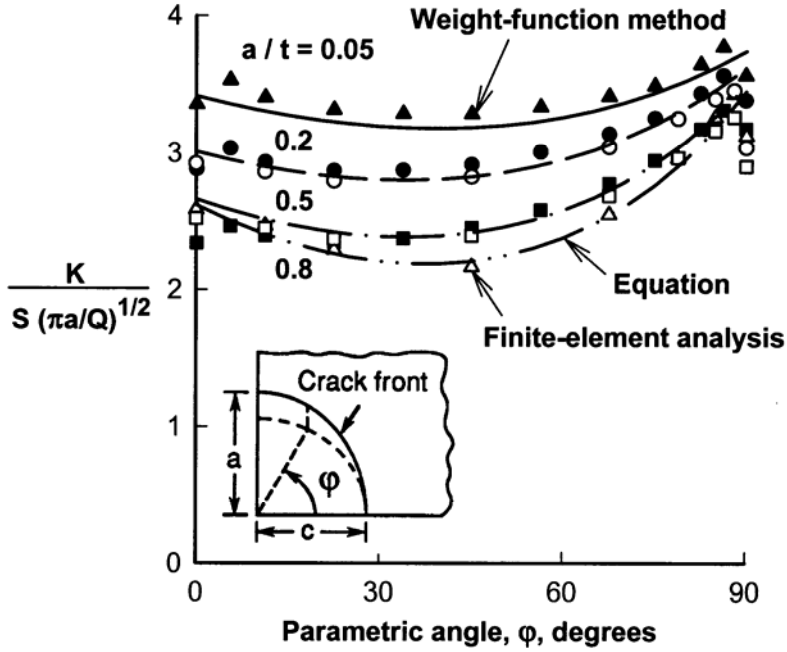

Figure 3. Comparison of WFM and the Finite Element Method for Corner Crack in Semicircular Edge Notch Under Remote Tension

The cracked fastener hole, as shown in figure 2, is a current option in the life-prediction code, FASTRAN [5], except for the interference (**I**) and the residual-stress field (σ_{rs}) loading. The K3DL code will be used with a version of the FASTRAN code that will allow the fatigue and fatigue crack growth analyses of small surface or corner cracks emanating from the hole under remote tension, remote bending, pin loading, and the residual-stress field.

As previously mentioned, the 2024-T3 aluminum alloy sheet material proposed for this study has been well documented. Hudson [26] and Phillips [27] have determined the fatigue crack growth properties over a very wide range in stress ratios ($R = P_{min}/P_{max}$) and crack growth rates that span over eight orders of magnitude. In the Advisory Group for Aerospace Research and Development (AGARD) short crack [28 and 29] and NASA/Chinese Aeronautical Establishment cooperative programs [30], the crack growth rates for very small cracks (10 to 2 mm) were determined over a wide range in stress ratios. Laz and Hillberry [31] conducted an extensive microstructural analysis of the inclusion particle distributions in this alloy. They identified the inclusion particle distributions and the nucleating particle distributions that initiated cracks, as shown in figure 4. The open bars show the percent of inclusions for a given inclusion depth (2a), and the solid bars show the percent of nucleating inclusions for a given nucleating depth. They also presented information on the length of the inclusion particles and nucleating particles in the width direction (not shown). The inclusion particle clusters were, generally, in pancake form and the length dimension was 2 to 3 times the depth. These results show that the extreme tails of the distribution control the inclusion particle sizes that initiate cracks.

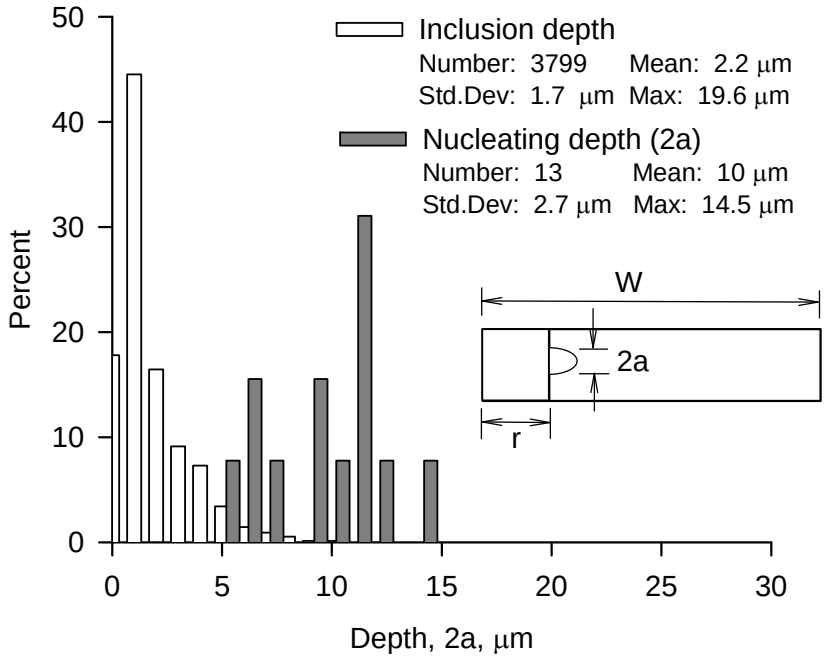

Figure 4. Inclusion and Nucleating Particle Sizes in 2024-T3 Aluminum Alloy [31]

In the AGARD program [28 and 29], fatigue tests were conducted on single edge notch tension specimens ($K_T = 3.15$) for three applied stress levels at $R = 0$. These specimens are very close to simulating the stress concentration for an open circular-hole specimen. These results are shown in figure 5. The open symbols show the results from several laboratories in Europe and North America. The arrows indicate that the fatigue test was terminated at these number of cycles (or runout). The FASTRAN life-prediction code was used to make fatigue life calculations on these specimens using the nucleating particle distributions from Laz and Hillberry [31]. Two initial crack sizes (or crack areas, 30 and 300 μm^2, respectively) were selected to cover the upper and lower bounds from these particle distributions. Thus, about 90 percent of the nucleating-particle sizes will fall within these bounds. Using the effective stress-intensity factor range-and-rate relationship, previously established for this alloy, the calculated cycles to break through (2a = B) were made. These results are shown as solid curves in figure 5 with a small-crack effective stress-intensity factor range threshold $(\Delta K_{eff})_{th} = 0.8$ MPa-m$^{1/2}$. The dashed line shows what would have happened if the small-crack $(\Delta K_{eff})_{th}$ had been set at 1.0 MPa-m$^{1/2}$. For applied stress levels higher than 125 MPa, the upper- and lower-bound calculations fit the scatter in the fatigue tests extremely well. Also, the lower-bound calculations fit the lower bound of the fatigue data very well.

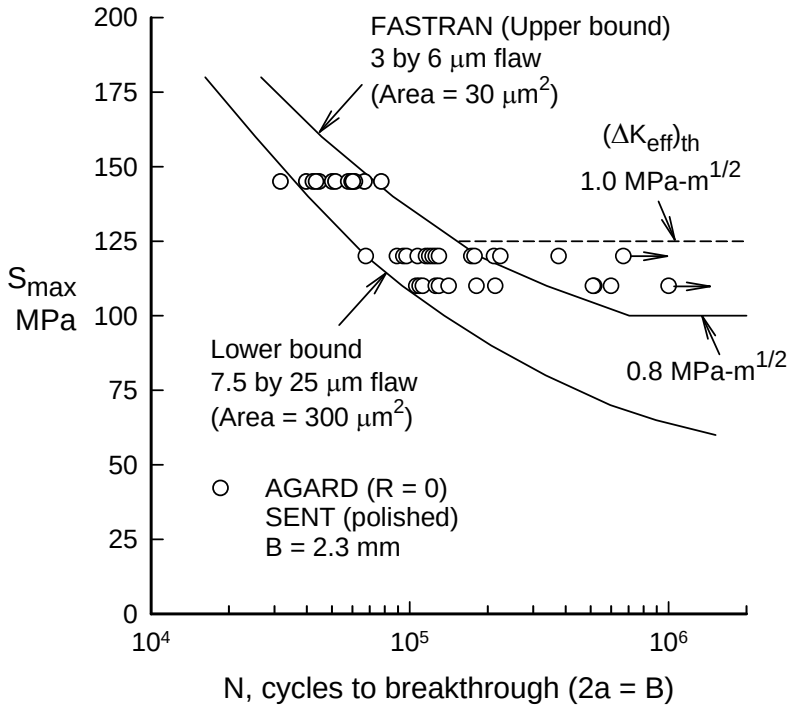

Figure 5. Measured and Calculated Fatigue Lives Using Small-Crack Theory and Extreme Inclusion Particle Sizes in 2024-T3 Aluminum Alloy $K_T = 3.15$ Specimens

Figure 6 compares the fatigue tests conducted in the WFD Evaluation project [3] on the circular-hole specimens with polished and production-quality holes with the previous AGARD data. The tests in the Boeing study were tested at the Beijing Institute of Aeronautical Materials at an R of 0.1. Due to the slightly higher stress ratio, the polished-hole specimens appear to be of the same family as the AGARD tests. (The calculated fatigue lives for $R = 0.1$ would have been about 30 percent longer than at $R = 0$ for the same stress level.) The production-quality hole tests conducted at nearly the same applied stress levels lasted over 5 times longer than the polished specimens, presumably due to the machining compressive residual stresses.

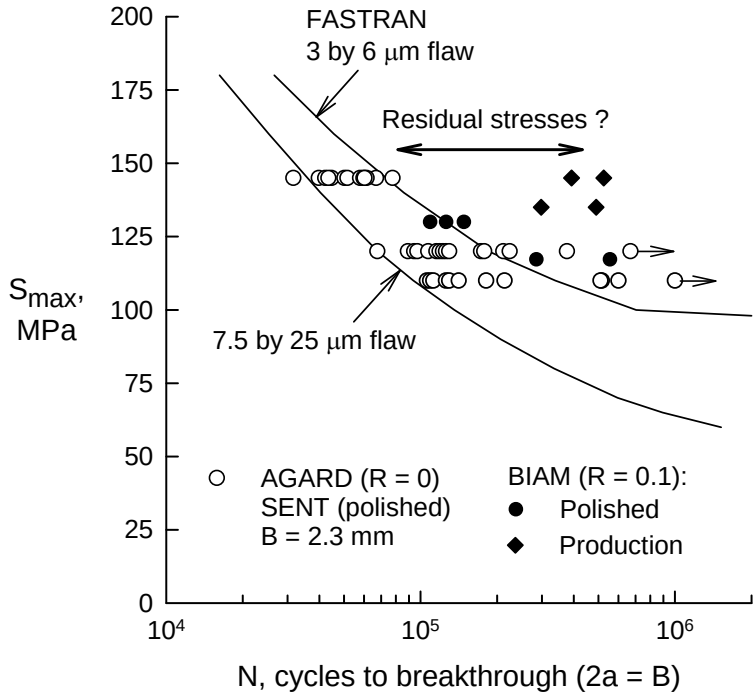

Figure 6. Comparison of Measured Fatigue Lives on Polished and Production-Quality Holes in 2024-T3 Aluminum Alloy With AGARD Data

1.3 RESEARCH OBJECTIVES.

The objectives were to study the effects of fastener hole quality, to account for residual stresses around fastener holes in the stress analysis of two- and three-dimensional cracks, and to improve the life-prediction methodology for cracks growing in laboratory lap joint specimens and in aircraft structural joints commonly used in fuselages. The material selected was 2024-T3 aluminum alloy sheet material. The NASA Langley Research Center provided the material for part of this study. Lockheed-Martin and Delta Air Lines produced specimens with production-quality holes using different drilling methods and fastener installation processes and laboratory lap joint specimens. Attempts were made to measure or to establish the magnitude and distribution of the residual stresses in the production-quality fastener holes; however, the as-drilled production-quality holes were found to have minimal residual stresses. Fatigue tests and analyses were conducted on specimens made of the 2024-T3 aluminum alloy with both production-quality and polished holes to calibrate the analysis methodology. Some polished-hole specimens were also subjected to an overload or an underload to induce compressive or tensile residual stresses to study the influence of these stresses on fatigue lives. In addition, some simple two-rivet-row lap splice joint specimens were made and tested under constant-amplitude loading. Fatigue analyses were conducted on both the two-rivet-row lap joint specimens and the results from the literature on three-rivet-row lap joint specimens to determine EIFS to fit these data.

Two-dimensional Green's function and three-dimensional weight function codes were developed to calculate the SIFs for through, surface, and corner cracks at an open hole under a wide variety of applied loading and with an arbitrary residual-stress distribution along the crack path. Both the two- and three-dimensional codes were used to calculate the SIF distributions for cracks at fastener holes under various applied loading conditions and residual-stress distributions. These SIF distributions were used with the FASTRAN code to calculate the influence of residual stresses on crack growth lives using the traditional elastic superposition method.

As a final verification of the approach developed, assessments of the life-prediction methodology on more realistic structural joint configurations were made using results from the destructive evaluation of a retired aircraft and extended fatigue testing of panels removed from the retired aircraft.

2. LABORATORY TEST SPECIMENS AND MATERIALS.

In the experimental test program, two specimen designs were used. The first was a single open-hole specimen and the second was a two-rivet-row lap joint specimen. The material used for the single open-hole specimens was 2024-T3 aluminum alloy bare material, whereas the lap joint specimens were made of 2024-T3 clad material.

2.1 STRAIGHT-DRILLED, SINGLE OPEN-HOLE SPECIMENS.

The specimen design selected for this study was a single open-hole specimen subjected to remote tensile loading, as shown in figure 7. The rationale for selecting this specimen was to isolate the influence of the hole-drilling process from the rivet or fastener installation. Thus, a detailed examination was made of the hole quality prior to rivet installation. Attempts were made to measure residual stresses and/or the extent of disturbed material, prior to fatigue testing.

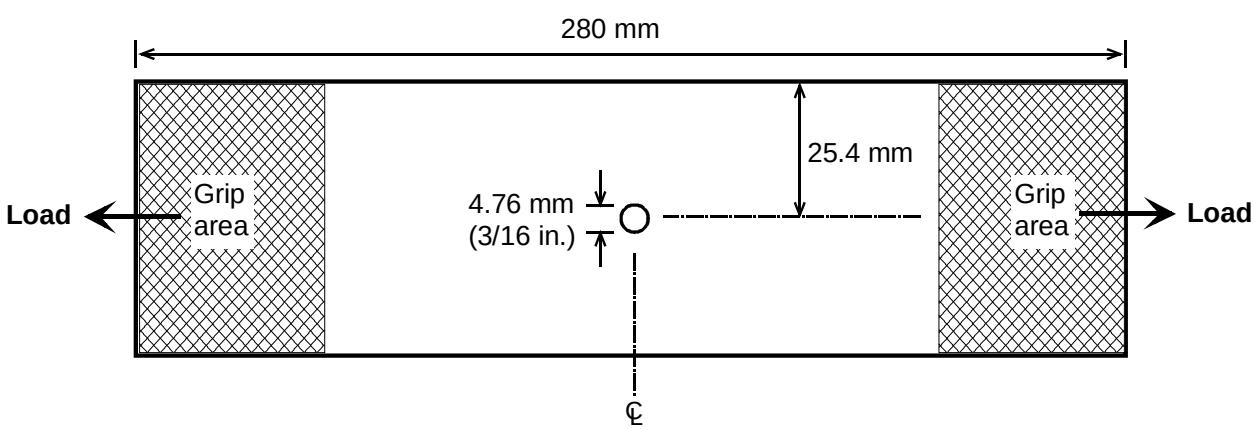

Figure 7. Single Open-Hole Specimen Configuration

Aluminum alloy (2024-T3 bare) sheet material was obtained from the NASA Langley Research Center. This material is widely used in the aircraft industry (fuselages and wings) and the material at NASA Langley has a well documented fatigue and fatigue crack growth history. A total of 120 blank specimens (51 x 280 x 2.3 mm) in the longitudinal transverse (LT) orientation

were machined, and 45 blank specimens in the transverse longitudinal (TL) orientation were machined from the same lot of material and shipped to Mississippi State University. Some specimens (15 LT and 15 TL) had a 4.76 mm (3/16 in.) hole drilled with a process to minimize residual stresses (three-drill process) and then chemically polished. The specimen layout for the LT orientation specimens is shown in figure 8. Similarly, 15 TL specimens were cut from the large sheets.

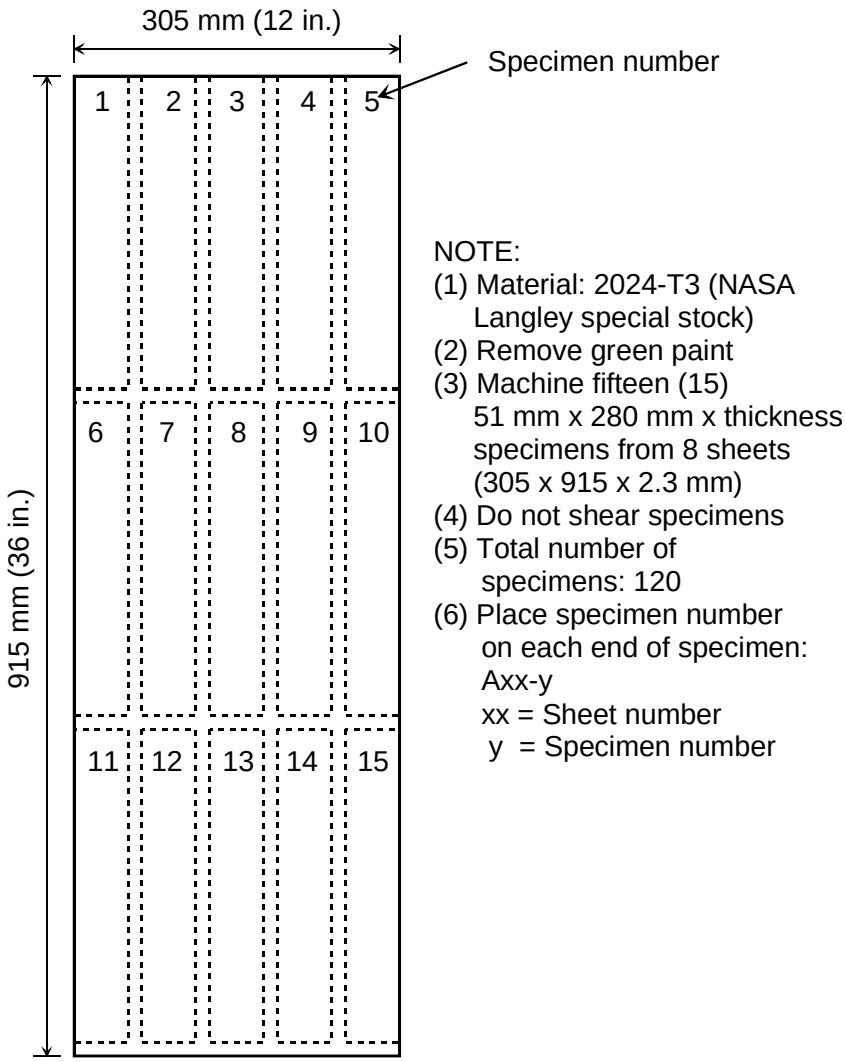

Figure 8. Specimen Layout for Single Open-Hole Configuration in the LT Orientation

Forty-five specimen blanks made of the 2024-T3 bare alloys were supplied to both the Lockheed-Martin Corporation and Delta Air Lines. A number of hole-drilling parameters were varied in preparing specimens with a single drilled hole (located in the center of the blank). During the preliminary investigation on hole drilling, eight factors were identified: (1) operator experience, (2) drill bit condition, (3) axial bit speed, (4) drill bit length, (5) pressure, (6) pilot hole, (7) drill block, and (8) material. These factors were considered in assessing the impact on drilled-hole quality [13].

2.2 COUNTERSUNK TWO-RIVET-ROW LAP JOINT SPECIMENS.

To study the influence of rivet installation on the fatigue behavior of simple lap joint specimens, a two-rivet-row lap joint specimen, as shown in figure 9, was prepared by Delta Air Lines and tested at Georgia Institute of Technology [14]. The lap joint specimen had two countersunk rivets installed under several conditions. The rivet conditions considered were (1) standard-driven rivets, (2) tight or overdriven rivets, and (3) underdriven rivets. All specimens were subjected to a remote stress of 124 MPa at a stress ratio, $P_{min}/P_{max} = 0$.

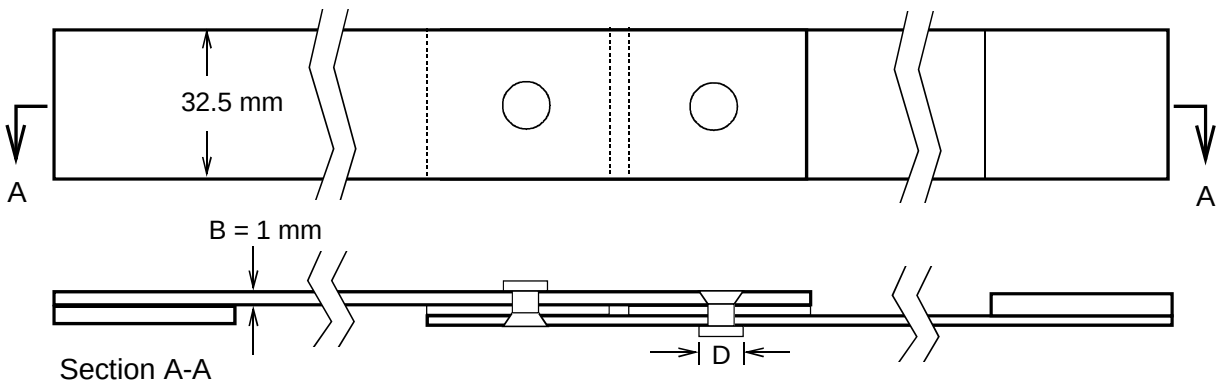

Figure 9. Two-Rivet-Row Lap Joint Specimen Configuration

3. EXPERIMENTS ON THE HOLE-DRILLING PROCESS.

The purpose of this study was to find a correlation between the drilling techniques and the fatigue life of aircraft fastener holes. During the experimental portion, which was conducted by the Georgia Institute of Technology, center holes were drilled into fatigue-tested 2024-T3 aluminum alloy specimens, replicating those used on actual aircraft. The details of this study are given in reference 13, but some typical results are given herein.

Through discussions held with engineers and laboratory personnel at Lockheed-Martin and Delta Air Lines, eight probable significant factors were identified:

1. Operator experience—since most aircraft rivet holes are drilled by hand, individual mechanics will likely drill holes in slightly different ways. Hopefully, the quality of the hole improves with the operator's experience.

2. Bit condition—as drill bits are used, they become dull, which would likely change the way the operator drills the hole, the quality of the hole surface, and increase the temperature gradient about the hole.

3. Axial bit speed—although fixed-speed, pneumatic drills are used, it was found that mechanics release the trigger at different times (such as when the drill bit penetrated the skin versus when the bit was completely withdrawn from the hole), which would likely produce different amounts of rifling inside the hole.

4. Bit length—two different sizes of bits are typically used in production, which may cause longer bits to bend, and shorter bits to “wobble” more during drilling.

5. Pressure—each mechanic applies a different amount of pressure on the drill, which could cause different amounts of plastic deformation and temperature gradients.

6. Pilot hole—sometimes mechanics drill a pilot hole before the final fastener hole. This reduces the amount of material to be removed and may affect the plastic deformation, temperature gradient, and speed of drilling.

7. Drill block—a guide is sometimes used by mechanics, which would likely improve hole quality.

8. Material—aircraft are typically constructed with both 2000- and 7000-series aluminum alloys, while the material provided is 2024-T3 aluminum alloy.

Discounting the material, these seven variables produced 96 possible combinations (the combination of a pilot hole and drill block is not typically used in industry). With a minimum of three replicates of each combination (six would be preferred for fatigue tests), this would require 288 fatigue test specimens. Not only are the experiments limited by the number of test speciments (~300 combinations, compared with the 90 specimens that were provided), but also by time. Therefore, a preliminary experimental program was devised to eliminate the variables that were likely to be insignificant.

The preliminary experiments were conceived to save both time and material. The concept was that multiple holes could be drilled in each specimen (see figure 10), and the holes could be compared for hole quality and residual-stress level. The number of holes to be drilled was further reduced by employing a design of experiments, using a fractional factorial combination.

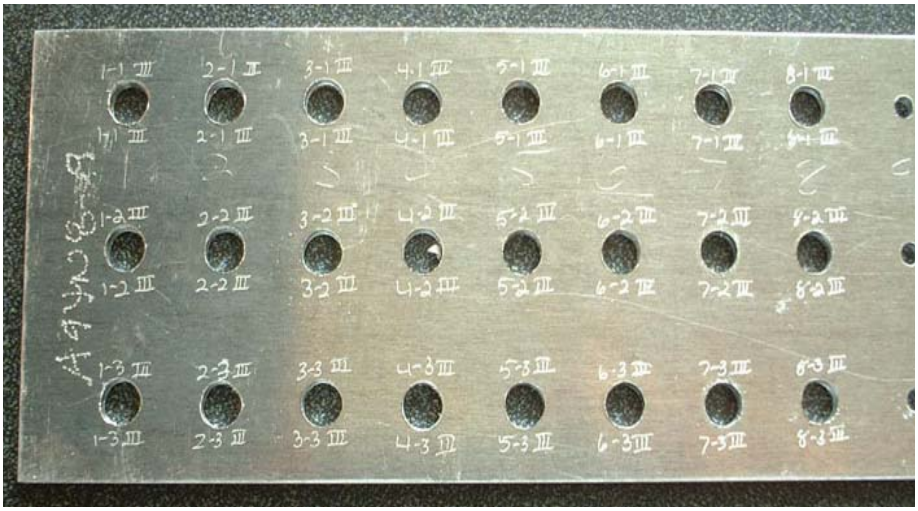

Figure 10. Multiple-Hole Specimen for the Preliminary Experiments

Approximately 100 holes were drilled at the Lockheed-Martin test facility. A pneumatic, fixed-speed drill, from the shop, was used for all holes. A number of used bits were taken from the bit recycling bin at the tool crib, and were retained after use. New bits were taken from the tool crib, and were retained after use, being used for only six holes each. The pilot holes were drilled the day before the test in two specimens, as shown in figure 11.

Figure 11. Drill, Bits, Drill Block, and Coupons Before Drilling Holes

During the drilling process, there was a very noticeable difference in the time taken to drill the holes with the dull versus sharp bits, and with the piloted versus nonpiloted holes. There was also a noticeable difference in chip size between piloted (very small chips) and nonpiloted (long, helical-shaped chips) holes. The first operator was a very experienced mechanic, the second was inexperienced. The holes were either drilled with the trigger depressed all the way from beginning to end ("full"), or fully stopped upon penetration and withdrawn from the hole while stopped. The mechanic either pressed down as hard as possible or as lightly as possible for the pressure variable. Finally, standard 150-mm (6-in.) and 75-mm (3-in.) bits were used for long and short bits, respectively. The material was rested on blocks of wood to keep from having to clamp the specimen, and the holes were drilled over the gap between the blocks so that there was nothing to disrupt the formation of the burr.

From the multiple-hole specimens, each section with a hole was cutout and each hole was sliced in half (so that two semicircular sections were made of each hole) using electric-discharge machining (EDM); they were mounted for viewing with an optical microscope equipped with a digital camera. Both sides of each hole were photographed and measured for surface length, hole length, coupon width, hole angularity (from perpendicular), entry burr size, and exit burr size (see figure 12).

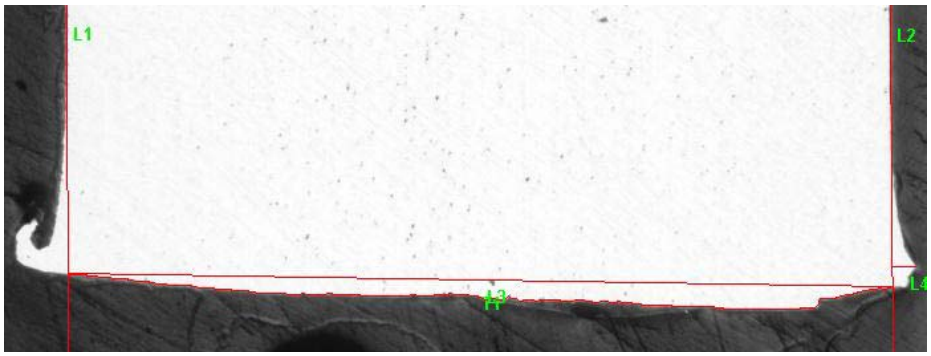

Figure 12. Sample of a Drilled-Hole Edge and Development of Burrs

Surface roughness was one criterion used to judge hole quality, since it should indicate the amount of plastic deformation induced on the surface from the cutting action of the drill. A surface roughness value was calculated by the deviation of the actual surface from a perfectly smooth surface. The actual surface was measured by the length of a line, which traced the hole bore surface, and was divided by a straight line from entry to exit (a "perfect" hole surface, drilled at the same angle as the actual hole) to give a unit-less, raw roughness value. However, this roughness value took into account both the small amplitude roughness, as well as the large, gouging deformations (see figure 13). To remove the large deformations, a factor accounting for the size, shape, and length of the deformations was determined, and a "corrected roughness" was calculated. The factor ranged from 0 to 9, and was figured in the following way:

- A 5 was given to a diagonal-shaped gouge, a 7 to a curved gouge, and a 9 to a step-shaped gouge.
- A 3 was given to a small gouge, a 6 to a medium gouge, and a 9 to a large gouge.
- These two numbers were averaged, and divided by the fraction of the bore surface that it encompassed.
- If multiple gouges were found on a hole surface, the above calculations were repeated, and the factors were added together.

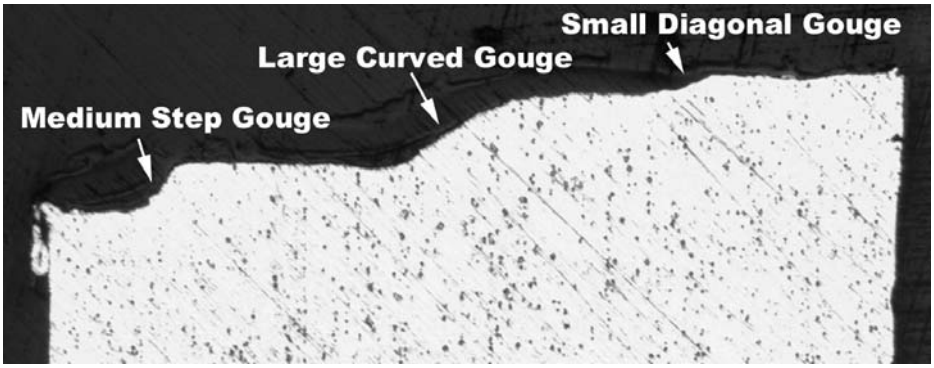

Figure 13. Sample of Different Gouge Shapes and Sizes

A second criterion of hole quality was burr length, since it would indicate the amount of deformation induced by the pressure of the bit and the movement of the bit through the hole. The value measured was simply the distance that the burr extended beyond the coupon surface. Since approximately half of the holes displayed burrs on the entry face, as well as the exit face, the entrance burrs were separately measured. It was interesting to note that there were three characteristic burr shapes observed. The first was a "curling" burr, which was very thin and curled back from the bore (figure 14(a)). The curling shape was easily disfigured, so many were flattened before being mounted. The second was a "triangular" burr, which curved back slightly from the bore, and dropped off sharply on the backside of the burr (see figure 14(b)). The final shape was a "bulge" burr, which had a rounded shaped and reached its maximum height much further from the bore than the triangular burr (figure 14(c)). There were also a wide variety of distances that the triangular and bulge burrs extended from the bore. All of these geometries were noted in the data, but only the length perpendicular to the specimen surface was measured due to time constraints and the limited scope of the experiment. The size and the shape of the burr may be indicative of the variables involved in the drilling process and may warrant future study.

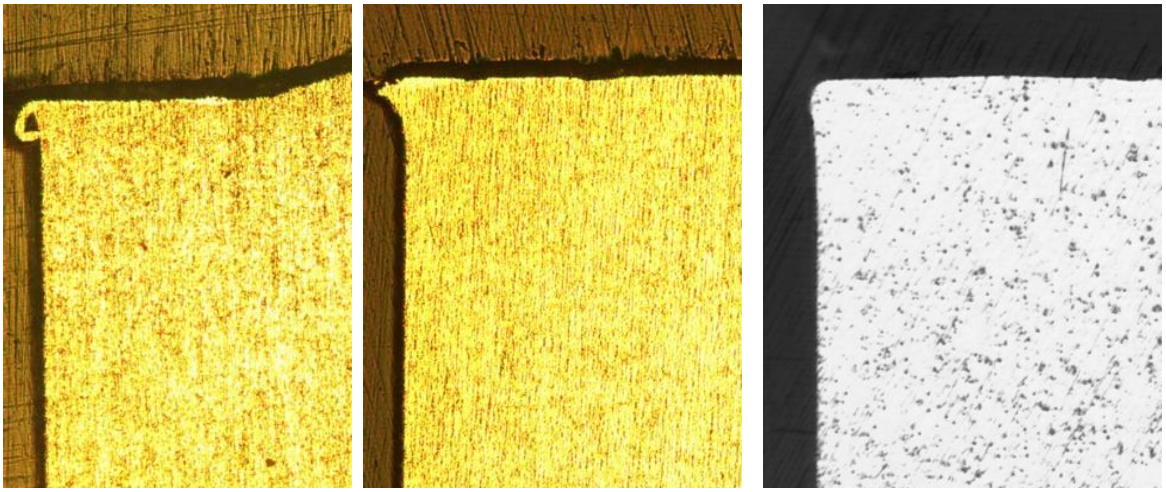

(a) Curling Burr (b) Triangular Burr (c) Bulge Burr

Figure 14. Different Types of Burrs Found on the As-Drilled Holes

The data was sorted by variable, each criterion was averaged over the variable, and the absolute value of the difference was calculated (e.g., all the roughness values for one operator were averaged, and all the roughness values for the other operator were averaged). The differences were compared and ranked. From these preliminary results, it was concluded that the pilot hole was clearly the most significant factor, followed by pressure, drill length, speed, and bit condition, in that order.

3.1 DEVELOPMENT OF HOLE-DRILLING METRICS.

During this study, four hole-quality metrics were developed: roughness, conicality, number of gouge marks, and angle of gouge marks. In addition, burr sizes and geometries were recorded, since three distinct burr types were easily distinguished, both at the entry and exit faces of the coupons.

Burrs may act as crack initiation sites. They may appear on the exit face (the side of the hole which the bit exits), the entry face, or both. The most noticeable type of burr is the curling burr, since it is long and slender and is usually found curled up like a cresting wave (figure 14(a)). This burr is believed to be the result of material from the end of the hole being pushed out and away from the bit as it exits the coupon, and is thought to have little correlation with residual stress levels induced during drilling. The triangular burr (figure 14(b)) may be formed in a similar manner as the curling burr. However, the base of the burr is wider than the burr is long. This burr may be more indicative of axial stresses induced during drilling, since it extends farther away from the bore of the hole. The bulge burr is composed of a hump outside the bore (figure 14(c)). This burr is thought to have a significant correlation to residual stresses in the hole, especially to axial stresses.

One advantage to correlating burrs with residual-stress levels is that the measurement of burrs can be done easily and nondestructively, since they appear outside the bore of the hole. The removal of burrs is an added machining expense, and the reduction of burr formation has been the subject of a number of investigations, so a literature review was conducted. A study by Min, et al. [32] identified three types of exit burrs, which correspond to the triangular and curling burrs and was attributed to small-scale plasticity at the exit face. Kim, et al. [33] identified the same types of burrs, but also recognized the importance of the entry burr, instead of restricting the analysis to burrs formed on the exit face. The paper stated that high feed rates, cutting speed, and tool wear increase the burr size. Also, smoothness of chip flow through the hole decreases burr size, indicating that burr formation is more than just a small-localized phenomenon. Ko and Lee [34] developed a different burr type classification, which was related to the presence or absence of a burr cap—a thin remnant of material pushed aside by the drill tip. This study attributed burr formation to material properties and drill geometry, as well as cutting conditions. None of these papers, nor any others found, explained the formation of the bulge burr.

The desire was to develop metrics that quantified hole quality. Since the effect of the size and shape of the burr on fatigue life could only be speculated, it was not used as a hole quality metric. However, the burr data was recorded and will be compared with fatigue-life and residual-stress data after those tests are performed.

Several different methods of measuring surface roughness were considered, but were rejected due to complications with the curved geometry of the holes. The metric decided upon was the ratio of the traced surface of the hole to the length of a straight line drawn across the bore, as shown in figure 15. The drilled holes were cut into two sections by EDM, polished, and mounted in epoxy. The holes were photographed with an optical microscope equipped with a digital camera and were analyzed with imaging software. The roughness was measured on each side of the cut bore, and the average value of the two sides was used. To determine the

endpoints of the traced and straight line used for measurement, edge lines were drawn along the entry and exit faces. The traced line was started at the intersection of the edge line and the hole bore and ended at the intersection at the other side of the hole. The imaging software traced the surface and calculated the trace length. A straight line was then drawn between the same two intersection points used for the trace line, and the length was again calculated using the imaging software. The trace-line length was then divided by the straight-line length, resulting in a number greater than or equal to 1. The process was repeated for the opposite side of the hole, and the average of the two values was calculated.

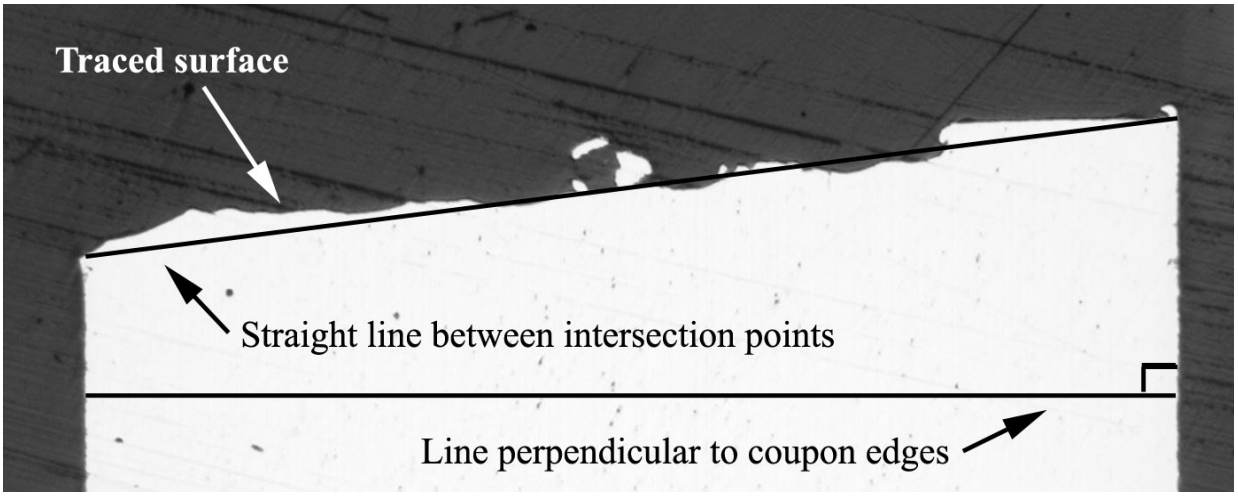

Figure 15. Roughness and Conicality Measurements

It was discovered that the typical hand-drilled hole was not only drilled at a slight angle from normal to the surface, but also had a larger diameter at the entry side than at the exit side. Thus, these holes were more like sections of a cone. Thus, conicality was used to describe the next metric. In production, the amount of deviation from normal, or angularity, is important, because highly angular holes may not accept a rivet. This angularity appears to be an issue of operator negligence, rather than a result of drilling variables such as bit sharpness. A conical hole, however, may have more of an effect after production. It may allow the fastener to loosen, reducing the fatigue life. A conical hole deviates from the ideally, straight hole, just as a rough hole does from an ideally smooth one (roughness factor = 1.0). Measuring this angle was straightforward. A line perpendicular to the two edge lines already drawn for the roughness measurements was added, and the difference between the angle of this perpendicular line and the angle of the straight line connecting the endpoints was calculated. Again, the imaging software gave the angle measurements. If the endpoint line angled towards the bore center at the exit face, the angle was considered positive. If it angled towards the bore center at the entry face, the angle was considered positive. This same angle was calculated on the opposite side of the bore, and the two angles were added (figure 15). Thus, a positive final angle meant that the hole had a larger diameter at the entrance than the exit, and the angle itself was the angle between the opposite edges of the cone.

The next two metrics, gouge angle and gouge number, required a different perspective on the hole. For these, the unmounted half of the hole was placed in the microscope, and a picture was

taken of the surface of the bore, rather than of its profile. It was also noticed that many of the holes had one or more gouges along the bore, the result of the bit cutting into the bore as the operator's hand strayed from normal. These gouges presented opportunities for large stress concentrations. Even with a visual inspection, grooves could be seen spiraling through the bores of the holes. Another common characteristic, noticeable to the eye, was relatively smooth, flat, and cylindrical section at the exit end of the holes. As viewed from the profile pictures, this region looked like a raised, flat region, and thus was labeled the plateau. This plateau was likely the result of the drill punching through the material at the end as soon as the tip of the drill sufficiently pierced through the specimen. This is substantiated by the absence of a plateau in the baseline set, which was machine drilled at a constant feed rate. These features are difficult to quantify, since they have complex and differing geometries. Therefore, after much consideration, the following two metrics were used.

The first, a count of the number of gouge marks was simple—the more gouges present, the higher the probability that a crack would initiate at one of these points. The bore surface was lit from an angle to reduce glare and bring out the surface features. This readily identified the gouges, which contrasted well above the roughness of the surrounding surface. Unfortunately, a camera is inferior to the human eye, and does not resolve the gouge marks as clearly; but even in the darker images, it was easy to count the gouges after some practice, as shown in figure 16.

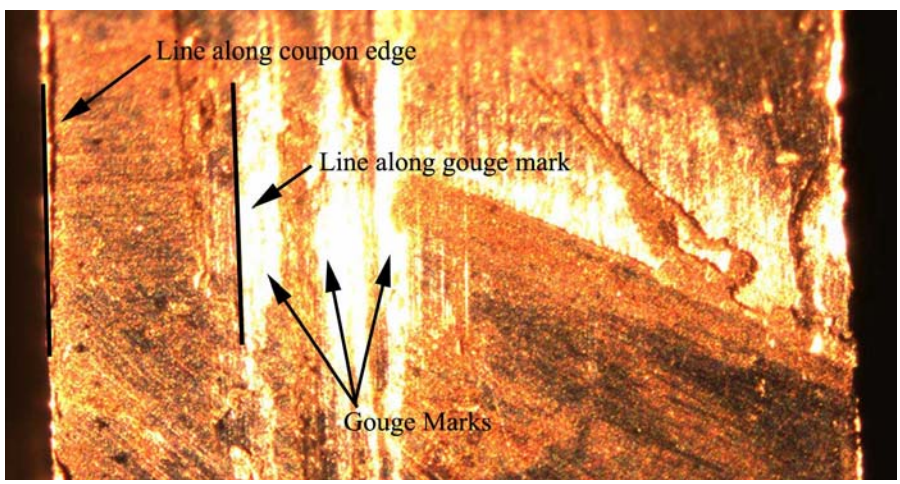

Figure 16. Typical Gouge Angle and Gouge Number Measurements

The second metric measured the angle of the gouges. As the angle approaches 90 degrees, or the drilling axis, the gouge essentially becomes a notch. At zero degrees, the gouge is oriented along the loading axis and has minimal effect. To measure this angle, a line was first drawn along one face of the specimen, and another was drawn along a gouge mark—either the best-defined mark, or the one with the highest angle, if there was a difference, which was rare. The difference between the angles of the two lines was calculated.

3.2 DRILLED-HOLE QUALITY RESULTS.

The results from the hole quality study are tabulated in table 1. Results were calculated using a software package to conduct an analysis of means; thus, the results in table 1 are based on the average values of each variable/factor combination.

Table 1. Summary of Metrics for Hand-Drilling Experiments

Variable	Roughness	Conicality	Gouge Angle	Gouge Number	Overall Score
Operator A	1.049	6.2	4.3	1.9	
Operator B	1.051	6.3	2.8	1.1	
Difference	0.002	0.0	*1.5*	***0.8***	
p-value	0.955	0.968	*0.127*	***0.002***	
Score	**0.012**	**0.008**	**0.315**	**0.617**	**0.238**
No pilot	1.065	7.8	5.4	1.3	
Pilot hole	1.035	4.8	1.8	1.7	
Difference	0.031	***3.0***	***3.5***	*0.4*	
p-value	0.341	***0.000***	***0.000***	*0.159*	
Score	**0.197**	**0.737**	**0.762**	**0.292**	**0.497**
Long bit	1.048	5.3	3.7	1.4	
Short bit	1.051	7.2	3.5	1.6	
Difference	0.003	***1.8***	0.2	0.2	
p-value	0.926	***0.030***	0.827	0.509	
Score	**0.020**	**0.443**	**0.046**	**0.137**	**0.161**
New bit	1.024	5.7	3.5	1.3	
Old bit	1.045	6.7	3.7	1.7	
Difference	*0.021*	1.0	0.2	***0.4***	
p-value	*0.117*	0.240	0.848	***0.097***	
Score	**0.132**	**0.242**	**0.040**	**0.342**	**0.189**
High pressure	1.044	5.6	3.0	1.4	
Low pressure	1.055	6.8	4.1	1.5	
Difference	0.012	*1.2*	1.1	0.1	
p-value	0.720	*0.157*	0.264	0.679	
Score	**0.075**	**0.291**	**0.231**	**0.086**	**0.171**
Full speed	1.047	6.3	3.6	1.5	
Stopped	1.053	6.2	3.6	1.5	
Difference	0.006	0.0	0.0	0.1	
p-value	0.860	0.970	0.999	0.806	
Score	**0.037**	**0.008**	**0.000**	**0.052**	**0.024**

Table 1. Summary of Metrics for Hand-Drilling Experiments (Continued)

Ranking	Roughness	Conicality	Gouge Angle	Gouge Number	Overall
1	Pilot	Pilot	Pilot hole	Operator	Pilot
2	Bit condition	Bit length	Operator	Bit condition	Operator
3	Pressure	Pressure	Pressure	Pilot hole	Bit condition
4	Withdrawal speed	Condition	Bit length	Bit length	Pressure

The first step in the analysis was to calculate the averages for each combination. For example, take the variable/factor combination of Operator versus Roughness. For the Operator variable, half of the 96 holes were drilled by Operator A, the experienced mechanic; and the other half were drilled by Operator B, the novice. Operator A produced holes with an average roughness of 1.049, while Operator B produced holes of average roughness 1.051. Each combination in the table represents the average of two halves of the entire population. Operator A drilled half of his holes with a pilot hole, just as Operator B did, and so on, with every combination.

Once the averages were calculated, the absolute value of the differences was calculated. For each unit, when one of the two variable options deviates from the population average, the other option must deviate an equal amount in the opposite direction. The difference represents the portion of population variability that is the result of a given variable. Comparing these differences among variables shows the relative importance of each variable.

The p-value, a measure of the statistical significance of the difference of means, was also calculated for each combination. The p-value is the probability that there really is no difference between the means, considering the variability of the data. A small p-value, generally recognized as 0.10 or less, indicates that there is very low plausibility that the variable has no effect at all on the factor. A p-value from 0.11 to 0.20 shows marginal significance. The variables with low p-values are highlighted in the table. P-values between 0.11 and 0.20 are italicized, while those less than 0.10 are in bold italics.

Next, a method for normalizing the factors was devised. Since the four metrics used were unlikely to be the only factors of hole quality affected, and the six variables considered were unlikely to be the only variables affecting hole quality, a statistical approach was used for the factor normalization. For each metric, the standard deviation of that factor was calculated over the entire population. The difference of means for each variable was then divided by the standard deviation. This number is labeled “Score” in table 1. The scores were averaged across metrics to yield an Overall Score. An alternate method would be to use a “pooled standard deviation” calculation, which takes the variability of the separate variables into account. However, it is the overall metric variability that should be normalized, so the population standard deviation is a more appropriate choice. The normalized scores are charted graphically in figure 17(a)-(e).

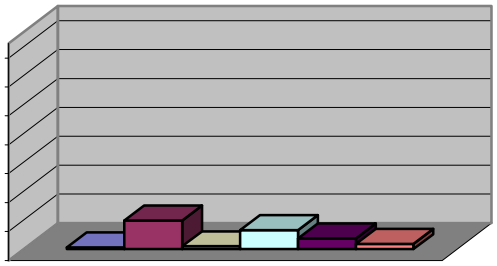

(a) Roughness

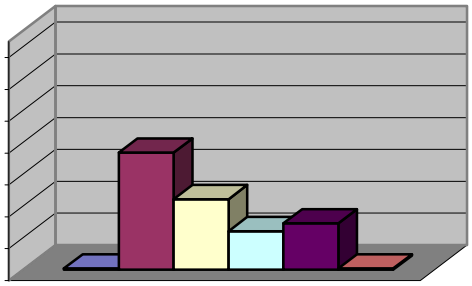

(b) Conicality

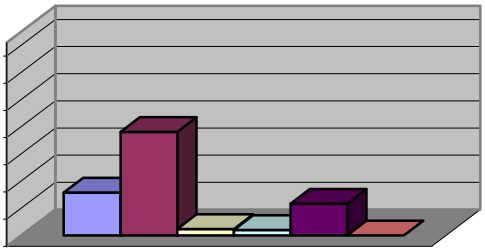

(c) Gouge angle

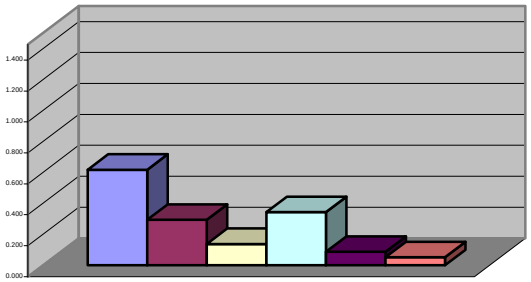

(d) Gouge number

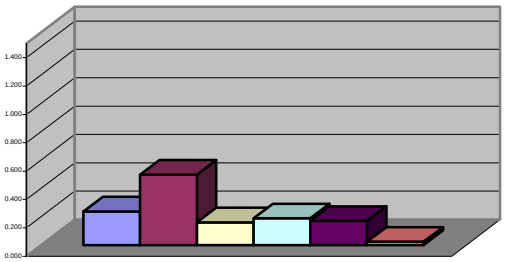

(e) Overall results

Variables in all charts, from left to right:
Operator, Pilot Hole, Bit Length, Bit Condition, Pressure, Withdrawal Speed

Figure 17. Summary of the Hand-Drilled Hole Rankings for the Various Metrics

Using the individual metric scores and the overall score, the variables were ranked to determine their relative influences. The ranking is at the bottom of table 1. The pilot hole is by far the most significant variable. This is logical, since the pilot hole removes a large volume of material, reducing the amount of cutting (i.e., deformation) to be done in the final drilling and producing a much smoother hole. A pilot hole also serves as a guide for the final drilling, reducing the conicality of the hole. As for the angle of gouge marks, the results for the pilot hole are counter-intuitive. The mechanics remarked on how much easier it was to drill a hole over a pilot hole, which should result in faster drilling. A hole drilled faster should make gouges at a steeper angle. However, holes drilled without a pilot hole are significantly steeper than those drilled with a pilot hole. The operator variable ranked second overall. It was hypothesized early on that human factors would produce large differences. Identifying human variables, however, is very complex and is outside the scope of this study.

The bit length, bit condition, and pressure variables ranked closely in the overall score. Bit condition greatly affected roughness, as expected, and also produced significantly different numbers of gouges, as expected. Bit condition may also greatly affect residual hoop stresses, since a sharp bit should cut cleanly through the material, while a dull bit should cause much more shearing. The mechanics also commented on how much harder it was to drill with a dull bit, and the long, spiraling chips also indicate that the dull bit was deforming the surface much more than the new bits, which produced characteristically small chips. Bit length scored high in conicality, with short bits resulting in much more conical holes than long bits. This is a human interaction, as shown in the machine drilling results (table 2). A long bit allows the operator to "eyeball" the drilling—allows him to see his work better—and gives him a longer lever arm on the drill, which makes it easier to correct the drill. Pressure applied to the drill ranked fairly consistently across the metrics, giving it a fairly high score in the end. Pressure, like bit length, is unlikely to affect hoop stresses, although pressure probably affects axial residual stresses.

Surprisingly, bit speed upon withdrawal had very little influence on any of the metrics. Although it was believed that stopping the bit before withdrawing could greatly roughen the surface. It may be that the bit traced along existing gouges, making them steeper and more likely to be crack initiation points, but an effective method of quantifying the sharpness of the gouges could not be established. However, if this was the case, withdrawal speed should have had a significant effect on roughness, as a steeper gouge would increase the surface area. As shown in tables 1 and 2, no such increase occurred.

A set of 24 holes was drilled using a drill press at Delta Air Lines. This was done in much the same way as the above set of 96 holes previously described, except that Operator and Withdrawal Speed were eliminated as variables. Withdrawal Speed was eliminated because the bit was always kept spinning in a press, and Operator was eliminated because the press is automated, eliminating human effects. Also, Pressure was replaced with Feed rate. Measurement and analysis was performed just as before, and the results are charted and tabulated in figure 18(a)-(e) and table 2.

An interesting result to note is that the sum of the scores for conicality equals over 2.7. Three times the standard deviation is approximately 99% of a normal distribution. This suggests that the four variables considered make up the vast majority of the variables affecting conicality, at least in machine drilling. It is surprising that conical shapes were produced at all, considering that the bits were rigidly fixed in the press, and also that the rankings for conicality are identical to hand drilling for the four variables used. Also significant is that Roughness and Gouge Number both sum to about 1.9, which is about 95% of a normal distribution.

Table 2. Summary of Metrics for Baseline Experiments

Variable	Roughness	Conicality	Gouge Angle	Gouge Number	Average Score
No Pilot	1.074	3.9	6.0	1.9	
Pilot Hole	1.076	0.7	3.2	0.8	
Difference	0.003	3.2	2.9	1.2	
p-value	0.804	0.001	0.218	0.069	
Score	**0.106**	**1.245**	**0.511**	**0.739**	**0.650**
Long Bit	1.089	3.2	6.5	1.7	
Short Bit	1.061	1.5	2.7	1.0	
Difference	0.028	1.7	3.7	0.7	
p-value	0.004	0.108	0.105	0.311	
Score	**1.110**	**0.660**	**0.665**	**0.422**	**0.714**
New Bit	1.069	2.6	5.5	1.3	
Old Bit	1.081	2.0	3.7	1.3	
Difference	0.013	0.7	1.9	0.0	
p-value	0.240	0.546	0.427	1.000	
Score	**0.490**	**0.254**	**0.333**	**0.000**	**0.269**
High Feed	1.078	1.6	4.7	1.9	
Low Feed	1.072	3.0	4.5	0.8	
Difference	0.006	1.3	0.3	1.2	
p-value	0.589	0.212	0.913	0.069	
Score	**0.227**	**0.518**	**0.046**	**0.739**	**0.382**
Ranking	**Roughness**	**Conicality**	**Gouge Angle**	**Gouge Number**	**Overall**
1	Bit Length	Pilot Hole	Bit Length	Pilot/Feed Rate	**Bit length**
2	Bit Condition	Bit Length	Pilot Hole		**Pilot hole**
3	Feed Rate	Feed Rate	Bit Condition	Bit Length	**Feed rate**
4	Pilot Hole	Bit Condition	Feed Rate	Bit Condition	**Bit condition**

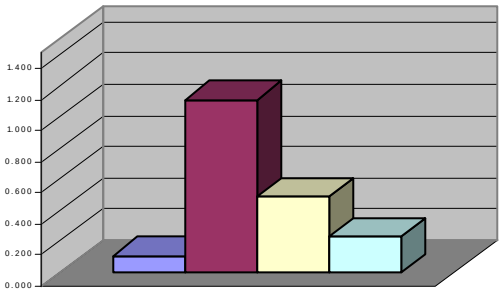

(a) Baseline roughness

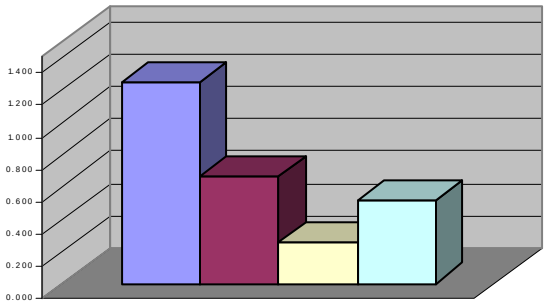

(b) Baseline conicality

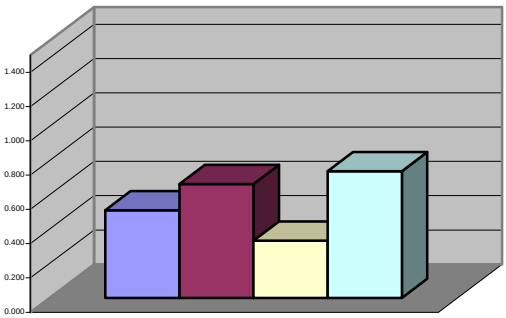

(c) Baseline gouge angle

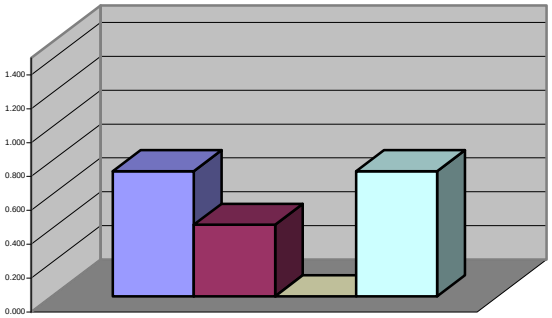

(d) Baseline gouge number

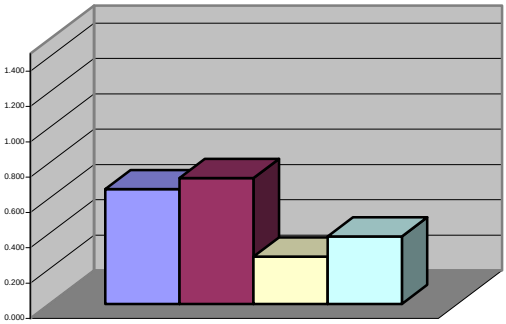

(e) Overall baseline

Variables in all charts, from left to right:
Pilot Hole, Bit Length, Bit Condition, Pressure

Figure 18. Summary of the Baseline-Drilled Hole Rankings for the Various Metrics

Bit Length replaced Pilot Hole as the overall most significant variable in the baseline test. The long bit caused a lot of chatter during the drilling, and probably produced rough holes. The longer bit also produced slightly triangular holes (figure 19(a) and (b)), which likely contributed to the conicality of the holes. This raises an interesting point. In hand drilling, the long bit resulted in a better hole (in regards to hole quality), since it reduced the conicality. In machine drilling, the long bit resulted in both a rougher and more conical hole.

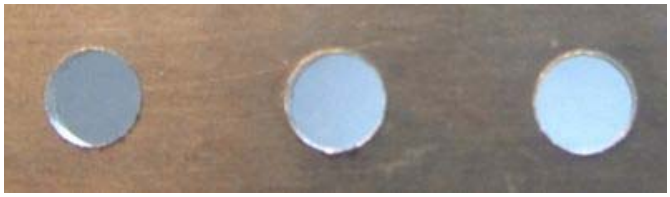

(a) Short bit

(b) Long bit

Figure 19. Examples of Holes Drilled with Short and Long Bits

4. FATIGUE TESTS ON SINGLE-HOLE SPECIMENS.

In literature review [13], no studies could be found on the magnitude or effects of residual stresses from the hole-drilling process. The measurement of residual stresses on pilot and test specimens, using X-ray diffraction, was not successful, mainly because the production-quality holes did not appear to exhibit significant residual stresses. Because of the absence of residual stresses in the production-quality holes, the project concentrated on hole-quality and life-prediction issues. However, to induce a residual-stress field of known magnitude, some single-hole test specimens were overloaded or underloaded to yield the hole and cause either compressive or tensile residual stresses.

In the hole-drilling study, eight variables were identified: (1) operator experience, (2) drill-bit condition, (3) drill-bit speed, (4) drill-bit length, (5) drill-bit pressure, (6) use of pilot hole, (7) drill block, and (8) the material. In addition, holes were drilled either by hand or by machine. Because the eight variables gave 192 different combinations and the project had only 90 specimens, a preliminary test program was designed to identify the most significant variables. The drilling block was eliminated because it is seldom used in practice. A design of experiments was used to reduce the number of test holes to 96. The drill-hole experiments and measurements identified four metrics: (1) surface roughness, (2) conicality, (3) gouge angle, and (4) number of gouges.

From the hole-drilling study, the fatigue test specimens (figure 7) had production-quality holes drilled either by hand or by machine for various combinations of the eight hole-drilling variables (see reference 13 for details).

To develop a control group of single-hole specimens that have nearly pristine hole surfaces, a group of specimens were drilled at NASA Langley Research Center using a three-drill process to minimize machining residual stresses. The specimens were then chemically polished with a procedure developed in the AGARD studies [28 and 29]. Fifteen LT orientation and 15 TL orientation single-hole specimens were drilled, polished, and tested at Georgia Institute of Technology.

4.1 CONSTANT-AMPLITUDE LOADING.

The polished and production-quality hole specimens were tested under constant-amplitude loading at three gross stress levels: (1) 172 MPa, (2) 145 MPa, and (3) 120 MPa, at $R = P_{min}/P_{max} = 0$ loading. However, the primary loading was the 145 MPa loading.

4.1.1 Polished Holes.

Figure 20 shows the results of tests conducted on the polished-hole specimens for both the LT and TL orientations. For comparison with data from the literature on single-hole specimens, made of the same material, data from Landers and Hardrath [35] are shown as open symbols. They had electropolished their specimens and conducted tests at two different hole diameter-to-width (D/W) ratios. The width and thickness of all specimens were identical, but the D/W ratio for the current specimens was slightly different. But the new chemically polished specimen results fell very close to the expected behavior, except for the four tests at the lowest stress level. Here, three specimens were tested for 3 to 4 million cycles and the tests were stopped. Only one test specimen failed early. However, the limited test results indicated that the orientation (LT and TL) may not be a significant factor in the fatigue behavior.

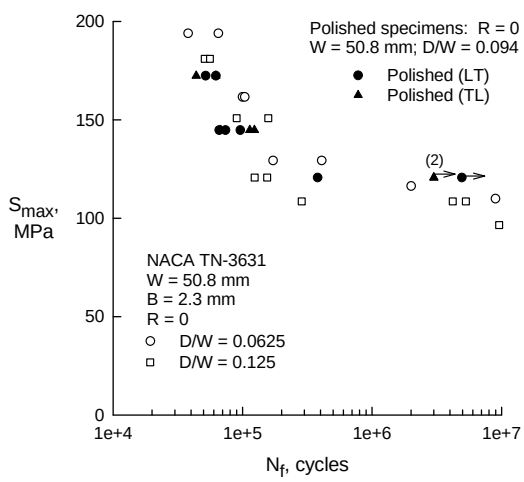

Figure 20. Comparison of Fatigue Lives for Electopolished and Chemically Polished Specimens Made of 2024-T3 Aluminum Alloy

4.1.2 Production-Quality Holes.

Results of the fatigue tests conducted on the production-quality drilled hole specimens are shown in figure 21. All of these tests were conducted in the LT orientation. Tests were conducted on specimens prepared with both new and old drill bits, with and without pilot holes, using either hand-drilled or machine-drilled holes. These results indicate that the fatigue lives are shorter than the electropolished specimens, presumably because of burrs and drilling marks on the holes. The drilling flaws appear to be more significant at the lower applied stress levels. The fatigue tests conducted on the production-quality drilled holes showed no significant difference in fatigue lives between the various drilling parameters, because the machining marks may have eliminated any residual stress affects, resulting in a shorter fatigue life compared to the polished hole specimens. The fatigue lives for the hand-drilled holes were shorter than the machined-drilled holes at the lowest stress level. Crack surfaces have been examined, and the majority of the cracks appear to have initiated along the bore of the hole, instead of the edge. The quality of the hole surfaces appear to be the controlling factor instead of residual stresses.

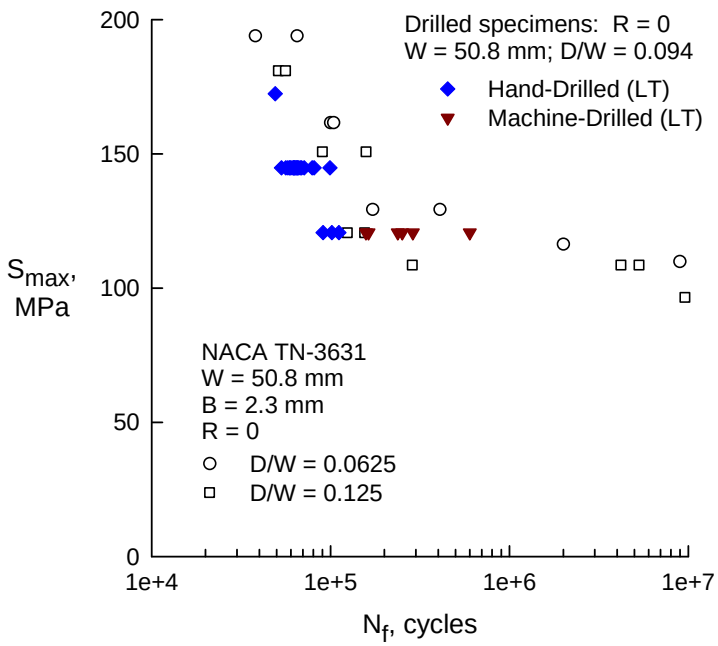

Figure 21. Comparison of Fatigue Lives for Polished and Production-Quality Open-Hole Specimens Made of 2024-T3 Aluminum Alloy

4.2 SPIKE OVERLOAD AND UNDERLOAD TESTS.

Because, the production-quality holes did not appear to have significant residual stresses, a group of polished-hole specimens were tested with either a 1.7 overload or a 1.7 underload prior to conducting the constant-amplitude fatigue test. The overload and underload yielded the material at the edge of the hole and produced either a compressive or tensile residual-stress field. After the one cycle of prior loading, the specimens were then subjected to a cyclic maximum applied gross stress of 145 MPa at $R = 0$ until failure.

The overload and underload fatigue test results are shown in figure 22, as solid symbols. Again, these results are compared with the previous electropolished specimens from National Advisory Committee for Aeronautics (NACA) TN-3631. As expected, the tensile overload caused significant compressive residual stresses at the edge of the holes and produced a large increase (order of magnitude) in the fatigue lives. However, the tests exhibited a large amount of scatter. This may have been due to the microcracks having SIF levels very close to the threshold for the 2024-T3 aluminum alloy. On the other hand, the compressive underload, which caused a tensile residual stress field at the edge of the hole, produced about a factor of 2 reduction in fatigue life.

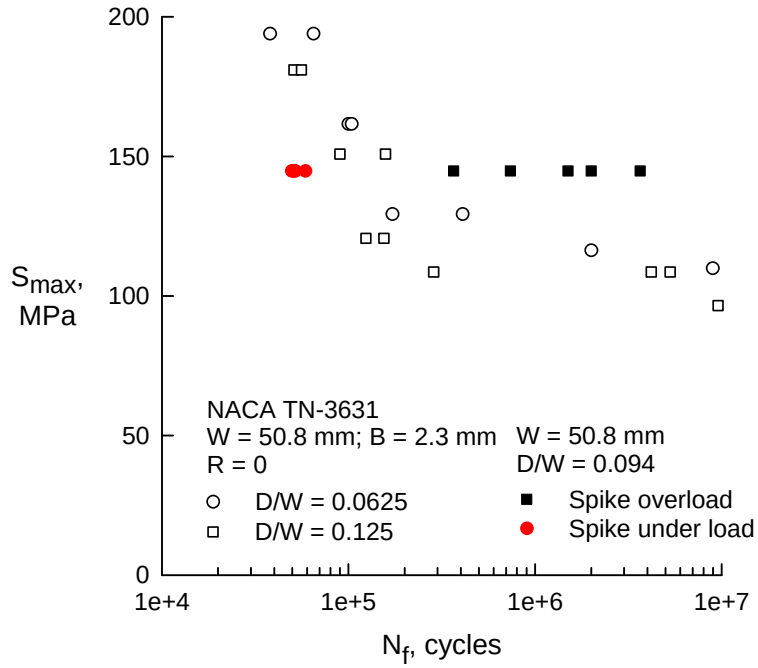

Figure 22. Comparison of Fatigue Lives for Polished Open-Hole Specimens Subjected to an Initial Overload or Underload Made of 2024-T3 Aluminum Alloy

Later, these tests will be analyzed with the elastic-plastic finite element method to study the residual-stress fields under the overload and underload conditions; and fatigue life analyses will be made with the FASTRAN code.

5. THREE-DIMENSIONAL WEIGHT FUNCTION ANALYSES.

A three-dimensional weight function code, K3D, [18-23] was enhanced herein to calculate SIFs due to (1) remote tension, (2) remote bending, (3) wedge-loading (to simulate rivet loading), and (4) an arbitrary residual-stress field for both corner and surface cracks at an open hole. The recent SIF solutions, developed by Fawaz and Andersson [24 and 25], for very deep corner cracks (a/t = 0.1 to 0.99), in a plate with an open hole subjected to remote tension and bending loads, were used to calibrate the new weight function code. The K3DL code, see appendix A, is used to generate SIF solutions for the crack configuration and loading of interest. These SIF solutions are then used with the FASTRAN life-prediction code to calculate fatigue crack growth and fracture.

The SIF results are presented here in the form of the dimensionless F parameter, the boundary-correction factor, as

$$F_i(\phi) = K(\phi) / [S_i \sqrt{(\pi\, a/Q)}] \tag{1}$$

where ϕ is the parametric angle, Q is the elliptic integral of the second kind, and S_i is a characteristic stress used to normalize the SIFs. For remote tension, $S_i = S_t$; for bending, $S_i = S_b$; and for wedge loading in the hole, $S_i = S_p$. The stress, S_p, is the pin-bearing stress P/(DB) in the hole, where P = applied load, D = hole diameter, and B = plate thickness. (Note that for a surface crack at an open hole, t = one-half the plate thickness; but for a corner crack at an open hole, t = full plate thickness.)

5.1 CALIBRATION OF WEIGHT FUNCTION.

Weight functions for a general case for this particular WFM is:

$$W_i = W_{2D,i}^{fixed} + T_i(r_i)(W_{2D,i}^{free} - W_{2D,i}^{fixed}) \tag{2}$$

where, r_i is a dimensionless restraining area, $r_i = r_i$(a/c, a/t, r/t, c/b); T_i is a monotonic transition function having the property of $T_i(\infty) = 0$ (used currently) and $T_i(0)=1$. Although this WFM has an exclusive advantage to avoid reference solutions and provide independent results in many cases, T_i needs to be determined in a general situation by calibration with reference solutions. The extensive results from Fawaz and Andersson [24 and 25] using highly refined FEA were used to calibrate the corner crack weight function. But the first step was to identify the major deviations between the current WFM and the FEA results.

Comparisons of the original WFM with the Fawaz-Andersson FEA results and the Newman-Raju equations [17] were made for two load cases: remote tension and remote bending. The crack configuration parameters considered were r/t = 1; a/c = 0.25, 0.333, 0.5, 1, 2, 3, and 4; a/t = 0.1 to 0.99, where applicable. Of ~130 cases involving ~400 solutions compared, a few are discussed here for a/c = 0.5 and 2; a/t = 0.1 and 0.95. It is noted that, unlike any other WFMs, the weight function results presented here are independent solutions without using any reference solutions for the crack configuration considered. For shallow cracks (small a/t ratios), the current WFM was in good agreement with the FEA results for tension and bending loads and the Newman-Raju equations for tension and a wide range in a/c ratios. But for the deep cracks (a/t >0.9 and a/c <2), there were large differences between the WFM and FEA results for both tension and bending loads. Thus, the corner crack weight function needed to be calibrated for deep cracks. For a/c = 2, the WFM results were in fair agreement with the FEA results. The extensive comparisons lead to the following three observations:

- Current weight function results are accurate for small a/t ratios for a wide range in a/c ratios;

- For a/c >2, all the results from the weight function method are accurate and no calibration of the weight function was necessary;

- Calibration of the weight function was necessary for a/c <2 with medium to deep cracks (the a/t range requiring calibration depends on a/c).

These observations are consistent with the expectations based on the characteristics of this particular WFM and experiences with other comparisons. The weight function for a corner crack at an open hole was developed and implemented into the K3DL code. Extensive comparisons have been made among the Fawaz-Andersson [25] FEA results, the improved WFM, and the Newman-Raju [17] equations for remote tension and remote bending. The calibration was based on the FEA results from Fawaz and Andersson for remote tension. The calibrated weight function produced very satisfactory agreement with the FEA results over a wide range in crack configuration for tensile loading. The bending results were not as good as tension, but still acceptable. Very little can be done about the bending case because the weight function is independent of load and cannot be adjusted for both tension and bending loads. Five a/c ratios were considered: 0.25, 0.5, 1, 1.5, and 2. The calibration function is a smooth, monotonic function of a/c and a/t and should behave well in between these a/c ratios.

5.2 COMPARISON OF K3DL WITH FEAs AND EQUATIONS.

The definitions of the corner crack configuration parameters are shown in figure 23. The K3DL code can analyze the corner crack configuration for a single corner crack (c1) or two symmetric corner cracks (c2) emanating from the hole in a plate subjected to remote tension, remote bending, wedge loading in the hole, and under any arbitrary residual-stress distribution. However, the solutions from the current code are basically for a cracked hole in an infinite body, and finite width corrections will have to be applied to these solutions for practical applications. Typical comparisons for remote tension and bending are shown in figures 24 to 29 for r/t = 1 and a/c = 0.5, 1 and 2 for a/t = 0.1 and 0.95, respectively. The figures show the Fawaz-Anderson FEA results, the previous developed equations by Newman-Raju [17] for remote tension and bending, the Zhao-Newman-Sutton equation [36] for remote bending, and the new K3DL results. (Note that one-half of the plate width is denoted as "b" in the K3DL code, but W or 2w is plate width in the current report.)

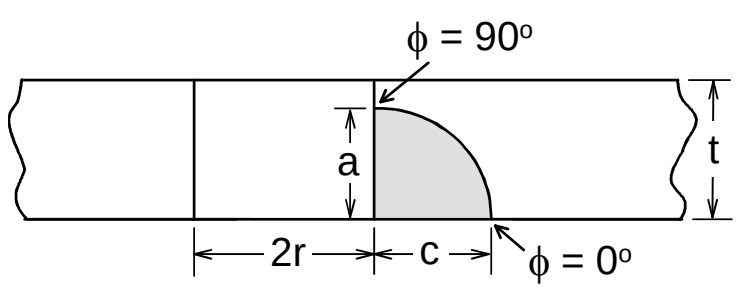

Figure 23. Definition of Crack Configuration Parameters for a Corner Crack at Open Hole

Figure 24(a) shows the boundary-correction factor, F_t, as a function of the parametric angle, ϕ, for the case of two symmetric corner cracks at an open hole in a very wide plate subjected to remote tension with a/c = 0.5 and a/t = 0.1. The square symbols are the Fawaz-Andersson FEA results, the solid curve is the Newman-Raju equation, and the circular symbols show the K3DL

results. The FEA results produce the "so-called" boundary-layer effect where the crack intersects a free surface. At the free surface, the SIF must be zero, because of the loss of the square-root singularity [37]. Thus, the peak value from the FEA results, which is slightly below the free surface, should be compared with the peak value from the K3DL code. For this case, the Newman-Raju equation produces lower SIFs over the complete crack front, whereas the K3DL code matches the FEA results very well.

Figure 24(b) shows the boundary-correction factor, F_b, as a function of the parametric angle, ϕ, for the case of two symmetric corner cracks at an open hole in a very wide plate subjected to remote bending, again, with a/c = 0.5 and a/t = 0.1. Here, the dashed curve shows the Newman-Raju [17] equation for bending, and the solid curve is an equation developed by Zhao, et al. [36]. The Newman-Raju equation overestimates the SIFs for shallow crack (a/t < 0.2) for remote bending. The Zhao, et al. equation was developed to correct this deficiency. Again, the K3DL code matched the FEA results very well.

Figure 25(a) and (b) show similar comparisons for a very deep (a/t = 0.95) crack for remote tension and bending loads, respectively. The Newman-Raju bending equations agree fairly well with the FEA results. But the Zhao, et al. equations, which were based on the original weight function code, had significant deficiencies. The K3DL code results show some differences from the FEA results, but the results are acceptable. Figures 26 to 29 show similar comparisons for a/c ratios of 1 and 2 for shallow and deep cracks. The K3DL code results matched the FEA results fairly well over the complete range of crack configuration parameters.

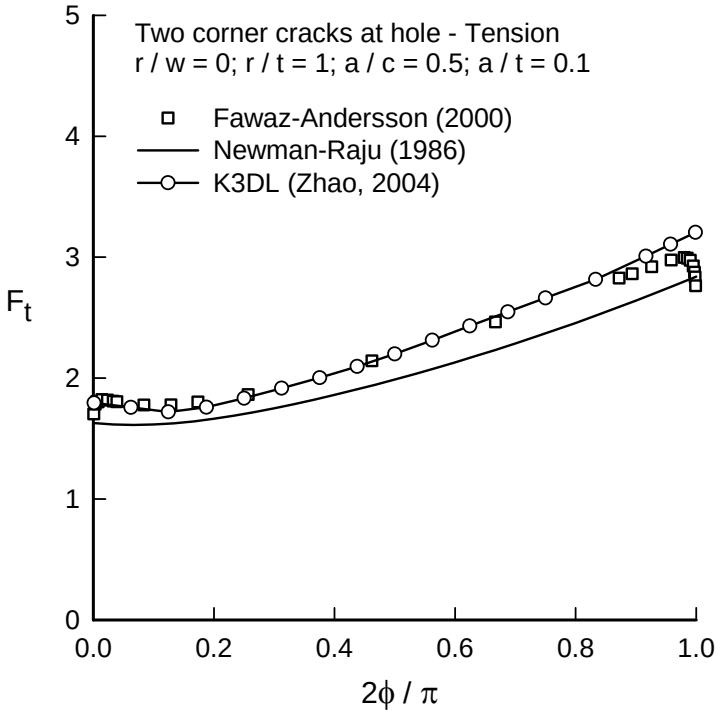

(a) Remote Tension

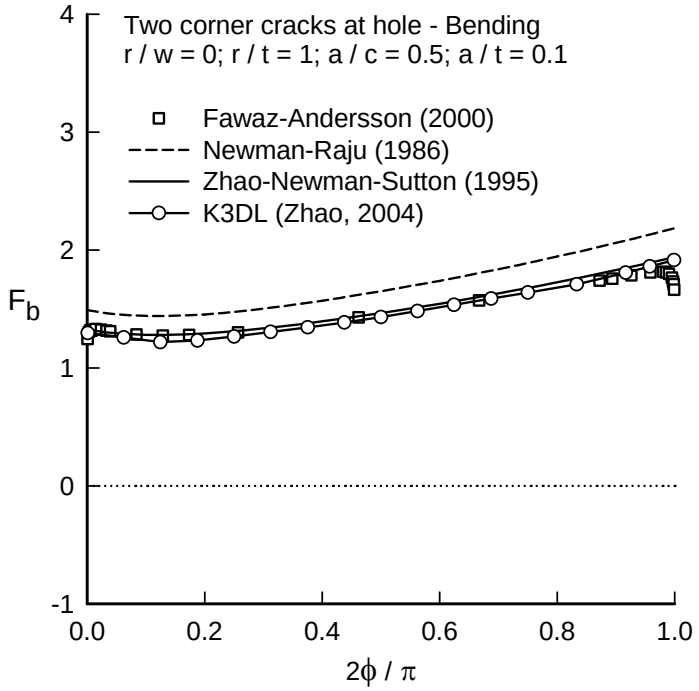

(b) Remote Bending

Figure 24. Comparisons of Boundary-Correction Factors for a/c = 0.5 With a/t = 0.1 Under (a) Remote Tension and (b) Remote Bending

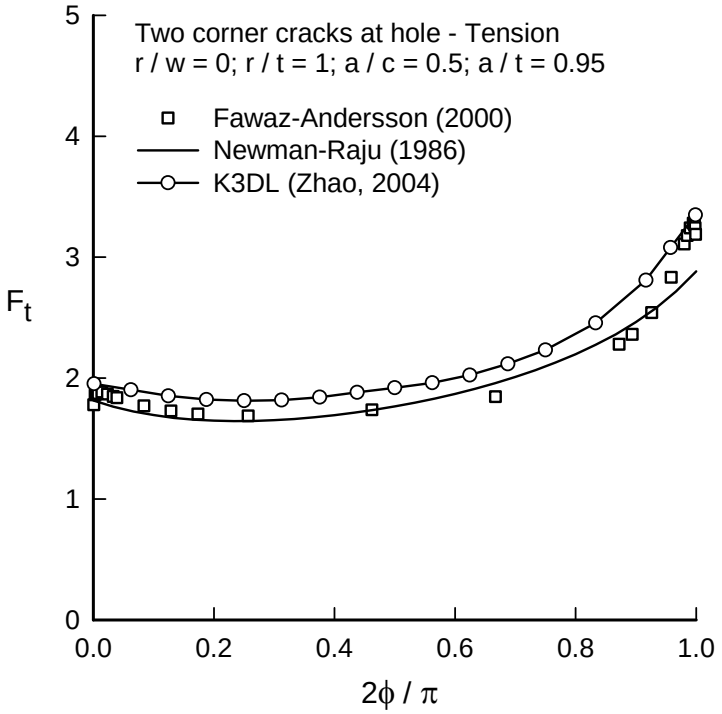

(a) Remote Tension

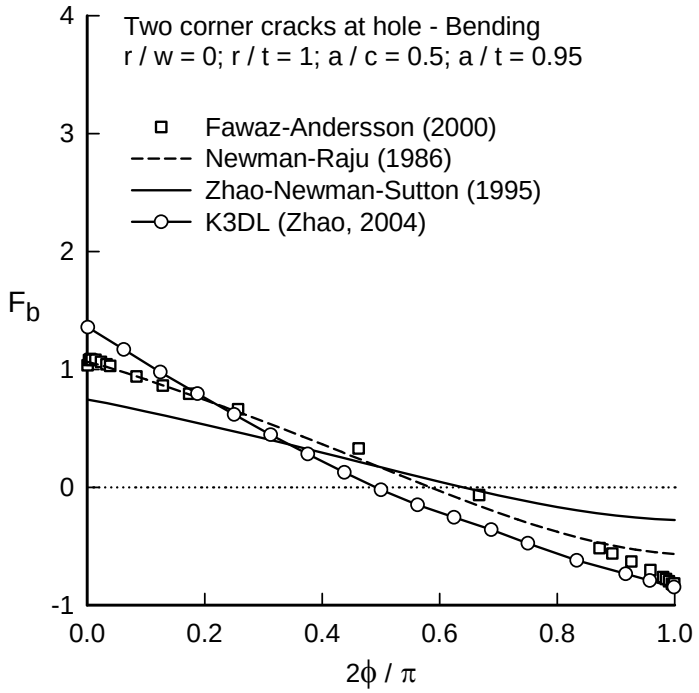

(b) Remote Bending

Figure 25. Comparisons of Boundary-Correction Factors for a/c = 0.5 With a/t = 0.95 Under (a) Remote Tension and (b) Remote Bending

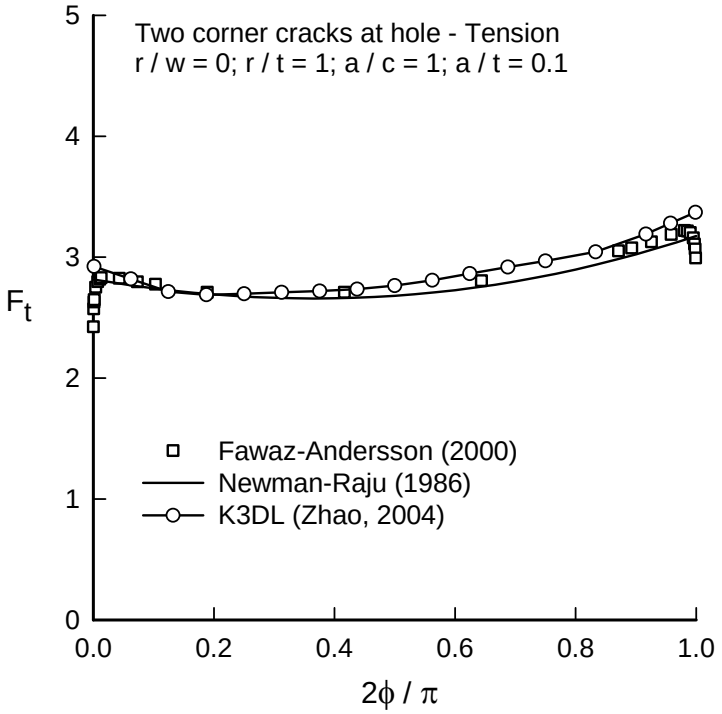

(a) Remote Tension

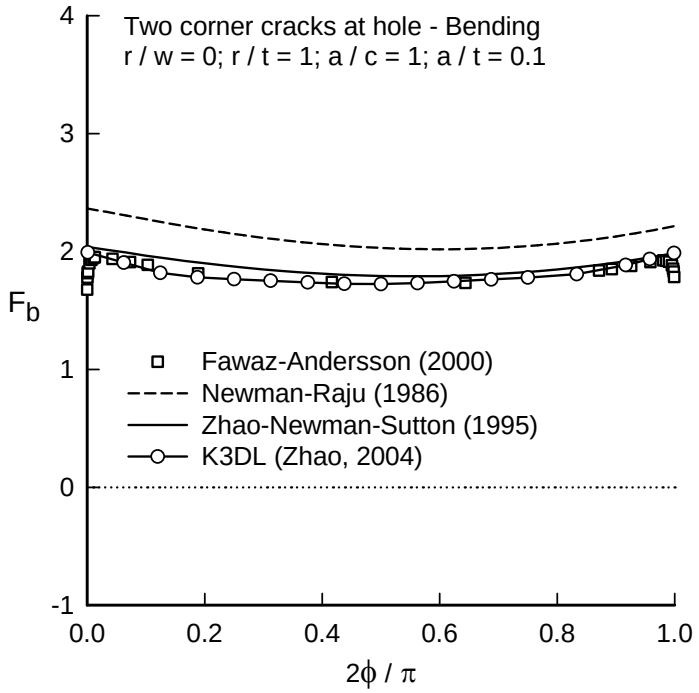

(b) Remote Bending

Figure 26. Comparisons of Boundary-Correction Factors for a/c = 1 With a/t = 0.1 Under (a) Remote Tension and (b) Remote Bending

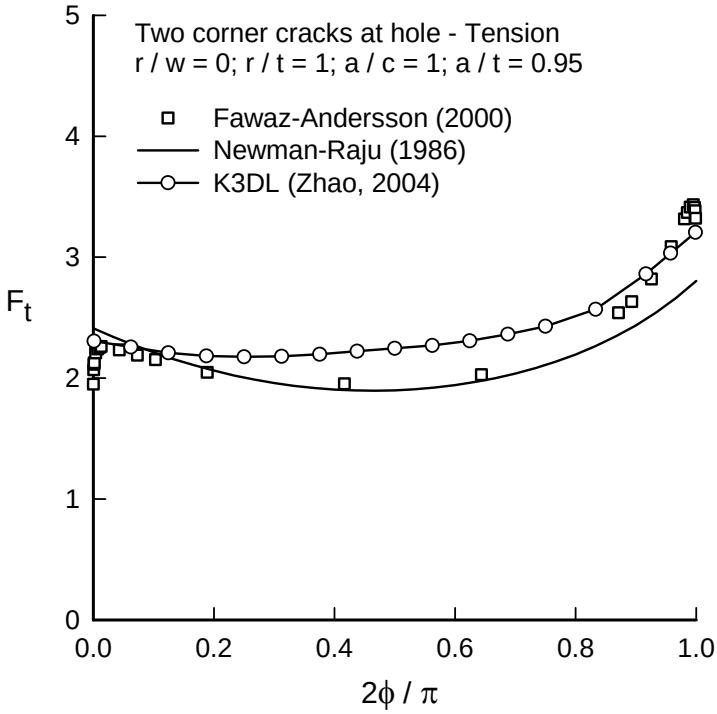

(a) Remote Tension

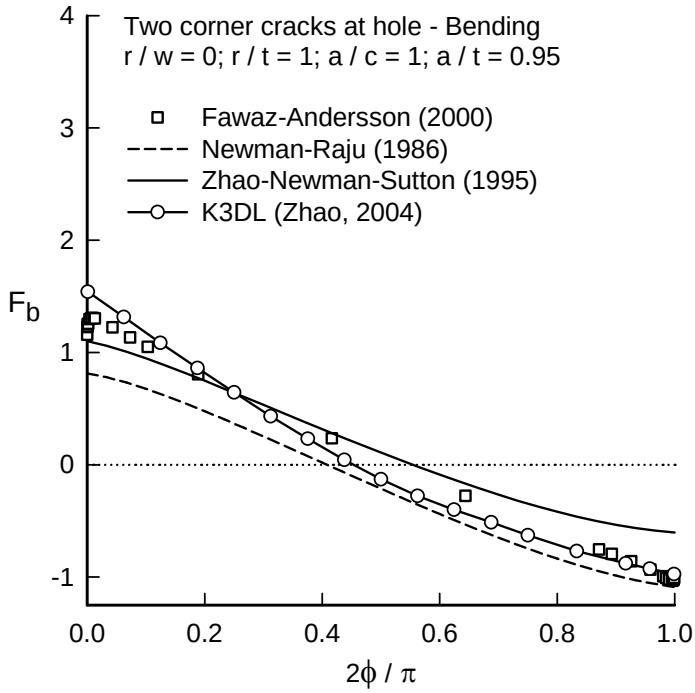

(b) Remote Bending

Figure 27. Comparisons of Boundary-Correction Factors for a/c = 1 With a/t = 0.95 Under (a) Remote Tension and (b) Remote Bending

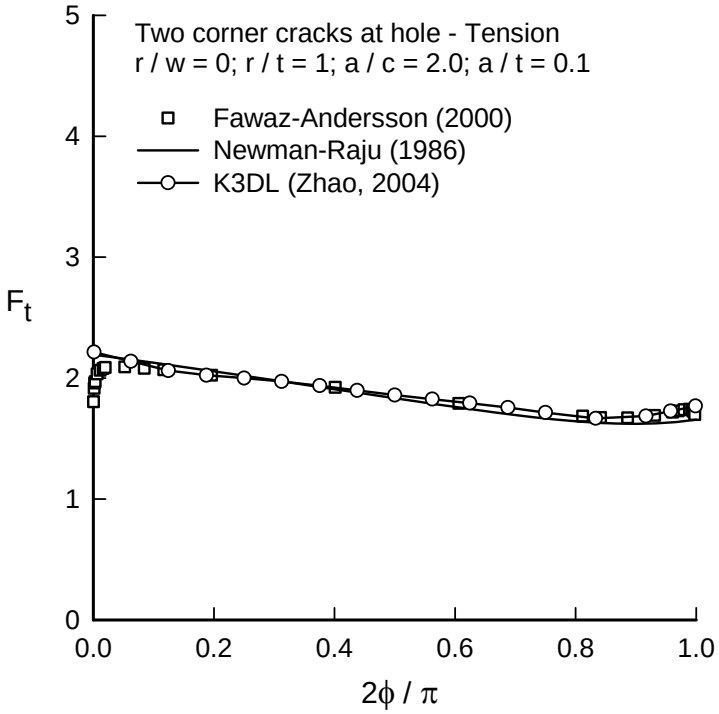

(a) Remote Tension

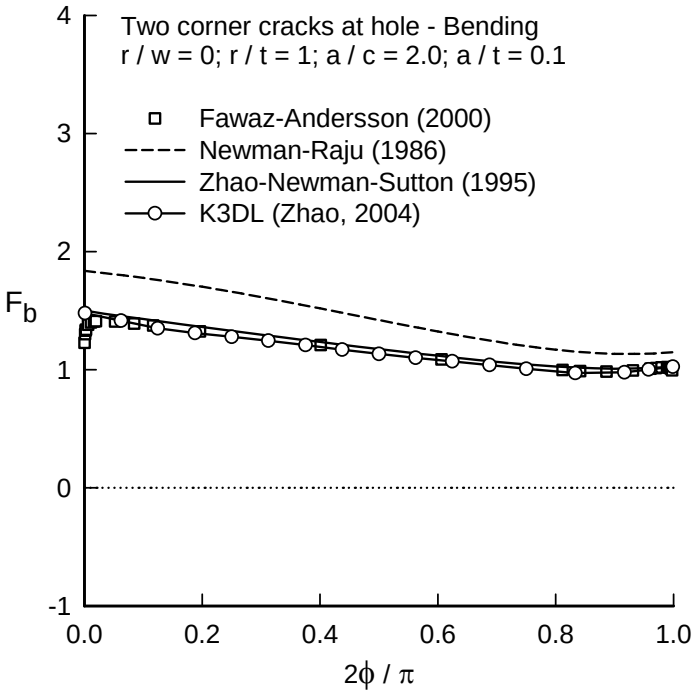

(b) Remote Bending

Figure 28. Comparisons of Boundary-Correction Factors for a/c = 2 With a/t = 0.1 Under (a) Remote Tension and (b) Remote Bending

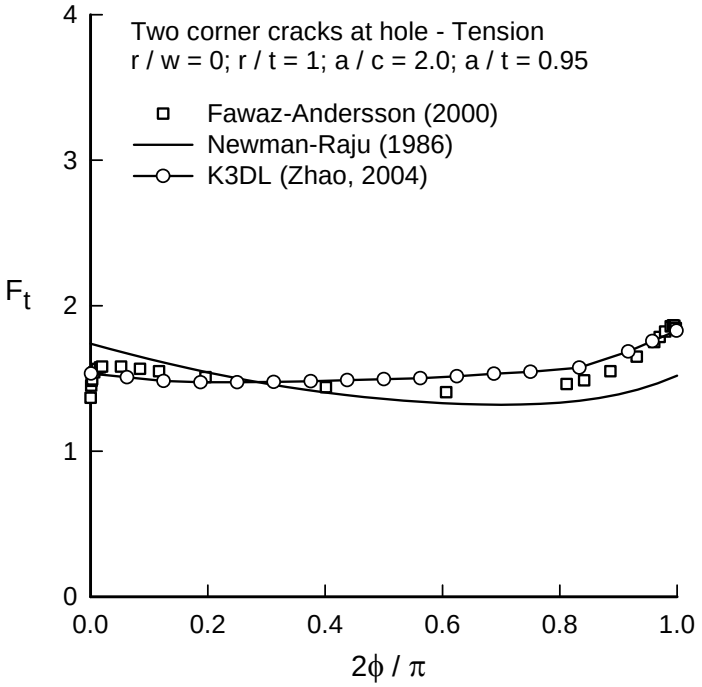

(a) Remote Tension

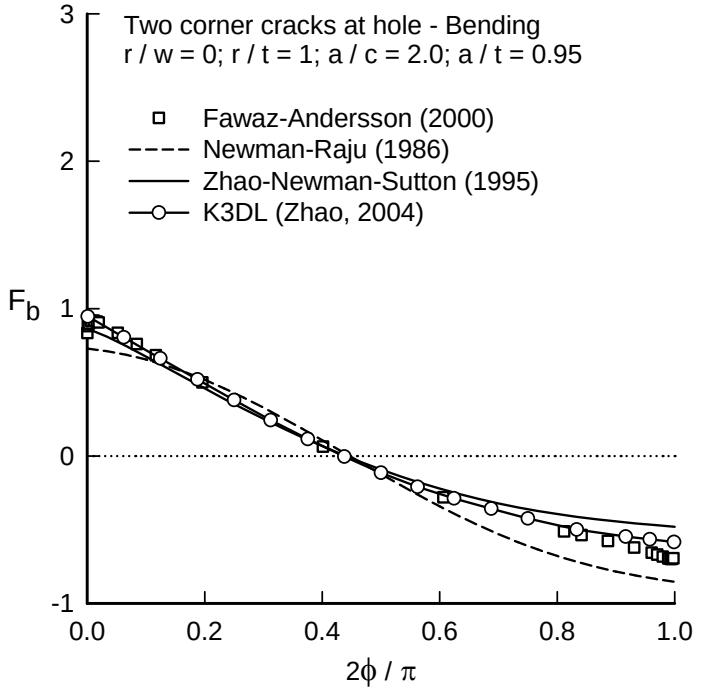

(b) Remote Bending

Figure 29. Comparisons of Boundary-Correction Factors for a/c = 2 With a/t = 0.95 Under (a) Remote Tension and (b) Remote Bending

5.3 CORNER CRACK AT HOLE.

For qualitative evaluation of the SIF results from the K3DL code, three applied load cases were considered: remote tension, remote bending, and wedge loading in the hole. Crack configurations considered herein are r/t = 1 (close to the single-hole test specimen, r/t = 1.04); a/c = 0.5, 1, 2; and a/t = 0.01 to 0.99. Only some typical results will be shown.

Some additional comparisons for remote tension and bending are shown in figures 30 and 31, respectively. The figures show the normalized SIF against a/t for two corner cracks at a circular hole. The figures also show comparison among the Fawaz-Anderson FEA results, the previously developed equations by Newman-Raju, the Zhao-Newman-Sutton equations for only remote bending, and the new K3DL results. The Fawaz-Andersson FEA results are the peak values near the free surfaces.

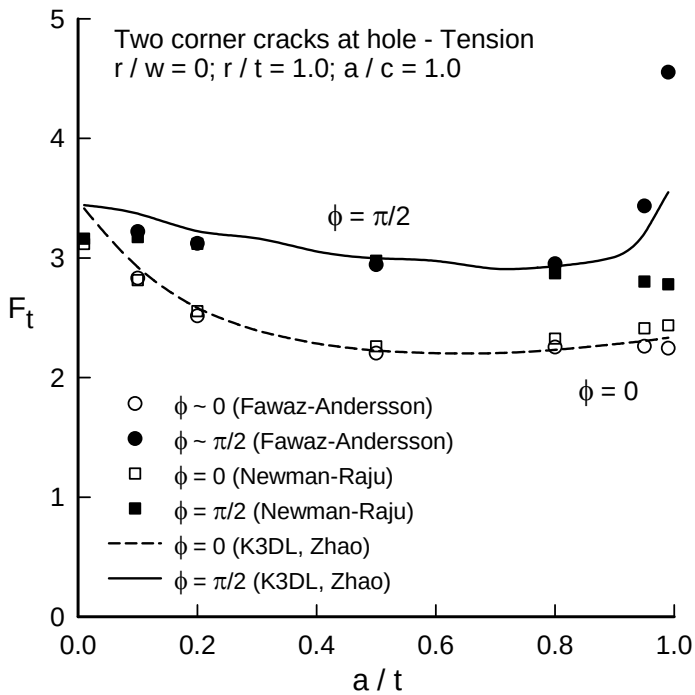

Figure 30. Comparison of Boundary-Correction Factors for Remote Tension From Various Analyses and Equations for r/t = 1 and a/c = 1

Figure 30 shows the boundary-correction factors at the free surface ($\phi = 0$) and at the bore of the hole ($\phi = \pi/2$). The K3DL results compare very well at the free surface and fairly well at the maximum depth location with the FEA results. At the maximum depth location, the K3DL results show slightly higher values at low a/t ratios than the FEA results. Also, the rapid rise in the boundary-correction factors for very deep cracks (a/t > 0.9) are not captured by the K3DL code, but the results are acceptable and exhibit the same trends. The Newman-Raju equations for a/t ratios less than 0.1 are modeling a boundary-layer effect (a reduction in the elastic stress concentration factor), which causes a slight drop in F_t near a/t = 0. This stress concentration factor reduction at the free surface may not be accounted for in the K3DL code. In addition, the

Fawaz-Andersson FEA results did not extend below an a/t value of 0.1. Further study is required to resolve this issue.

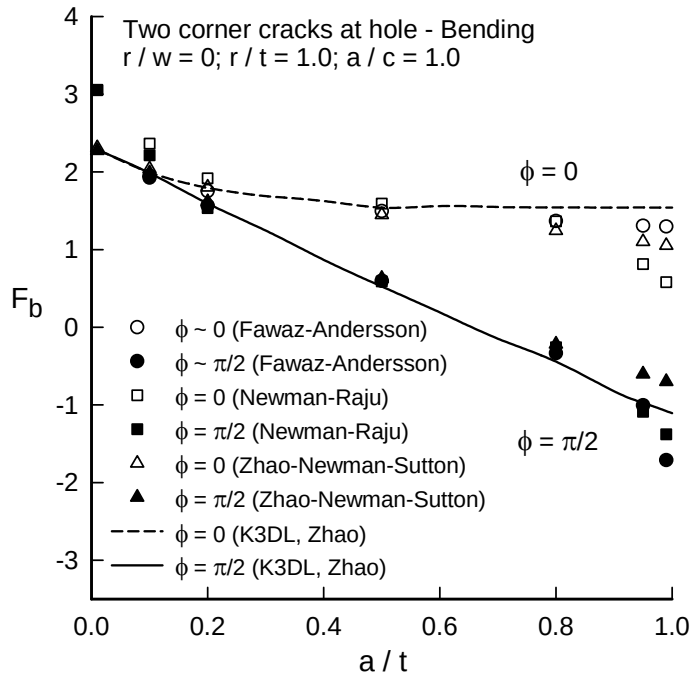

Figure 31. Comparison of Boundary-Correction Factors for Remote Bending From Various Analyses and Equations for r/t = 1 and a/c = 1

Figure 31 shows the boundary-correction factors for the case of remote bending. The K3DL code results are not as good as the case of tension for deep cracks. Here, the K3DL code gave higher SIFs for the deep cracks. The weight functions are independent of loading, and nothing can be done to modify the weight function for the bending load differences. However, these results are acceptable because under pure bending, the cracks will not grow beyond an a/t ratio of about 0.66 due to the very low or negative SIFs. In the case of combined tension and bending, the bending results for a/t > 0.66 are used, but the bending contribution to the total SIF will decrease. The Newman-Raju equations for a/t ratios less than 0.2 severely overestimate the boundary-correction factors and do not approach the correct limit. The stress concentration factor for a circular hole in a plate under bending (such as Reissner's solution [38]) was not taken into account. The Zhao-Newman-Sutton equations were developed to correct this deficiency in the Newman-Raju equations and approach the limiting stress concentration factor for a plate with a hole under bending.

5.3.1 Remote Applied Loads.

Figure 32 shows the boundary-correction factor distribution for remote tension, S_t, applied to a plate with a single corner crack at an open hole. The crack configuration had r/t = 1 and a/c = 1 with a/t ratios varying from 0.01 to 0.99. The solid symbols near $2\phi/\pi = 1$ show the influence of the back face as the corner crack becomes very deep (rapid rise in F_t).

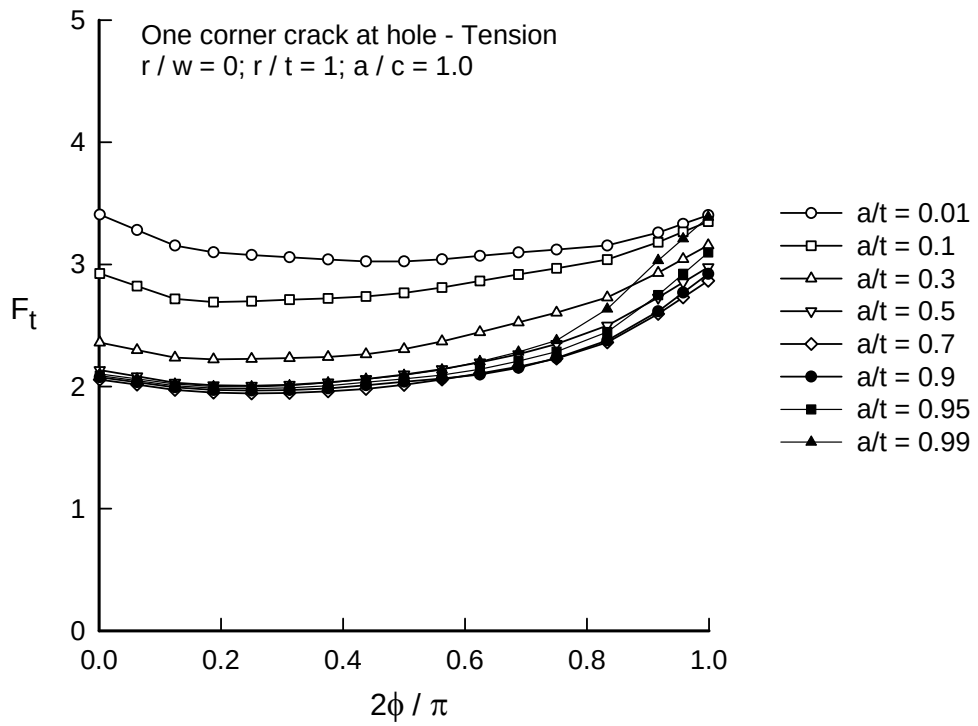

Figure 32. Normalized SIFs (F_t) Under Remote Tension for Shallow to Deep Cracks

Normalized boundary-correction factors for remote bending (applied outer fiber bending stress, S_b) are shown in figure 33 for r/t = 1 and a/c = 1 with a/t ratios varying from 0.01 to 0.99. Again, the crack configuration is a single corner crack at an open hole. The negative boundary-correction factors for deep cracks are only useful under combined loading, such that the sum of the SIFs is positive.

Figure 34 shows the boundary-correction factors (F_w) for wedge loading in the hole. The crack configuration is the same, as shown in figures 32 and 33, but the wedge loading is applied as a normal stress on the hole boundary with a cos(θ)-distribution (see appendix A). Wedge loading is used to simulate the effects of fastener loading on the Mode I SIF. (For simulated fastener loading, no information on the shear mode SIF is provided.)

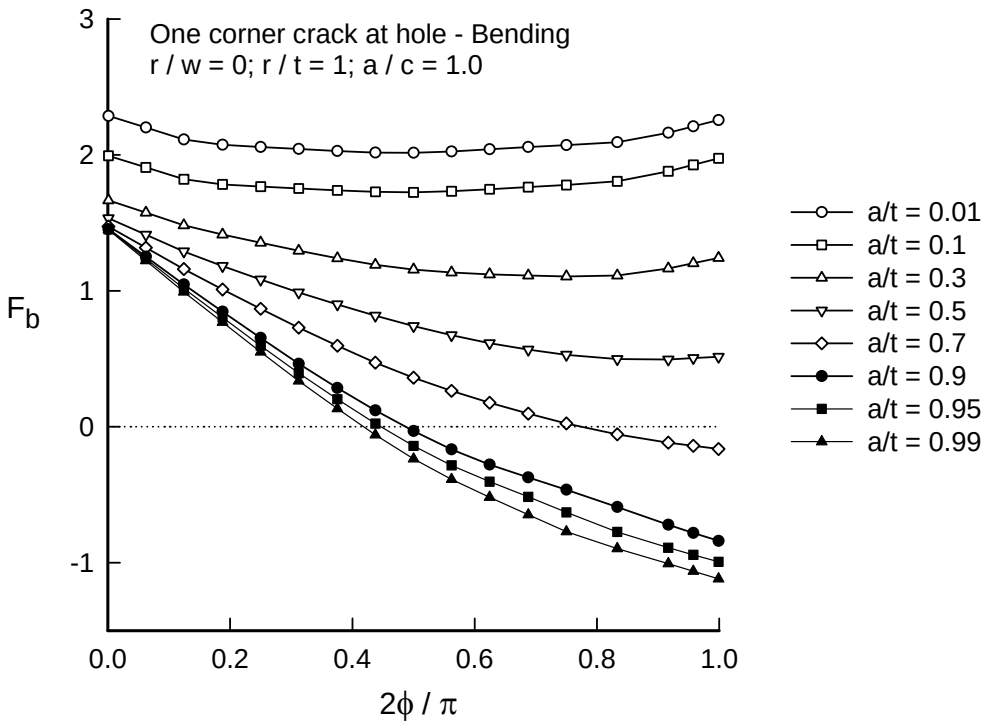

Figure 33. Normalized SIFs (F_b) Under Remote Bending for Shallow to Deep Cracks

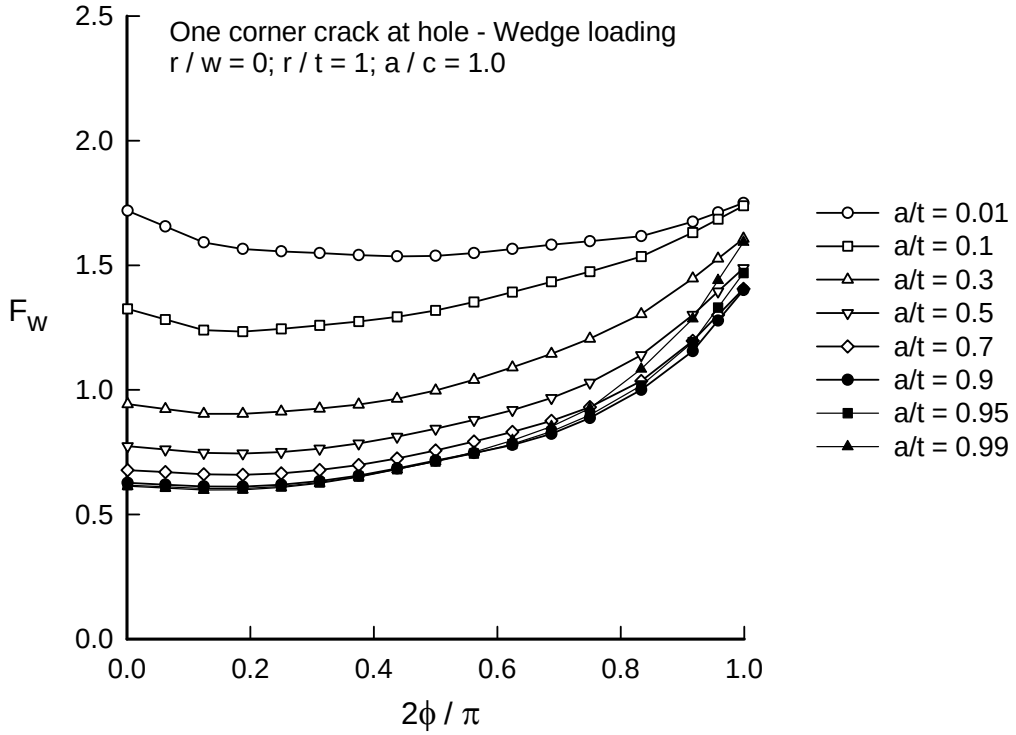

Figure 34. Normalized SIFs (F_w) Under Wedge Loading for Shallow to Deep Cracks

5.3.2 Residual-Stress Distributions.

The K3DL code was modified to conduct a stress analysis of either surface or corner crack(s) at an open hole with an arbitrary residual-stress field along the crack path. The residual-stress, σ_{rs}, distributions is expressed as

$$\sigma_{rs}/S_0 = a_0 + a_1\,\xi + a_2\,\xi^2 + a_3\,\xi^3 + a_4\,\xi^4 \tag{3}$$

where S_0 is a reference stress, such as the yield stress of the material, a_i (i = 1, 2, 3, 4) are the coefficients selected to fit the residual-stress distribution, and ξ (= x/r) is the normalized coordinate distance from the edge of the hole (see appendix A).

A comparison of residual-stress distributions caused by an overload or by cold-working a hole and the use of the polynomial equation was made. Figure 35 shows a comparison of the residual stresses caused by the 1.7 overload on a specimen with an open hole and the polynomial equation chosen to fit these results. The solid curve is the calculated residual stresses from ZIP2D [39] as a function of the normalized distance from the edge of the hole (ξ), and the dashed curve is the 4th degree polynomial equation chosen to fit these results. The equation coefficients, a_0 to a_4, are used to compute the SIFs from the K3DL code.

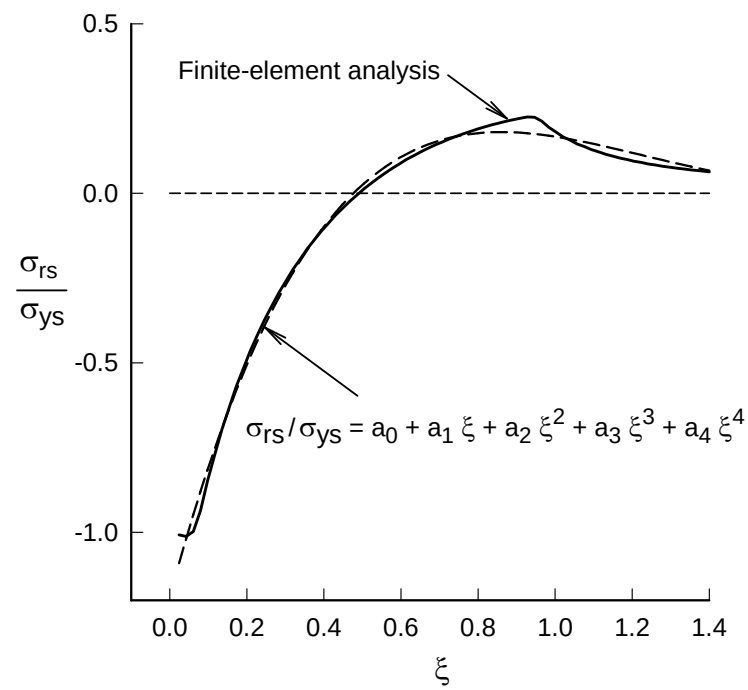

Figure 35. Comparison of Residual Stresses From an Overload and the Equation Chosen to fit the Results

For illustrating the residual-stress capability in K3DL, an example residual-stress field due to cold expansion of a circular hole is considered. The residual-stress distributions are from Park and Atluri [40]. Three different ratios of plastic zone radius (R_y) to hole radius are considered:

R_y/r = 1.1, 1.3, and 1.5. The crack configurations considered are r/t = 1 (close to the single-hole test specimen); a/c = 1; and a/t = 0.01 to c/r = $(x/r)_{max}$ (valid range of polynomial expression for the residual stresses).

Figure 36a shows the residual-stress distributions, where $\xi = 0$ is at the edge of the hole. The yield stress σ_{ys} is used to normalize the residual stress, σ_r. The curve for $S_r(x/r)$_1104 is for the case of $R_y/r = 1.1$ with a valid range of $\xi \leq 0.4$. The residual-stress distribution $S_r(x/r)$_1306 is for $R_y/r = 1.3$ with a valid range of $x/r \leq 0.6$. And $S_r(x/r)$_1508 is for $R_y/r = 1.5$ with a valid range of $\xi \leq 0.8$.

An example of an SIF solution from one of the residual-stress distributions is shown in figure 36b. As expected, for the given residual-stress field, small cracks exhibit the most influence of the residual stresses, i.e., large negative values for F. In the elastic superposition method, these boundary-correction factors must be added to the SIFs from the applied loading. The residual-stress effect becomes small as the crack becomes larger and tends to zero at the plate surface ($\phi = 0$). At the hole surface ($\phi = \pi/2$), the residual-stress effect remains significant because the crack front is always in the compressive residual-stress field at this location.

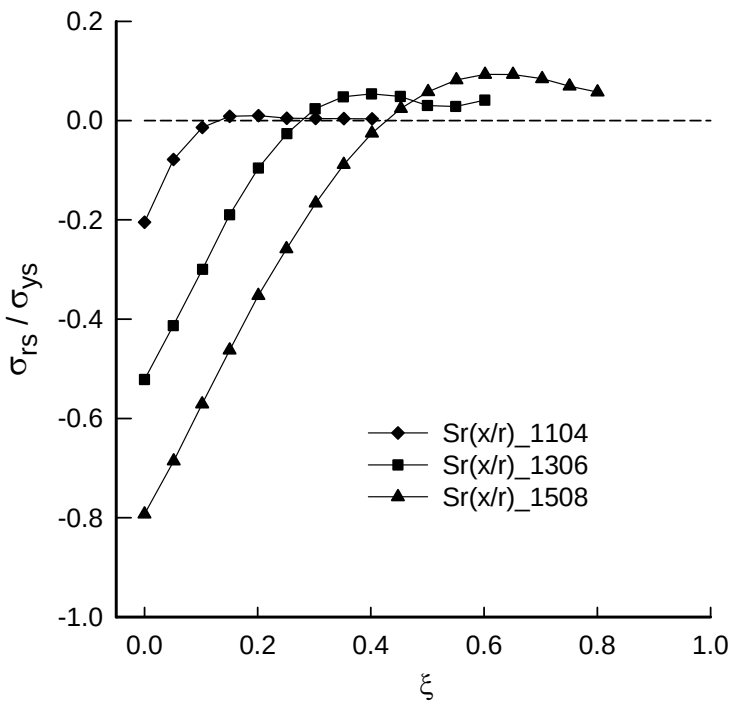

Figure 36a. Residual-Stress Distributions of a Cold-Worked Hole for Three Different R_y/r Ratios

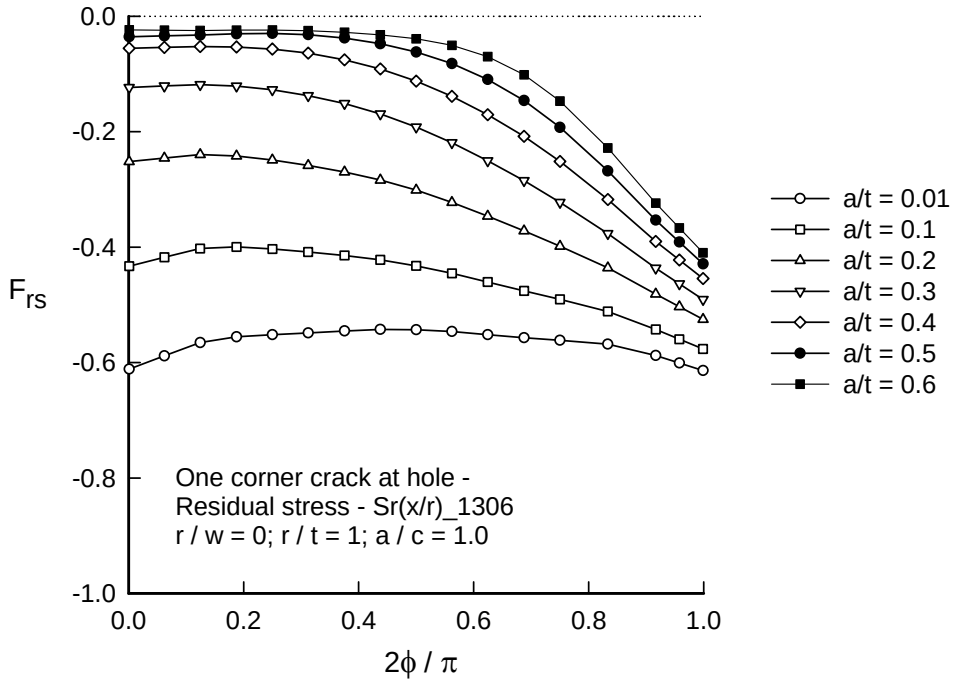

Figure 36b. Normalized SIFs Under Residual-Stress Distribution for $R_y/r = 1.3$

5.4 SURFACE CRACK AT HOLE.

The K3DL code can analyze a single surface crack (s1) or two symmetric surface cracks (s2) emanating from the center of a circular hole, as shown in figure 37, subjected to remote tension, wedge loading in the hole, and under any arbitrary residual-stress distribution along the crack path. (Note that remote bending was not used because the surface crack would not grow in a semielliptical manner.) The K3DL code defines the width of the cracked plate as 2b, whereas the total width is commonly defined as W or 2w. However, the solutions from the current code are basically for a cracked hole in an infinite body and finite width corrections will have to be applied to these solutions for practical applications.

The SIF results are calculated and presented in the form of the dimensionless F parameter, the boundary-correction factor, as given by equation 1. Since Newman and Raju [41] developed a wide range of SIF solutions for the surface crack emanating from a circular hole using FEA as well as equations, comparisons are made among the FEA results, the equations, and the K3DL code. Again, the particular crack configuration selected had an r/t ratio of unity and the a/c ratio was also unity. This crack configuration was selected because these are common crack configuration parameters used in the aircraft industry.

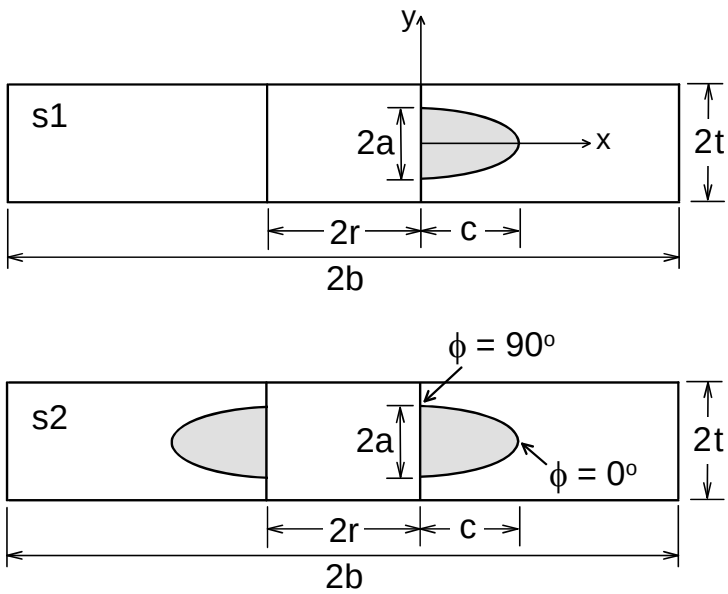

Figure 37. Definition for the Surface Crack Configuration Parameters

Figure 38 shows the correction factors as a function of the crack-depth-to-plate-thickness (a/t) ratio for two symmetric surface cracks located at the center of a circular hole (r/t = 1; a/c = 1) subjected to remote tension. The solid and dashed curves are the results from the K3DL code at the free surface location ($\phi = 0$) and the maximum depth location ($\phi = \pi/2$); the symbols are the results from the Newman-Raju equations [17]. The free surface results compared very well, except for the deep cracks; however, the maximum depth location exhibited some major differences. The rapid rise in the correction factor from K3DL for deep cracks is similar to the rise shown for the corner crack problem.

To study the source of these differences, comparisons were also made with the finite element results from Tan, et al. [42]. Figure 39 shows the distribution of the correction factor against the normalized parametric angle, $2\phi/\pi$, for the case of a/t = 0.2. The open circular symbols show the early finite element results [16], which showed a rapid drop-off in the correction factor near the maximum depth location. This drop-off was later found to be due to ill-shaped elements near the hole boundary [42]. The method used by Raju and Newman [16 and 41] to generate their models produced ill-shaped elements in the region where the crack front intersected the hole boundary. These elements produced a stiffer model and significantly reduced the SIF. However, in developing the wide-range equations, Newman and Raju [17 and 41] neglected this rapid drop-off, as shown by the solid curve. The method used by Tan, et al. [42] generated a model with low aspect ratio elements in the region of the crack front and hole boundary. Their model produced results higher (about 7%) than the equations near the maximum depth location. The solid symbols show the recent results from the K3DL code, which were slightly higher than the FEA results from Tan, et al. Thus, it is concluded that the K3DL code is producing more accurate SIFs than the Newman-Raju equations.

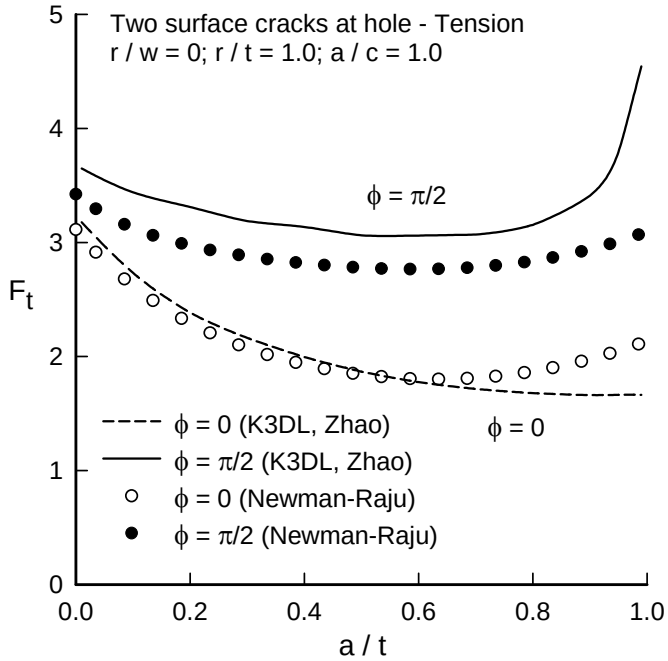

Figure 38. Comparison of K3DL Results and Equations for a Surface Crack Configuration

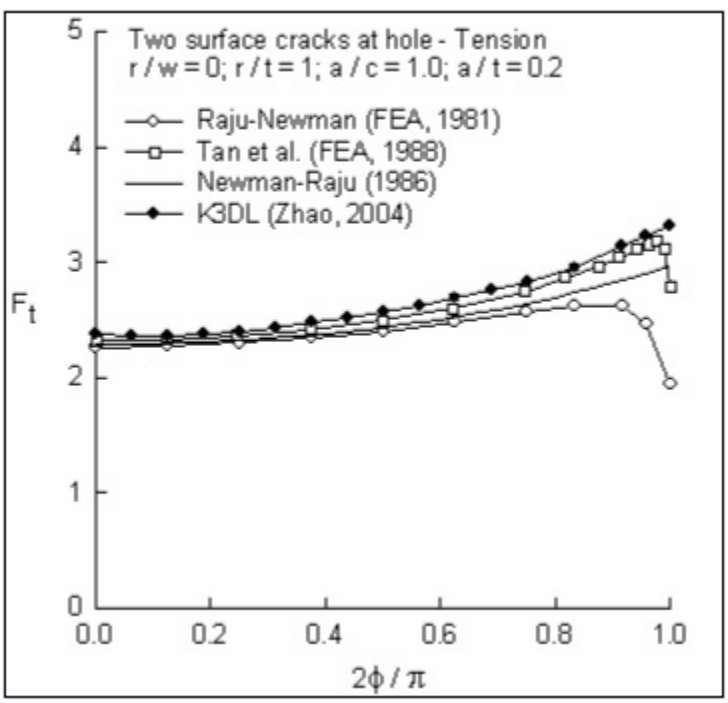

Figure 39. Comparison of Results for a Surface Crack Configuration Using Various Models and Equations

6. TWO-DIMENSIONAL GREEN'S FUNCTION ANALYSES.

The SIF solutions for a pair of concentrated forces applied to the upper and lower crack surfaces are used as a Green's function to generate the SIF solutions for the same crack configuration subjected to any arbitrary stress distribution on the crack surfaces. A two-dimensional code, SIFK2D, was developed to calculate the SIFs for several different through crack configurations under arbitrary loading on the crack surfaces: (1) a crack in an infinite plate, (2) an edge crack in a semi-infinite plate, (3) a single crack emanating from a circular hole in an infinite plate, and (4) two symmetric cracks emanating from a circular hole in an infinite or finite width plate. Application of the Green's function code to these four crack configurations are presented and discussed in appendix B.

In this section, the code was used to calculate the SIFs for a single crack emanating from a circular hole in an infinite plate subjected to remote uniform stress using the Green's function, developed by Shivakumar and Forman [43]. In addition, the application to a single crack at a circular hole under both remote uniform stress and a residual-stress distribution is analyzed and discussed.

6.1 SINGLE CRACK AT OPEN HOLE UNDER REMOTE TENSION.

The single crack at a hole is perhaps one of the most important crack configurations in the aircraft industry because of the very large number of fastener holes in the wings and fuselages. The crack configuration is shown in figure 40, where the crack length, c, is measured from the edge of the hole. The crack configuration was first analyzed by Bowie [44] using conformal mapping, but later Newman [45] obtained a more accurate solution using boundary collocation.

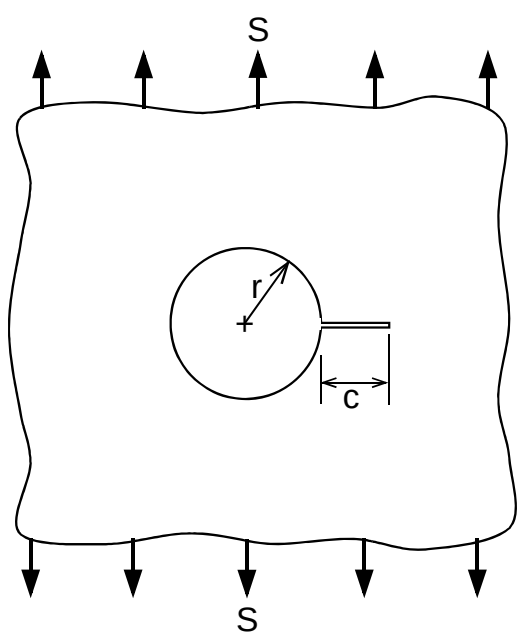

Figure 40. Single Crack at an Open Hole in an Infinite Plate Subjected to Uniform Remote Stress

Figure 41 shows the normalized SIF solution using the SIF2D code as a function of the c/r ratio. The circular symbols show the Green's function solution and the dashed curve shows an equation developed by Newman [46]. Later, slight improvements were made to the equation for either a single or two symmetric cracks emanating from the hole [47]. Both solutions approach the theoretical limit of 0.707 as the c/r ratio approaches infinity. The equation also approaches the theoretical limit as c/r approaches zero (1.1215 times the local stress concentration).

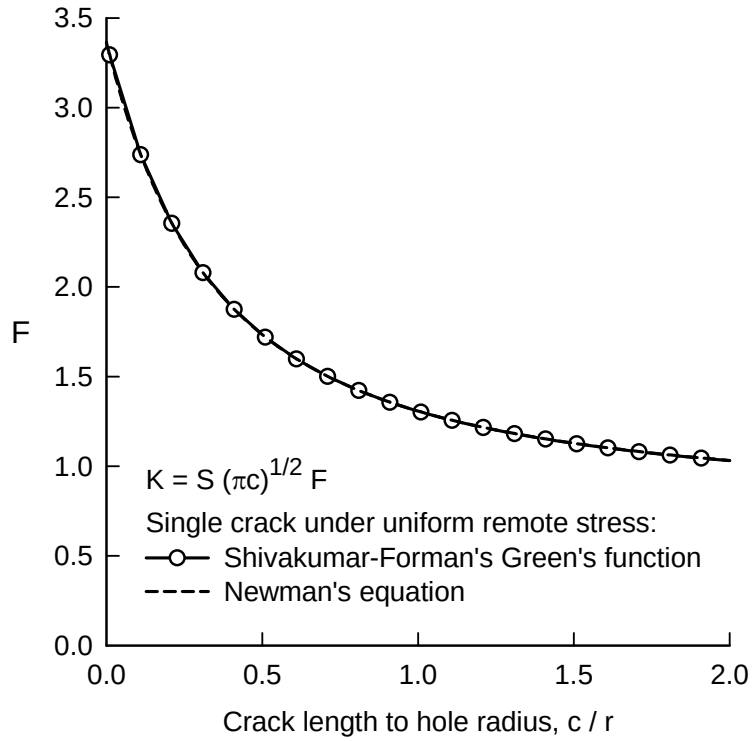

Figure 41. Comparison of Normalized SIFs for a Single Crack at an Open Hole Subjected to Uniform Remote Stress

6.2 GENERAL STRESS DISTRIBUTIONS FOR CRACKS AT HOLES.

The SIF2D code was developed with several options for analyzing the effects of arbitrary stress distributions along the crack location. The stresses along the crack location could be input in either a table or equation format. In the code, the normal stress equations were implemented in either positive or negative powers as

$$\sigma = A_1 + A_2(x/r) + A_3(x/r)^2 + A_4(x/r)^3 + A_5(x/r)^4$$
$$\text{or} \tag{4}$$
$$\sigma = A_1 + A_2(r/x) + A_3(r/x)^2 + A_4(r/x)^3 + A_5(r/x)^4$$

The code is valid for expressions up to x^4 (or fourth order degree polynomial equations) only, but the code could be easily modified for higher order terms. To illustrate the use of the code for an arbitrary stress distribution around the hole, a single crack emanating from the edge of the hole

under both remote uniform stress and a residual-stress distribution, σ_{rs}, as shown in figure 42, was analyzed.

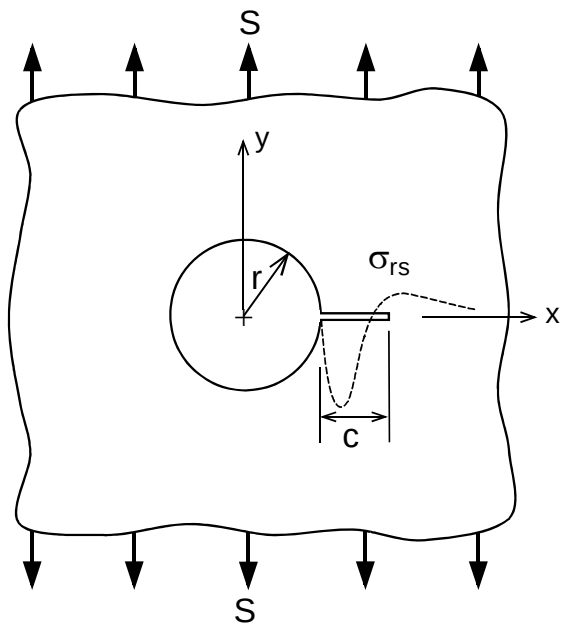

Figure 42. Single Crack at an Open Hole Subjected to Remote Stress and Residual-Stress Distribution

From a previous study [48], sponsored by the FAA, the residual stresses around a cold-worked, reamed, and slotted hole were determined from an FEA of a 7075-T6 aluminum alloy. These residual stresses are shown in figure 43a. The residual stresses were normalized by the yield stress of the material and plotted against x/r; the edge of the hole was at $x/r = 1$. The EDM notch, which has no residual stresses applied along the notch surfaces, extended to an x/r ratio of about 1.05. Each data point shows the input values into the residual-stress table. Figure 43b shows the stresses along the intended path of the crack at maximum and minimum applied stress (solid and dashed curves, respectively). The dash-dot curve shows the stresses without the presence of residual stresses from elasticity theory by Timoshenko [49]. Using the SIF2D code, the SIFs at maximum and minimum applied stress with and without the residual stresses are shown in figure 43c. At the tip of the EDM notch (assumed to be a crack), the SIF is unaffected by the presence of the residual stresses and is identical to that caused by the Timoshenko stresses around a hole. But as the crack extends, the maximum SIF (solid curve) sharply drops and reaches a minimum after a small amount of crack extension. The SIF at the minimum applied stresses is always negative, as shown by the dashed curve. The differences between the solid and dashed curves give the stress-intensity factor range, ΔK; and the effective stress ratio ($R_{eff} = K_{min}/K_{max}$) is shown in figure 43d. These values are used in the various codes to make fatigue crack growth life predictions.

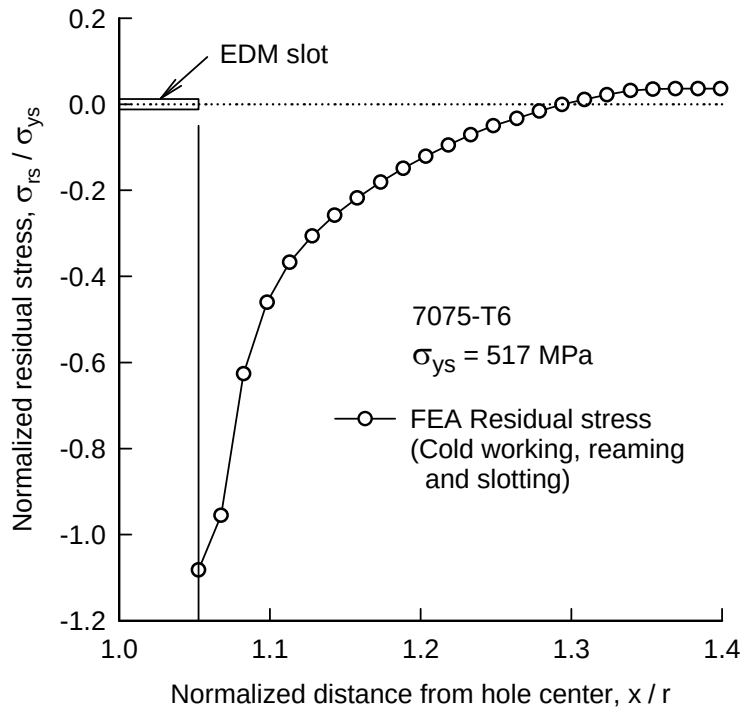

Figure 43a. Calculated Residual Stresses Around a Circular Hole From Cold Working, Reaming, and Slotting

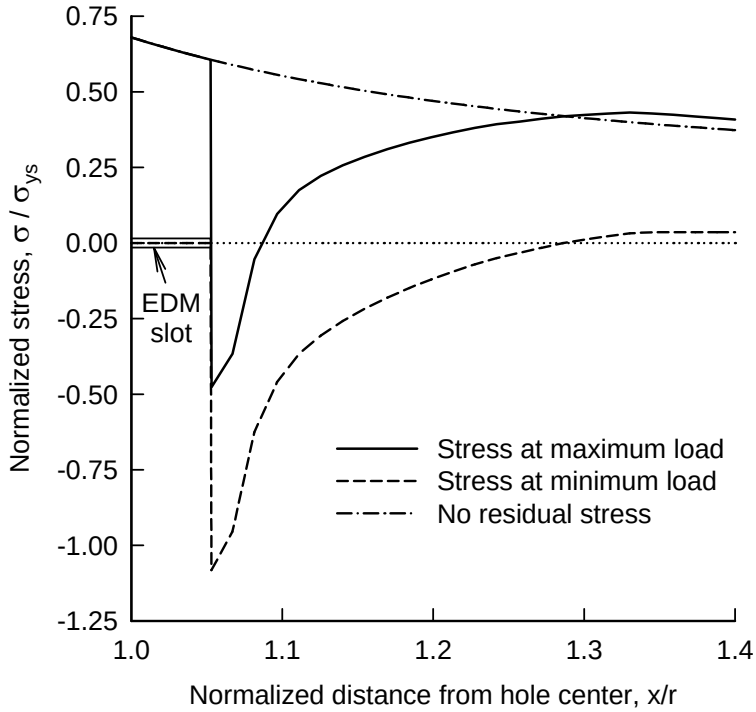

Figure 43b. Residual Stresses Around a Circular Hole at Maximum and Minimum Applied Stresses

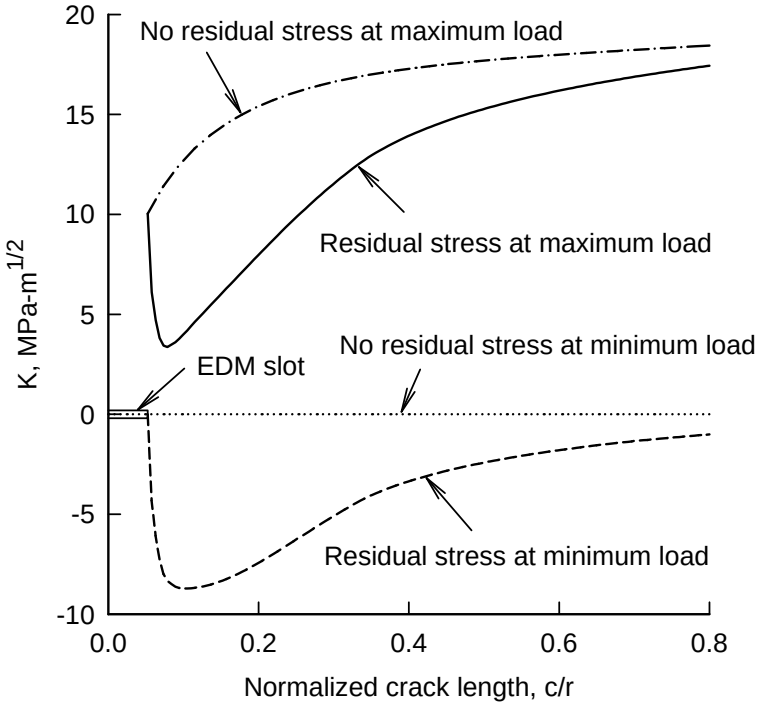

Figure 43c. Calculated SIFs With and Without Residual Stresses at Maximum and Minimum Applied Stresses

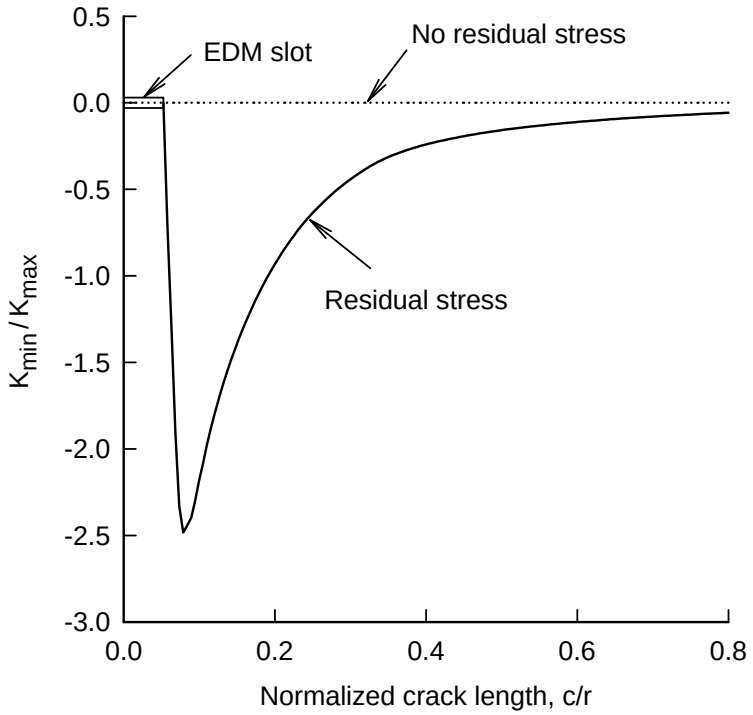

Figure 43d. Calculated Stress Ratio (K_{min}/K_{max}) With and Without Residual Stresses at Maximum and Minimum Applied Stresses

7. FINITE ELEMENT ANALYSIS OF SINGLE-HOLE SPECIMEN.

Because the drilled single-hole test specimens appear to have no residual stresses or because the drilling flaws were large enough to offset the effects of the residual stresses on fatigue life, the finite element method was used to study the residual stresses caused by a 1.7 overload and a 1.7 underload. These residual stresses were used later to verify the capabilities of the FASTRAN [5] life-prediction code, which accounts for the influence of residual stresses on crack growth and the decay in the residual stresses as the crack grows. In addition, the FEAs were used to simulate fatigue crack growth and crack closure; comparisons were made between the FEAs and the FASTRAN simulations.

7.1 ELASTIC AND ELASTIC-PLASTIC STRESS ANALYSES.

The two-dimensional, elastic-plastic finite element code, ZIP2D [39], has been used to analyze the single-hole specimen. A two-dimensional finite element model of the test specimen was developed and the mesh is shown in figure 44. The model had about 3500 elements and 3700 degrees of freedom. The material was assumed to be elastic-perfectly plastic with a flow stress of 345 MPa (50 ksi). Figure 45 shows the shape and size of the plastic zone at the 1.7 overload (about 72% of the flow stress). The model is one-quarter of the specimen, and the x and y coordinates are normalized by the hole radius.

Figure 46 shows the nodal average stresses along the centerline of the specimen (x axis) at three levels of loading. The normal stress, σ_{yy}, has been normalized by the flow stress of the material, and the distance, again, is normalized by the hole radius. The insert in figure 46 shows the loading that was applied to the finite element model. The dash-dot curve (A) shows the normal stresses at the 1.7 overload (S_{max}/σ_o = 0.72 or 248 MPa) that correspond to the plastic zone shown in figure 45. The dashed curve (B) shows the compressive residual stresses that develop at the hole surface and the balancing tensile stresses away from the hole. The solid curve (C) shows the normal stresses at the constant-amplitude loading (145 MPa or 21 ksi).

In figure 47, the nodal average stresses along the centerline of the specimen after the 1.7 underload are, again, shown at three levels of remote loading. The insert shows the loading that was applied to the finite element model. The dash-dot curve (A) shows the normal stresses at the 1.7 underload (S_{max}/σ_o = – 0.72 or – 248 MPa). The dashed curve (B) shows the tensile residual stresses that develop at the hole surface and the balancing compressive stresses away from the hole, and the curve (C) shows the normal stresses at the constant-amplitude loading (145 MPa).

Figure 48 shows a summary of the stress distributions after the overload, after the underload, and during the constant-amplitude loading. The results from the overload produced very low stresses near the hole boundary (0.2 as compared to 1.05 times the flow stress), whereas the underload caused higher stresses than the constant-amplitude loading. However, the differences were not as large as those for the overload (1.1 σ_o as compared to 1.05 σ_o). These results partly explain why the overload caused the fatigue lives to be an order of magnitude longer than the constant-amplitude results. However, the fatigue lives after the underload were only about a factor of 2 less than the constant-amplitude case.

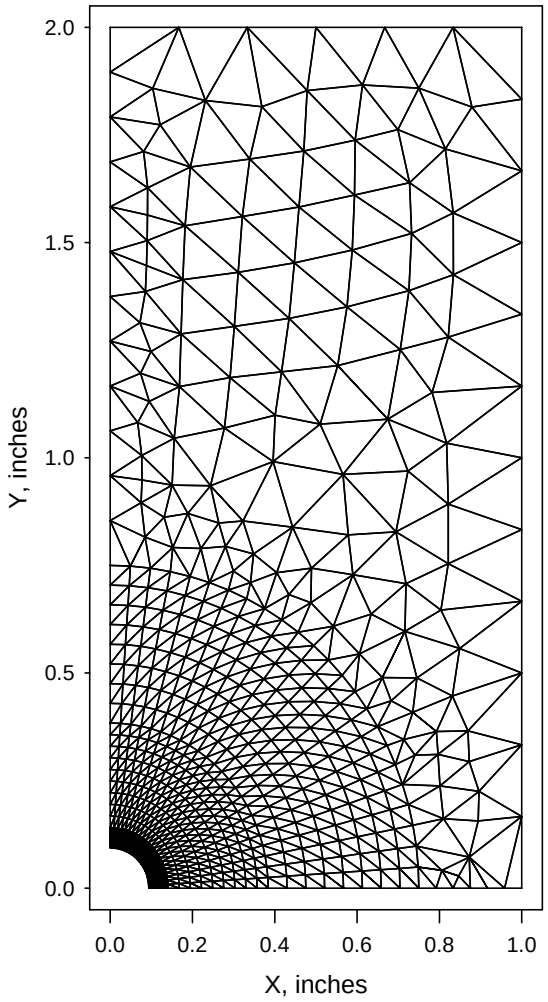

Figure 44. Two-Dimensional Finite Element Model of the Single-Hole Fatigue Test Specimen

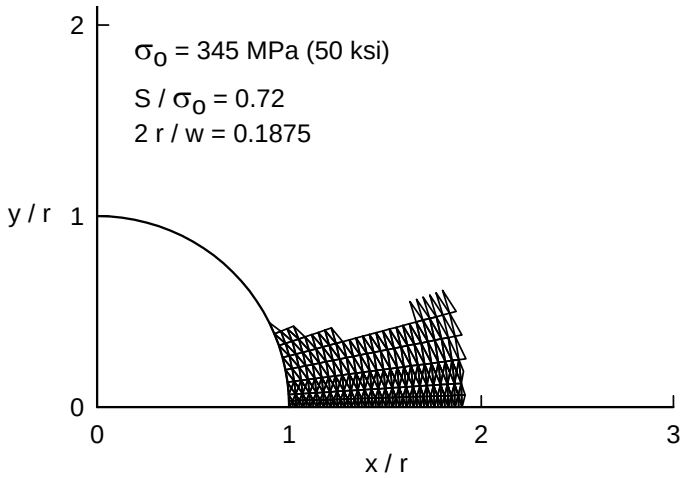

Figure 45. Plastic Zone Shape and Size After the 1.7 Overload on the Open-Hole Specimen (One-quarter of specimen)

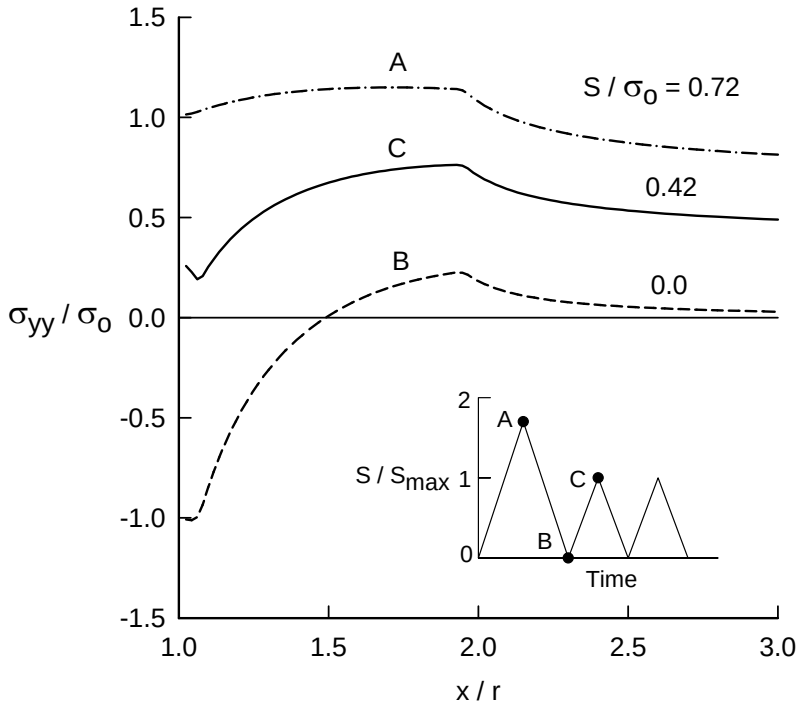

Figure 46. Nodal Average Stresses Along x Axis for 1.7 Overload, Zero Load, and Constant-Amplitude Loading Used in Fatigue Tests

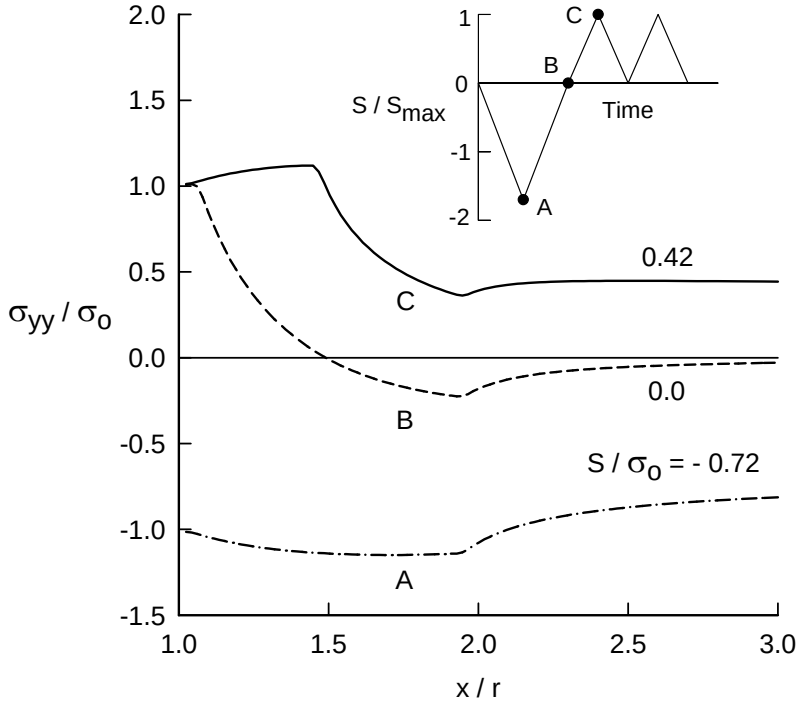

Figure 47. Nodal Average Stresses Along x Axis at the 1.7 Underload, Zero Load, and Constant-Amplitude Loading Used in Fatigue Tests

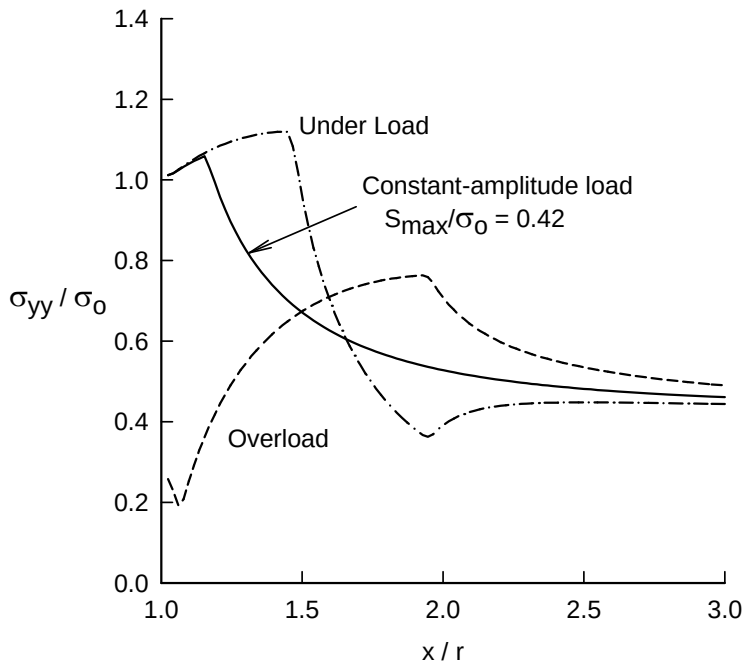

Figure 48. Nodal Average Stresses Along x Axis After Overload, Underload, and Constant-Amplitude Loading Used in Fatigue Tests

7.2 SIMULATED FATIGUE CRACK GROWTH AND CRACK CLOSURE.

Fatigue tests were conducted on the production-quality open-hole specimens under either constant-amplitude loading, a single-spike overload followed by constant-amplitude loading, or a single-spike underload followed by constant-amplitude loading. Elastic-plastic finite element analyses of these loading conditions were conducted to determine the stress states around the hole. In particular, the effects of residual stresses on fatigue crack growth and crack closure due to overloads and underloads were studied and compared to the FASTRAN code [5].

The two-dimensional finite element code, ZIP2D [39], was used again with a very refined model of a crack emanating from a circular hole to simulate fatigue crack growth and crack closure under plane-stress conditions. The mesh had about 7000 elements and 3600 nodes. Although the model was highly refined, the smallest element size (0.02 mm) was orders of magnitude larger than the actual fatigue crack growth rates. Thus, comparisons were also made with two crack growth simulations from FASTRAN. In the first simulation, the crack growth increment was equal to the element size in the finite element model. In the second simulation, the actual fatigue crack growth rates for a crack in the 2024-T3 aluminum alloy were used.

Figure 49 shows the crack-opening stress, S_{op}, normalized by the maximum applied stress, as a function of crack length for constant-amplitude loading. The initial crack length c_i was one element size (0.02 mm). The solid curve represents the FEA results and the other curves represent the FASTRAN simulations. The larger element size could produce higher crack-opening stresses from the FEA. FASTRAN, using the actual crack growth increments, produced

a lower crack-opening stress than the FEA. Higher crack-opening stresses were obtained from FASTRAN simulations using the larger crack growth increments, as used in the FEA.

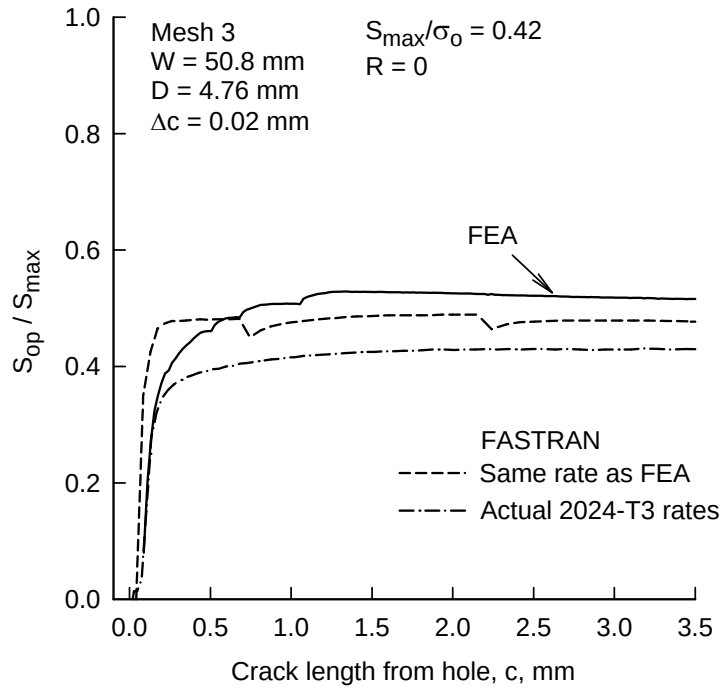

Figure 49. Crack-Opening Stresses for Constant-Amplitude Loading for a Crack Emanating From a Circular Hole

Appling the 1.7 overload followed by the same constant-amplitude loading (as shown in figure 49), produced very high crack-opening stresses, as shown in figure 50. The FASTRAN simulations also produced high crack-opening stresses and had similar behavior, but the crack-opening stresses approached a lower value than the FEA results as the crack grew away from the hole. Again, this could be due to the larger element size in the FEA. Figure 51 shows the results of the 1.7 underload followed by the same constant-amplitude loading. The extent of the influence of the underload was about 2 mm of crack growth before the opening levels stabilized, very similar to the overload case. Again, the FASTRAN simulations produced lower crack-opening stresses than the FEA, but larger size crack growth increments in FASTRAN produced slightly higher crack-opening stresses.

Figures 52 and 53 show a comparison of all load cases from the FEA and FASTRAN simulations, respectively. In both cases, the overload caused a much larger influence on crack-opening stress levels than the same magnitude of underload. Both the overload and underload results approached the constant-amplitude results as the crack grew away from the hole. These results show that the influence of the overload and underload occurs over a larger amount of crack growth for FASTRAN than with the FEA. This may be due to the tensile biaxial stress field around the hole in the FEA, whereas in FASTRAN, the constraint factor was assumed to be unity. A slightly higher constraint factor, such as 1.15, would have reduced the length of influence.

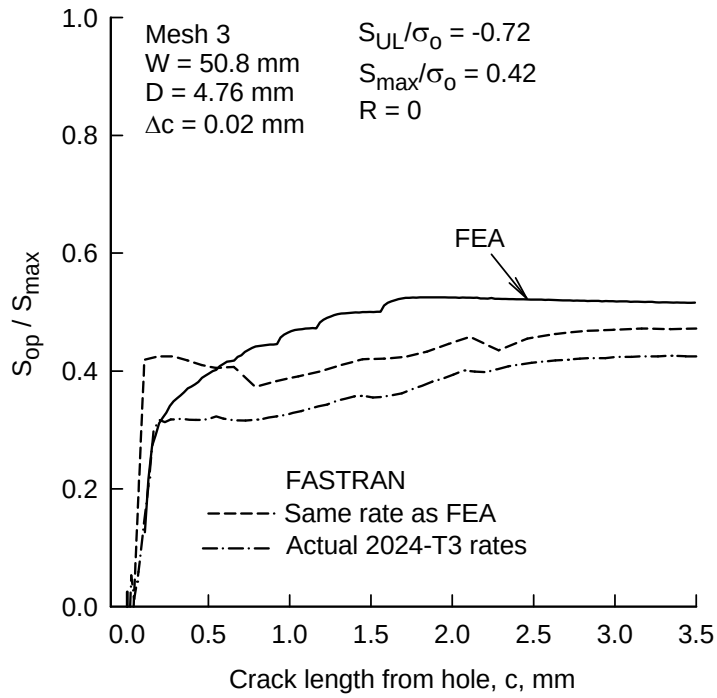

Figure 50. Crack-Opening Stresses for a Single-Spike Overload Followed by Constant-Amplitude Loading for a Crack at a Hole

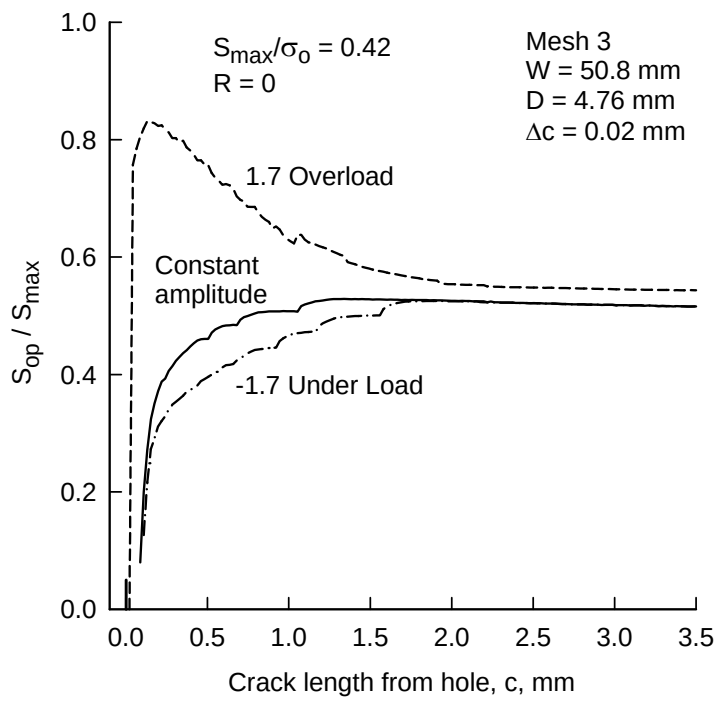

Figure 51. Crack-Opening Stresses for a Single-Spike Underload Followed by Constant-Amplitude Loading for a Crack at a Hole

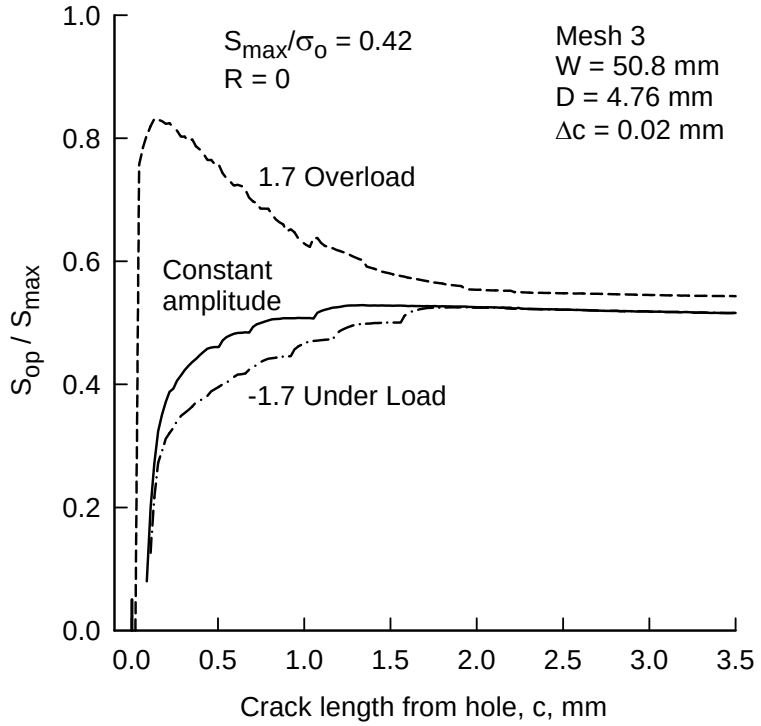

Figure 52. Comparison of Crack-Opening Stresses From FEA for the Three Load Cases

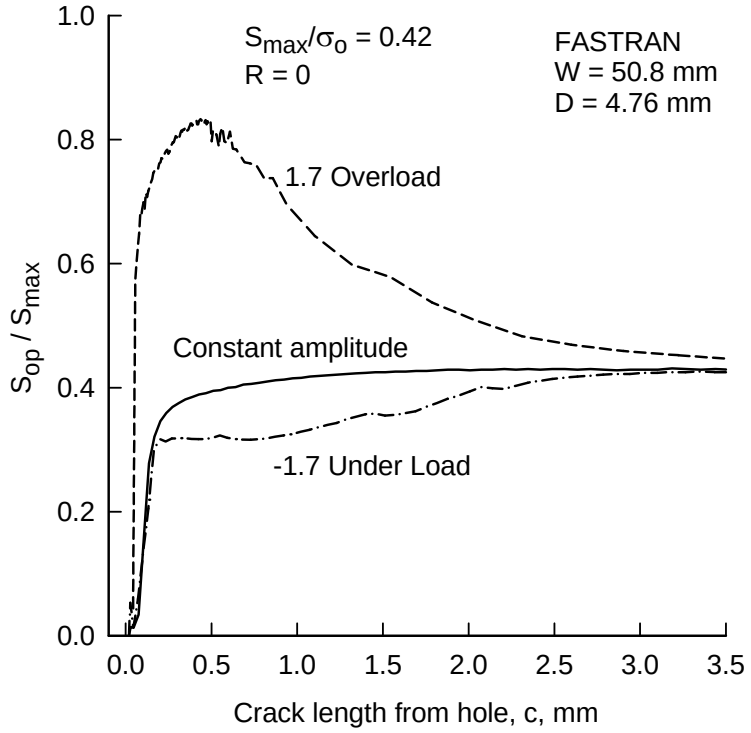

Figure 53. Comparison of Crack-Opening Stresses From FASTRAN for the Three Load Cases

8. FATIGUE ANALYSIS OF SINGLE-HOLE SPECIMENS.

Over the past 2 decades, various studies on small- or short-crack growth behavior in metallic materials have led to the realization that the fatigue life of many engineering materials is affected by crack growth from microstructural features, such as inclusion particles, voids, or slip band formation (see references 28-30). Concurrently, improved fracture mechanics analyses of some of the crack tip shielding mechanisms, such as plasticity-induced crack closure [47], and analyses of surface or corner crack configurations [16, 22, and 25] have led to more accurate crack growth and fatigue life-prediction methods. Thus, small-crack theory is the treatment of fatigue as a crack propagation process from a microdefect (or crack) to failure [6 and 8]. Herein, small-crack theory is used to calculate the fatigue behavior of the 2024-T3 aluminum alloy specimens tested in the current program. The details of the analysis procedures are given in reference 50 and are not repeated here. See appendix C for improvements made in FASTRAN to calculate fatigue lives.

8.1 FATIGUE ANALYSES BASED ON SMALL-CRACK THEORY.

Prior to conducting the fatigue (S-N) test on the single-hole test specimens made of the 2024-T3 aluminum alloy material, FASTRAN was used to analyze the older fatigue data on the same material for open-hole specimens with hole diameters that are slightly lower and higher than that used in the current test program. Figure 54 shows the fatigue data from NACA TN-3631 [35]. The specimens were 51 mm wide and had D/W ratios of 0.0625 and 0.125. (The D/W ratio for the current test specimens is 0.094.) The fatigue data extends from the fatigue limit to extremely high stress levels (above the yield stress of the material). Note that the aluminum alloy does not have a well-defined endurance limit. The symbols show the test data on specimens that had been electropolished. In the FASTRAN analysis, a semicircular surface crack located along the hole bore was assumed to cause the fatigue failure of the specimens. The radius of the surface crack was varied until a best fit of the data was found. A 6-μm (0.00024-in.) flaw was found to fit the mean of the test data quite well. However, in the range of applied stress levels from 150 to 250 MPa, the calculated lives fell somewhat short of the test data (about a factor of 2 or less). The reason for this behavior is not known, but this behavior has been observed on other comparisons made on the 2024-T3 aluminum alloy. The upper and lower (dashed) curves show the effects of flaw size on fatigue lives and bound most of the test data quite well. From previous studies, these flaw sizes are related to the inclusion particle clusters in the 2024-T3 aluminum alloy material [6, 28, and 31].

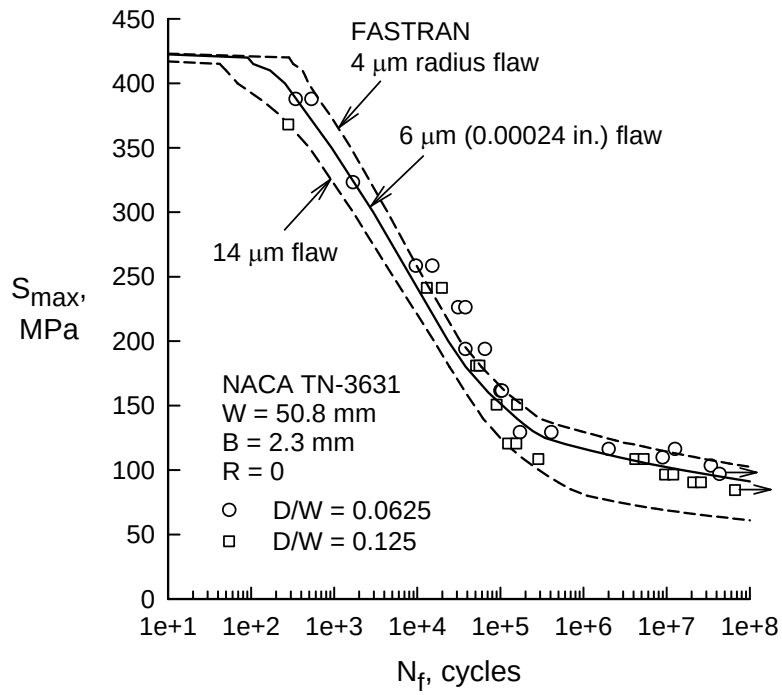

Figure 54. Comparison of Fatigue Data on the 2024-T3 Aluminum Alloy Open-Hole Specimens With FASTRAN Calculations Using Three Flaw Sizes

8.2 CONSTANT-AMPLITUDE LOADING TESTS.

FASTRAN was used to establish the stress levels for the fatigue test program on polished and production-quality specimens. Figure 55 shows S-N data on 2024-T3 aluminum alloy specimens with hole diameters that smaller and larger than the project test specimen [35]. The dashed curves are upper- and lower-bound calculations using inclusion particle distributions in the 2024-T3 aluminum alloy. The solid curve shows calculations based on a flaw size to fit the mean of the test data. Three stress levels were selected for the polished specimens, as shown by the three horizontal lines, denoted by A, B, and C. A number of tests were conducted at each stress level, but B was the primary stress level used in the test program. Identical series of tests were conducted for the LT and TL orientations. A number of polished specimens were also tested under a single overload or an underload (to induce a residual stress field) followed by constant-amplitude loading at a gross applied stress level of 145 MPa (21 ksi).

The polished specimens were drilled and chemically polished at the NASA Langley Research Center and tested at Georgia Institute of Technology. Both LT and TL specimens were drilled and polished. These results are shown as solid symbols in figure 56. Very little difference was observed between the LT and TL orientations for the limited test results, but the results at the two lowest stress levels did not agree as well as expected with the older fatigue data. The baseline applied stress level (145 MPa or 21 ksi) results fell short of the previous data, but the limited results at the lowest stress level produced nearly all runouts (no failure after 3 million cycles).

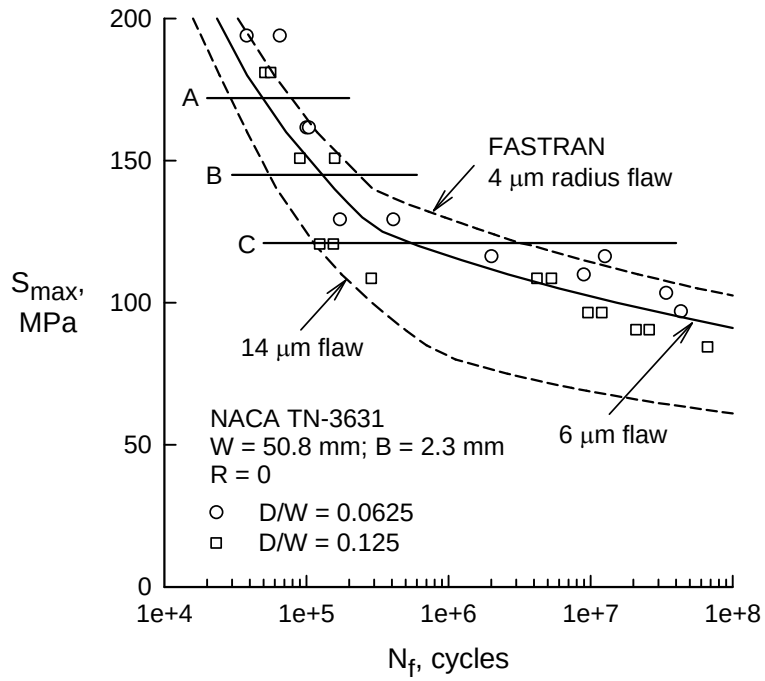

Figure 55. Stress Against Cycles for 2024-T3 Aluminum Alloy Sheet Material With a Central Hole Under $R = 0$ Conditions

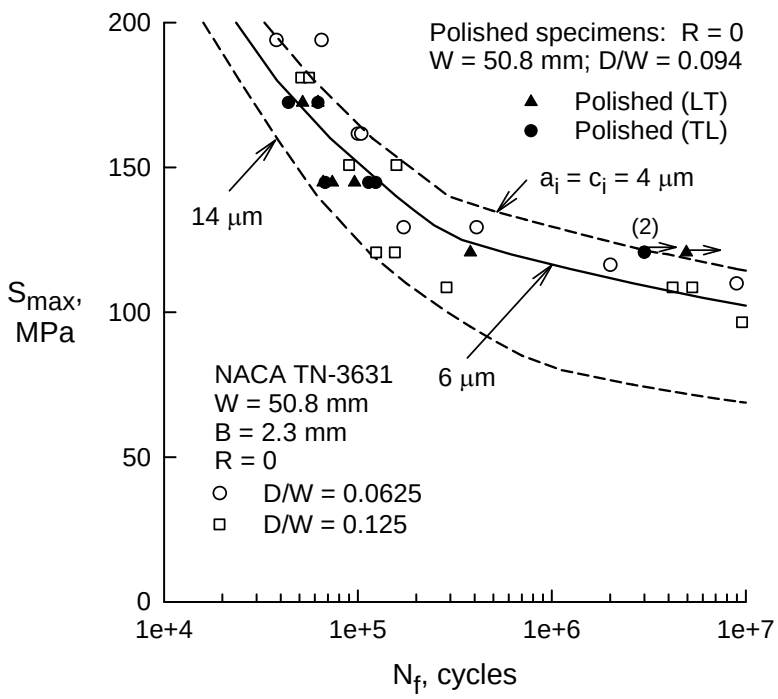

Figure 56. Comparison of Fatigue Lives for Electropolished and Chemically Polished Specimens Made of 2024-T3 Aluminum Alloy

The production-quality, drilled-hole specimen results are shown in figure 57. All of these tests were in the LT orientation, but most specimens were hand drilled, while a smaller subset was machine drilled. Again, at the two lowest test stress levels, the hand-drilled specimens fell short of the expected behavior, presumably due to drilling marks. However, the limit results on the machine-drilled specimens fell closer to the mean of the older polished data. The machine-drilling process may have produced less drilling marks than the hand-drilled holes.

Figure 58 shows a summary of all the constant-amplitude test data. This figure shows all the specimens that were tested at Georgia Institute of Technology, the electropolished NACA data [35], and the calculated results from FASTRAN, using upper and lower bounds based on initial defect sizes. The polished specimens indicated that the LT and TL orientations did not affect the fatigue lives. However, the polished specimens at the lowest test stress level (121 MPa) did not agree with the electropolished results from the NACA report. Three out of four specimens were classified as runouts and did not fail after 3 million cycles. But three drilled-hole test specimens (diamonds), tested at the lowest applied stress level, failed at fatigue lives much lower than the NACA results. These results indicated that either the drilling defects were large enough to cause shorter fatigue lives or that tensile residual stresses may be present. At the highest test stress level (172 MPa), the limited test data on the polished (three tests) and hole-drilled (one test) results fell close together and agreed with the calculated median (dashed) curve.

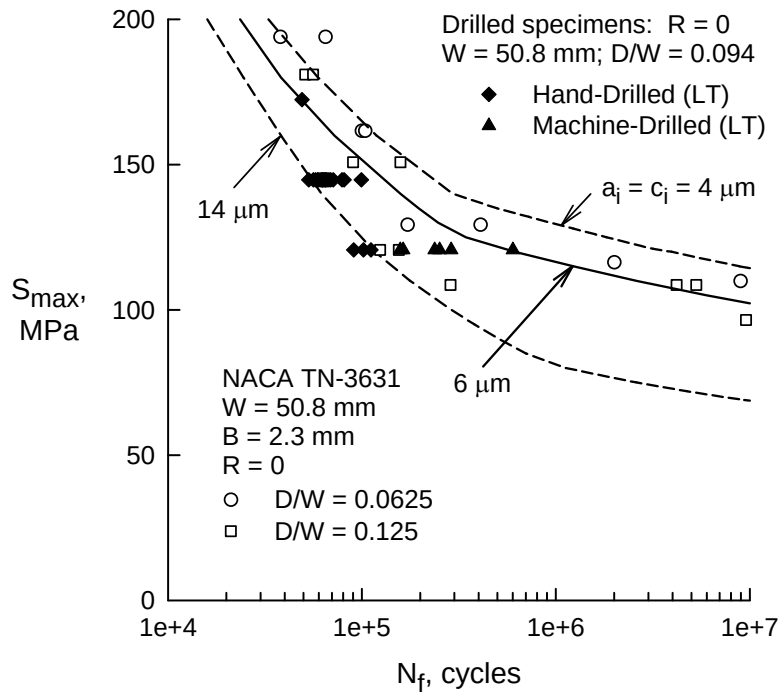

Figure 57. Comparison of Fatigue Lives for Polished and Production-Quality Open-Hole Specimens Made of 2024-T3 Aluminum Alloy

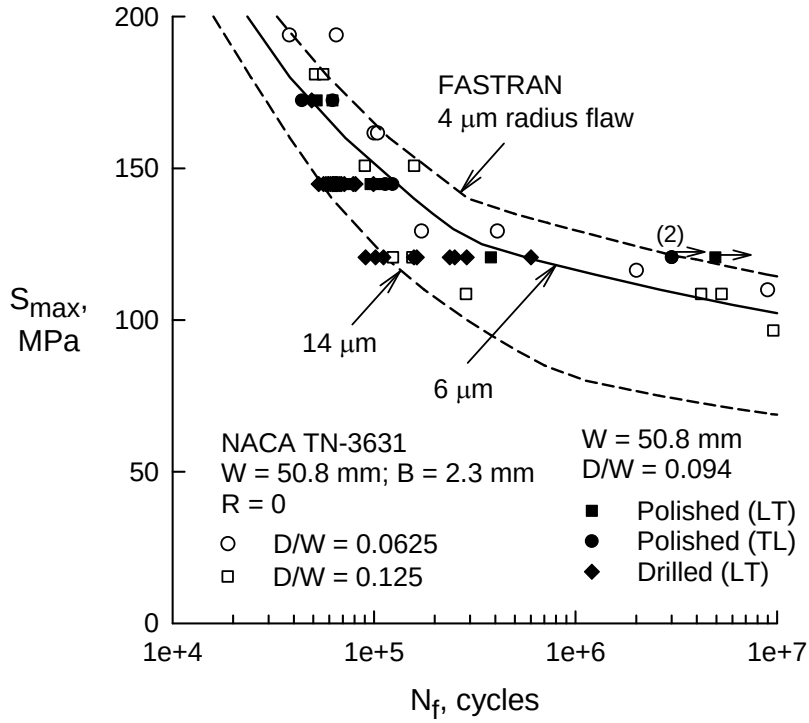

Figure 58. Fatigue Lives for Drilled-Hole and Baseline Specimens as a Function of Stress Level

Surprisingly, the polished test data at the medium stress level also fell short of the limited NACA data and the predicted mean results (solid curve). Also, the polished test data were not too different from the drilled-hole test data. This behavior was unexpected. The edge of the hole would yield under these loading conditions, if compressive residual stresses were not present. But this stress level is close to the same applied stress level used in the previous test and analysis program [3], which showed an effect of hole drilling and longer fatigue lives.

8.3 SPIKE OVERLOAD AND UNDERLOAD TESTS.

Because the production-quality holes did not appear to have significant residual stresses, a group of polished-hole specimens were tested with either a 1.7 overload or a 1.7 underload prior to conducting the constant-amplitude fatigue test. The overload and underload yielded the material at the edge of the hole and produced either a compressive or tensile residual-stress field, respectively. After one cycle of prior loading, the specimens were subjected to a cyclic maximum applied gross stress of 145 MPa at R = 0 until failure.

Figure 59 shows the fatigue tests on the overload and underload tests as solid triangular symbols. Again, these results are compared with the previous electropolished specimens from NACA TN-3631. As expected, the tensile overload caused significant compressive residual stresses at the edge of the holes and produced a large increase (order of magnitude) in the fatigue lives. However, the tests did exhibit a large amount of scatter. This may have been due to the microcracks having SIF levels very close to the threshold for the 2024-T3 aluminum alloy. On

the other hand, the compressive underload, which caused a tensile residual-stress field at the edge of the hole, produced about a factor of 2 reduction in fatigue life.

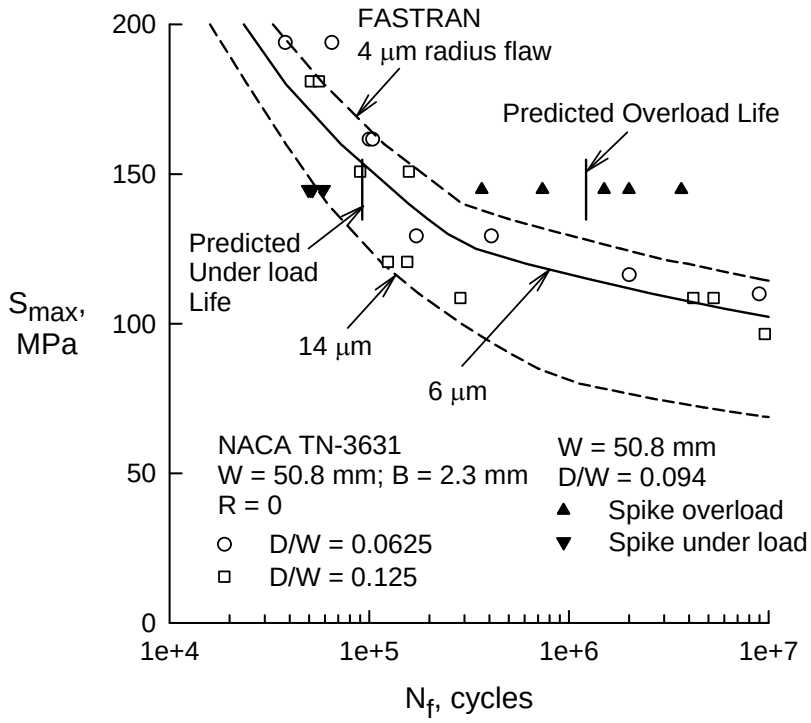

Figure 59. Fatigue Lives for Polished Specimens Subjected to Overload or Underload Prior to Constant-Amplitude Loading

FASTRAN predicted a factor of 10 increase in fatigue life after the overload and a 23% reduction in fatigue life after the underload using the 6-μm flaw size, as shown in figure 58 (vertical lines). FASTRAN was unable to correlate the hole-drilled specimens with a single EIFS without either considering a tensile residual-stress field at the edge of the hole or a statistical variation because of the limited test results at the highest and lowest test stress level. As shown by the three curves in figure 58, a 6-μm flaw would be needed at the highest stress level, but about a 10-μm flaw size would be needed at the lowest stress level. A tensile residual-stress field could be eliminated at the higher applied stress level (due to hole yielding), but may be retained at the lower applied stress levels. These data require further study.

Figure 60 shows a comparison of specimens tested at the median stress level (145 MPa). The baseline (polished) results are shown as the solid symbols and the horizontal line is their average life. The production-quality hole specimens (old or new drill bit; with or without a pilot hole) fell together in a very tight band (open circular symbols). The small horizontal line is the average of the drilled-hole specimens (30% lower than the baseline fatigue life). Surprisingly, the 1.7-overload tests showed a large amount of scatter. The effect of the overload increased the fatigue life more than 18 times longer than the polished specimens. However, the 1.7-underload tests showed a reduction in the fatigue life of only about 40% from the baseline tests.

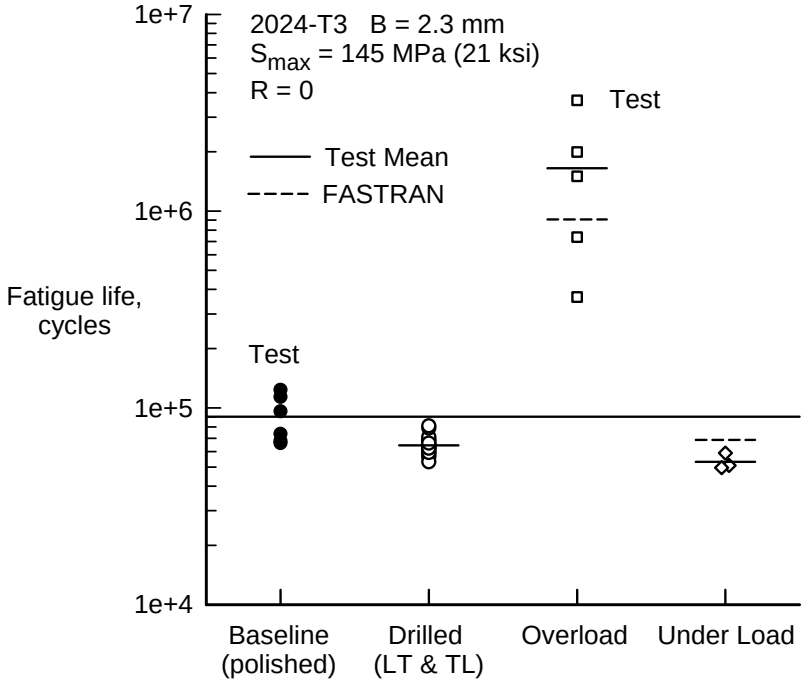

Figure 60. Comparison of Test and Predicted Fatigue Lives for Single-Hole Specimens

9. FATIGUE ANALYSIS OF LABORATORY LAP JOINT SPECIMENS.

During the past decade, research on the aging aircraft fleets by the FAA, NASA, and the DoD have generated test and analysis data on riveted lap joints from simple laboratory specimens to curved test panels [51]. The results on the laboratory specimens have been used to improve and verify the fatigue and crack growth methodologies for lap joint configurations. In preparing for the fatigue life predictions on the FT-2 panel (removed from a retired B-727 aircraft and tested at the FAA William J. Hughes Technical Center), it was believed that some analyses of laboratory lap splice joints would help determine the initial discontinuity size or initial flaw size to be used in the analyses. Based on the teardown information being generated on the B-727 [9-12], the cracking observed on the right side of the aircraft and the noncracking observed on the left side may indicate that the left side had "tight" rivets. Even the cracking on the right-hand side had indications of tight rivets because the cracks were not located at the 0- and 180-degree locations, but at various locations on the opposite side of the rivet from the rivet load.

Herein, two studies on simple lap joint specimens were used to establish appropriate crack configurations and the EIFSs. These crack configurations and EIFS values were then used to calculate fatigue lives and crack growth in fuselage lap joints in a retired narrow-body passenger aircraft and for a curved panel cut from the retired aircraft and tested in a pressure-box facility.

9.1 STRESS ANALYSIS OF CRACKS AT RIVET-LOADED FASTENER HOLES.

Stress-intensity factors for a corner crack or a through crack emanating from a typical fastener-loaded hole under remote applied stress, remote bending, bypass stress, fastener load, and interference, as shown in figure 61, are given in reference 52. One of the restrictions for the corner crack equations is that the crack aspect ratio, a/c, is fixed, and the influence of rivet interference is based on a simple approximation. Stress-intensity factor equations for a surface crack in a plate under remote tension and bending are given in reference 53.

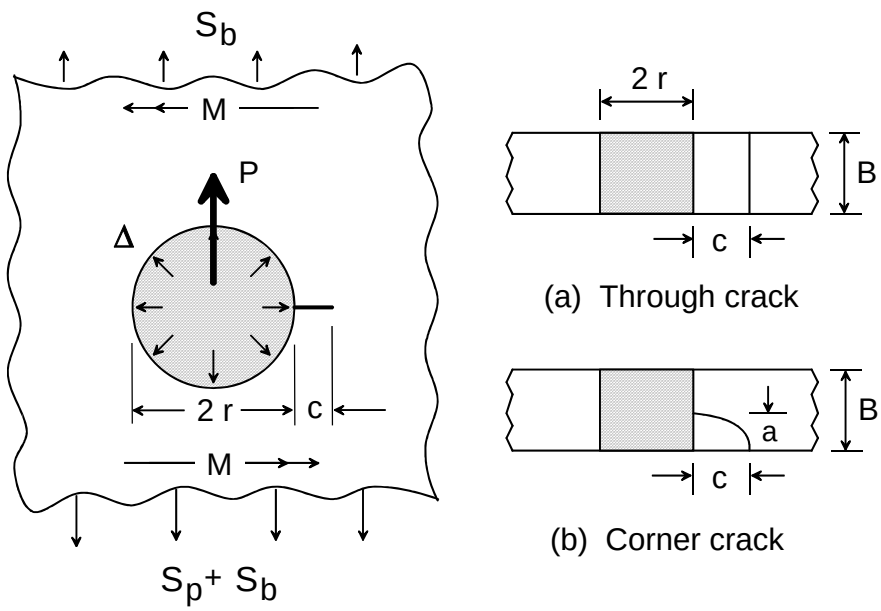

Figure 61. Crack Configuration and Loading for Rivet-Loaded Hole

9.2 MATERIAL CRACK GROWTH PROPERTIES.

The material used in the laboratory lap joint specimens and the narrow-body fuselage structure was 2024-T3 thin-sheet clad aluminum alloy. Fatigue crack growth rate data on a clad aluminum alloy were obtained from Schijve, Jacobs, and Tromp [54]. The yield stress was 360 MPa, and the ultimate tensile strength was 490 MPa. These data covered a wide range of stress ratios (R = -0.1 to 0.73). Previously, Newman [55] had developed steady-state crack-opening stress equations from the FASTRAN crack closure model for middle-crack tension, M(T), specimens subjected to constant-amplitude loading at various stress levels, stress ratios (R), and constraint factors (α). These equations were used to develop the effective stress-intensity factor range against rate relation for the clad alloy, as shown in figure 62. The symbols show the test data for the various stress ratio tests. The data correlated very well with the same constraint factors that had been used for the bare material [56]. Additional small-crack data on a thin-sheet 2024-T3 bare aluminum alloy [57] were used to estimate the effective SIF range results at extremely low crack growth rates near threshold. The solid curve shows the ΔK_{eff} baseline relation (see table 3) used in all subsequent fatigue and crack growth calculations. The dashed curve shows the relation obtained from the bare material. For most of the data, the clad and bare results agreed quite well.

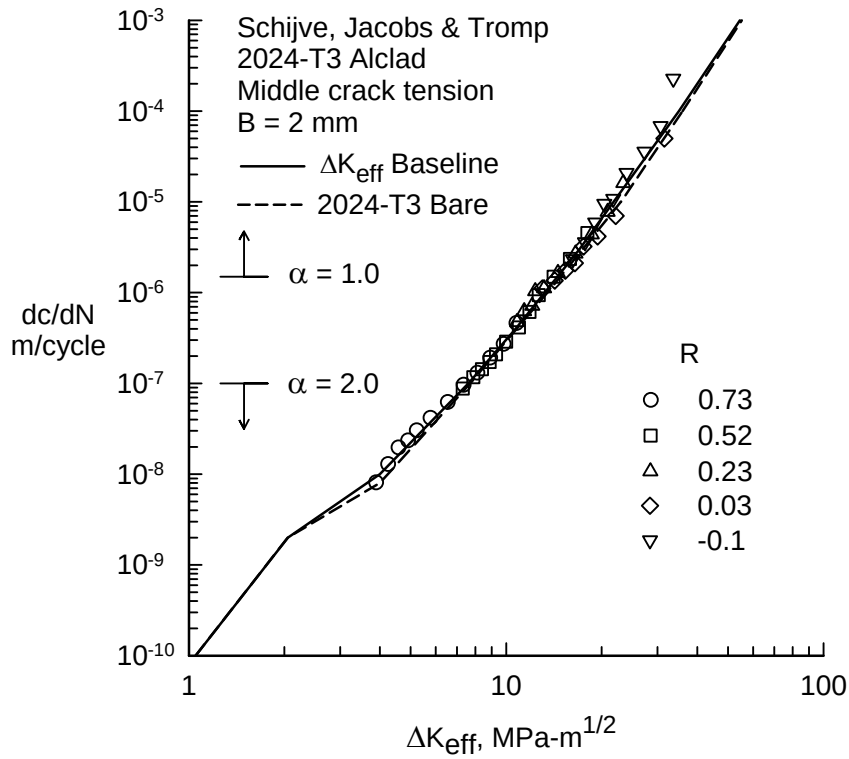

Figure 62. Fatigue Crack Growth Rate Properties for 2024-T3 Alclad Material

Table 3. Effective Stress-Intensity Factor Against-Rate Relation for 2024-T3 (Alclad)

ΔK_{eff}, MPa-m$^{1/2}$	dc/dN, m/cycle
0.75	1.00e-11
1.05	1.00e-10
2.05	2.00e-09
4.00	1.00e-08
7.60	1.00e-07
10.7	4.00e-07
17.0	3.00e-06
35.0	1.00e-04
85.0	1.00e-02
$\alpha = 2.0$	1.00e-07
$\alpha = 1.0$	1.50e-06

9.3 NORTHWESTERN UNIVERSITY THREE-RIVET-ROW TEST SPECIMENS.

Conner, Fine, and Achenbach [58] conducted a large number of lap joint tests on specimens, as shown in figure 63. The specimens were prepared by riveting together two Alclad 2024-T3 aluminum alloy panels, one with three countersunk rivet holes and one with three straight-shank holes. The rivets were made of 2017-T4 aluminum alloy and the hole diameter was about

4.8 mm. The specimens were fatigue tested at remote stress levels of 103 to 180 MPa at a stress ratio of 0.1. When the specimens were fatigued at the lowest stress levels (103 and 129 MPa), the cracks initiated and grew as "eyebrow" cracks at the faying surface on the straight-shank hole side, but when the higher stress levels were applied (154 and 180 MPa) the cracks initiated as corner cracks along the faying surface.

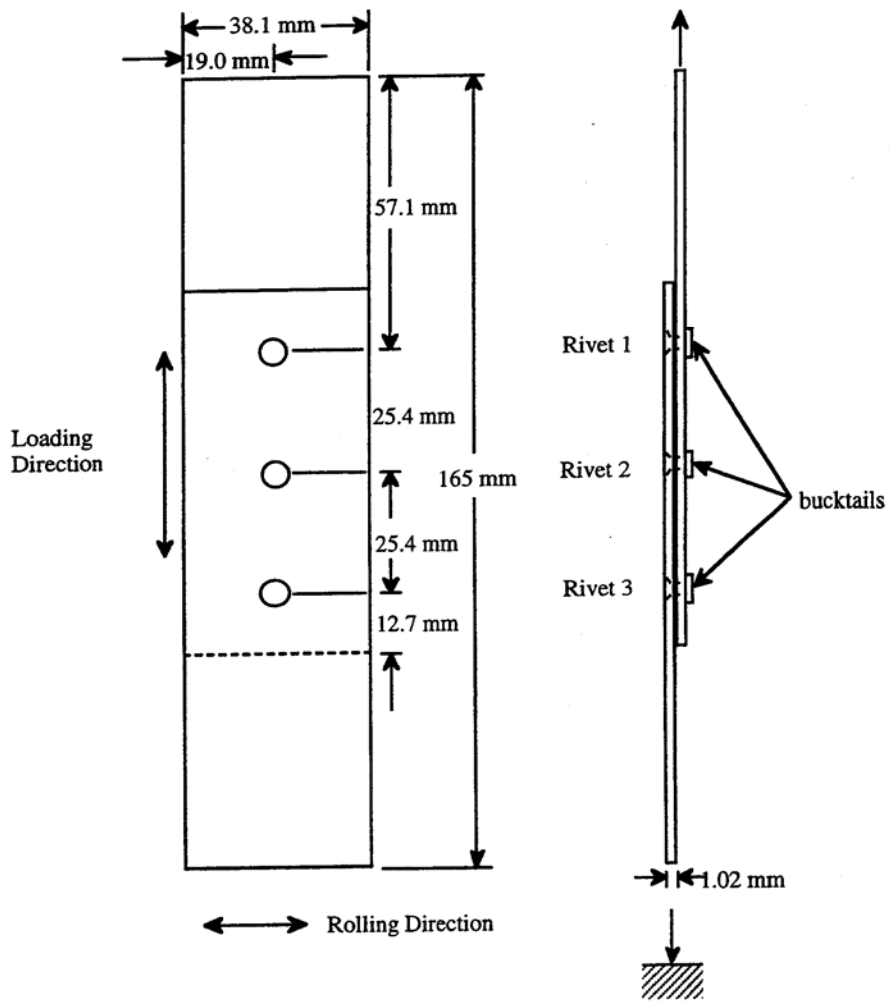

Figure 63. Three-Rivet-Row Lap Joint Specimen Tested at Northwestern University

The latter is the typical crack configuration used in the national aging aircraft programs for the FAA and NASA. At the lowest applied stress levels, the cracks in the lap joint specimens initiated and grew as eyebrow cracks at the opposite end of the hole from the fastener loads, as shown by the C-scan in figure 64a. But at the highest applied stress levels, the cracks in the lap joint specimens initiated and grew at approximately the 0 and 180 degree locations, as shown in figure 64b.

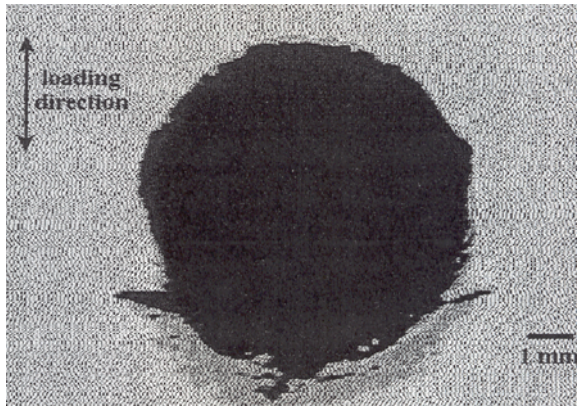

Figure 64a. Initiation Sites for Cracks in Lap Joint Specimens Tested at Low-Applied Stress Levels

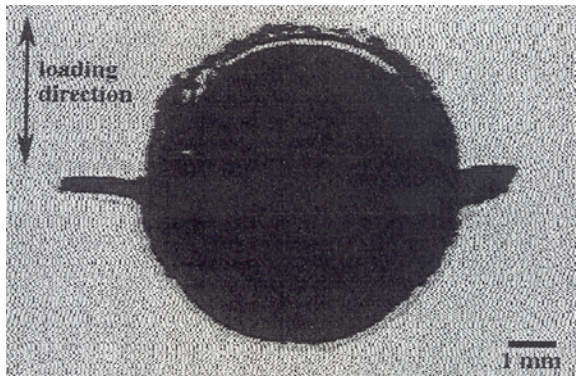

Figure 64b. Initiation Sites for Cracks in Lap Joint Specimens Tested at High-Applied Stress Levels

FASTRAN was used to calculate the fatigue lives of these specimens using two different crack models. The first was the eyebrow-type crack, shown in figure 65. Here, a surface crack which was assumed as the initial crack size was subjected to remote tension and bending loads. The rivet was totally neglected in these analyses. The bending stress was estimated from the Hartman-Schijve strength of materials approach [59] and was 0.34 times the remote applied stress. Figure 66a shows the results of tests conducted with 103 MPa with $R = 0.1$. The crack length, 2c, was measured using an acoustic microscope and includes the hole diameter plus crack growth on both sides of the hole. In the eyebrow crack analyses, an initial surface crack length, c_i, of 2.4 mm was assumed. The initial crack depth, a_i, was then chosen to fit the bounds of the three test specimens. The 15-μm deep crack gave nearly an upper bound and the 30-μm deep crack gave a lower bound.

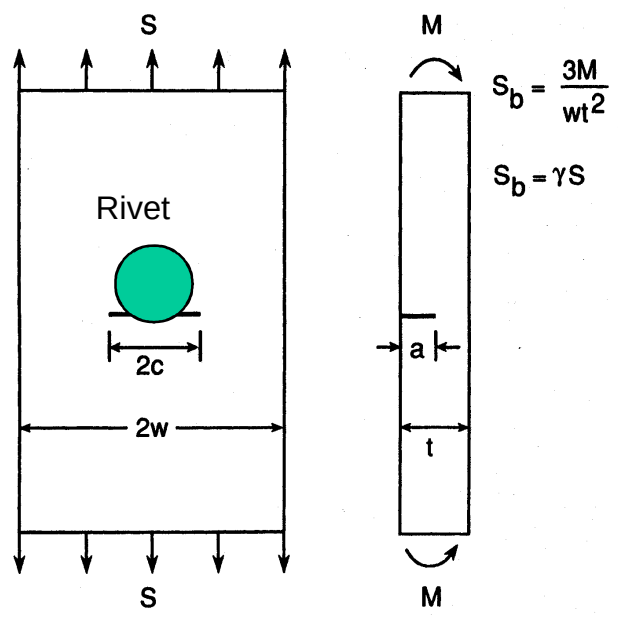

(a) Tension (b) Bending

Figure 65. Crack Configuration Modeled for the Eyebrow Crack

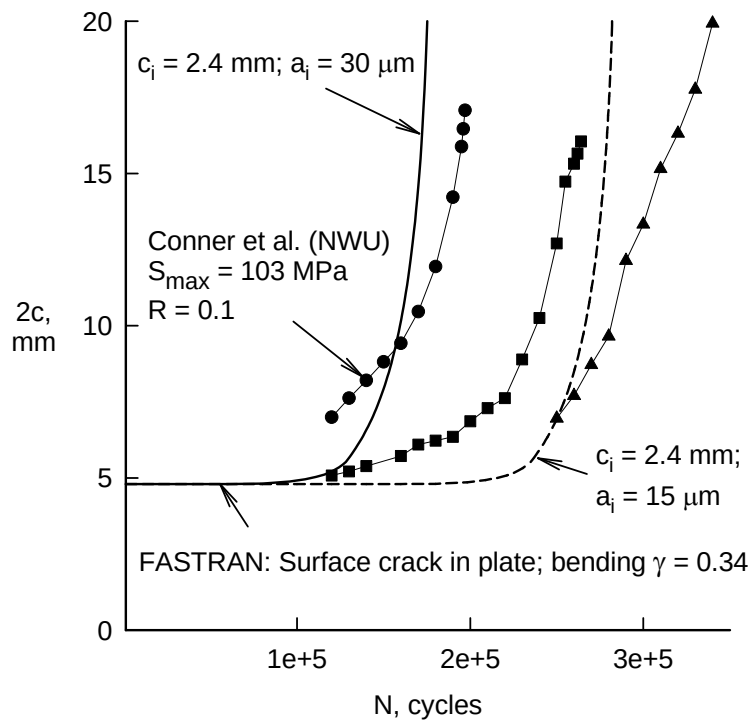

Figure 66a. Crack Growth in Riveted Lap Joint at a Low-Applied Stress Level

For tests conducted at a higher-applied stress level, as shown in figure 66b, the crack configuration used in the tests and analyses was a corner crack located at the edge of the straight-shank hole. The bending stress was calculated to be 0.39 times the applied stress. Again, the crack length, 2c, was measured with the acoustic or optical microscope and the crack length included the hole diameter. The initial corner crack size was, again, chosen to fit the upper and lower bounds of the test data. Here, a 50- and 100-μm crack fit the results fairly well.

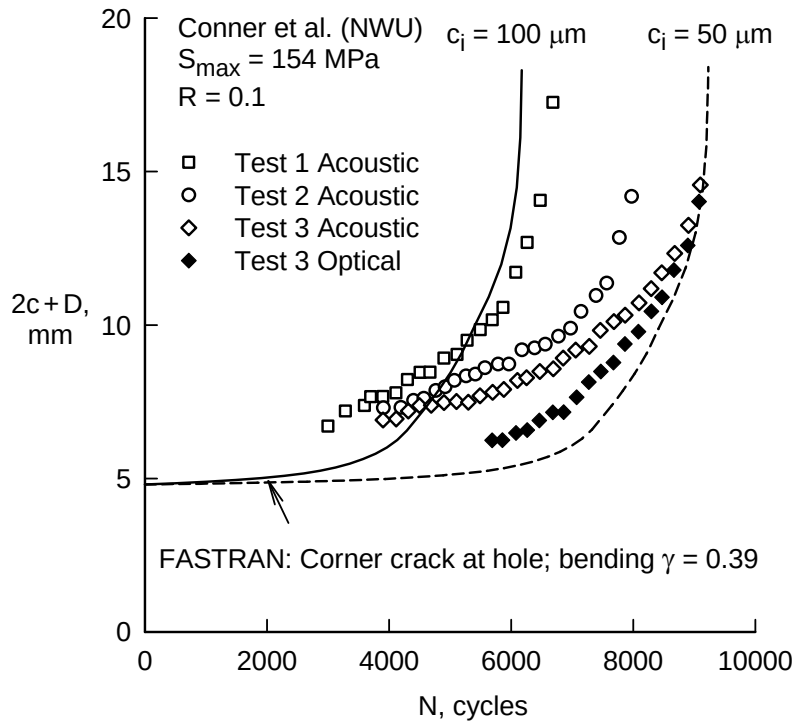

Figure 66b. Crack Growth in Riveted Lap Joint at a High-Applied Stress Level

9.4 GEORGIA INSTITUTE OF TECHNOLOGY AND DELTA AIR LINES TWO-RIVET-ROW TEST SPECIMENS.

Recently, two-rivet-row lap joint specimens were tested at Georgia Institute of Technology [14]. The lap joint specimen is shown in figure 67. Several rivet conditions were considered: (1) standard-driven rivets, (2) tight or overdriven rivets, or (3) underdriven rivets. All specimens were subjected to a remote stress of 124 MPa. Figure 68a shows the fatigue test results on the underdriven rivet condition, which had an average life of about 80,000 cycles. In the fatigue analyses, a semicircular corner crack (a/c = 1) was assumed to occur along the faying surface of straight-shank hole. Various EIFS values were assumed. It was found that a 6-μm crack fit the average results quite well. The upper and lower bounds were captured quite well by the 4- and 15-μm crack, respectively. The test results for the standard- and overdriven rivets are shown in figure 68b. Here, it was found that the standard- and overdriven rivets produced nearly the same cycles to failure. The average fatigue life was about 60% larger than for the underdriven rivets. Again, a semicircular corner crack was assumed as the EIFS; but an interference value of 7 μm

was needed to fit the mean of the test results with a 6-μm initial crack. Again, the fatigue scatter was captured quite well by the 4- to 15-μm initial crack.

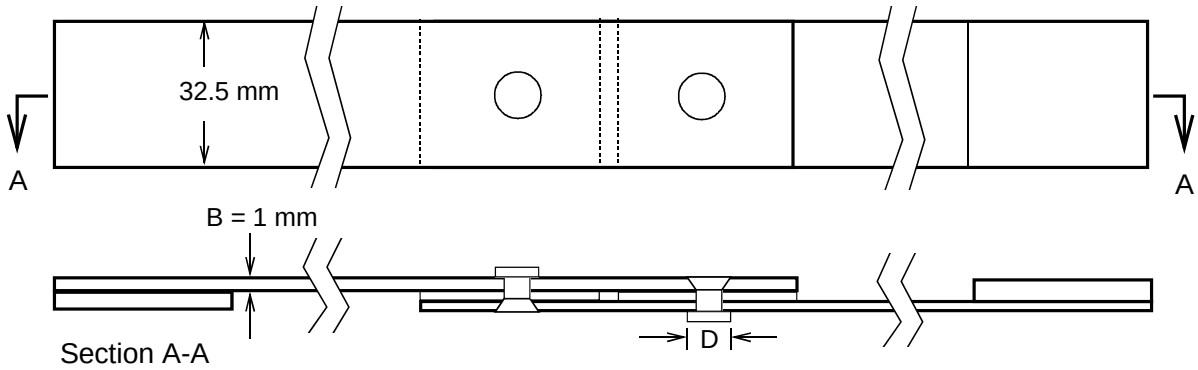

Figure 67. Two-Rivet-Row Lap Joint Specimen Tested at Georgia Institute of Technology

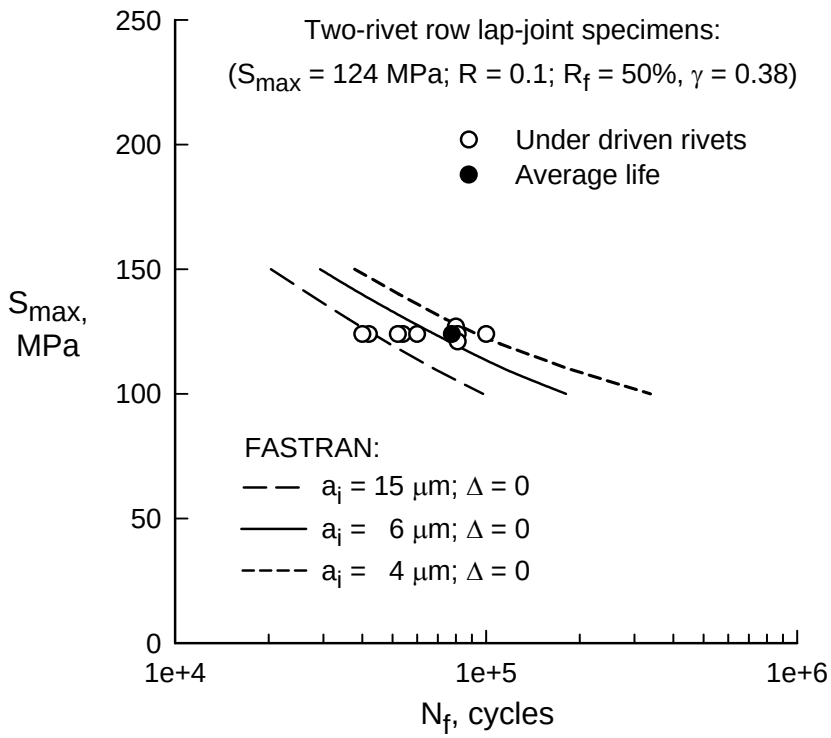

Figure 68a. Fatigue Lives of Lap Joint Specimens With Underdriven Rivets

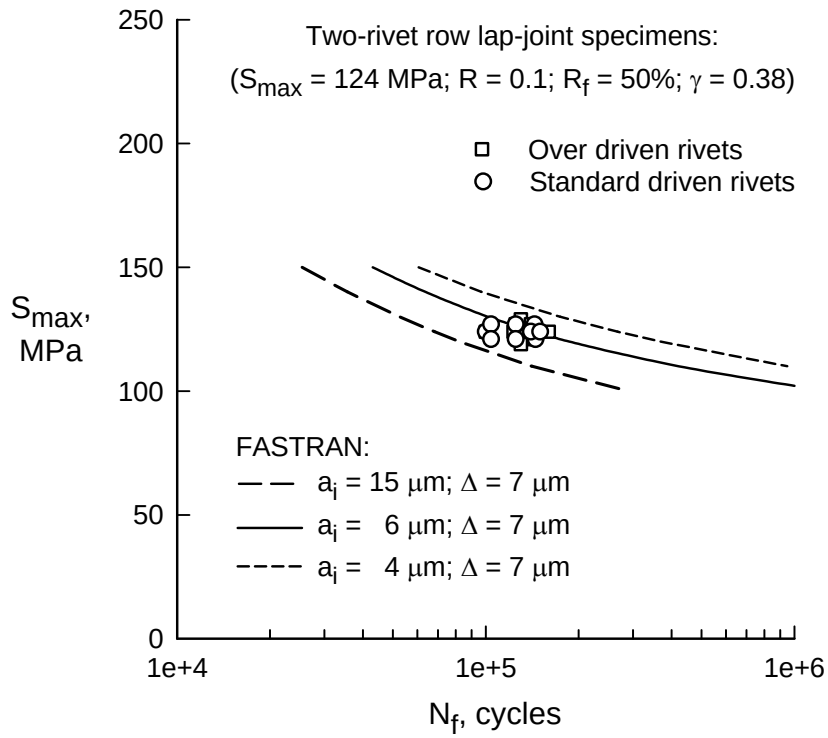

Figure 68b. Fatigue Lives of Lap Joint Specimens With Standard and Overdriven Rivets

10. FATIGUE ANALYSIS OF CURVED LAP JOINT TEST PANELS.

One of the objectives of the B-727 teardown investigation was to remove panels from a retired narrow-body aircraft [9-12] after about 60,000 flights and conduct continued fatigue tests on the large panels. These panel tests and the teardown investigation were to establish the current state of cracking in the fuselage during an actual flight history and to provide cracking data from continued fatigue testing to verify life-prediction methods and codes.

Two of the curved fuselage panels removed from the retired aircraft were tested in a pressure-box at the FAA William J. Hughes Technical Center [10]. Prior to testing, predictions were made on the expected fatigue life of the FT-2 panel, shown in figure 69. Because these panels were removed from the side of the aircraft, which had apparently tight rivets, the surface crack model (see figure 66b) was used to make fatigue life and crack growth predictions. Figures 70 and 71 show the predicted crack length, 2c, against cycles, N, for two levels of bending. The flight history was assumed to be at 94.5 MPa at $R = 0$ for 59,495 cycles, and the stress applied to the FT-2 panel was 98 MPa at $R = 0.1$ until failure. The original life predictions were made with a 100-μm depth initial surface crack, which predicted failure in about 150,000 cycles (see figure 70). After nearly 100,000 pressure cycles on the FT-2 panel, the test was terminated due to loading fixture failures. But close examination of the lap joint region indicated no cracking. Later, the FT-1 panel was tested to 180,000 cycle, again, with no indication of cracking. Recall that the initial crack depths that needed to fit the lap joint laboratory specimens ranged from 15- to 30-μm. Using these values produced no significant cracking after 100,000 cycles and failure from 200,000 to over 300,000 cycles. Whether the FT-1 and FT-2 panels could have withstood

this large increase in pressure cycles could not be determined. However, the predictions seem to be reasonable for the tight-rivet conditions.

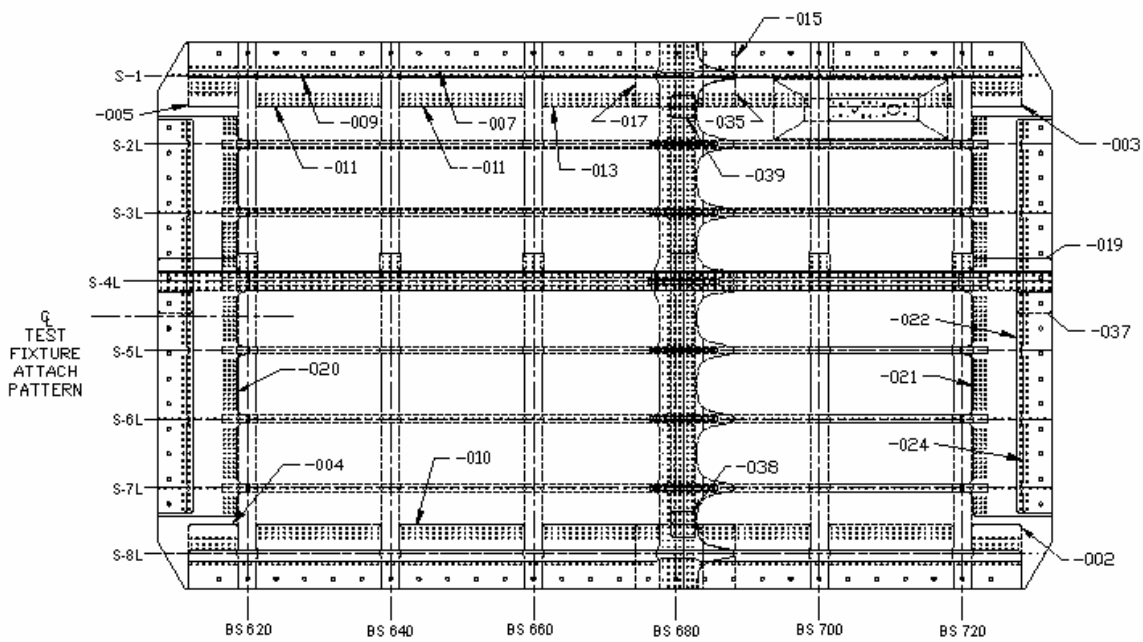

Figure 69. Curved Panel (FT-2) From Narrow-Body Aircraft Tested at the FAA William J. Hughes Technical Center

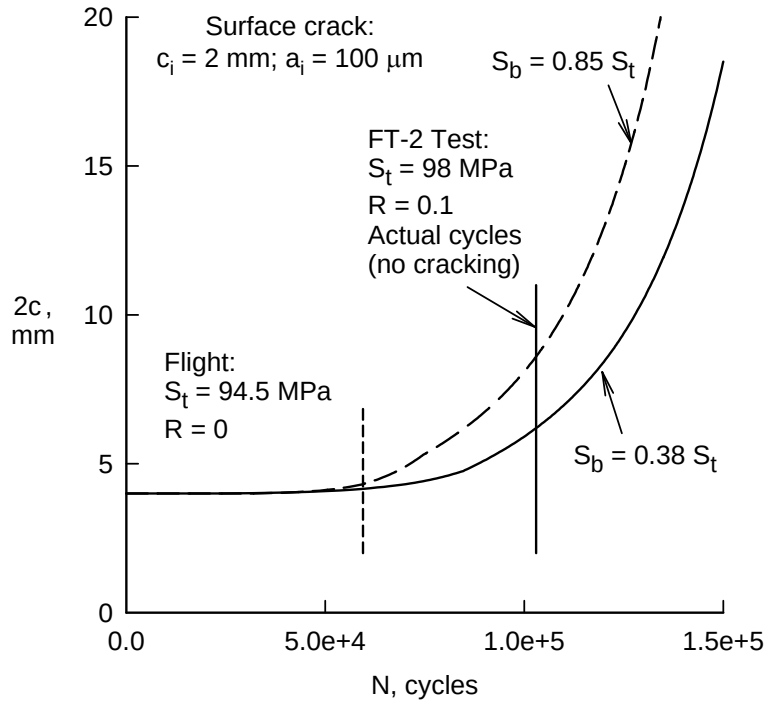

Figure 70. Influence of Secondary Bending on Predicted Crack Growth in Narrow-Body Aircraft

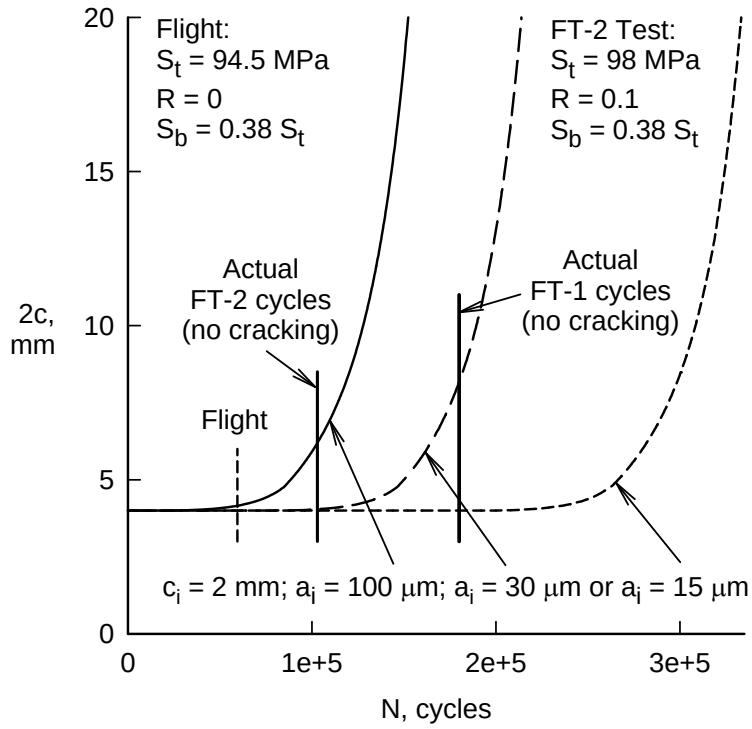

Figure 71. Predicted Crack Growth in Narrow-Body Aircraft and Continued Testing at the FAA William J. Hughes Technical Center

11. FATIGUE ANALYSIS OF CRACKING IN B-727 TEARDOWN AIRCRAFT.

The FAA [9] teamed with Delta Air Lines [10-12] to conduct a destructive evaluation of a retired, narrow-body passenger aircraft that had nearly 60,000 flights. Some of the objectives of the program were to characterize the state of MSD at riveted fastener holes in the fuselage of an aircraft at the design service goal, and to develop or verify analysis methods that can correlate and predict the state of MSD at any point in time. For the narrow-body aircraft, observations on cracking from the destructive examination of the fuselage joints indicated that one side of the aircraft appeared to have tight (within specifications) rivets, whereas the other side of the aircraft appeared to have underdriven (55%) rivets [11 and 12]. Faying surface origins were predominate, despite a majority of underdriven rivets. A large number of cracks were examined with a scanning electron microscope (SEM) to count striations and to backtrack the cracking history to reconstruct the crack length against flight cycle behavior [12]. The measured crack length against flight cycle results tended to fall within a fairly narrow band considering the complexity of the structural joints. Several curved fuselage panels were removed from the other side of the fuselage, and one panel was tested in a pressure-box facility.

The objective of this section is to use FASTRAN [5] and small-crack theory to calculate fatigue lives and crack growth in the narrow-body aircraft. Comparisons were made between AFGROW [60] and FASTRAN for crack growth in the narrow-body aircraft and the reconstructed crack length against flight pressure cycle history.

The retired, narrow-body passenger aircraft was destructively examined to determine the state of cracking in the fuselage lap joint regions on one side of the aircraft [11 and 12]. On the other side, several curved fuselage panels were removed from the aircraft. A drawing of structural details around the horizontal lap joint is shown in figure 68. Fatigue cracks would be expected to be present and grow in the horizontal three-rivet row lap joint near the center of the panel. Figure 72 shows the cross section at a rivet location showing the inner and outer sheets with an internal doubler and the countersunk rivet. Cracks were expected to initiate and grow from the faying surface as corner cracks or surface cracks. In the following, comparisons were made between the measured and calculated cracking in the aircraft fuselage structure and the cracking in a curved fuselage panel removed from the aircraft and tested at the FAA William J. Hughes Technical Center.

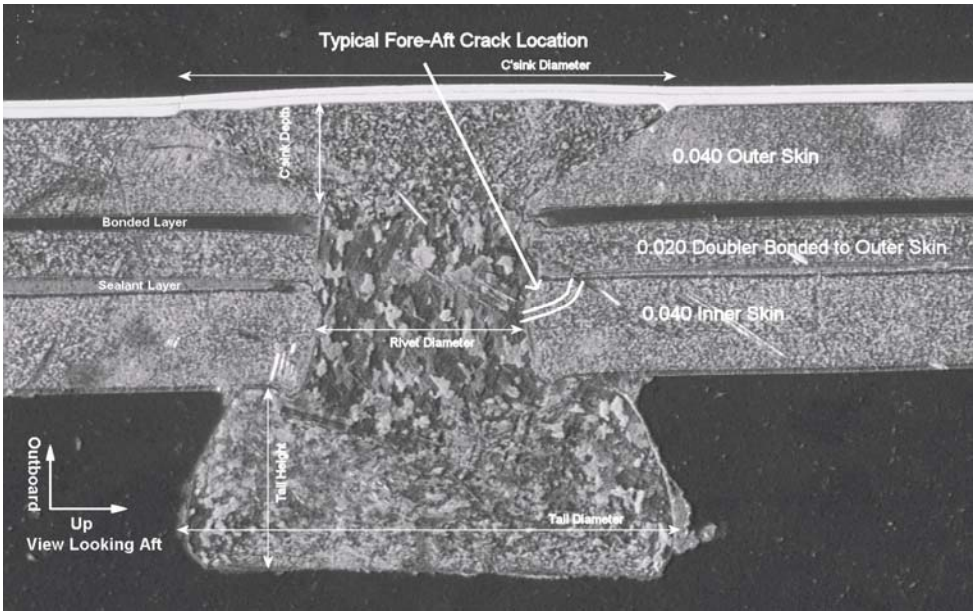

Figure 72. Typical Rivet Configuration in Narrow-Body Aircraft

AFGROW and FASTRAN have both been used to calculate the cracking in the retired aircraft during its 60,000 pressure cycle history. Of concern was the restriction in FASTRAN that the a/c ratio had to be held constant, such as a/c = 1. Figure 73 shows a comparison of the a/c ratio for a test case, which had 37% fastener load, 63% bypass load, and 85% bending. The solid curve is the result from AFGROW for a corner crack growing at a fastener-loaded hole in which crack growth is independent in the a and c directions (a/c variable). The predicted a/c ratio was almost unity until the crack began to break through the sheet thickness (a/t = 1). For a/t ratios greater than unity, AFGROW analyses modeled an oblique crack front until the crack transitions into a straight-through crack. However, FASTRAN assumes that the a/c ratio is held constant at unity until breakthrough. Thereafter, a straight-through crack is assumed until failure. Because of the compensating effects of the remote loads causing higher stress-intensity factors along the depth, a direction, and bending causing lower stress-intensity factors along the depth direction, the crack in AFGROW was predicted to grow nearly as a quarter-circular (a/c = 1) crack.

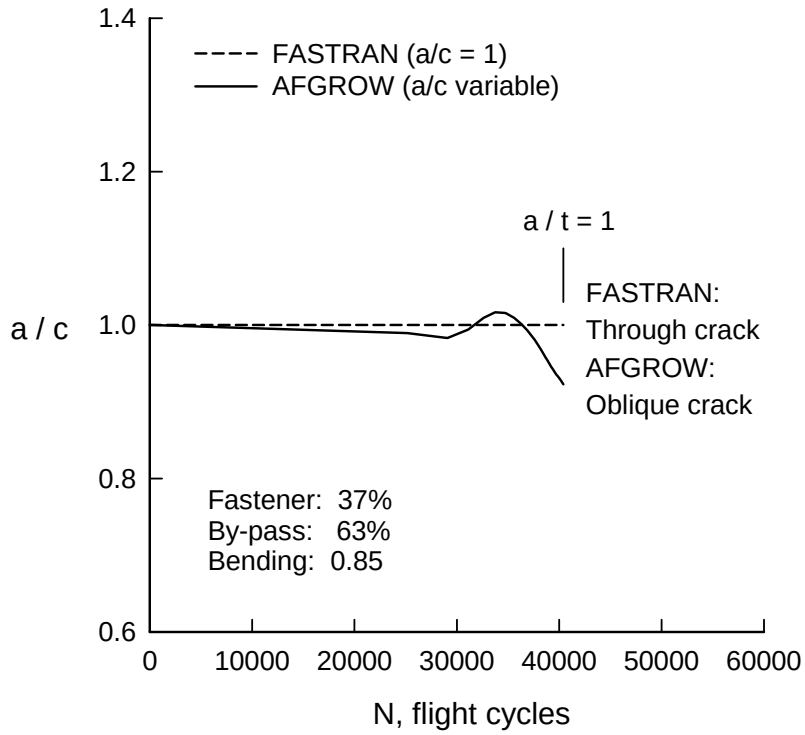

Figure 73. Measured and Calculated Crack Growth From Riveted Joints in Narrow-Body Aircraft

A large number of rivet locations have been examined from the retired passenger aircraft and a large number of cracks were found emanating from the rivet holes. A number of these cracks were examined in an SEM to count striations and to backtrack the cracking history to reconstruct the crack length against flight cycle behavior [12]. Some of these results are shown in figure 74. The open symbols show results on a surface crack emanating along the faying surface but near the fastener hole, and the solid symbols show a corner or surface crack emanating from the edge of the fastener hole. The dashed curve is a calculated result from AFGROW using an EIFS of 5-μm radius corner crack. The EIFS value was chosen to roughly fit the mean of the measured data. The solid curves show calculations made with FASTRAN for three values of EIFS ranging from 9- to 20-μm radius corner crack. Both codes produced essentially the same results, in that, the shape of the crack length against flights curves were similar. The only major difference was in the small-crack regime (5 to 20 μm), where FASTRAN predicted faster crack growth. FASTRAN calculations were also carried out to failure, which indicated that if not repaired or replaced, the fuselage is predicted to go to failure from 70,000 to 90,000 flights.

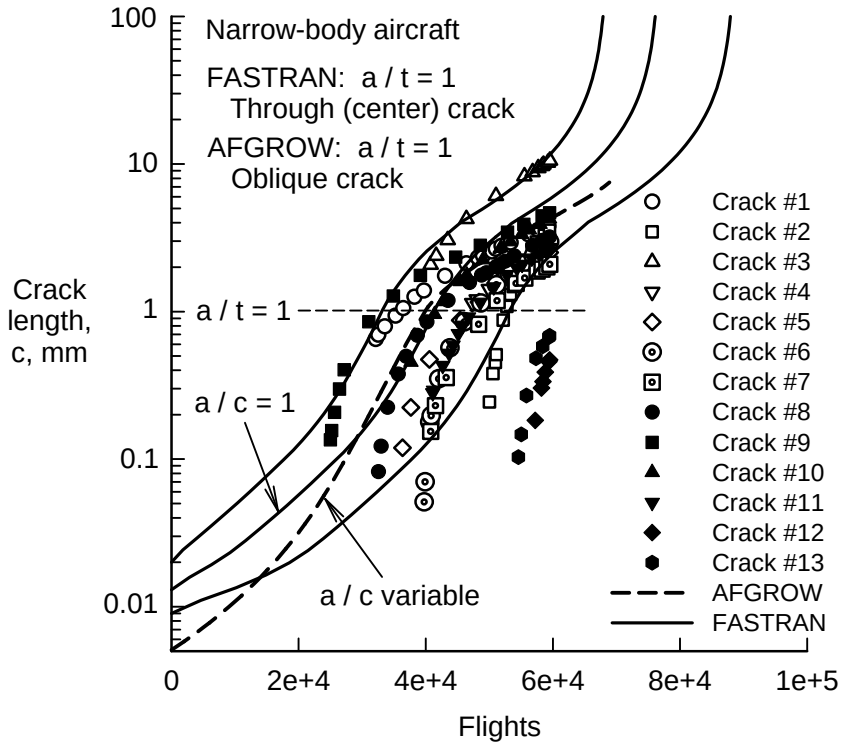

Figure 74. Comparison of AFGROW and FASTRAN Crack-Shape Analyses for a Typical Riveted Lap Joint

12. SUMMARY.

This report is the result of a study conducted on the influence of residual stresses and production-quality holes on the fatigue behavior of laboratory coupons, laboratory flat-riveted lap joint specimens, curved-riveted lap joint panels from a retired narrow-body aircraft, and data from the retired aircraft destructive evaluations. The influence of residual stresses was accounted for in the life-prediction methodology by developing stress-intensity factor solutions and codes for both two- and three-dimensional cracked bodies. The influence of the production-quality hole was accounted for by developing EIFS values to fit the experimental test data on the coupons and riveted lap joint panels.

The material selected was 2024-T3 aluminum alloy (bare and clad) sheet because of its use in the majority of the current fleet of commercial aircraft. The NASA Langley Research Center supplied the bare material for part of this study because their material has a well-documented fatigue and fatigue crack growth history. Lockheed-Martin Aeronautics Company and Delta Air Lines, Inc. provided production-quality drilled-hole coupons, the two-rivet lap joint specimens, and guidance on the critical parameters studied in this investigation.

Attempts to measure or to establish the magnitude and distribution of the residual stresses in the production-quality drilled fastener holes were unsuccessful. However, fatigue tests conducted on the coupons made of the 2024-T3 bare material, with both production-quality and polished holes, indicated that the residual stresses may be low compared to previous studies; this, in turn,

indicated that production-quality drilled holes generated compressive residual stresses that had a significant impact on the fatigue life. The three-dimensional finite element simulations of the riveting-installation process demonstrated that residual stresses were induced around the fastener hole due to the severe plastic deformations and the various riveting parameters.

Two- and three-dimensional stress analyses were developed to calculate the SIFs for through, surface, and corner cracks emanating from a straight-shank fastener hole under various applied (remote tension, bending, fastener) loading and with an arbitrary residual-stress distribution. These analyses were only for straight-shank holes, i.e., the countersunk configuration was not considered. The two-dimensional SIF code was based on Green's functions, whereas the three-dimensional SIF code was based on a weight function analysis. The Green's function code (SIFK2D) and the weight-function code (K3DL) are stand-alone codes, and they were used to generate stress-intensity factor solutions for the FASTRAN life-prediction code.

Fatigue-life analyses on the polished and production-quality single-hole specimens and the two-rivet lap joint specimens were made using the small-crack theory and the usual EIFS values for open-hole and lap joint specimens. Fatigue crack growth rate data on bare material was used on the polished and production-quality single-hole specimens, while Alclad material data was used on the lap joint specimens, curved panels, and the actual aircraft joint analyses. The predicted results on both the open-hole and two-rivet lap joint specimens agreed well with the test data. An assessment on the impact of loose and tight rivets on the fatigue life of more realistic structural configurations was made using the results from the EIFS values determined from laboratory-riveted lap joint specimens and previous analyses of test results from a wide-body fuselage aircraft. Studies at Delta Air Lines indicated that the right and left sides of the retired narrow-body (B-727) aircraft had quite different cracking behaviors. Predictions made on the curved-panel tests conducted at the FAA FASTER facility indicated that the panels on one side of the aircraft could withstand about 90,000 additional pressure cycles to failure (the panel had been subjected to about 60,000 flights before testing); whereas, the data and analyses from the destructive teardown of the retired aircraft by Delta Air Lines (lap joints from the other side of the aircraft) indicated that only an additional 10,000 flights would have been required to cause failure, if the fuselage had not been retired, inspected, or repaired.

13. REFERENCES.

1. National Aging Aircraft Research Program Plan, United States Department of Transportation, Federal Aviation Administration, William J. Hughes Technical Center, Atlantic City International Airport, October 1993.

2. Harris, C.E., Newman, J.C., Jr., Piascik, R., and Starnes, J., Jr., "Analytical Methodology for Predicting Widespread Fatigue Damage Onset in Fuselage Structure," *Journal of Aircraft*, Vol. 35, 1998, pp. 307-317.

3. Private Communication, Dr. Jin Yu, The Boeing Company, "Widespread Fatigue Damage Evaluation," 2001.

4. Hsu, C.I., Lo, J., Yu, J., Lee, X.G., and Tan, P., "Residual Strength Analysis Using CTOA Criteria for Fuselage Structures Containing Multiple Site Damage," *Engineering Fracture Mechanics*, Vol. 70, No. 3-4, 2003, pp. 525-546.

5. Newman, J.C., Jr., "FASTRAN II—Fatigue Crack Growth Structural Analysis Program," NASA TM-104159, February 1992.

6. Newman, J.C., Jr., Swain, M.H., and Phillips, E.P., "An Assessment of the Small Crack Effect for 2024-T3 Aluminum Alloy," Small Fatigue Cracks, R.O. Ritchie and J. Lankford, eds., 1986, pp. 427-452.

7. Wu, X.R., Newman, J.C., Jr., Zhao, W., Swain, M.H., Ding, C.F., and Phillips, E.P., "Small Crack Growth and Fatigue Life Predictions for High-Strength Aluminum Alloys: Part I—Experimental and Fracture Mechanics Analysis," *Fatigue and Fracture of Engineering Materials and Structures*, Vol. 21, 1998, pp. 1289-1306.

8. Newman, J.C., Jr., Wu, X.R., Swain, M.H., Zhao, W., Phillips, E.P., and Ding, C.F., "Small Crack Growth and Fatigue Life Predictions for High-Strength Aluminum Alloys: Part II – Crack Closure and Fatigue Analysis," *Fatigue and Fracture of Engineering Materials and Structures*, Vol. 23, 2000, pp. 59-72.

9. Bakuckas, J.G, Jr., Carter, A., and Steadman, D., "Destructive Evaluation and Extended Fatigue Testing of Retired Aircraft Fuselage Structure," *Ninth International Fatigue Congress*, Atlanta, GA, USA, May 14-19, 2006.

10. Mosinyi, B.R., Bakuckas, J.G., Awerbuch, J., Lau, A.C., and Tan, T.-M., "Experimental and Analytical Characterization of Damage Growth in Fuselage Structure During Full-Scale Fatigue Testing, *Ninth International Fatigue Congress*, Atlanta, GA, USA, May 14-19, 2006.

11. Jury, D., Ramakrishnan, R., and Carter, A., "Rivet Installation and Hole and Faying Surface Quality Studies in a Lap Joint From a Retired Commercial Aircraft," *Ninth International Fatigue Congress*, Atlanta, GA, USA, May 14-19, 2006.

12. Ramakrishnan, R., Steadman, D., and Carter, A., "Crack Growth History Reconstruction of Lap Joint Fatigue Cracks," *Ninth International Fatigue Congress*, Atlanta, GA, USA, May 14-19, 2006.

13. Ralph, W.C., Johnson, W.S., Toivonen, P., Makeev, A., and Newman, J.C., Jr., "Assessment of Hole Drilling Procedures on Hole Quality and the Resulting Fatigue Lives," FAA report DOT/FAA/AR-07/56,V2, March 2009.

14. Atre, A. and Johnson, W.S., "A Finite Element and Experimental Investigation on the Fatigue of Riveted Lap Joints in Aircraft Applications," FAA report DOT/FAA/AR-07/56,V3, March 2009.

15. Kang, J., Johnson, W.S., and Clark, D.A., "Three-Dimensional Finite Element Analysis of the Cold Expansion of Fastener Holes in Two Aluminum Alloys," *ASME Journal of Engineering Materials and Technology*, Vol. 124, April 2002.

16. Raju, I.S. and Newman, J.C., Jr., "Stress-Intensity Factors for Two Symmetric Corner Cracks," *Fracture Mechanics*, ASTM STP 677, 1979, pp. 411-430.

17. Newman, J.C., Jr. and Raju, I.S., "Stress-Intensity Factor Equations for Cracks in Three-Dimensional Finite Bodies Subjected to Tension and Bending Loads," *Computational Methods in the Mechanics of Fracture*, Vol. 2, S.N. Atluri, ed., 1986, pp. 311-334.

18. Zhao, W., Sutton, M.A., and Newman, J.C., Jr., "K3D—A Program for Determining Stress Intensity Factors of Surface and Corner Cracks from a Hole," ASTM STP 1321, 1997, pp. 656-670.

19. Zhao, W., Wu, X.R., and Yan, M.G., "Weight Function Method for Three-Dimensional Crack Problems-I," *Engineering Fracture Mechanics*, Vol. 34, No. 3, 1989, pp. 593-607.

20. Zhao, W., Wu, X.R., and Yan, M.G., "Weight Function Method for Three-Dimensional Crack Pproblems-II," *Engineering Fracture Mechanics*, Vol. 34, No. 3, 1989, pp. 609-624.

21. Zhao, W., Sutton, M.A., and Newman, J.C., Jr., "K3D—A Program for Determining Stress-Intensity Factors of Surface and Corner Cracks From a Hole," ASTM STP 1321, *American Society for Testing and Materials*, West Conshohocken, PA, 1997, pp. 656-670.

22. Zhao, W., Newman, J.C., Jr., Sutton, M.A., Wu, X.R., and Shivakumar, K.N., "Analysis of Corner Cracks at Hole by a 3-D Weight Function Method With Stresses From Finite Element Analysis," NASA TM-110144, 1995.

23. Zhao, W., Newman, J.C., Jr., Sutton, M.A., Wu, X.R., and Shivakumar, K.N., "Analysis of Surface Cracks at Hole by a 3-D Weight Function Method with Stresses from Finite Element Analysis," NASA TM-110145, 1995.

24. Fawaz, S.A. and Andersson, B. "Accurate Stress-Intensity Factor Solutions for Unsymmetric Corner Cracks at a Hole," *Fourth Joint DoD/FAA/NASA Conference on Aging Aircraft*, 15-18 May 2000, St. Louis, MO.

25. Fawaz, S.A. and Andersson, B., "Accurate Stress-Intensity Factor Solutions for Corner Cracks at a Hole," *Engineering Fracture Mechanics*, Vol. 71, 2004, pp. 1235-1254.

26. Hudson, C.M., "Effect of Stress Ratio on Fatigue Crack Growth in 7075-T6 and 2024-T3 Aluminum Alloy Specimens," NASA TN D-5390, 1969.

27. Phillips, E.P., "The Influence of Crack Closure on Fatigue Crack Growth Thresholds in 2024-T3 Aluminum Alloys," ASTM STP 982, 1988, pp. 505-515.

28. Newman, J.C., Jr. and Edwards, P.R., "Short-Crack Growth Behaviour in an Aluminum Alloy—an AGARD CooperativeTest Programme," AGARD R-732, 1988.

29. "Short-Crack Growth Behaviour in Various Aircraft Materials," P.R. Edwards and J.C. Newman, Jr., eds., AGARD R-767, 1990.

30. Newman, J.C., Jr., Wu, X.R., Venneri, S.L., and Li, C.G., "Small-Crack Effects in High-Strength Aluminum Alloys," NASA RP-1309, May 1994.

31. Laz, P.J. and Hillberry, B.M., "The Role of Inclusions in Fatigue Crack Formation in Aluminum 2024-T3," *Fatigue 96*, Lutjering G. and Nowack, H., eds., Berlin, Germany, pp. 1293-1298, 1996.

32. Min, S., Kim, J., and Dornfeld, D.A., "Development of a Drilling Burr Control Chart for Low Alloy Steel - AISI 4118," *Journal of Materials Processing Technology*, Vol. 113, No. 1-3, 2001, pp. 4-9.

33. Kim, J., Min, S., and Dornfeld, D.A., "Optimization and Control of Drilling Burr Formation of AISI 304L and AISI 4118 Based on Drilling Burr Control Charts," *International Journal of Machine Tools and Manufacture*, Vol. 41, No. 7, 2001, pp. 923-936.

34. Ko, S.-L. and Lee, J.-K., "Analysis of Burr Formation in Drilling With a New-Concept Drill," *Journal of Materials Processing Technology*, Vol. 113, No. 1-3, 2001, pp. 392-398.

35. Landers, C.B. and Hardrath, H.F., "Results of Axial-Load Fatigue Tests on Electro-Polished 2024-T3 and 7075-T6 Aluminum Alloy Sheet Specimens With Central Holes," NACA TN-3631, 1956.

36. Zhao, W., Newman, J.C., Jr., and Sutton, M.A., "Use of Weight Functions to Improve Stress-Intensity Factors for Small Corner Cracks Emanating From a Hole Under Remote Bending," unpublished, 1995.

37. Benthem, J.P. and Koiter, W.T., "Asymptotic Approximations to Crack Problems," *Methods of Analysis of Crack Problems*, Chapter 3, G.C. Sih, ed., Noordhoff International Publishing, January 1972.

38. Reissner, E., "The Effect of Transverse Shear Deformation on the Bending of Elastic Plates," *Journal of Applied Mechanics*, Vol. 12, No. 1, 1945, pp. A69-A77.

39. Newman, J.C., Jr., "Finite-Element Analysis of Fatigue Crack Propagation—Including the Effects of Crack Closure," Ph.D. Thesis, Virginia Polytechnic Institute and State University, 1974.

40. Park, J.H. and Atluri, S.N., "Fatigue Growth of Multiple Cracks Near a Row of Fastener Holes in a Fuselage Lap-Joint," *Computational Mechanics*, Vol. 13, No. 3, 1993, pp. 189-203.

41. Newman, J.C., Jr. and Raju, I.S., "Stress-Intensity Factor Equations for Cracks in Three-Dimensional Finite Bodies," NASA TM-83200, August 1981.

42. Tan, P.W., Raju, I.S., Shivakumar, K.N., and Newman, J.C., Jr., "Evaluation of Finite-Element Models and Stress-Intensity Factors for Surface Cracks Emanating From Stress Concentrations," ASTM STP 1060, 1990, pp. 34-48.

43. Shivakumar, V. and Forman, R.G., "Green's Function for a Crack Emanating From a Circular Hole in an Infinite Sheet," *International Journal of Fracture*, Vol. 16, 1980, pp. 305-316.

44. Bowie, O.L., "Analysis of an Infinite Plate Containing Radial Cracks Originating at the Boundaries of an Internal Circular Hole," *Journal of Mathematics and Physics*, Vol. 35, 1956, pp. 60.

45. Newman, J.C., Jr., "An Improved Method of Collocation for the Stress Analysis of Cracked Plates With Various Shaped Boundaries," NASA TN D-6376, 1971.

46. Newman, J.C., Jr., "Predicting Failure of Specimens With Either Surface Cracks or Corner Cracks at Holes," NASA TN D-8244, 1976.

47. Newman, J.C., Jr., "A Nonlinear Fracture Mechanics Approach to the Growth of Small Cracks," AGARD CP-328, 1983, pp. 6.1-6.26.

48. Daniewicz, S.R. and Newman, J.C., Jr., "Development and Validation of Crack Growth Models and Life Enhancement Methods for Rotorcraft Damage Tolerance," DOT/FAA/AR-07/50, November 2007.

49. Timoshenko, S. and Goodier, J.N., *Theory of Elasticity*, 2nd Edition, McGraw-Hill, New York, NY, 1951.

50. Newman, J.C., Jr., Phillips, E.P., and Swain, M.H., "Fatigue-Life Prediction Methodology Using Small-Crack Theory and a Crack-Closure Model," *FAA-NASA Symposium on the Continued Airworthiness of Aircraft Structures*, DOT/FAA/AR-97/2, July 1997, pp. 331-356.

51. "The Second Joint NASA/FAA/DoD Conference on Aging Aircraft," C.E. Harris, ed., NASA CP-208982, 1999.

52. Newman, J.C., Jr., Harris, C.E., James, M.A., and Shivakumar, K.N., "Fatigue-Life Prediction of Riveted Lap-Splice Joints Using Small-Crack Theory," *Fatigue in New and Aging Aircraft, ICAF*, Vol. I, EMAS Publishing, UK, 1997, pp. 523-539.

53. Newman, J.C., Jr. and Raju, I.S., "Stress-Intensity Factor Equations for Cracks in Three-Dimensional Finite Bodies Subjected to Tension and Bending Loads," *Computational Methods in the Mechanics of Fracture*, Vol. 2, S.N. Atluri, ed., 1986, pp. 311-334.

54. Schijve, J., Jacobs, F.A., and Tromp, P.J., "Environmental Effects on Crack Growth in Flight-Simulation Tests on 2024-T3 and 7075-T6 Material," NLR-TR 68117 U, National Aerospace Laboratory, 1968.

55. Newman, J.C., Jr., "A Crack Opening Stress Equation for Fatigue Crack Growth," *International Journal of Fracture*, Vol. 24, 1984, pp. R131-Rl35.

56. Newman, J.C., Jr., "Effects of Constraint on Crack Growth Under Aircraft Spectrum Loading," *Fatigue of Aircraft Materials*, Delft University Press, 1992, pp. 83-109.

57. Newman, J.C., Jr., "A Review of Modeling Small-Crack Behavior and Fatigue-Life Predictions for Aluminum Alloys," *Fatigue and Fracture Engineering Materials and Structures*, Vol. 17, No. 4, 1994, pp. 429-440.

58. Conner, Z., Fine, M.E., and Achenbach, J.D., "Quantitative Investigation of Surface and Subsurface Cracks Near Rivets in Riveted Joints Using Acoustic, Electron and Optical Microscopy," NASA CP-208982, Part 1, 1999, pp. 240-243.

59. Hartman, A. and Schijve, J., "The Effect of Secondary Bending on Fatigue Strength of 2024-T3 Alclad Riveted Joints," NLR TR 69116 U, National Aerospace Laboratory, 1969.

60. AFGROW Users Guide, Version 4.0005.12.10, J.A. Harter, Wright-Patterson Air Force Base, OH, 2002.

APPENDIX A—THREE-DIMENSIONAL WEIGHT FUNCTION METHOD AND USER GUIDE

A.1 INTRODUCTION.

K3DL (K3D_v3.5) is a computer program for calculating the Mode-I stress-intensity factors for semielliptical surface crack(s) and quarter-elliptical corner crack(s) emanating from a circular hole in a wide plate under various loading conditions. The following four crack configurations are considered: a single surface crack (s1) at the center of hole bore, two symmetric surface cracks (s2) at center of hole bore, a single corner crack (c1) at the edge of the hole, and two symmetric corner cracks (c2) at the edge of the hole. The loading conditions fall into two categories: (1) predefined loads, which include remote tension, remote bending (corner cracks only), wedge loading in the hole, and biaxial loads and (2) user-defined loads, which allow users to analyze any loading conditions of interest, provided the pertinent uncracked stress distributions can be represented by a polynomial.

The analysis method used in K3D is a three-dimensional (3-D) weight function method developed in references A-1 and A-2, and enhanced during the National Aeronautics and Space Administration (NASA) Aircraft Structural Integrity Program with detailed analysis of the above crack configurations given in references A-3 and A-4. The first version of K3D is described in reference A-5.

Version 3.5 of the K3D computer code (K3DL) extends the crack depth range from a/t = 0.90 to 0.99. Two new load categories were added: (1) residual stress cases due to a cold-worked hole and (2) user-defined load using a polynomial equation. More importantly, the weight function for corner cracks has been calibrated against the accurate finite element solutions recently developed by Fawaz and Andersson [A-6 and A-7]. As a result of the calibration, the K3DL results for corner cracks are no longer subject to the limitation requiring sufficient restraining areas and are believed to be reasonably accurate for the entire a/t range with arbitrary a/c ratios for a wide plate.

For version 3.5, the form of input to K3DL has been changed from an interactive mode to file input, which is more efficient and convenient for mass production of stress-intensity factors.

A.2 THEORY AND GENERAL FEATURES.

The 3-D weight-function method [A-1 and A-2] was developed based on the slice synthesis model [A-8], the general weight-function expressions for two-dimensional (2-D) crack problems [A-9], and the exact solutions for a pressurized embedded elliptical crack in an infinite body [A-10]. The basic idea of this approach is to decompose a 3-D cracked body into two types of orthogonal slices of infinitesimal thickness. Each slice is in a generalized plane-stress state while containing a through-thickness crack. The properties of the 3-D cracked body are built into the slices by considering two effects: (1) the mechanical coupling between adjacent slices and (2) the restraining effect of the uncracked area on the cracked slices. The 3-D property of a plane crack with elliptic-arc front is further assumed to be divisible into two parts: (1) the fundamental part that is common to all such cracks regardless of their configuration (corner

crack, surface crack, or embedded crack), the relative size of the crack with respect to the width or thickness, or loading condition and (2) the particular part that depends on the given configuration and loading conditions. The fundamental part of the solutions is obtained by using the known exact stress and crack-face displacement solutions for a pressurized embedded elliptical crack in an infinite body [A-10]. For brevity, herein, the focus is on two symmetric corner cracks at a hole in describing the method.

A.2.1 MODELING AND THE WEIGHT FUNCTIONS.

Figure A-1 shows a typical configuration to be considered. Although remote tension is shown, the crack configuration can be subjected to any other Mode I loading, or combinations thereof. This cracked body is decomposed, as shown in figure A-2, into two types of orthogonal slices of infinitesimal thickness. Each slice is assumed to be in a generalized plane-stress state. The symbols R_a and R_c in figure A-2, defined as the restraining areas, represent the uncracked area outside the sliced region. Designating the slices parallel to the a axis of the crack as a-slices and those parallel to the c axis as c-slices, the subscripts "a" or "c" denote quantities corresponding to a- or c-slices, respectively. Note that a-slices correspond to edge-cracked configurations, whereas c-slices correspond to symmetric cracks from hole configurations, as shown in figure A-3(a) and (b), respectively. Referring to figure A-3, another distinction needs to be made: basic slices and spring slices. The a-slice in figure A-3(a) is designated as a basic slice, because the thin slice is subjected to the same applied load, S, and has the same elastic modulus, E, as the 3-D cracked body. The c-slice in figure A-3(b) is called a spring slice, because it is subjected to no externally applied load, and has a different elastic modulus, E_s, which will be described in the forthcoming sections. The loading of the spring slices in figure A-3(b) is such that the superposition of the two kinds of slices satisfies the loading condition of the original 3-D crack problem. Note that in figure A-3, the springs are placed on the slices' boundaries towards where the crack extends and the distributed forces, P(x,y), are applied to the crack faces. These two elements simulate, respectively, the restraining effect due to the uncracked area R_i and the mechanical coupling between the adjacent basic slices due to the internal stress present on the free-body diagram of an a-slice. P(x,y) is the z component of the uncracked stress induced by all the internal coupling stresses acting on an a-slice's surface. It is noted that representing the internal coupling stress by P(x, y) is sufficient, involving no assumption, and is justified by the superposition principle. The other components of the uncracked stress, which are not normal to the crack surface, do not play a role in the model for Mode I crack problems and can be discarded. Thus, all the 3-D properties necessary for considering Mode I crack problems have, in principle, been incorporated into the slice models, and hence, their effects can be represented.

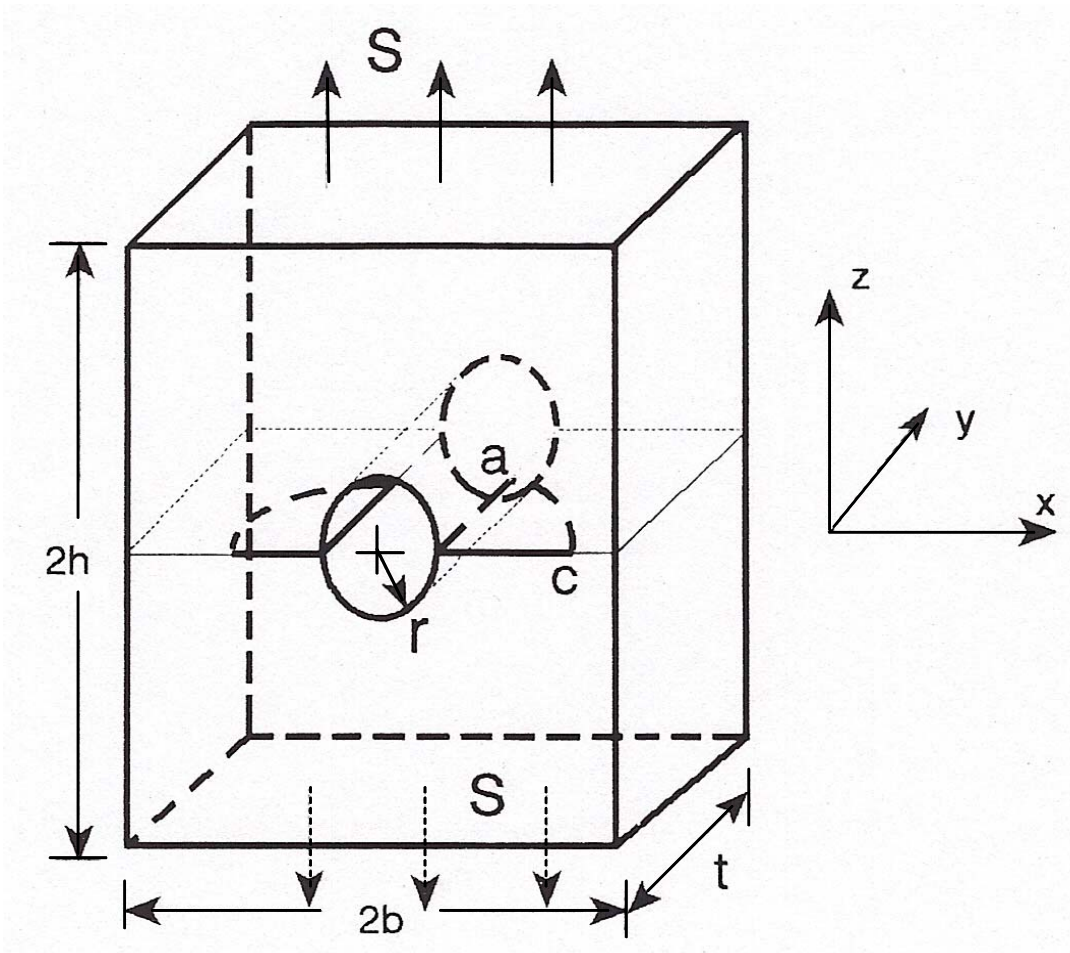

Figure A-1. Two Symmetric Corner Cracks at a Hole Under Remote Tension

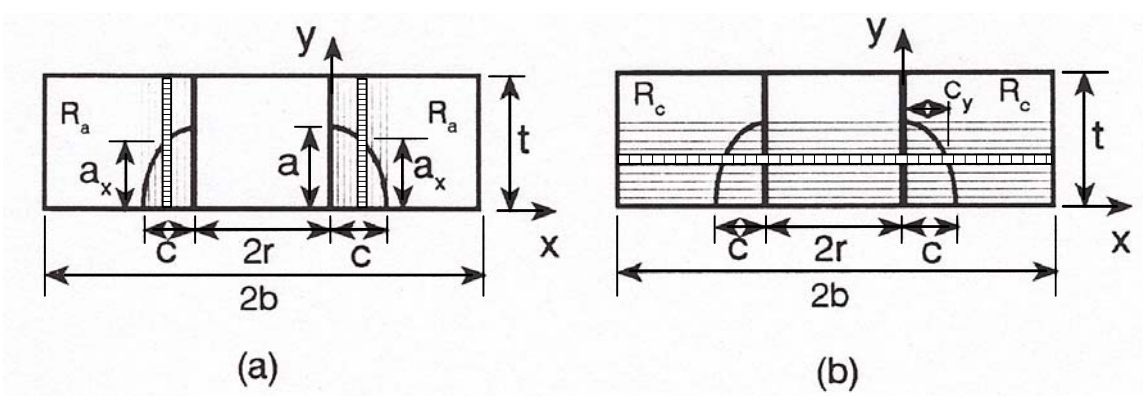

Figure A-2. Decomposition of the Corner Cracked Body Into (a) a-Slices and (b) c-Slices

Before determining P(x,y) (the load aspect), the weight function (the configuration aspect) will be considered. The slices shown in figure A-3 have elastic boundary constraints exerted by constraining springs with stiffness k_i (i = a,c). To represent the constraining effect of the uncracked

area outside the sliced region, the stiffness k_i is a function of restraining area R_i (i = a,c). Using a properly nondimensionalized form for R_i, gives

$$r_a = \frac{R_a}{c^2} = 2\frac{a}{c}\left(\frac{b}{c} - \frac{r}{t}\frac{t}{a}\frac{a}{c} - 1\right)\frac{t}{a} \tag{A-1a}$$

$$r_c = \frac{R_c}{a^2} = 2\frac{c}{a}\left(\frac{b}{c} - \frac{r}{t}\frac{t}{a}\frac{a}{c}\right)\left(\frac{t}{a} - 1\right) \tag{A-1b}$$

in which r_i, ($i = a,c$), varies from 0 to ∞. In general, k_i, as a function of r_i, cannot be determined without embarking upon 3-D analysis. However, the following judgment can be made: k_i is a monotonic function of r_i. That is, $k_i \to 0$ as $r_i \to 0$ (which is the case shown in figure A-4), and $k_i \to \infty$ as $r_i \to \infty$ (which is the case shown in figure A-5). Thus, these two limiting conditions serve as the lower and the upper bounds for the slices in figure A-3. Based on these bounding conditions, the weight functions are constructed for the slices shown in figure A-3 as follows

$$W_i = W_{2D,i}^{\text{fixed}} + T_i(r_i)(W_{2D,i}^{\text{free}} - W_{2D,i}^{\text{fixed}}) \tag{A-2}$$

where W_i ($i = a, c$) is the weight function for the slices in figure A-3. $W_{2D,i}^{\text{fixed}}$ and $W_{2D,i}^{\text{free}}$ are the weight functions for the 2-D cracks with fixed-boundary condition (figure A-5) and with free-boundary condition (figure A-4), respectively. $T_i(r_i)$, designated as the transition factor, is an unknown function of restraining area, r_i, which satisfies $T_i(\infty) = 0$ and $T_i(0) = 1$. Although equation A-2 reduces the determination of the weight functions for the slices in figure A-3 to the determination of the transition factor $T_i(r_i)$, as was done for an embedded elliptical crack [A-1], it does not change the fact that, in general, it cannot be determined without 3-D analysis.

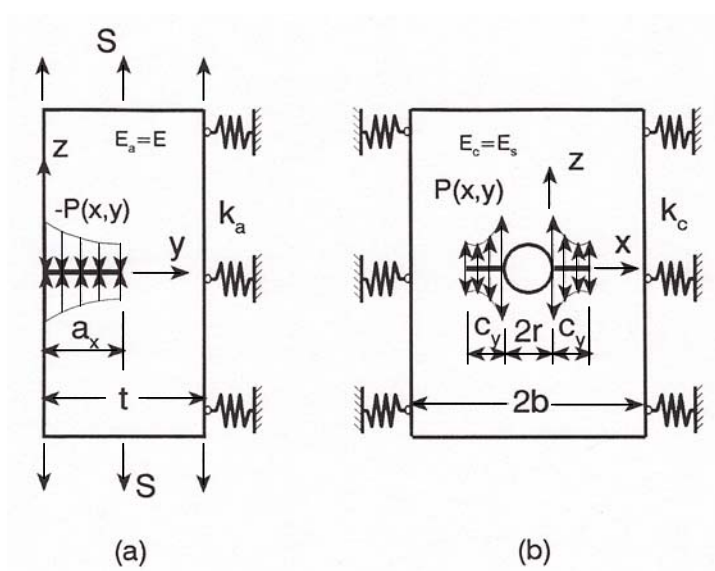

Figure A-3. Positive Spring Stiffness ($0 < ki < \infty$), (a) a-Slices and (b) c-Slices

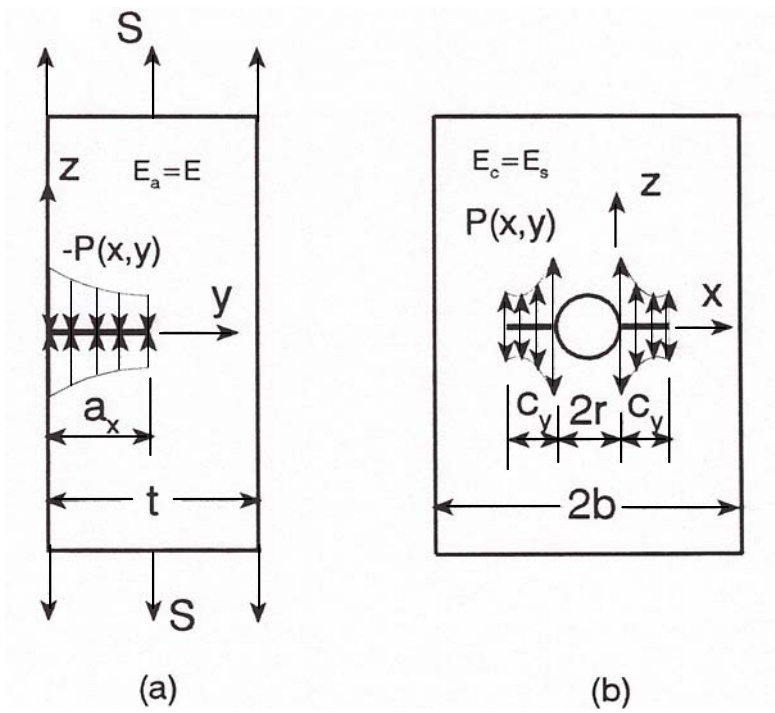

Figure A-4. Zero Spring Stiffness (k_i = 0), (a) a-Slices and (b) c-Slices

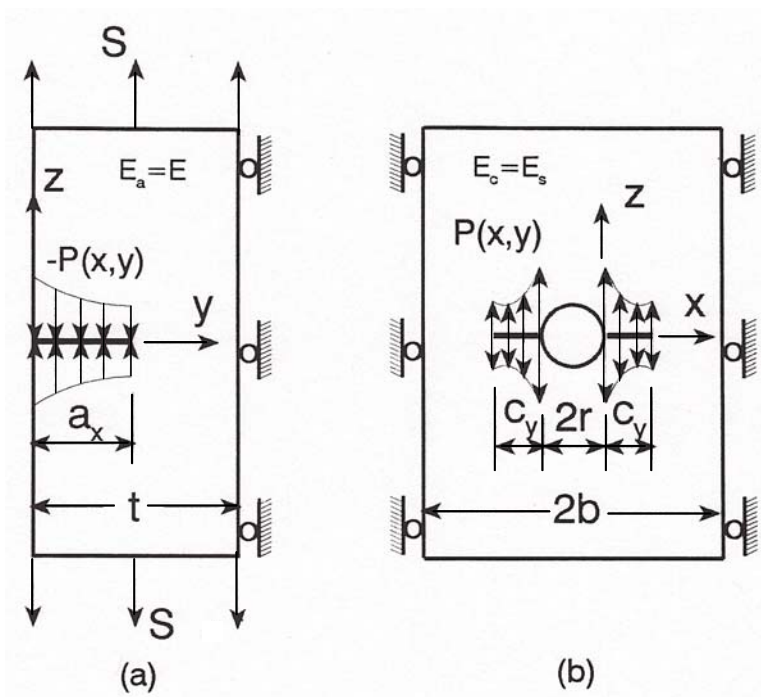

Figure A-5. Infinite Spring Stiffness (k_i = ∞), (a) a-Slices and (b) c-Slices

However, equation A-2 can be used under two types of situations. The first situation is ($W_{2D,i}^{\text{free}}$-$W_{2D,i}^{\text{fixed}}$) = 0 and $T_i(r_i) = 0$, the first term $W_{2D,i}^{\text{fixed}}$ alone can be used as W_i. This corresponds to cases of (1) an elliptical crack in an infinite body, (2) a surface crack in a semi-infinite body, or (3) a corner crack in a quarter-infinite body; where both a/t and c/b are zero. The second situation is ($W_{2D,i}^{\text{free}}$-$W_{2D,i}^{\text{fixed}}$) > 0 and $T_i(r_i) = 0$. Mathematically, this is for $r_i = \infty$, situations that result in infinite width or infinite thickness dimensions.

Physically, the situations where $W_{2D,i}^{\text{fixed}}$ can be used as W_i are not limited to the cases of $r_i = \infty$. $W_{2D,i}^{\text{fixed}}$ applies to a wide range of cases in which the presence of a crack will not cause localized deformation on the boundary surfaces where the constraining springs of the slices act. This is why, unlike any other weight function methods in the literature, this method has an exclusive advantage to provide accurate stress-intensity factors for many practical situations without using any reference solutions. This fact, in turn, verified that the assumptions made in developing the method are sound [A-11].

A.2.1.1 Plate of Infinite Width.

For the case of an infinite width $(c+r)/b = 0$ and $T_i(r_i) = 0$. The particular weight functions W_i for the corner cracks reduce to $W_{2D,i}^{\text{fixed}}$, and they are given by

$$W_a = W_{de}(a_x, y) \tag{A-3a}$$

$$W_c = W_{h2}(c_y, x) \tag{A-3b}$$

where W_{de} is the weight function for double edge cracks and W_{h2} is the weight function for two symmetric cracks emanating from a hole in an infinite plate.

A.2.1.2 Plate of Finite Width.

Accurate stress-intensity factor solutions for corner cracks emanating from a hole in a wide plate were recently developed by Fawaz and Andersson using an hp-version finite element method [A-6 and A-7]. Thus, it became feasible to determine the transition factor $T(r)$ in equation A-2 by calibrating the weight function against the finite element analysis (FEA) data. The first step was to identify when the weight-function results start to deviate from the FEA results. This was achieved by comparing stress-intensity factors obtained using the lower bound weight function, equation A-3, with those from the FEA [A-6 and A-7].

The comparison led to the following three observations. First, the weight-function results are accurate for small a/t ratios and any a/c ratio. Second, for $a/c > 2$, the results from the weight-function method are accurate for the entire range of $a/t \leq 0.99$, thus no calibration of the weight function was necessary. Third, calibration of the weight function is necessary for $a/c \leq 2$ for medium to deep cracks (the a/t range requiring calibration depends on a/c, because the restraining area is a strong function of both a/t and a/c).

These observations are consistent with the expectations based on the characteristics of this particular weight-function method and the experiences. Using a selected set of the FEA data for remote tension at r/t = 1 [A-6 and A-7], a transition factor has been determined as a simple function of a/c and a/t ratios, through a trial and error process. As a result of the calibration, the K3DL results for corner cracks are no longer subject to the limitation requiring sufficient restraining areas and are believed to be reasonably accurate for the entire a/t range with arbitrary a/c ratios for a wide plate.

A.2.2 SOLUTION PROCEDURES.

As mentioned earlier, the solution to a 3-D crack problem is divided into two parts: the fundamental part and the particular part. These will be described in the following sections.

A.2.2.1 Fundamental Part.

This part of the solution provides two fundamental relations. The first one is between the elastic moduli of the basic slices and the spring slices. The second one is between the stress-intensity factors for a 3-D cracked body and the slices. The first relation determines the elastic modulus of the spring slices. The second allows the determination of stress-intensity factors for a 3-D cracked body by using the stress-intensity factors for the slices. These relations have been obtained [A-1] by calibrating the method against the exact solutions for stress-intensity factors and crack-face displacements of a pressurized embedded elliptical crack in an infinite body [A-10]. These relations [A-1] are discussed briefly in the following sections.

A.2.2.1.1 Elastic Modulus of Spring Slices.

The spring slices are devised to represent the mechanical coupling between adjacent basic slices, which are modeled by springs. While the spring force is a function of applied loads and configuration parameters, the stiffness of the spring can be reasonably assumed to be a function of material and the crack aspect ratio only. The results are

$$\frac{E_s}{E} = \left(\frac{\Phi}{1-\nu^2} - 1\right)\frac{c}{a} \quad a/c \le 1 \tag{A-4a}$$

$$\frac{E_s}{E} = \frac{\Phi}{1-\nu^2} - \frac{c}{a} \quad a/c > 1 \tag{A-4b}$$

where ν is the Poisson's ratio, and Φ is the complete elliptic integral of the second kind.

A.2.2.1.2 Stress-Intensity Factors.

Referring to figure A-6 for definition of crack parameters, the following equation gives the relation between stress-intensity factors $K(\varphi)$ for a 3-D crack at location φ on the crack front, and the stress-intensity factors K_i for the two orthogonal slices intersecting at a common point (x,y) as

$$K(\phi) = \frac{(-1)^n}{1-\eta^2}\left\{K_a^4(x,a_x) + \left[\frac{E}{E_s}K_c(y,c_y)\right]^4\right\}^{\frac{1}{4}} \tag{A-5}$$

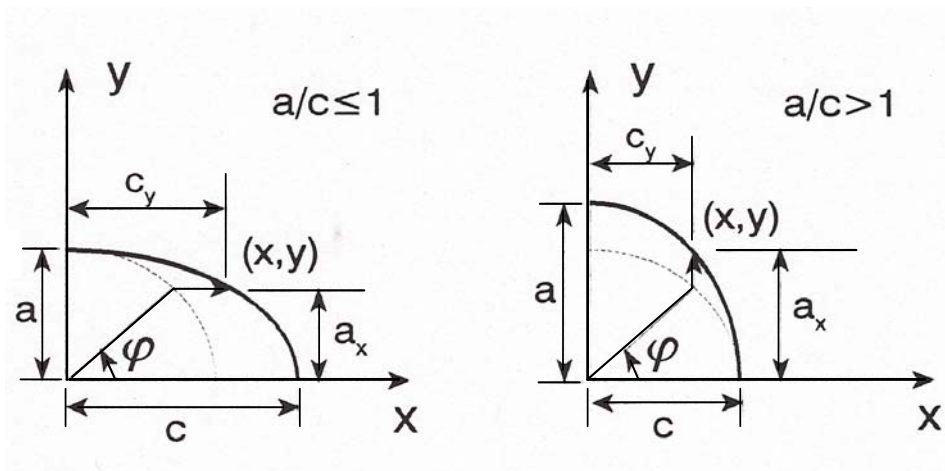

Figure A-6. Definition of Crack Parameters

where n = 1 for $K_i \leq 0$ and n = 2 for $K_i > 0$. η is an empirical function of ν, a/c and $\Delta\varphi$ for considering the transition between plane-strain and plane-stress states near the intersection point of crack front with the free surface [A-3 and A-4]. The validity of equation A-5 has been proven analytically for a pressurized embedded elliptical crack in an infinite body [A-1] and numerically for various cracks of elliptic-arc front in finite bodies under a variety of loading conditions, see for example references A-1 to A-4 and A-11, indicating that the assumptions made in the method are valid. Note that the derived fundamental solutions are universally applicable to any other planar cracks of elliptical, semielliptical, or quarter-elliptical crack front.

A.2.2.2 Particular Part.

This part of the solution process for a 3-D crack problem deals with the particular configuration and loading conditions of the problem in question. The stress-intensity factors for both types of orthogonal slices are determined, with the aid of the fundamental solution, by using 2-D weight-function theory [A-9, A-12, and A-13]. Then, the stress-intensity factors for the 3-D crack are obtained by using the fundamental relations given above. For the case of an infinite width plate, the slices are reduced to those in figure A-5. Their weight functions are given in equation A-3. Using the 2-D weight-function theory [A-9, A-12, and A-13], the stress-intensity factors for the slices are

$$K_a(x,a_x) = \int_0^{a_x}[\sigma(x,y) - P(x,y)]W_{de}(a_x,y)dy \tag{A-6a}$$

$$K_c(y,c_y) = \int_0^{c_y}P(x,y)W_{h2}(c_y,x)dx \tag{A-6b}$$

The crack-face displacements for the slices are:

$$V_a(a_x,x,y) = \frac{1}{E_a}\int_y^{a_x} K_a(x,\xi)W_{de}(\xi,y)d\xi \tag{A-7a}$$

$$V_c(c_y,x,y) = \frac{1}{E_c}\int_x^{c_y} K_c(y,\xi)W_{h2}(\xi,x)d\xi \tag{A-7b}$$

in which $E_a = E$, $E_c = E_s$, which is given by equation A-4. The only unknown in these equations is the spring force $P(x,y)$, which can be determined by the compatibility requirement on the crack-face displacements as

$$V_a(a_x,x,y) = V_c(c_y,x,y) \tag{A-8}$$

Then, $K(\varphi)$ is obtained by using equation A-5.

For those who have knowledge of the slice synthesis method [A-8 and A-14], it is helpful to point out the important differences between the current 3-D weight-function method and the slice synthesis method [A-8 and A-14]. The differences lie in the following three aspects: (1) concept, (2) formulation, and (3) accuracy. First, the restraining area concept proposed in this method allows consideration of the effect of the uncracked area, which proved to be the most important factor affecting the accuracy. Following this concept, the key issue and task of the method is to determine the 3-D weight functions, rather than synthesizing the 2-D slices [A-8 and A-14]. Second, the fundamental solutions derived as part of this method allows determination of stress-intensity factors along the entire crack front, not just at the two end points as in the slice synthesis method [A-8 and A-14]. Third, for many practical cases of surface and corner cracks, while the current method produces accurate results without using any reference solutions, the results based on the slice synthesis method [A-8] are often in error even for relatively small cracks of a/t < 0.4. To correct large errors in stress-intensity factors from the slice synthesis method [A-8], Saff and Sanger [A-14] used a finite element method to calculate surface crack stress-intensity factor for remote tension, thus to obtain a correction factor on stress-intensity factor from the slice synthesis method [A-8].

A.2.3 UNCRACKED STRESS DISTRIBUTION.

A.2.2.1 Three-Dimensional Solutions.

The uncracked stress distribution, $S(x,y)$, used in the weight-function method, was obtained by the 3-D FEA [A-15]. To facilitate its application, the uncracked stress distribution was then fitted using the following equation:

$$s(\xi,\zeta)/S_0 = \sum_{i=1}^{I}\sum_{j=1}^{J} C_{ij}\left(\frac{\xi}{r}\right)^{2-2i}\left(\frac{\zeta}{T}\right)^{q} \tag{A-9}$$

where

I = highest order in E/r
J = highest order in E/T

where $q = 2j\text{-}2$ for remote tension and wedge loading, and $q = 2j\text{-}1$ for remote bending. The S_0 is a reference stress and $S_0 = S_t = S$ for remote tension; $S_0 = S_w = P/(2rt)$ for wedge loading, and $S_0 = S_b$ (remote outer fiber bending stress) for remote bending. The applied load in the hole is designated as P. The coordinate system used in equation A-9 is shown in figure A-7. The local stress variation in the thickness direction occurs in the proximity of the hole, even for the in-plane loading cases of remote tension and wedge loading. The 3-D solutions account for the stress variations along the plate thickness direction. Therefore, the use of the 3-D solutions is recommended whenever possible and is especially beneficial for the cases of small r/t ratios in combination with small a/t or c/r ratios.

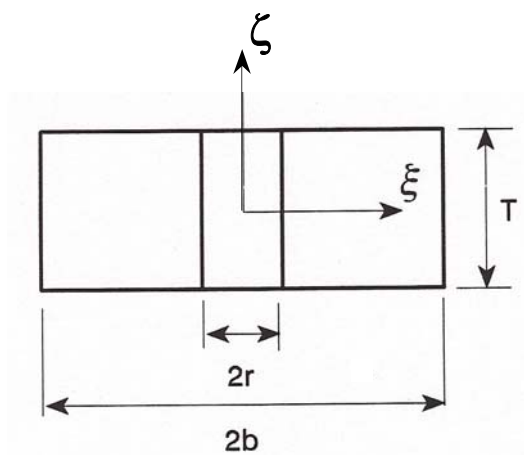

Figure A-7. Coordinate System Used for 3-D Stress Distributions

The user-defined load is also expressed in the same form as equation A-9. Note that equation A-9 is based on a coordinate system different from the ones used in the weight functions, as shown in figure A-8. Therefore, a coordinate transformation is performed in K3DL to convert $s(\xi, \zeta)$ to $S(x, y)$, which is expressed as

$$S(x,y)/S_0 = \sum_{i=1}^{I}\sum_{j=1}^{J} e_{ij}\left(\frac{x}{r}+1\right)^{2-2i}\left(\frac{y}{t}\right)^{q} \tag{A-10}$$

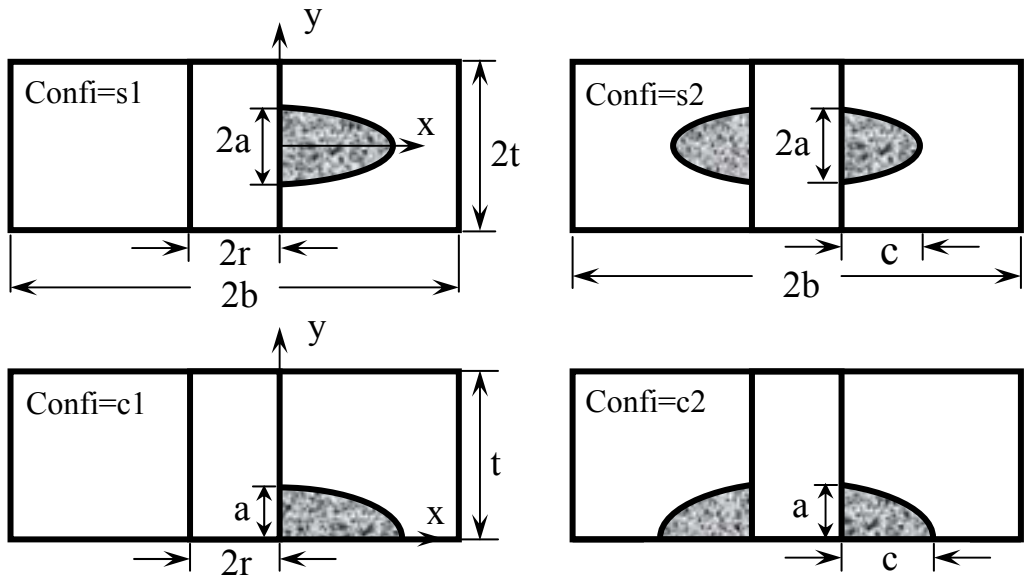

Figure A-8. Four Crack Configurations Considered in K3D: Confi = s1, s2, c1, and c2

A.2.3.2 Two-Dimensional Solutions.

Various 2-D uncracked stress solutions are taken from references A-16 to A-20. An ordinary polynomial is used to express the uncracked stress distribution from these 2-D analyses:

$$S(x,y)/S_0 = \sum_{i=1}^{I}\sum_{j=1}^{J} z_{ij}\left(\frac{x}{r}\right)^i\left(\frac{y}{t}\right)^j \tag{A-11}$$

where $z_{ij} = 0$ for $j > 0$, except for bending. These 2-D stress solutions do not give as accurate stress-intensity factor solutions as using the 3-D stresses for small cracks (c/r<0.2) with a small hole (r/t <1), but satisfactory results are achieved as the crack and/or hole gets larger (see discussions in references A-3 and A-4).

A.2.4 CRACK CONFIGURATIONS.

Figure A-8 shows the four crack configurations considered, where Confi is the crack configuration identifier used in K3DL. It also shows the coordinate system used and the configuration parameters. It is assumed that the height and width of the plate are large enough to ignore the finite height and width effects.

A.2.5 DIMENSIONLESS CONFIGURATION PARAMETERS.

All the geometrical dimensions involved in determining stress-intensity factors are grouped into three dimensionless parameters. They are the hole radius, r/t, the crack aspect ratio, a/c, and the crack depth, a/t. Since K3DL has extended the applicable a/t range to a/t ≤ 0.99, there are no practical limitations on a/c and a/t ratios. However, the crack length should not exceed the 2 times of the hole radius, i.e., c/r ≤ 2, where the c/r ratio is obtained by using the three dimensionless parameters as c/r = (a/t)/(a/c)/(r/t). This limitation is practically unimportant because it is more than likely that a corner or surface crack will penetrate through the thickness and become a through crack prior to reaching c/r = 2.

A.2.6 LOAD TYPES.

Loading conditions can be predefined or user-defined. The predefined loads are either from 3-D solutions that correspond to several r/t ratios for which stress solutions from 3D finite element analysis are available, or from 2-D solutions, which are independent of r/t ratios. Illustrations are given in the following to show the various predefined loading conditions considered. Except for remote bending, all the other loading conditions are applicable to both corner cracks and surface cracks. For 3-D uncracked stress solutions for remote tension and wedge loading in the hole, distinctions are made in r/t ratios for surface cracks and corner cracks. The x/r limits are also given for the cases in which x/r limit is less than 2 (LI = 2-4, 9, where LI is the load identifier in K3DL). It is important to observe these limits to ensure the accuracy of the stress-intensity factor solutions.

A.2.6.1 Predefined Loads From 2-D Analysis.

Various predefined loads from 2-D analysis are shown in figure A-9(a-g), with the corresponding LI value indicated. The applicable range of x/r is also given if it is less than 2.

A.2.6.2 Predefined Loads From 3-D Analysis.

Various predefined loads from 3-D analysis are shown in figure A-10(a-c), with the corresponding LI value indicated. The applicable ranges of x/r are all greater than 2, the weight function's current limit in c/r.

A.2.6.3 Cold-Worked Hole Residual Stress.

Three cases are included for the cold-worked-hole residual stresses. They are shown in figure A-11. The applicable *x*/*r* ranges are, respectively, 0.4, 0.6, and 0.8, as indicated by the curves.

A.2.6.4 User-Defined Loads Using Polynomial Coefficients.

This load type increases versatility and convenience for considering any load, whether it is applied or residual stress that can be represented as a fourth-order polynomial. Without requiring a separate load file, this option reads the polynomial coefficients from the same input file to K3DL.

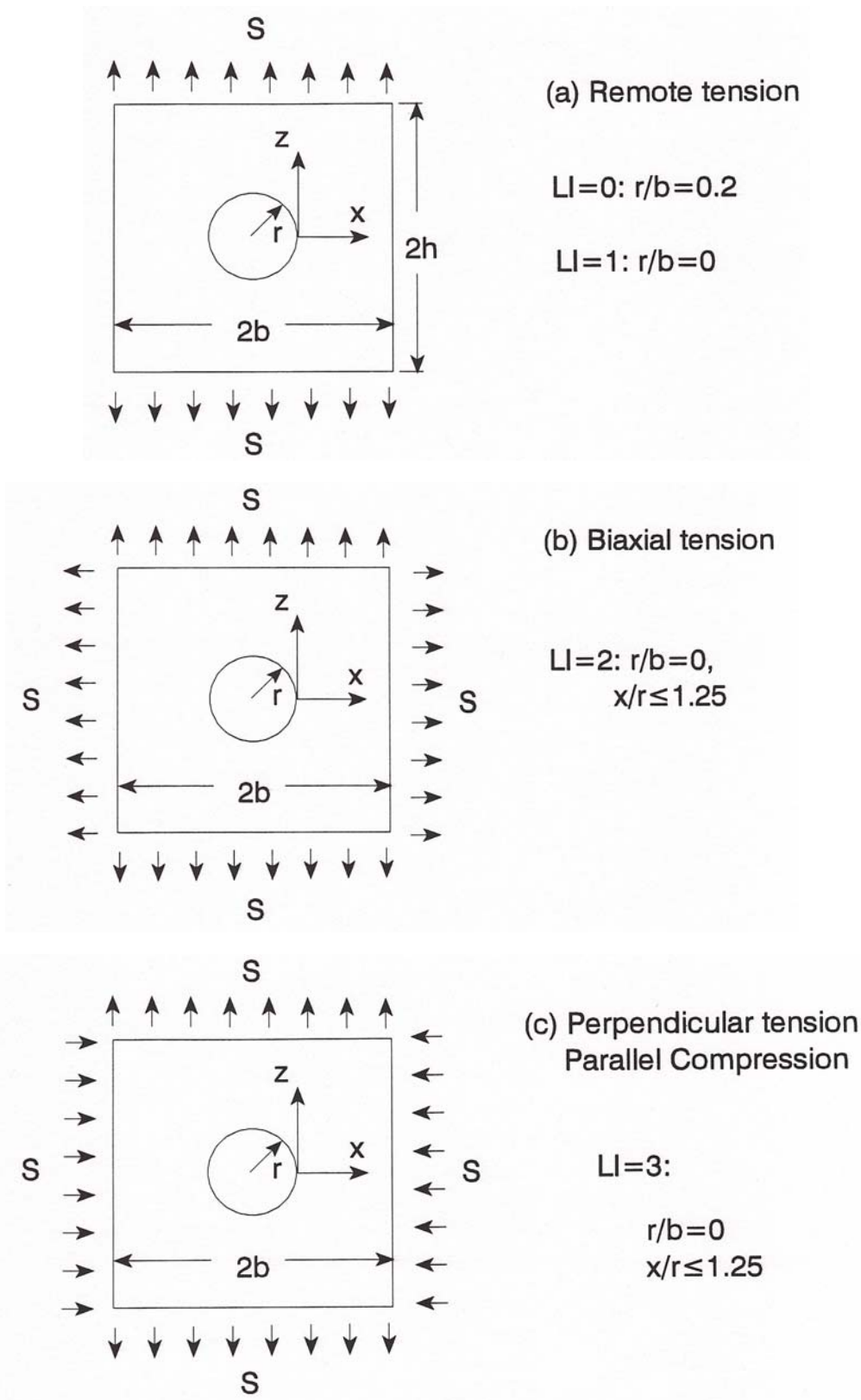

Figure A-9. Predefined Loading for 2-D Analyses

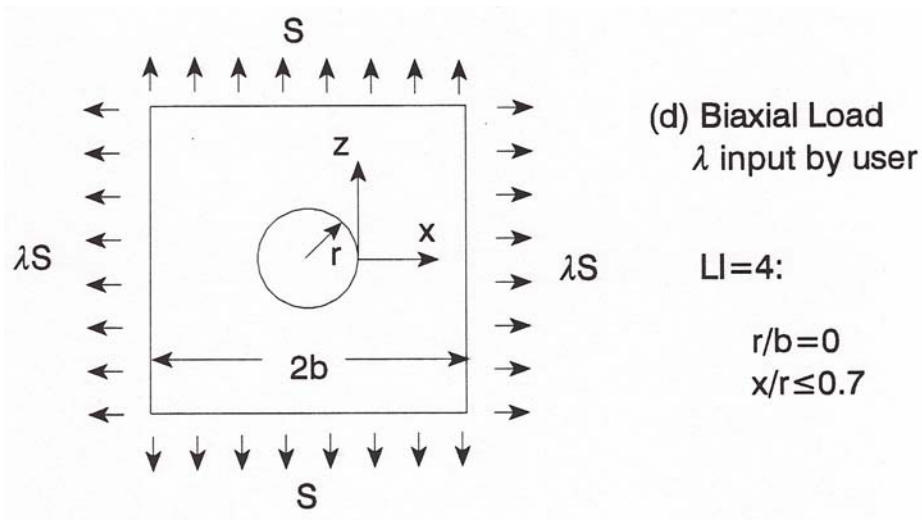

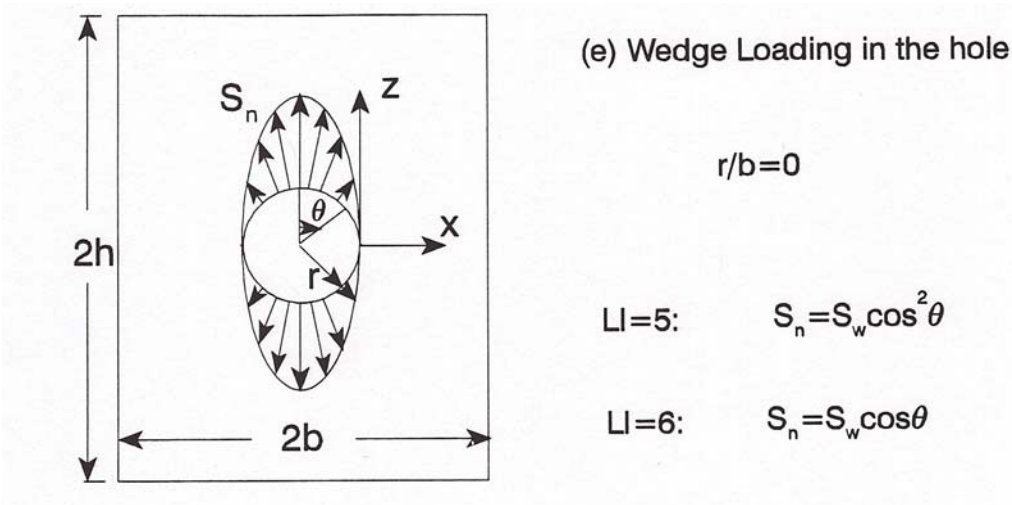

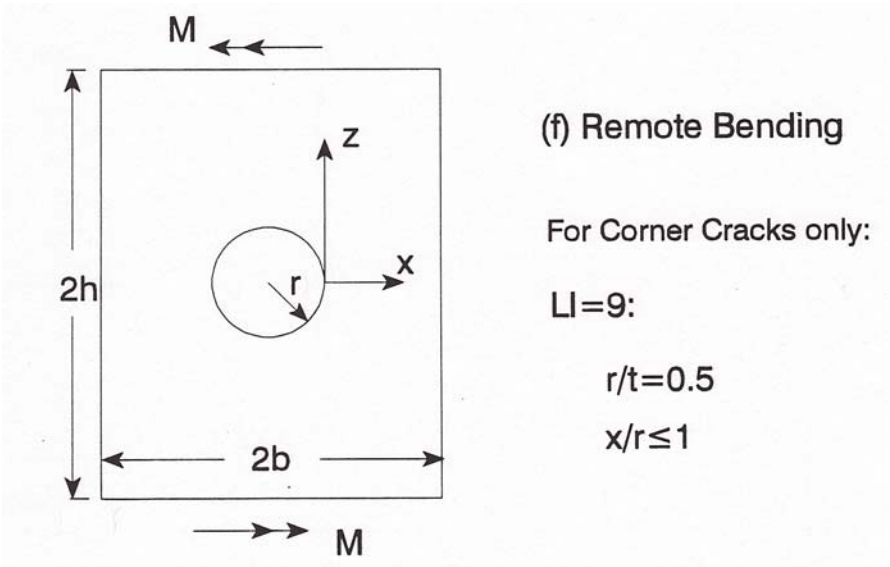

Figure A-9. Predefined Loading for 2-D Analyses (Continued)

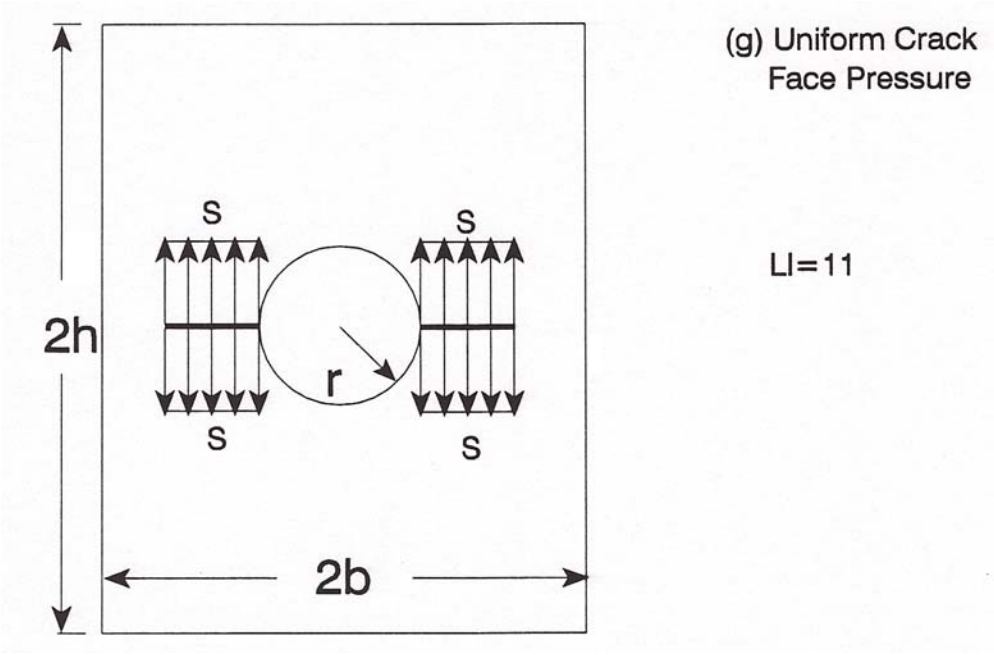

Figure A-9. Predefined Loading for 2-D Analyses (Continued)

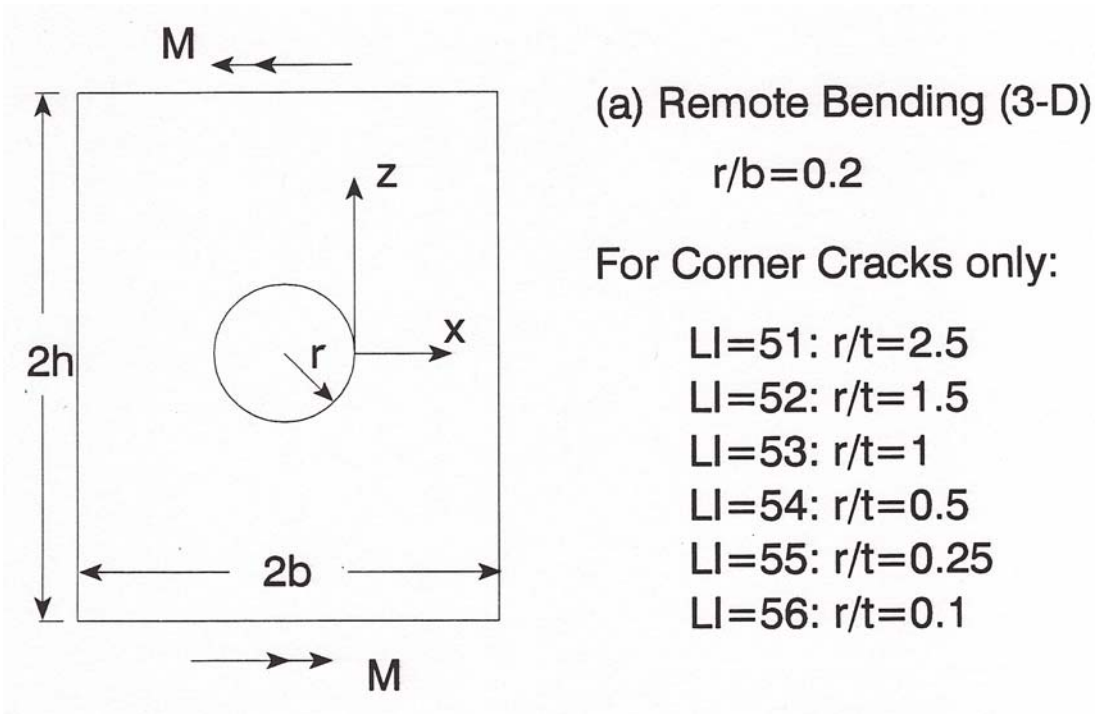

Figure A-10. Predefined Loading for 3-D Analyses

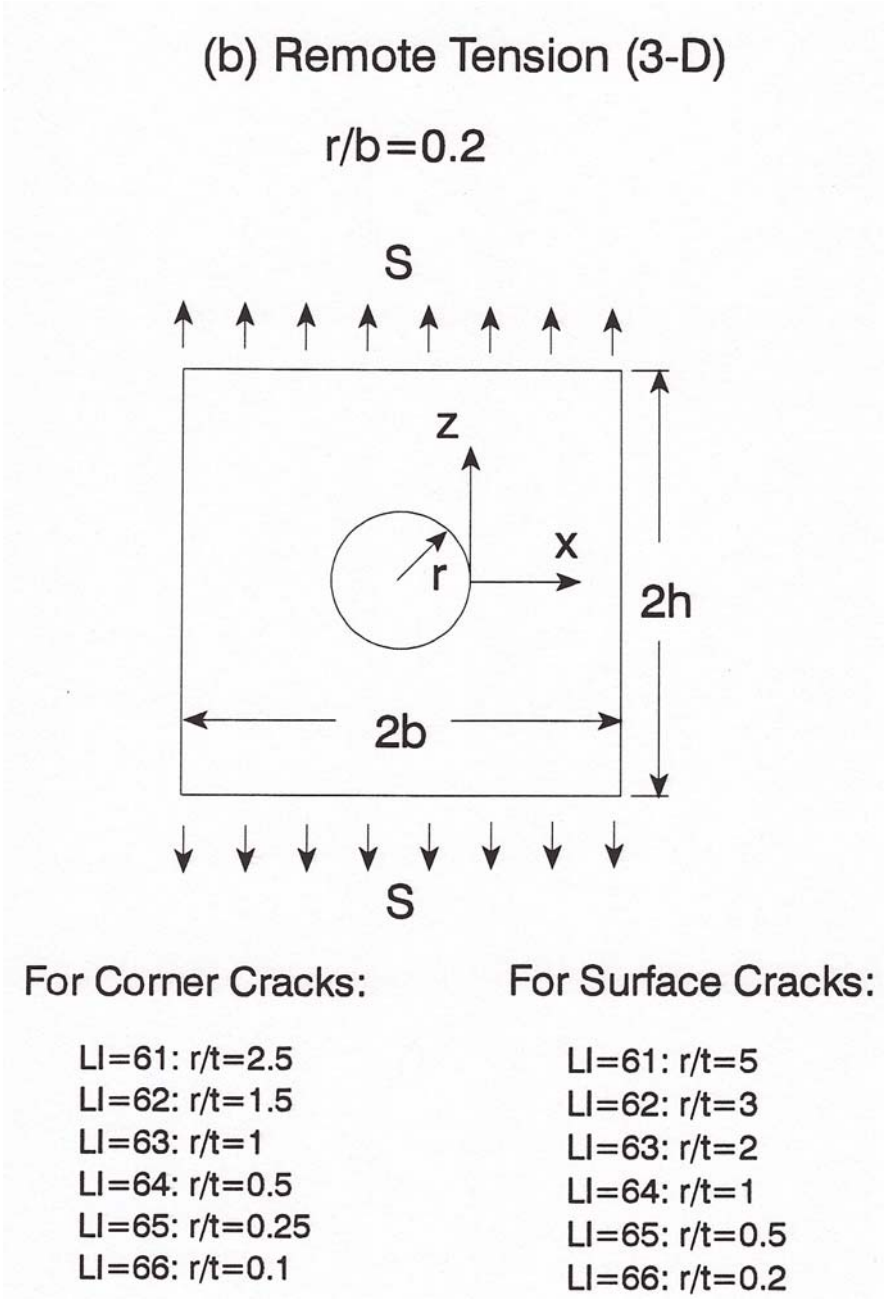

Figure A-10. Predefined Loading for 3-D Analyses (Continued)

(c) Wedge Loading in the Hole (3-D)

$r/b=0.2$ $\quad S_n=S_w\cos\theta$

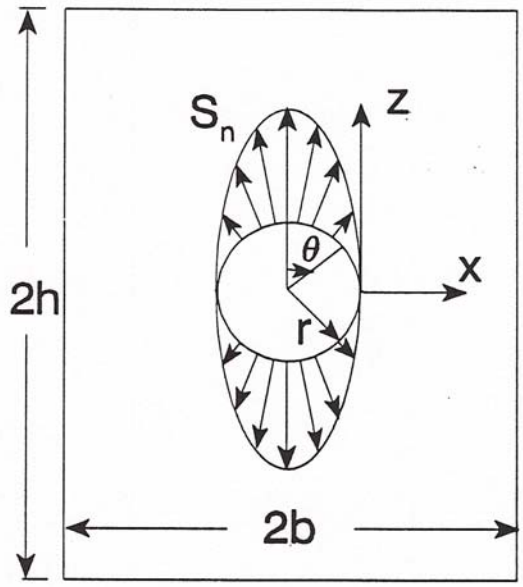

For Corner Cracks:

LI=71: r/t=2.5
LI=72: r/t=1.5
LI=73: r/t=1
LI=74: r/t=0.5
LI=75: r/t=0.25
LI=76: r/t=0.1

For Surface Cracks:

LI=71: r/t=5
LI=72: r/t=3
LI=73: r/t=2
LI=74: r/t=1
LI=75: r/t=0.5
LI=76: r/t=0.2

Figure A-10. Predefined Loading for 3-D Analyses (Continued)

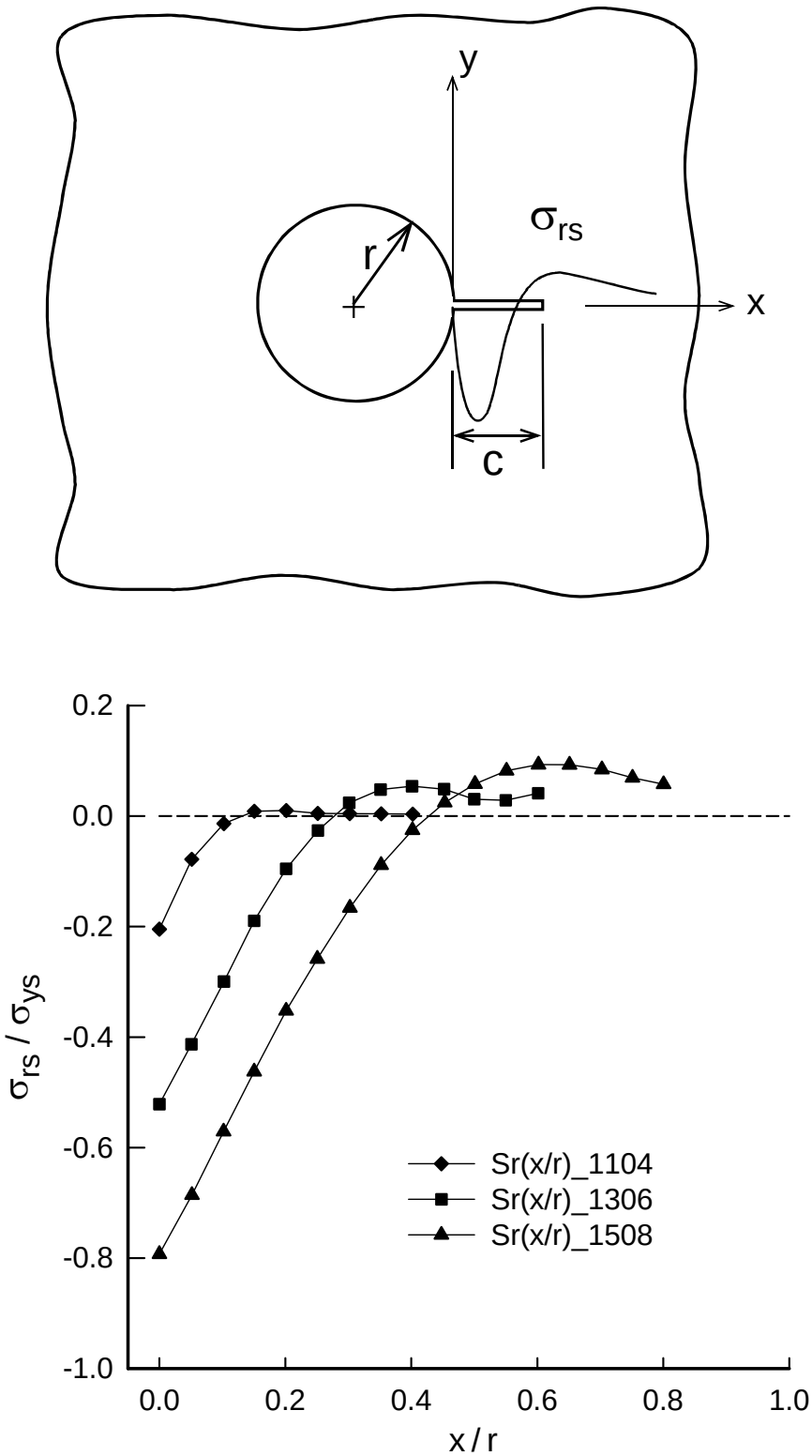

Figure A-11. Predefined Loading for Cold-Worked Hole Residual Stresses: LI = 91, 92, and 93

A.2.6.5 User-Defined Loads Using File loadn.in.

For more complicated cases, user-defined load represented by equation A-9 is stored in a file named loadn.in under C:\K3D_35\LOADUSER\. The user's task is to fit the uncracked normal stress distribution of interest to the form of equation A-9. Then, put the fitting coefficients in "loadn.in" in the format as demonstrated in the following example.

Example of user-defined load:
from frt010t.dat: r/T = 0.1, tension

```
 4,5,0
C(1,1) =,    1.0015
C(2,1) =,    0.5686
C(3,1) =,    1.3635
C(4,1) =,    0.1362

C(1,2) =,    0.0546
C(2,2) =,   -2.4735
C(3,2) =,   10.9350
C(4,2) =,   -5.7419

C(1,3) =,   -1.9571
C(2,3) =,   73.8347
C(3,3) =, -292.3556
C(4,3) =,  157.7183

C(1,4) =,    12.1344
C(2,4) =,  -537.1776
C(3,4) =, 2335.5908
C(4,4) =, -1302.9163

C(1,5) =,   -19.9296
C(2,5) =,  963.5619
C(3,5) =, -5364.8208
C(4,5) =, 3101.1921
```

As shown in this example, C(i, j) correspond to C_{ij} in equation A-9. The first three lines can be any legal characters. The fourth line contains three integers in the order of I, J, ISYM, where

I = the highest order in ξ/r,
J = the highest order in ζ/T,
ISYM = 0 for symmetric load,
= 1 for antisymmetric load, with respect to the ξ-axis, see figure A-7.

It should be noted that C(i, j) is grouped in terms of j = 1, 2, ..., J, and each group is separated with another by a blank line.

A.2.7 OUTPUT FILE.

The output file contains a title, dimensionless geometrical parameters, loading condition, and five typical coefficients of the stress equation. Following these items are the results of dimensionless stress-intensity factors, F, versus parametric angles along the crack front expressed in degrees. The dimensionless stress-intensity factors, F, are represented as

$$F(\phi) = K(\phi) / (S_o\sqrt{\pi a / Q}) \tag{A-12}$$

where S_0 is the reference stress, Q is equal to Φ^2 and given by the following equations [A-21].

$$Q = 1 + 1.464(\frac{a}{c})^{1.65}, \quad \frac{a}{c} \le 1 \tag{A-13a}$$

$$Q = 1 + 1.464(\frac{c}{a})^{1.65}, \quad \frac{a}{c} > 1 \tag{A-13b}$$

The parametric angle always starts from the c axis (see figure A-6).

A.2.8 BOUNDARY LAYER TREATMENT.

At the intersection of the crack front with the free surface, also known as the boundary layer, the stress singularity is weaker than 1/2 at the interior points for $\nu > 0$ [A-21 to A-23]. Theoretically, the stress-intensity factor is not meaningful in the boundary layer. However, experimental evidences have consistently shown that stress-intensity factors based on the neighboring interior points can correlate well with the fatigue crack propagation data for various 3-D cracks, see for example reference A-24. Assuming a 1/2 stress singularity a priori, the 3-D weight-function method does not reflect the weaker singularity in the boundary layer. The stress-intensity factors obtained by using the 3-D weight-function method have good agreement with the finite element solutions in the interior, but are slightly higher in the boundary layer in most of the cases. Based on the observations that the finite element solutions correlate experimental data well, an empirical treatment is adopted in the weight-function solutions such that the stress-intensity factors at the intersection points are replaced by extrapolations, using values at the two inner points.

A.2.9 LIMITATIONS FOR SURFACE CRACKS.

As described earlier, for surface crack, the current weight function method does not use the general form of the weight functions given by equation A-2. Instead, a simplified form, equation A-3, is used, which is valid for $T_i(r_i) = 0$. Physically, this situation corresponds to the cases in which the crack will not cause localized deformation on the boundary surfaces where the constraining springs of the slices act. For this situation to be true, the restraining areas, r_i, are required to be greater than, or equal to, a critical value, $\underline{r}_i$. The value of $\underline{r}_i$ can be determined by comparing the stress-intensity

factor solutions from the weight-function method with the finite element analysis for a series of cases with different r_i values.

Based on the available data, $\underline{r}_a = 13.5$ is recommended for surface cracks. Since the current weight function (W_c) and the uncracked stress solutions are for the cases of a wide plate ($r/b \leq 0.2$), the values of r_c are not of concern (any practical case in this range will produce a negligible $T_c(r_c)$, and make equation A-3b valid). For corner cracks, r_i values are calculated from equation A-1. For surface cracks, r_i values can be obtained by doubling the corresponding values for corner cracks.

Use of the K3DL for the cases with smaller restraining areas than $\underline{r}_a$ may underestimate the actual solution because of the omission of the second term in equation A-2. In this case, the obtained solution serves as a lower bound only. However, it follows from equation A-1 that small r_a values occur when a small a/c ratio (for example 0.4) combines with a large a/t ratio (for example 0.6), which is not a commonly encountered situation.

A.3 USER GUIDE.

A.3.1 FORMAT OF THE INPUT FILE.

The name of the input file to K3DL is K3D_35.in. For efficient file management, the input is structured such that only one of the four crack configurations (c1, c2, s1, and s2) is permitted in a given K3D_35.in file. A file can contain as many cases as desired with different configuration parameters and/or loads. All or portion of the cases contained in the K3D_35.in file can be calculated in a single execution of K3DL, depending on a control parameter in the file. The description given below in this section applies to all load categories, except a special case for category P, which is described in section A.3.3.

Once the crack configuration is specified in an input file, only five data lines are needed for a given case. The format of the input file, K3D_35.in, is best illustrated by using an example, as given below. In looking at a K3D_35.in file, it contains the following:

```
* confi = 'c2'
c2
* r/t,  a/c,   a/t;   job name = 'c2ten10_03_01'
1.00 0.300 0.01
c2ten10_03_01
* LOADC = '3', LI = 63; CAGAIN = 'n'o
3
63
no
```

The above file is the format for a single case input file. The lines starting with an "*" are comment lines. The others are data lines. The meaning and contents of each line are explained one by one, as follows.

- * confi = 'c2': A comment indicating that this file is for the two corner cracks.

- c2: A character value telling K3DL that the analysis is for the two corner cracks.

- * r/t, a/c, a/t; job name = 'c2ten10_03_01': A comment suggesting the contents of the two following data lines—the first is for values of r/t, a/c, and a/t; the second is the job name for the case.

- 0.300 0.01: Values for r/t, a/c, and a/t, in that order, separated by a space or a comma.

- c2ten10_03_01: A character value for the job name, the output file name for the resulting stress-intensity factor will be c2ten10_03_01.txt, i.e., job name suffixed with .txt. Here, the name was chosen to signify that it is for the two corner cracks (c2), under remote tension (ten), with r/t = 1.0 (10), a/c = 0.3 (03), and a/t = 0.01 (01).

- LOADC = '3', LI = 63; CAGAIN = 'n'o: A comment suggesting the contents of the three following data lines—the first is a character value for the load category, the second is an integer value for load identification number in the category, the third is a character value to indicate whether this is the end of the execution, or to continue with another case for the two corner cracks.

- 3: A character value indicating that the uncracked stress distribution is from the 3-D finite element analysis [A-10].

- 63: An integer value for load identification number, 63 is for remote tension with r/t = 1.0.

- no: A character value to indicate that this is the end of the execution.

This single case input file can be extended to include as many cases as desired. To do so, simply change the character value of the last line from no to yes, and add additional sections for cases to be analyzed. Separate each section with a blank, or a comment line.

An extended version of the above K3D_35.in file is given below. Please note that the last line of the last section is no, to conclude the execution of K3DL. Replace yes with no to end at that section.

```
* confi = 'c2', r/t = 1.00, a/c = 0.3
c2
* r/t a/c a/t ; job name = 'c2ten10_03_01'
1.00 0.3 0.01
c2ten10_03_01
* LOADC = '3', LI = 63; CAGAIN = 'y'es
3
63
yes

1.00 0.3 0.10
c2ten10_03_10
*
3
63
yes

1.00 0.3 0.20
c2ten10_03_20
*
3
63
yes

1.00 0.3 0.30
c2ten10_03_30
*
3
63
yes

1.00 0.3 0.40
c2ten10_03_40
*
3
63
yes

1.00 0.3 0.50
c2ten10_03_50
*
3
63
yes
```

```
1.00 0.3 0.60
c2ten10_03_60
*
3
63
No
```

A.3.2 INPUT SPECIFICATIONS.

The admissible values of the data lines in K3D_35.in are given in this section. As described in the previous section, there are six data lines in a single case K3D_35.in input file. The six data lines are in the following order.

1. Crack configuration
2. Dimensionless configuration parameters
3. Job name for output file for stress-intensity factors
4. Load category
5. Load identification number
6. Execution control

The input specifications for these six items are as follows.

A.3.2.1 Crack Configuration.

The admissible values for the crack configurations are: c1, c2, s1, and s2; for one corner crack, two symmetric corner cracks, one surface crack, and two symmetric surface cracks, respectively, as shown in figure A-8.

A.3.2.2 Dimensionless Configuration Parameters.

The admissible a/t ratio is $a/t \leq 0.99$. There is no practical limit for r/t and a/c ratios. However, the resulting c/r ratio must be in the range of $c/r \leq 2$.

A.3.2.3 Job Name.

The job name may consist of any legal characters and spaces, and up to 70 characters long. The result file name for the stress-intensity factor is "jobname.txt".

A.3.2.4. Load Category.

Admissible character values for the load category are 2, 3, u (or U), r (or R), and p (or P), for uncracked stress distribution from 2-D analysis, 3-D finite element analysis, user-defined residual-stress field, or polynomial coefficients entered by the user, respectively.

A.3.2.5 Load Identifier.

Admissible LI for each load category is summarized as follows.

Load Category 2:

LI = 0: Remote Tension r/b = 0.2

1: Remote Tension r/b = 0

2: Biaxial Tension r/b = 0, x/r < = 1.25

3: Perpendicular Tension, Parallel Compression r/b = 0, x/r < = 1.25

4: Biaxial Load, λ Input by User r/b = 0, x/r < = 0.70

5: Wedge Loaded Hole: $\cos^2\theta$ -distribution, r/b = 0

6: Wedge Loaded Hole: $\cos\theta$ -distribution, r/b = 0

9: Remote Bending r/t = 0.5, x/r < = 1, for corner cracks only

11: Uniform Crack Face Pressure

Load Category 3:

LI = 51 : 3-D Bending, r/b = 0.2, r/T = 2.50, for corner cracks only
52 : 3-D Bending, r/b = 0.2, r/T = 1.50, for corner cracks only
53 : 3-D Bending, r/b = 0.2, r/T = 1.00, for corner cracks only
54 : 3-D Bending, r/b = 0.2, r/T = 0.50, for corner cracks only
55 : 3-D Bending, r/b = 0.2, r/T = 0.25, for corner cracks only
56 : 3-D Bending, r/b = 0.2, r/T = 0.10, for corner cracks only

61 : 3-D Tension, r/b = 0.2, r/T = 2.50
62 : 3-D Tension, r/b = 0.2, r/T = 1.50
63 : 3-D Tension, r/b = 0.2, r/T = 1.00
64 : 3-D Tension, r/b = 0.2, r/T = 0.50
65 : 3-D Tension, r/b = 0.2, r/T = 0.25
66 : 3-D Tension, r/b = 0.2, r/T = 0.10

71 : 3-D Wedge Load: Cos, r/b = 0.2, r/T = 2.50
72 : 3-D Wedge Load: Cos, r/b = 0.2, r/T = 1.50
73 : 3-D Wedge Load: Cos, r/b = 0.2, r/T = 1.00
74 : 3-D Wedge Load: Cos, r/b = 0.2, r/T = 0.50
75 : 3-D Wedge Load: Cos, r/b = 0.2, r/T = 0.25
76 : 3-D Wedge Load: Cos, r/b = 0.2, r/T = 0.10

Note that T is the plate thickness (see figure A-7). For corner cracks, T = t, while for surface cracks, T = 2t (see figure A-8). Therefore, for surface cracks, the corresponding r/t ratios for the above load cases are twice those for corner cracks, see figure A-10.

Load Category U:

LI = 84: User-defined stress distribution, stored in file
C:\K3D_35\LOADUSER\loadn.in

Load Category R:

LI = 91: Residual stress due to hole cold expansion, $R_y/r = 1.1$, $x/r <= 0.4$
LI = 92: Residual stress due to hole cold expansion, $R_y/r = 1.3$, $x/r <= 0.6$
LI = 93: Residual stress due to hole cold expansion, $R_y/r = 1.5$, $x/r <= 0.8$

The R_y is the radius of the elastic-plastic zone boundary due to cold expansion of the hole. The corresponding distribution of the residual stress is given in figure A-11.

Load Category P:

LI = 200: User-entered coefficients for any fourth-order polynomial stress field

A.3.3 FORMAT OF THE INPUT FILE FOR LOAD CATEGORY P.

The previous descriptions on the input are applicable to this case as well, with one exception: an additional data line is required following the LI. This additional data line is to provide the five coefficients for a fourth-order polynomial, in the sequence of α_0, α_1, α_2, α_3, α_4, as defined in the following equation

$$S(x)/S_0 = \sum_{i=0}^{4} \alpha_i \left(\frac{x}{r}\right)^i \qquad \text{(A-14)}$$

where the origin of the *x* axis is at the edge of the hole, as shown in figures A-8 through A-11. An example input file for this case is as follows.

```
* s2pol2010_p200.in: Jim's overload residual stress
s2: 2 surface cracks
*rt    ac    at
2.00 1.000 0.50
s2pol201050_p200
* LOADC = 'P', LI = 200; CAGAIN = 'n'o
P
200
-1.1921   4.2668    -4.568   1.9487    -0.2885
no
```

A.3.4 CONTENTS OF THE OUTPUT FILE.

The following is the content of file "c2ten10_03_06.txt", obtained using the input file described earlier.

```
*** TWO CORNER CRACKS AT HOLE  r/b = 0 ***

r/t =   1.0000  a/c =   0.3000   a/t =   0.6000

3D TENSION, r/b = 0.2, r/t = 1.00

e00 =    0.994   e10 =    0.000   e20 =    0.690   e30 =    0.000   e40 =    0.635

NORMALIZED STRESS-INTENSITY FACTOR: F = K/[S(pi*a/Q)^.5]

 degree       F

   0.1      1.1824
   5.6      1.1740
  11.2      1.1654
  16.9      1.1660
  22.5      1.1842
  28.1      1.2275
  33.8      1.2879
  39.4      1.3533
  45.0      1.4213
  50.6      1.4953
  56.2      1.5798
  61.9      1.6803
  67.5      1.8034
  75.0      2.0156
  82.5      2.3420
  86.2      2.6012
  89.9      2.8605
```

Note that for confirmation purposes, the fourth entry in the output file contains five coefficients, which are partial terms of the coefficients of the stress distribution used.

A.3.5 EXAMPLE FILES.

For quick up and running of K3DL, five example input files are included in the distribution CD, and will be stored in C:\K3D_35\EXAMPLE directory after installation. The result files obtained using these example input files are also included in the same directory. These example files can be

used to verify the installation. The example input files can also be used as a template for generating additional input files for other cases. The five example input files are described below.

- K3D_35.in: The content of the file is the same as that described in section A.3.1.
- K3D_35_c2ten1003.in: Input file for two corner cracks (c2), under remote tension (ten), with r/t = 1.0 (denoted as 10) and a/c = 0.3 (03). The above K3D_35.in is a copy of this file. To use this or any other input file than K3D_35.in, save a copy of it as K3D_35.in, i.e., overwrite the existing K3D_35.in with the one to be calculated.
- K3D_35_s2ten2010.in: Input file for two surface cracks (s2), under remote tension (ten), with r/t = 2.0 (20) and a/c = 1.0 (10).
- K3D_35_c1ben2520.in: Input file for one corner crack (c1), under remote bending (ben), with r/t = 2.5 (25) and a/c = 2.0 (20).
- K3D_35_s1wed2005.in: Input file for one surface crack (s1), under wedge loading (wed), with r/t = 2.0 (20) and a/c = 0.5 (05).

A.4 COMPUTER INSTALLATION.

A.4.1 INSTALLATION.

The instructions for installing the K3DL program is given herein and is included in the program CD. The file name is "how_to_install.txt".

To install K3D version 3.5 to the C drive on your PC:

Double click on the file name "install.bat", in the program CD.

Then, drag "shortcut to k3d_35.exe" in C:\K3D_35 onto your Desktop.

A.4.2 EXECUTION.

To run K3D version 3.5:

Double click on the filename "k3d_35.exe" in C:\K3D_35.

Or, double click on the "shortcut to k3d_35.exe" icon on your Desktop.

A.4.3 VERIFICATION.

A sample input file to K3D version 3.5, k3d_35.in, is included in C:\K3D_35. Running K3DL will produce result files in the same directory. For verification, compare the results obtained using the sample input file with those in the C:\K3D_35\EXAMPLE subdirectory.

A.5 REFERENCES.

1. Zhao, W., Wu, X.R., and Yan, M.G., "Weight Function Method for Three-Dimensional Crack Problems-I," *Engineering Fracture Mechanics*, Vol. 34, No. 3, 1989, pp. 593-607.

2. Zhao, W., Wu, X.R., and Yan, M.G., "Weight Function Method for Three-Dimensional Crack Problems-II," *Engineering Fracture Mechanics*, Vol. 34, No. 3, 1989, pp. 609-624.

3. Zhao, W., Newman, J.C., Jr., Sutton, M.A., Wu, X.R., and Shivakumar, K.N., "Analysis of Corner Cracks at Hole by a 3-D Weight Function Method With Stresses From Finite Element Analysis," NASA TM-110144, 1995.

4. Zhao, W., Newman, J.C., Jr., Sutton, M.A., Wu, X.R., and Shivakumar, K.N., "Analysis of Surface Cracks at Hole by a 3-D Weight Function Method With Stresses From Finite Element Analysis," NASA TM-110145, 1995.

5. Zhao, W., Sutton, M.A., and Newman, J.C., Jr., "K3D—A Program for Determining Stress-Intensity Factors of Surface and Corner Cracks From a Hole," ASTM STP 1321, American Society for Testing and Materials, West Conshohocken, PA, 1997, pp. 656-670.

6. Fawaz, S.A. and Andersson, Börje, "Accurate Stress-Intensity Factor Solutions for Corner Cracks at a Hole," *Engineering Fracture Mechanics*, Vol. 71, 2004, pp. 1235-1254.

7. Fawaz, S.A., Andersson, Börje, and Newman, J.C., Jr., "Experimental Verification of Stress-Intensity Factor Solutions for Corner Cracks at a Hole Subject to General Loading," *22th Symposium of the International Committee on Aeronautical Fatigue*, 7-9 May 2003, Lucerne, CH, publisher.

8. Fujimoto, W.T., "Determination of Crack Growth and Fracture Toughness Parameters for Surface Flaws Emanating From Fastener Holes," *AIAA/ASME/SAE 17th Structures, Structural Dynamics, and Material Conference*, King of Prussia, PA, 1976, pp. 522-531.

9. Wu, X.R. and Carlsson, J., *Weight Functions and Stress-Intensity Factor Solutions*, Pergamon Press, 1991.

10. Irwin, G.R., "Crack Extension Force for a Part-Through Crack in a Plate," *Journal of Applied Mechanics*, Vol. 29, 1962, pp. 651-654.

11. Zhao, W., Newman, J.C., Jr., and Sutton, M.A. "A Three-Dimensional Weight Function Method - Evaluation and Applications," ASTM STP 1296, American Society for Testing and Materials, West Conshohocken, PA, 1997, pp. 563-579.

12. Bueckner, H.F., "A Novel Principle for the Computation of Stress-Intensity Factors," *ZAMM*, Vol. 50, 1970, pp. 529-546.

13. Rice, J.R., "Some Remarks on Elastic Crack-Tip Stress Fields," *International Journal of Solids and Structures*, Vol. 8, 1972, pp. 751-758.

14. Saff, C.R. and Sanger, K.B., "Part-Through Flaw Stress-Intensity Factors Developed by a Slice Synthesis Technique," ASTM STP 833, R.J. Sanford, ed., American Society for Testing and Materials, West Conshohocken, PA, 1984, pp. 24-43.

15. Shivakumar, K.N. and Newman, J.C., Jr., "Stress Concentrations for Straight-Shank and Countersunk Holes in Plates Subjected to Tension, Bending, and Pin Loading," NASA TP-3193, 1992.

16. Timoshenko, S.P. and Goodier, J.N., *Theory of Elasticity*, McGraw-Hill, 1970.

17. Rooke, D.P. and Tweed, J., "Stress-Intensity Factors for a Crack at the Edge of a Loaded Hole," *International Journal of Engineering Science*, Vol. 18, 1980, pp. 109-121.

18. Nishioka, T. and Atluri, S.N., "Integrity Analysis of Surfaced-Flawed Aircraft Attachment Llugs: A New, Inexpensive, 3-D Alternating Method," *AIAA/ASME/ASCE/ AHS 23rd Structures, Structural Dynamics and Materials Conference*, 10-12 May 1982, pp. 287-300.

19. Howland, R.C., "On the Stresses in the Neighborhood of a Circular Hole in a Strip Under Tension," *Philosophical Transactions of the Royal Society of London*, A, Vol. 229, 1930, pp. 49.

20. Perez, R., Ray, S.K., and Grandt, A.F., Jr., "Application of a Weight Function Method to Predict the Fatigue Life of Corner Cracked Holes Loaded in Bending," *Engineering Fracture Mechanics*, Vol. 28, 1987, pp. 283-291.

21. Raju, I.S. and Newman, J.C., Jr., "Stress-Intensity Factors for Corner Cracks in Rectangular Bars," ASTM STP 969, T.A. Cruse, ed., 1988, pp. 43-55.

22. Hartranft, R.J. and Sih, G.C., "An Approximate Three-Dimensional Theory of Plates With Application to Crack Problems," *International Journal of Engineering Science*, Vol. 8, 1970, pp. 711-729.

23. Benthem, J.P., "State of Stress at the Vertex of a Quarter-Infinite Crack in a Half Space," *International Journal of Solids and Structures*, Vol. 13, 1977, pp. 479-492.

24. Newman, J.C., Jr. and Raju, I.S., "Prediction of Fatigue Crack-Growth Patterns and Lives in Three-Dimensional Cracked Bodies," *Advances in Fracture Research*, Vol. 3, S.R. Valluri, D.M.R. Taplin, P. Rama Rao, J.F. Knott, and R. Dubey, eds., Pergamon Press, Inc., 1986, pp. 1597-1608.

APPENDIX B—TWO-DIMENSIONAL GREEN'S FUNCTION METHOD AND USER GUIDE

B.1 INTRODUCTION.

The stress-intensity factor solutions for a pair of concentrated forces applied to the upper and lower crack surfaces are used as a Green's function to generate the stress-intensity factor solutions for the same crack configuration subjected to any arbitrary stress distribution on the crack surfaces. Herein, a two-dimensional (2-D) code, SIFK2D, is developed to calculate the stress-intensity factors for several different through crack configurations under arbitrary loading on the crack surfaces: (1) a crack in an infinite plate, (2) an edge crack in a semi-infinite plate, (3) a single crack emanating from a circular hole in an infinite plate, and (4) two symmetric cracks emanating from a circular hole in an infinite- or finite-width plate.

The analysis code, SIFK2D, was developed to calculate the stress-intensity factors using the Green's functions developed by Irwin [B-1] for a crack in an infinite plate, Hartranft and Sih [B-2] for an edge crack in a semi-infinite plate, Shivakumar and Forman [B-3 to B-5] for a single or two symmetric cracks emanating from a circular hole in an infinite plate, and Newman [B-6] for two symmetric cracks emanating from a circular hole in an infinite- or finite-width plate. Stress-intensity factors obtained from using Shivakumar-Forman Green's functions are compared with those developed by Newman [B-6 and B-7] for a single or two symmetric cracks emanating from a circular hole in an infinite- or finite-width plate. Stress-intensity factors are obtained for these cases in which the concentrated (or wedge) forces act on the crack surfaces. The solutions are obtained for various loading cases where the expressions for the normal stresses in the absence of a crack are known (such as normal stresses in the neighborhood of a hole [B-8]) along the line in which the actual crack lies. These solutions are compared with exact or numerical solutions from the Tada, Paris, and Irwin Handbook [B-9].

B.2 CRACK IN AN INFINITE PLATE.

The Mode I stress-intensity factor for a single crack of length, 2c, subjected to remote uniform stress, S, in an infinite plate [B-9], as shown in figure B-1, is

$$K_I = S\sqrt{\pi c} \tag{B-1}$$

The Mode I stress-intensity factor for a crack in infinite plate with a pair of concentrated forces acting on the crack face, shown in figure B-2, is given by

$$K_I = \frac{2Pc}{\sqrt{\pi c}\sqrt{c^2 - b^2}} \tag{B-2}$$

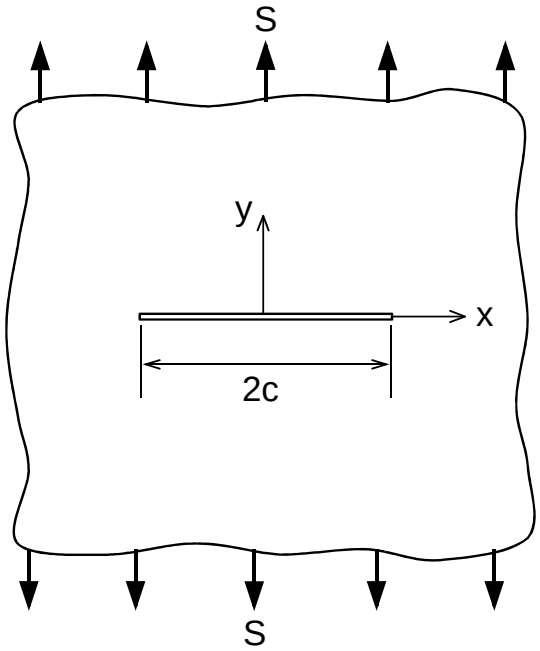

Figure B-1. Crack in an Infinite Plate Subjected to Remote Uniform Stress

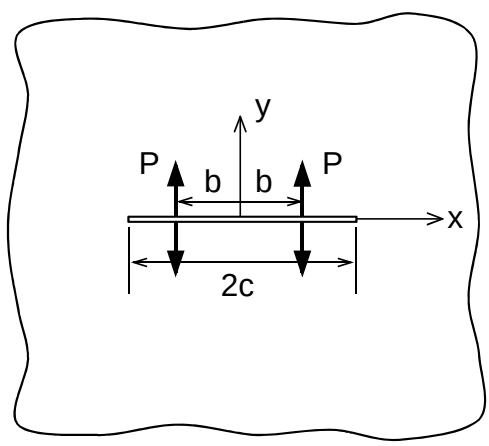

Figure B-2. Crack in an Infinite Plate With Symmetric Pair of Concentrated Forces on Crack Faces

The SIFK2D.for FORTRAN code was used to calculate the stress-intensity factors for a crack in an infinite plate by using the Green's function from the concentrated force solution, given by equation B-2, from the stress analysis handbook [B-9]. Although the stress-intensity factor solution for a crack in an infinite plate subjected to remote uniform applied stress can be found by equation B-1, this configuration was used to help develop the Green's function code. The concentrated force solutions are useful through superposition techniques to develop solutions for arbitrary loading on the same crack configuration. The technique involves first solving for the stresses present on the crack surface with the crack absent and then using the concentrated force solutions to apply distributed forces to eliminate these stresses on the crack surfaces. For the internally cracked infinite plate, the concentrated force solution is given by equation B-2, which

can be integrated to obtain stress-intensity factors. In this solution, the load P is replaced with $\bar{\sigma}dx$ and b with x for the integration, where $\bar{\sigma} = \bar{\sigma}(x,0)$ is the normal stress on the crack surface with the crack absent. Input of the crack surface loading is made either in equation or in tabular form. Herein, the integrals were evaluated by numerical integration, where the crack surface was divided into a number of incremental elements, Δx. Initially, only concentrated forces were used to calculate the stress-intensity factor for all elements. Because the stress-intensity factor solution is very sensitive to the stress distribution near the crack tip, a crack tip element was introduced to improve the convergence of the numerical integration scheme. For simplicity, a uniform stress was applied on the crack tip element as

$$\bar{\sigma} = \frac{\sigma_1 + \sigma_2}{2} \tag{B-3}$$

where σ_1 and σ_2 are the stresses acting on the crack tip element at $x = c$ and $x = c\text{-}\Delta x$, respectively. In the numerical integration routine, the exact stress-intensity factor solution was used for the crack tip element as

$$K_{Tip} = \frac{2}{\pi}\bar{\sigma}\sqrt{2\pi(\Delta x)} \tag{B-4}$$

A convergence study was made to determine the number of elements required to achieve an accurate solution, as shown in figure B-3, for a crack in an infinite plate subjected to uniform applied remote stress. The normal stress used in the Green's function code was A_1 equal unity (see equation B-5) or the applied stress, S = 1. The exact solution for F is unity. The open symbols show the results for the code using only concentrated forces for all elements, and the convergence rate to the exact solution was very slow. Using the code with the crack tip element greatly improved the rate of convergence, in that even ten elements produced a solution within 1 percent of the exact solution. These results show that 100 to 1000 elements are required to achieve a very accurate solution.

However, for stress distributions with higher stress gradients, the usefulness of the constant-stress crack tip element needed to be evaluated. Figure B-4 shows the results obtained from the stress-intensity factor code for a crack in an infinite plate subjected to a linear-stress distribution. (Note that the stress distribution must be symmetric about the y axis in the current code.) The stress-intensity factor solution has been normalized by the exact solution [B-9]. Again, 100 to 1000 elements produced a very accurate solution.

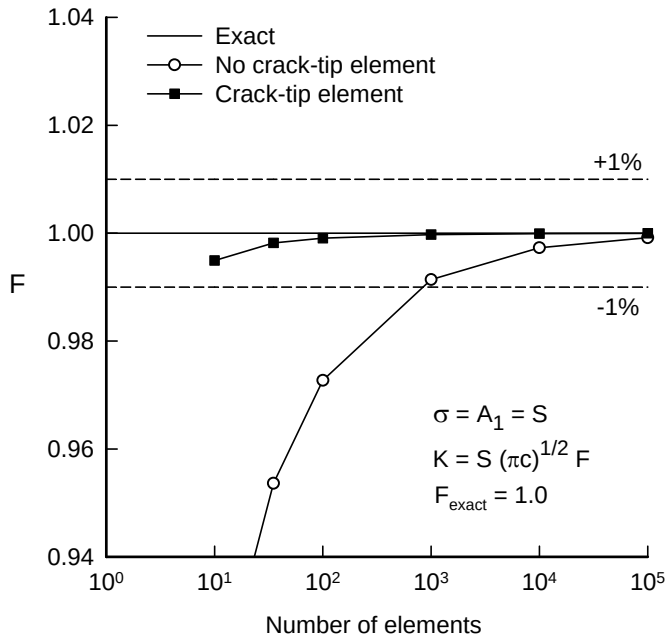

Figure B-3. Convergence Study of an Internally Cracked Plate Under Uniform Stress

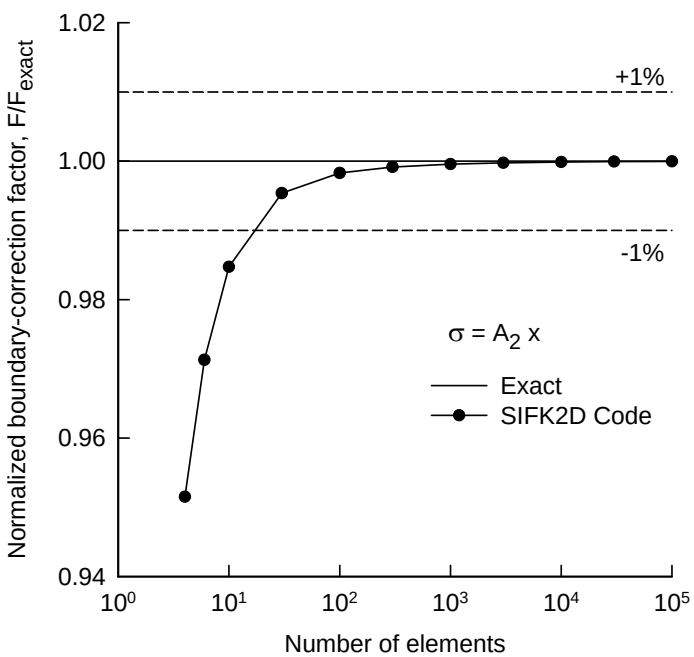

Figure B-4. Convergence Study of an Internally Cracked Plate Under Linear Stress

In the code, the normal stresses acting on the crack surfaces were implemented in equation form to be of either positive or negative powers as

$$\sigma = A_1 + A_2\, x + A_3\, x^2 + A_4\, x^3 + A_5\, x^4$$
$$\sigma = A_1 + A_2/x + A_3/x^2 + A_4/x^3 + A_5/x^4 \qquad \text{(B-5)}$$

However, the stress distribution must be symmetric about the y axis in the current code.

B.3 EDGE CRACK IN A SEMI-INFINITE PLATE.

The stress-intensity factor for an edge crack in semi-infinite plate with a pair of concentrated forces acting on the crack face [B-2 and B-9], as shown in figure B-5, is given by equation B-6, which is same as equation B-2, but with a geometric correction factor to account for the free surface.

$$K_I = \frac{2Pc}{\sqrt{\pi c}\sqrt{c^2 - b^2}} F(b/c)$$
$$F(b/c) = 1.3 - 0.3(b/c)^{5/4} \qquad \text{(B-6)}$$

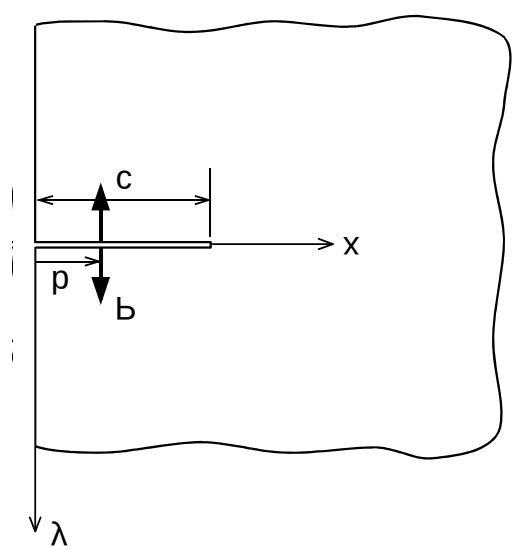

Figure B-5. Edge Crack in Semi-Infinite Plate With Concentrated Forces on Crack Faces

The SIFK2D code has been used to calculate the stress-intensity factors for the edge-crack configuration under two different loadings. One has a uniform remote applied stress (figure B-6) and the other has fourth-order stress distribution acting on the crack surfaces. The same Green's function technique, as explained earlier, was used for these crack configurations. Again, the stress distributions on the crack surfaces may either be used in equation (equation B-5) or in table form.

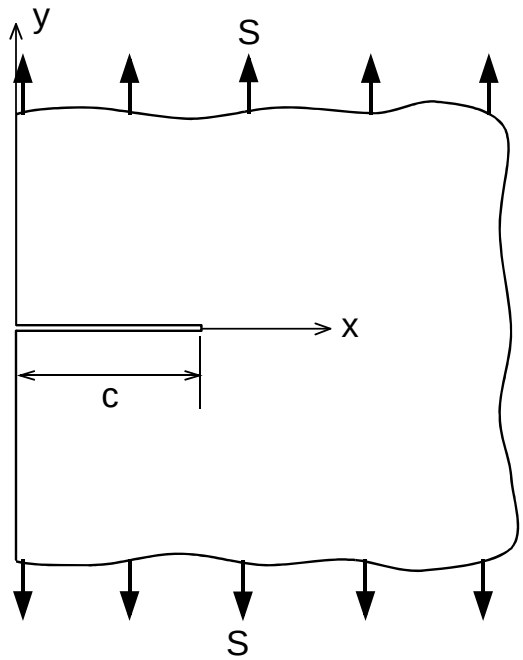

Figure B-6. Edge Crack in Semi-Infinite Plate With Remote Uniform Stress

The stress-intensity factor solution for an edge crack in a semi-infinite plate subjected to remote uniform stress [B-9] is

$$K_I = 1.1215\, S\, \sqrt{\pi c} \tag{B-7}$$

The SIFK2D code produced a boundary-correction factor (F) of 1.1219 using 1000 elements (recommended value). To subject the SIFK2D code to a more severe loading, the edge crack configuration was subjected to a fourth-order stress distribution. These results are shown in figure B-7. The stress-intensity factor has been normalized by the accurate handbook value. Even with the severe stress gradient, 100 to 1000 elements produced a solution that was within 0.5 percent of the handbook solution.

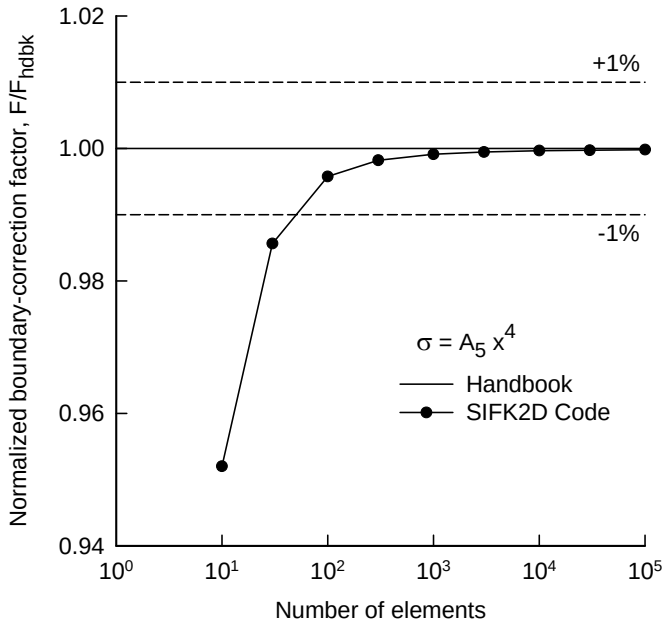

Figure B-7. Normalized Stress-Intensity Factors for an Edge Crack in Semi-Infinite Plate Under a Fourth-Order Stress Distribution

B.4 SINGLE CRACK FROM A CIRCULAR HOLE IN AN INFINITE PLATE.

Shivakumar and Forman [B-3 and B-4] developed stress-intensity factor solutions for a pair of concentrated forces applied to a crack emanating from a circular hole in an infinite plate, see figure B-8.

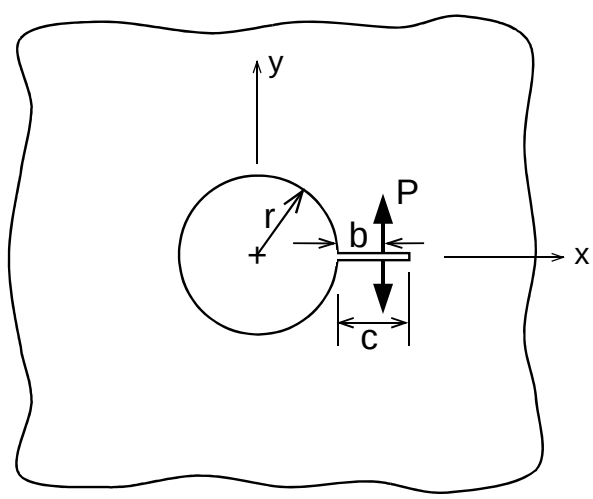

Figure B-8. Single Crack Emanating From a Circular Hole in an Infinite Plate With Concentrated Forces on Crack Faces

The stress-intensity factor equations were given by

$$K_I = \frac{P}{\sqrt{\pi c}} F(\lambda, \beta) \tag{B-8}$$

where

$$\lambda = c/r$$

$$\beta = b/c$$

$$F = [2\beta/(1-\beta)]^{1/2} + C(\alpha,\beta)\{2(1+F_\beta)/(1-\beta^2)^{1/2} - [2\beta/(1-\beta)]^{1/2}$$

$$\alpha = (1+\lambda)^{-1}$$

$$C(\alpha,\beta) = \sum_{m=1}^{5} C_{m,0}\alpha^{m/2} + \sum_{m=1}^{5}\sum_{n=1}^{3} C_{m,n}\alpha^{m/2}\beta^{n/2}$$

$$F_\beta = (1-\beta^2)(0.2945 - 0.3912\beta^2 + 0.7635\beta^4 - 0.9942\beta^6 + 0.5094\beta^8)$$

The coefficients of $C_{m,n}$ were determined in reference B-3 to fit the numerical results and are listed in table B-1.

Table B-1. The Coefficients of $C_{m,n}$

$C_{m,n}$				
m	$C_{m,0}$	$C_{m,1}$	$C_{m,2}$	$C_{m,3}$
1	0.8164	-4.5911	7.6059	-3.8529
2	0.0492	17.3181	-36.8465	20.6753
3	-0.4831	-30.5563	75.4833	-44.3540
4	-0.1746	26.2877	-73.1167	44.2607
5	0.7952	-8.4570	26.8666	-16.7296

The SIFK2D code was used to calculate stress-intensity factors for a single crack emanating from circular hole in an infinite plate using the Green's functions developed by Shivakumar and Forman [B-3 and B-4]. Two types of loading conditions were tested. For simplicity, a uniform stress was applied on the crack surfaces so that the equation for the normal stress would be $\sigma = 1.0$ and then a more complex equation, such as the Timoshenko stress distribution for a circular hole under remote uniform stress were used. In the code, the normal stress equation was implemented to be of either positive or negative powers as

$$\sigma = A_1 + A_2(x/r) + A_3(x/r)^2 + A_4(x/r)^3 + A_5(x/r)^4$$

$$\text{or} \tag{B-9}$$

$$\sigma = A_1 + A_2(r/x) + A_3(r/x)^2 + A_4(r/x)^3 + A_5(r/x)^4$$

The code is valid for expressions up to x^4 (or 4th degree polynomial equations) only, but could be easily modified for higher-order terms. For simple uniform stress, $\sigma = 1$, the coefficients are $A_1 = 1$, $A_2 = A_3 = A_4 = A_5 = 0$. The code has an option to select either positive or negative powers of x, depending upon the stress distribution. The other loading assumed for testing the validity

of code was the Timoshenko stress distribution for a hole in an infinite plate [B-8]. The normal stress equation is given by

$$\sigma = 1 + 0.5(r/x)^2 + 1.5(r/x)^4 \tag{B-10}$$

and the coefficients would be $A_1 = 1$, $A_2 = 0$, $A_3 = 0.5$, $A_4 = 0$, $A_5 = 1.5$.

Assume a single crack at a circular hole in an infinite plate under remote uniform stress. This remote uniform stress produces normal stresses according to Timoshenko [B-8], as given by equation B-10, with the crack absent. The SIFK2D code input for this loading condition may be made either in equation or in table form. Here, the equation form was used and the crack surfaces were divided into 1000 elements based on the previous convergence studies. Using the Green's function developed by Shivakumar and Forman, the stress-intensity factors are calculated for the Timoshenko stress distribution and the results are shown in figure B-9, as symbols. These results have also been compared with an equation developed by Newman [B-6 and B-7] (dashed curve).

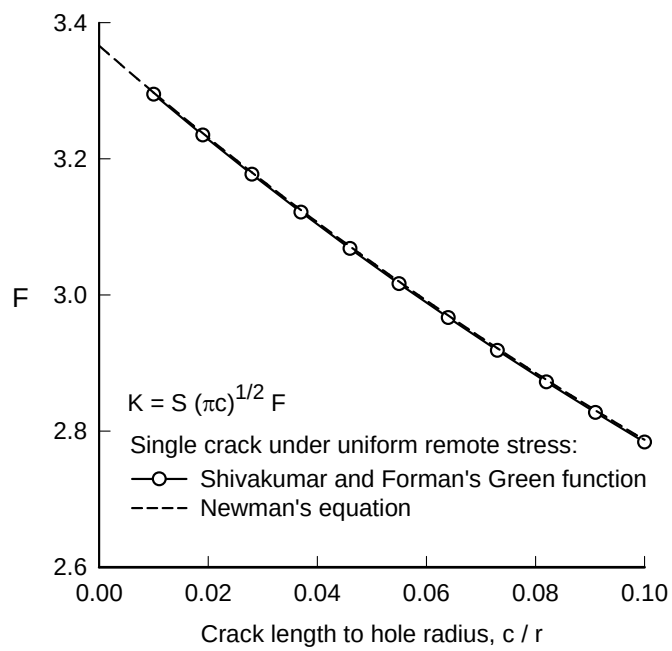

Figure B-9. Comparison of Boundary-Correction Factors for a Single Crack at a Circular Hole Between Newman's Equation and the Shivakumar-Forman Green's Function

Newman's equation was based on results from a boundary-collocation analysis [B-6 and B-7] and is

$$K_h^s = K_\infty^s F_h^s = S\sqrt{\pi d}\, F_h^s \tag{B-11}$$

where K_∞^s is for a crack in an infinite plate without a hole, $d = r + c$, and F_h^s is the boundary-correction factor for the circular hole.

The equation for F_h^s is

$$F_h^s = \sqrt{1-\frac{r}{d}}\, f_n \tag{B-12}$$

where n = 1 is for a single crack and n = 2 is for two symmetric cracks. The functions f_n determined to fit the numerical results from reference B-7 were

$$f_1 = 0.707 + 0.765\lambda + 0.282\lambda^2 + 0.74\lambda^3 + 0.872\lambda^4 \tag{B-13a}$$

and

$$f_2 = 1 + 0.358\lambda + 1.425\lambda^2 - 1.578\lambda^3 + 2.156\lambda^4 \tag{B-13b}$$

where $\lambda = r/d = r/(r+c)$.

B.5 TWO SYMMETRIC CRACKS FROM A CIRCULAR HOLE IN AN INFINITE- OR FINITE-WIDTH PLATE.

Newman [B-6] obtained the stress-intensity factors for two symmetric cracks emanating from a circular hole subjected to symmetric pairs of concentrated forces in an infinite plate, as shown in figure B-10, from a boundary-collocation analysis. An equation was fit to the numerical results and is given by

$$K_h^p = K_\infty^p F_h^p = \frac{2Pd}{\sqrt{\pi d(d^2-b^2)}} F_h^p \tag{B-14}$$

where K_∞^p is for a crack in an infinite plate without a hole, $d = r + c$, and F_h^p is the boundary-correction factor for the circular hole.

The equation for the boundary-correction factor is

$$\begin{aligned} F_h^p &= 1 + A_1\left(\frac{1-\gamma}{1-\lambda}\right) + A_2\left(\frac{1-\gamma}{1-\lambda}\right)^2 \\ A_1 &= -0.02\lambda^2 + 0.558\lambda^4 \\ A_2 &= 0.221\lambda^2 + 0.046\lambda^4 \end{aligned} \tag{B-15}$$

where γ = b/d and λ = r/d for $\lambda \le \gamma \le 1$ and $0 \le \lambda < 1$.

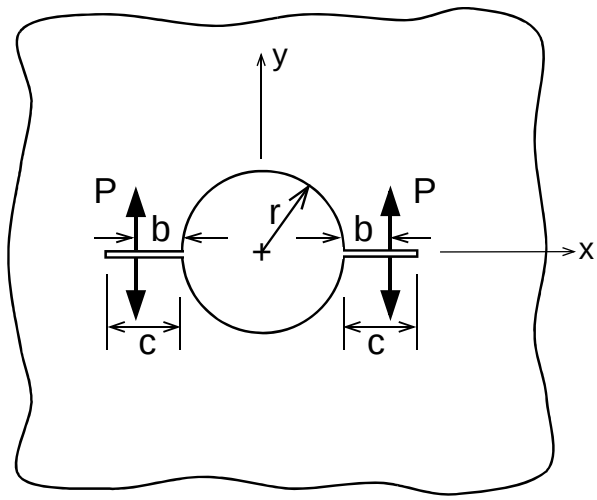

Figure B-10. Two Symmetric Cracks at a Circular Hole in an Infinite Plate Subjected to Concentrated Forces on the Crack Surfaces

Shivakumar and Forman [B4 and B-5] also developed stress-intensity factor solutions for two symmetric cracks emanating from a circular hole subjected to a symmetric pair of concentrated forces in an infinite plate. These equations are

$$K_I = \frac{P}{\sqrt{\pi c}} F_I(c^{\pm}) \quad \text{(B-16)}$$

where $F_I(c^+)$ refers to the right crack tip and $F_I(c^-)$ refers to the left crack tip.

$$F_I(c^+) = [(1+\beta)/(1-\beta)]^{1/2} + A^+(\alpha,\beta) \times [2(1+F_\beta)/(1-\beta^2)^{1/2} - \{(1+\beta)/(1-\beta)\}^{1/2}]$$
$$F_I(c^-) = [(1-\beta)/(1+\beta)]^{1/2}[1 - A^-(\alpha,\beta)]$$

where

$$A^{\pm}(\alpha,\beta) = \sum_{m=1}^{6} A_{m,0}^{\pm} \alpha^{m/2} + \sum_{m=1}^{6}\sum_{n=1}^{3} A_{m,n}^{\pm} \alpha^{m/2} \beta^{n/2}$$
$$F_\beta = (1-\beta^2)(0.2945 - 0.3912\beta^2 + 0.7635\beta^4 - 0.9942\beta^6 + 0.5094\beta^8)$$

The coefficients of $A_{m,n}^{\pm}$ are determined to fit the numerical results in references B-4 and B-5 and are listed in table B-2.

Table B-2. The Coefficients of $A^{\pm}_{m,n}$ and $A_{m,n}$

m	$A^{+}_{m,0}$	$A^{+}_{m,1}$	$A^{+}_{m,2}$	$A^{+}_{m,3}$
1	0.1206	-0.0152	0.0247	0.2199
2	-0.9213	-1.0104	2.3663	-5.1128
3	5.6288	0.7841	-5.23304	22.1371
4	-11.1246	2.0877	5.4043	-44.1147
5	9.9127	-2.7520	-7.3772	43.7751
6	-2.6132	0.9076	4.8125	-16.9059
m	$A^{-}_{m,0}$	$A^{-}_{m,1}$	$A^{-}_{m,2}$	$A^{-}_{m,3}$
1	0.1370	-0.3747	0.7558	-0.2165
2	0.0769	1.8495	-5.7783	0.2717
3	7.4482	-10.4449	30.1129	-3.8853
4	-19.4000	24.3391	-73.9272	16.4607
5	21.3576	-23.1096	77.4179	-21.6280
6	-8.6197	7.7426	-28.5877	8.9970
m	$A_{m,0}$	$A_{m,1}$	$A_{m,2}$	$A_{m,3}$
1	0.8164	-4.5911	7.6059	-3.8529
2	0.0492	17.3181	-36.8465	20.6753
3	-0.4831	-30.5563	75.4833	-44.3540
4	-0.7146	26.2877	-73.1167	44.2607
5	0.7952	-8.4570	26.8666	-16.7296

B.5.1 INFINITE-WIDTH PLATE.

The Green's functions developed by Newman [B-6] and Shivakumar-Forman [B-4 and B-5] for two symmetric cracks emanating from a circular hole in an infinite plate were used to calculate the stress-intensity factors for two different loading conditions. The two loading conditions were: (1) uniform stress acting on the crack surface and (2) the Timoshenko stress distribution for a circular hole under uniform remote stress acting along the crack surface. The input for these loading conditions was made in equation form, but the loading could also have been input in tabular form.

For the uniform stress case, the crack surface was divided into 1000 elements based on the previous convergence studies. Various c/r ratios were considered and the solutions were within ±0.5 percent of the handbook solutions using either the Newman or Shivakumar-Forman Green's functions.

The second loading considered was the Timoshenko stress distribution acting along the crack surface (equation B-10). This loading condition is equivalent to the case of a remote uniform stress, S, applied to the same crack configuration, as shown in figure B-11. First, a convergence study was made on the two symmetric crack configuration. For this study, a c/r ratio was selected as 0.1. Both the Newman and Shivakumar-Forman Green's functions were used. For

this crack configuration, a FADD2D [B-10] boundary-element analysis was made and these results are shown as the solid horizontal line shown in figure B-12. The symbols show the results from the Shivakumar-Forman and Newman Green's function analyses using a wide range in elements. Again, more than ten elements are required to achieve a solution within 1 percent of the FADD2D solution.

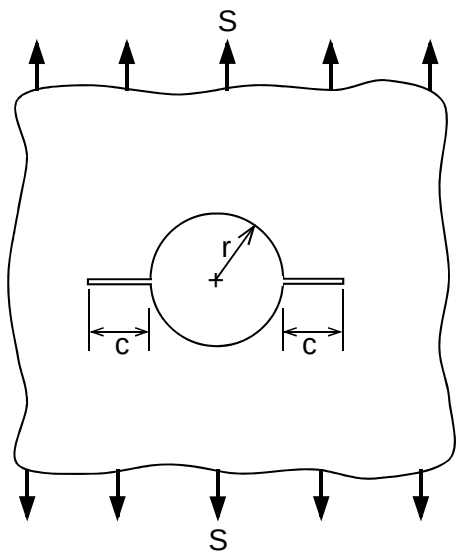

Figure B-11. Two Symmetric Cracks From a Hole Subjected to Remote Uniform Stress

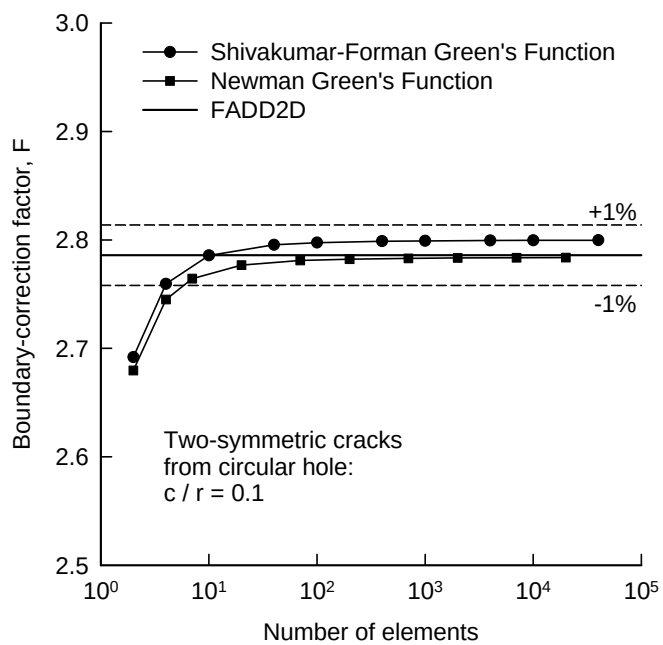

Figure B-12. Comparisons of Stress-Intensity Factors From the Two Green's Functions for Two Cracks at a Hole Under Remote Tension

Figure B-13a shows the normalized stress-intensity factors for two symmetric cracks from a hole under remote uniform stress from c/r ratios of 0.01 to 4. All SIFK2D solutions from the Green's functions and the Newman equation agreed within 1 percent over the wide range in c/r ratios. An expanded view for c/r ratios less than 0.1 are shown in figure B-13b. These results show that the Shivakumar-Forman equations produce more accurate stress-intensity factor solutions, but the Newman Green's function gave results within about 1 percent for a c/r ratio of 0.01. The percent differences between the two Green's function approaches and the equation are shown in figure B-14. The equation is within ±0.2 percent of accurate boundary collocation [B-6 and B-7] or boundary-element [B-10] solutions. As the c/r ratio approaches zero, the Shivakumar-Forman equations continue to produce accurate stress-intensity factor solutions and these equations are recommended for use on other loading conditions applied to the two-symmetric cracks from a hole configuration. However, the Newman Green's function equations are much simpler and easier to program than the Shivakumar-Forman equations.

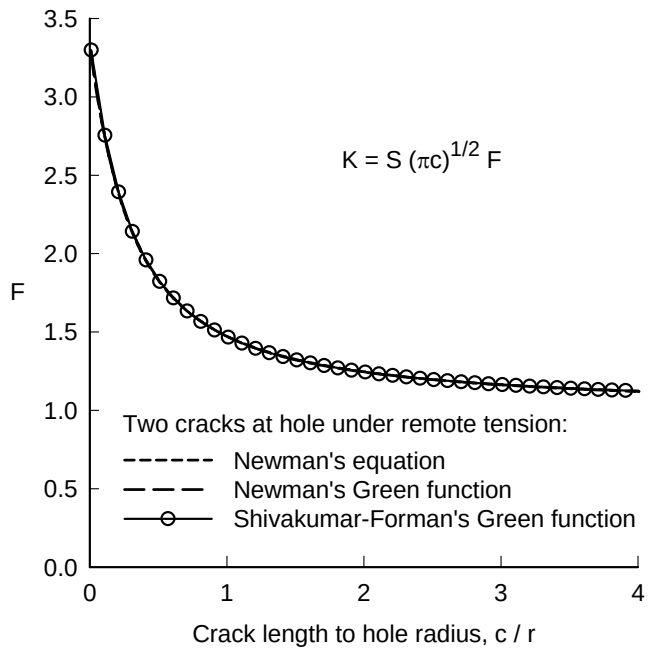

Figure B-13a. Normalized Boundary-Correction Factor for Two Symmetric Cracks at a Hole

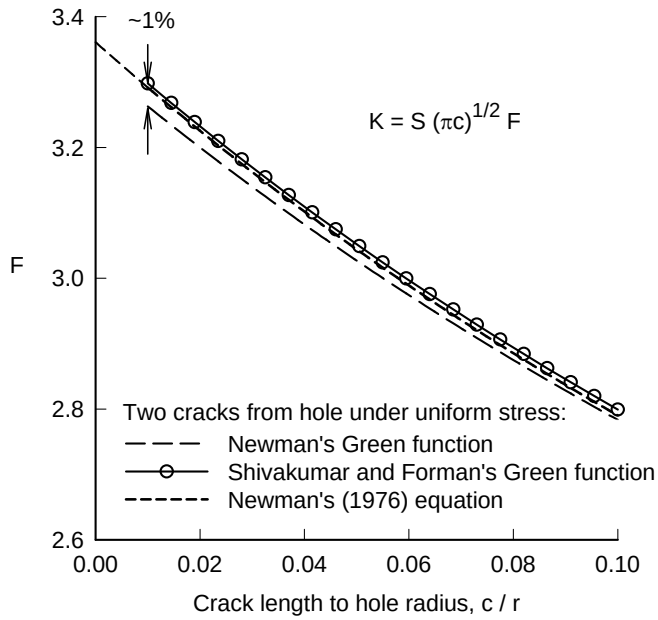

Figure B-13b. Normalized Boundary-Correction Factor for Two Symmetric Cracks at a Hole—Expanded View

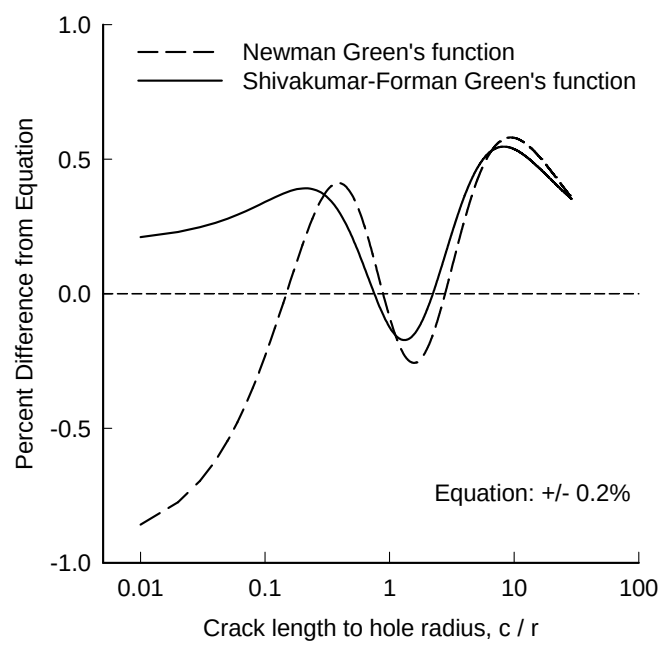

Figure B-14. Percent Difference Between Newman and Shivakumar-Forman Green's Functions and Newman's Equation for Two Symmetric Cracks at a Hole

B.5.2 FINITE-WIDTH PLATE.

The equations given in the preceding sections for stress-intensity factors (equations B-12 and B-13) by Newman [B-6] are for cracks emanating from a circular hole in an infinite plate. But these quantities are influenced by the finite width of the plate. Therefore, some approximate

finite-width corrections were developed in reference B-6. The stress-intensity factor for a crack in a finite-width plate is

$$K = K_{\infty} F_W \tag{B-17}$$

where K_∞ is the stress-intensity factor for cracks emanating from a circular hole in an infinite plate and F_W is the finite-width correction for the particular loading condition.

B.5.2.1 Remote Uniform Stress.

The approximate boundary-correction factor for two symmetric cracks emanating from a circular hole in a finite-width plate subjected to uniform stress is

$$F_W^S = \sqrt{\sec\left(\frac{\pi r}{2W}\right)\sec\left(\frac{\pi d}{2W}\right)} \tag{B-18}$$

where $d = c + r$ for $r/W \leq 0.5$ and $d/W \leq 0.7$. (Note that W is one-half of the width of the crack configuration.) Equation B-17 is within ±2 percent of boundary-collocation results [B-7]. The equation accounts for the influence of width on the stress concentration at the edge of hole and the influence of width on stress-intensity factors.

B.5.2.2 Partially Loaded Crack.

The approximate boundary-correction factor for two symmetric cracks emanating from a circular hole in a finite-width plate subjected to partial loading on the crack surface was obtained from the infinite periodic array of cracks solution [B-6 and B-9]. The modified correction factor is

$$F_W^{\sigma} = \left[\frac{\sin^{-1} B_2 - \sin^{-1} B_1}{\sin^{-1}\left(\frac{b_2}{d}\right) - \sin^{-1}\left(\frac{b_1}{d}\right)}\right]\sqrt{\sec\left(\frac{\pi d}{2W}\right)} \tag{B-19}$$

where

$$B_K = \sin\left(\pi b_K / 2W\right) / \sin\left(\pi d / 2W\right)$$

for $r/W \leq 0.25$ and $d/W \leq 0.7$. These equations have been incorporated into the SIFK2D code for the case of two symmetric cracks emanating from a circular hole in a finite-width plate.

B.6 USER GUIDE FOR SIFK2D.FOR.

Input Data File:

1. READ(*,*) TITLE

   Any 80-character title that describes the problem.

2. READ(*,*) NGREEN (If NGREEN = 0, 1 or 2 go to step 5)

   NGREEN = 0 – Crack in infinite plate
   = 1 – Edge crack in semi-infinite plate
   = 2 – Single crack from circular hole in infinite plate (default Shivakumar-Forman Green's function solution)
   = 3 – Two symmetric cracks from circular hole in infinite- or finite-width plate

3. READ(*,*) NSOLT, NFWC

   NSOLT = Solution type
   = 1 – Newman Green's function solution
   = 2 – Shivakumar-Forman Green's function solution

   NFWC = Finite-width correction
   = 1 – No finite-width correction (infinite plate)
   = 2 – Finite-width correction

4. READ(*,*) WIDTH (NGREEN = 3 and NFWC = 2 only)

   WIDTH = w = Half-width of plate (2w is total width of plate)

5. READ(*,*) RAD, CRK1, CRK2, INC

   RAD = Radius of circular hole (RAD = 0 if NGREEN = 0 or 1)

   CRK1 = Initial crack length

   CRK2 = Final crack length

   INC = Number of crack increments

6. READ(*,*) NOE

   NOE = Number of elements along crack surface (usually set to 1000)

7. READ(*,*) NEOT (If NEOT = 2 go to step 10)

   NEOT = Equation or table form

= 1 – Crack-surface stresses in equation form
= 2 – Crack-surface stresses in table format

8. READ(*,*) NOP

NOP = Positive powers or negative powers of 'x' in the stress function
= +1 Positive powers of 'x'
= –1 Negative powers of 'x'

9. READ(*,*) A1, A2, A3, A4, A5

A1, A2, A3, A4, A5 = Coefficients of polynomial equation
(For either positive or negative powers of 'x')

10. READ(*,*) TABLE

TABLE = Create stress-distribution table filename (like hole.txt)
Filename (up to 20 characters):
TITLE – Any description of stress data table (up to 80 characters)
NUM
X(1) SIG(1)
X(2) SIG(2)
… …
X(NUM) SIG(NUM)
NUM = Number of points in stress data table (i = 1 to NUM)
X(i) = Coordinate distance measured from the center of the circular hole
SIG(i) = Corresponding value of normal stress

B.6.1 EXAMPLE OF INPUT AND OUTPUT FILES FOR SINGLE CRACK FROM A HOLE.

Examples of input and output data files for a single crack emanating from a circular hole in an infinite plate using the exact normal stresses solution from Timoshenko [B-8] and the Shivakumar-Forman Green's function are as follows [B-3 and B-4].

Input file:

```
SINGLE CRACK FROM CIRCULAR HOLE (REMOTE STRESS)
2
1.0  0.01  0.1  100
1000
1
-1
1  0  0.5  0  1.5
```

Output file:

```
SINGLE CRACK FROM CIRCULAR HOLE (REMOTE STRESS)
NGREEN =  2
RAD =   0.1000E+01
NUMBER OF ELEMENTS (NOE) = 1000
NEGATIVE POWERS: A1,A2,A3,A4,A5
  0.10000E+01   0.00000E+00   0.50000E+00   0.00000E+00   0.15000E+01
SINGLE CRACK FROM CIRCULAR HOLE
SHIVKUMAR-FORMAN SOLUTION
     CRACK          KI              F
   0.10000E-01   0.58398E+00   0.32947E+01
   0.10900E-01   0.60856E+00   0.32887E+01
   0.11800E-01   0.63202E+00   0.32826E+01
        ⋮             ⋮             ⋮
        ⋮             ⋮             ⋮
        ⋮             ⋮             ⋮
   0.98200E-01   0.15510E+01   0.27925E+01
   0.99100E-01   0.15557E+01   0.27882E+01
   0.10000E+00   0.15604E+01   0.27839E+01
```

B.6.2 EXAMPLE OF INPUT AND OUTPUT FILES FOR TWO-SYMMETRIC CRACKS FROM A HOLE.

Examples of input and output data files for two symmetric cracks emanating from a circular hole in a finite-width plate using a table input format for the normal stresses in an uncracked plate along the line of the intended crack location and the Newman Green's function are as follows [B-6].

Input file:

```
TWO-SYMMETRIC CRACKS FROM CIRCULAR HOLE
3
1  2
4.0
```

```
1.0  0.001  0.2  100
1000
2
hole.txt
```

The table, hole.txt, of normal stresses along a radial line from a circular hole perpendicular to the remote applied stress, S, in an uncracked plate was obtained from the Timoshenko [B-8] stress solution for a hole in an infinite plate for demonstration. In general, a finite element or boundary-element analysis may be used to generate the normal stresses in the uncracked plate of interest. The normal stresses along the intended crack location are used in the K2D code to calculate the stress-intensity factors as a function of crack length from the hole. The hole.txt file is given by:

```
Circular Hole in Plate (S = 1)
32
1.00000   3.00000
1.00500   2.96541
1.01000   2.93162
1.01500   2.89861
1.02000   2.86635
1.03000   2.80403
1.04000   2.74448
1.06000   2.63314
1.08000   2.53121
1.10000   2.43774
1.12500   2.33150
1.15000   2.23570
1.17500   2.14909
1.20000   2.07060
1.30000   1.82105
1.40000   1.64556
1.50000   1.51852
1.60000   1.42419
1.70000   1.35261
1.80000   1.29721
1.90000   1.25360
2.00000   1.21875
2.10000   1.19051
2.20000   1.16734
2.30000   1.14812
2.40000   1.13202
2.50000   1.11840
2.60000   1.10679
2.70000   1.09681
```

```
2.80000   1.08818
2.90000   1.08066
3.00000   1.07407
```

Output file:

```
TWO-SYMMETRIC CRACKS FROM CIRCULAR HOLE
NGREEN =  3
NSOLT =  1
WIDTH =   0.4000E+01
RAD =   0.1000E+01
NUMBER OF ELEMENTS (NOE) = 1000
TABLE FILENAME = hole.txt
TWO-SYMMETRIC CRACKS FROM CIRCULAR HOLE
NEWMAN SOLUTION
     CRACK          KI             F             FW
  0.10000E-02   0.18863E+00   0.33655E+01   0.10131E+01
  0.29900E-02   0.32492E+00   0.33525E+01   0.10132E+01
  0.49800E-02   0.41772E+00   0.33396E+01   0.10133E+01
  0.69700E-02   0.49229E+00   0.33269E+01   0.10135E+01
        ⋮             ⋮             ⋮             ⋮
        ⋮             ⋮             ⋮             ⋮
        ⋮             ⋮             ⋮             ⋮
  0.19403E+00   0.19576E+01   0.25073E+01   0.10287E+01
  0.19602E+00   0.19630E+01   0.25015E+01   0.10289E+01
  0.19801E+00   0.19684E+01   0.24957E+01   0.10291E+01
  0.20000E+00   0.19736E+01   0.24899E+01   0.10293E+01
```

B.7 REFERENCES.

1. Irwin, G.R., "Analysis of Stresses and Strains Near the End of a Crack Transversing a Plate," Transactions ASME, *Journal of Applied Mechanics*, Vol. 24, 1957, pp. 361.

2. Hartranft, R.J. and Sih, G.C., "Alternating Method Applied to Edge and Surface Crack Problems," *Mechanics of Fracture*, *Vol. 1*, *Methods of Analysis and Solutions of Crack Problems*, edited by G.C. Sih, Chapter 4, Noordhoff, 1973, pp. 179-238.

3. Shivakumar, V. and Forman, R.G., "Green's Function for a Crack Emanating From a Circular Hole in an Infinite Sheet," *International Journal of Fracture*, Vol. 16, 1980, pp. 305-316.

4. Shivakumar, V., Forman, R.G., and Rosencranz, R., Jr., "Green's Function Solution and Applications for Cracks Emanating From a Circular Hole in an Infinite Sheet," Applied Science Publishers Ltd., England, 1983.

5. Shivakumar, V. and Forman, R.G., "Green's Function for Two Cracks of Equal Length From a Circular Hole in an Infinite Sheet," *Research Mechanics Letters*, Vol. 1, 1981, pp. 563-569.

6. Newman, J.C., Jr., "A Nonlinear Fracture Mechanics Approach to the Growth of Small Cracks," AGARD CP-328, 1983, pp. 6.1-6.26.

7. Newman, J.C., Jr., "An Improved Method of Collocation for the Stress Analysis of Cracked Plates With Various-Shaped Boundaries," NASA TN D-6376, 1971.

8. Timoshenko, S. and Goodier, J.N., *Theory of Elasticity*, 2nd Edition, McGraw-Hill, New York, NY, 1951.

9. Tada, H., Paris, P.C., and Irwin, G.R., *The Stress Analysis of Cracks Handbook*, ASME Press, New York, NY, 2000.

10. Chang, C.C. and Mear, M.E., "A Boundary Element Method for Two-Dimensional Linear Elastic Fracture Analysis," *International Journal of Fracture*, Vol. 74, 1996, pp. 219-251.

APPENDIX C—IMPROVEMENTS TO FASTRAN—FATIGUE CRACK GROWTH LIFE-PREDICTION CODE

C.1 INTRODUCTION.

The previous FASTRAN crack-closure model and life-prediction code, see references C-1 to C-4, distributed to industry is Version 3.81. The basic FASTRAN code has not changed since the early 1990s, but a number of coding bugs have been fixed and a number of new stress-intensity factor (K) solutions and options have been added. There were four significant changes made to the current release version of FASTRAN (Version 3.82).

1. A new table lookup for cracks emanating from holes
2. Make the transcendental functions (sin, cos, etc.) double precision
3. Replaced SUBROUTINE OPEN(SO,SIG) with SUBROUTINE OPEND(SO,SIG)
4. Implemented K-analogy for both two- and three-dimensional crack configurations

C.2 NEW TABLE LOOKUP.

For cracks emanating from holes (NTYP = -99), a new table look-up format was implemented. The FASTRAN code uses the stress-intensity factor equation in the form

$$K = S\,(\pi\, c')^{1/2}\, F \tag{C-1}$$

where $c' = c + r$, c is the crack length measured from the edge of the hole, r is the hole radius, and F accounts for the influence of the hole and external boundaries on the stress-intensity factor. The older table look-up version input values of F against c'/w. However, a more accurate form is

$$K = S\,(\pi\, c)^{1/2}\, F_c \tag{C-2}$$

where the stress-intensity factor is expressed in term of the crack length measured from the hole. The new table look-up version input values of F_c against c/w, and then the code converts to the required form as $F = (c/c')^{1/2}\, F_c$.

To illustrate the improved table look-up procedure, an example of two symmetric cracks growing from a circular hole in 2024-T3 aluminum alloy is used. In FASTRAN, the case of two symmetric cracks from a hole is NTYP = -4, and the stress-intensity factors are given by a very accurate equation. In contrast, the stress-intensity factors are approximated by the new table look-up method by using 17, 30, or 50 points, respectively, as shown in figure C-1. The comparison of the fatigue crack growth predictions from an initial small crack length of 0.02 mm is shown in figure C-2. All predictions are within a few percent (< 3%) of the more accurate predictions using the equation.

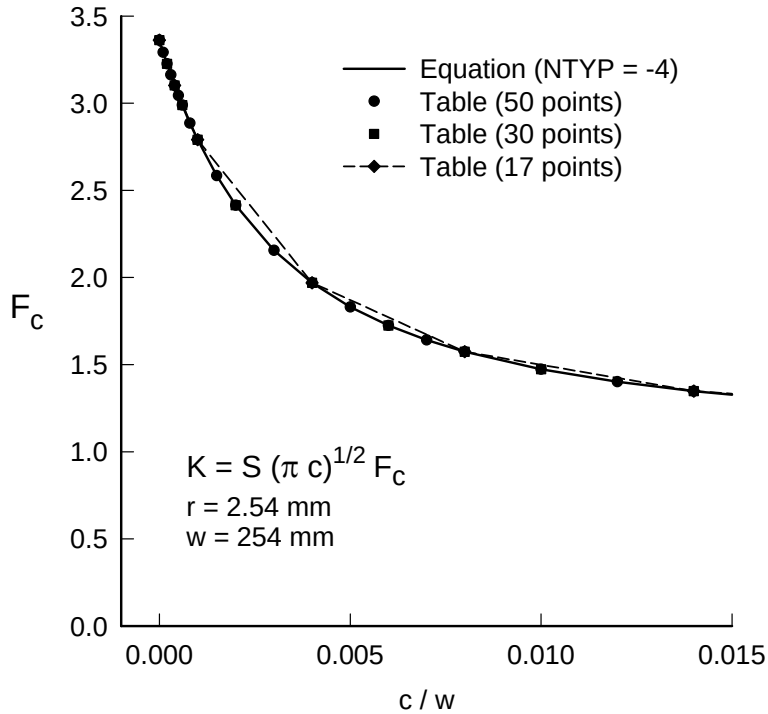

Figure C-1. Stress-Intensity Factors for Two Symmetric Cracks at a Hole Using an Equation or Various Points in Table Look-Up Procedure

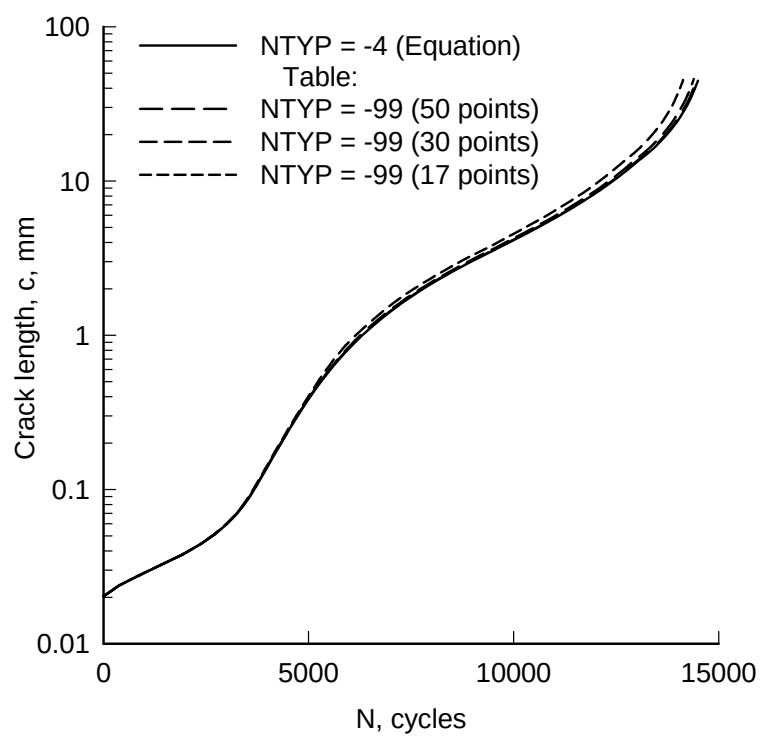

Figure C-2. Fatigue Crack Growth Predictions Made on 2024-T3 Aluminum Alloy Using the Equation or Various Table Look-Up Approximations

C.3 DOUBLE-PRECISION OPERATION.

In the early use and development of FASTRAN, using workstations, the code was compiled using double precision. However, the code is now generally used on PCs. The code uses IMPLICIT REAL*8 (A-H,O-Z) command and the transcendental functions (e.g., sin and cos) are changed to double precision. Thus, compilation of the code will automatically be double precision.

C.4 SUBROUTINE OPEND(SO,SIG).

Some compilers have difficulty with the subroutine named "open," since this command is used. Thus, the subroutine has been renamed OPEND, since this routine calculates the crack-opening stress levels from crack surface displacements. (Currently, this subroutine is not used. The crack-opening stresses are calculated from SUBROUTINE OPENK, which uses the contact stress-intensity factors to calculate the crack-opening stresses.)

C.5 K-ANALOGY.

The FASTRAN code has two analytical crack-closure models in the current code (Version 3.81). One is a modified Dugdale model (MDM) for a "central crack in a finite-width plate" and the other is the MDM for "two symmetric cracks emanating from a circular hole." These models are used to calculate the crack-opening stresses during crack growth under various specified load histories. It was found many years ago that K-analogy may be used to transfer crack-opening stress histories from one crack configuration to the other. The FASTRAN (Version 3.81) had K-analogy was implemented for only the compact tension specimen. The revised FASTRAN code (Version 3.82) has been updated to apply K-analogy to all two-dimensional (2-D) crack configurations, like that used for the compact specimen. K-analogy has also been implemented for all three-dimensional (3-D) crack configurations, such as the surface and corner crack configurations, by using the "highest" stress-intensity factor of the two locations (maximum depth or free-surface locations) used to propagate a 3-D crack. By using the highest stress-intensity factor, the code will error on the conservative side, i.e., the crack-opening stress levels will be lower, and crack growth rates will be higher, than using the average K value.

FASTRAN Code modification:

```
Old coding in FASTRAN Version 3.8 (NASA version)
C
      KAPP=0
      IF(KCONST.EQ.0.AND.NTYP.EQ.2) KAPP=1
c
c     KAPP=1
c     IF(NTYP.EQ.1) KAPP=0
c     IF(NTYP.EQ.2.AND.KCONST.EQ.1) KAPP=0
C
```

New coding in FASTRAN Version 3.82

```
C
c       KAPP=0
c       IF(KCONST.EQ.0.AND.NTYP.EQ.2) KAPP=1
C (See Subroutine APPK)
        KAPP=1
        IF(NTYP.EQ.1.OR.NTYP.EQ.-4) KAPP=0
        IF(NTYP.EQ.2.AND.KCONST.EQ.1) KAPP=0
C
```

Subroutine APPK

```
C
      SUBROUTINE APPK
C CALCULATES RSF FOR K-ANALOGY
C USES CENTER-CRACK SIMULATION FOR NTYP GREATER THAN OR EQUAL TO ZERO
C USES CRACK FROM HOLE SIMULATION FOR NTYP LESS THAN ZERO
      IMPLICIT REAL*8 (A-H,O-Z)
      COMMON/BIGC/A,C,D,DMAX,PI,CPI,S(50),Y(50),G(50),H(50),X(50),
     1V(50),XX(10),XY(10),PCT(10),W,T,FA,FC,FD,FS(50),SYIELD,SULT,
     2DISP(50,50),ALP,CMAX,DS(50),RAD,SMINC,OMEGA,AMIN,XKT,RADIUS,
     3DCMAX,GAMMA,SMINSP,SMAXSP,RSF,CI,CN,AI,AN,SC(50),DELTA,EMOD,
     4RIVETS,RLF1,RLF2,WR,WJ,
     5LFAST,LTYP,NTYP,MELE,KF,M,NALP,NRHO,NEP,NBCF,NFLT,MAXFLTS,NPC,
     6NODKL,KNTYP
      REAL KF,M
      FA=0.0
      NTYPX=NTYP
      NTYP=1
      IF(NTYPX.LT.0) NTYP=-4
      NTYPZ=NTYP
      CALL EBCF(C)
      FCCT=FC
      NTYP=NTYPX
      CALL BCF(0,C,0)
      FCT=FC
      IF(FA.GT.FC) FCT=FA
      RSF=FCT/FCCT
c
c     CW=C/W
c     WRITE(4,1111) NTYPZ,NTYP,CW,FCT,FCCT,RSF
c1111 FORMAT(2X,'NTYPZ=',I3,2X,'NTYP=',2X,I3,2X,'CW=',E11.4,
c    12X,'FCT=',E11.4,2X,'FCCT=',E11.4,2X,'RSF=',E11.4)
c
      RETURN
      END
C
```

To illustrate the K-analogy concept, figure C-3(a) shows a general 2-D crack configuration and figure C-3(b) shows the FASTRAN model (central crack in a finite-width panel subjected to remote uniform stress, NTYP = 1). The objective is to apply an applied stress, S', to the model to give the same K history as applied to the specimen. The crack-opening stress calculated from the model is then used on the general crack configuration. For example, the stress-intensity

factor for the general crack configuration is

$$K_{con} = P/(WB)\ \sqrt{(\pi c)}\ F_{con} \tag{C-3}$$

where P is the applied load and F_{con} is the boundary-correction factor. Note that equation C-3 is expressed as a stress, $P/(WB)$, times the square root of the crack length. This form is a general form and the boundary-correction factor accounts for configuration details. The stress-intensity factor for the center-crack tension model is

$$K_{cct} = S'\ \sqrt{(\pi c)}\ F_{cct} \tag{C-4}$$

Equating equations C-3 and C-4 gives

$$S' = (P/(WB)\ F_{con}/F_{cct} \tag{C-5}$$

Thus, S' is then applied to the model in FASTRAN and the crack-opening stress is calculated. This value is then used with equation C-3 to calculate the effective stress-intensity factor and, consequently, the fatigue crack growth rate.

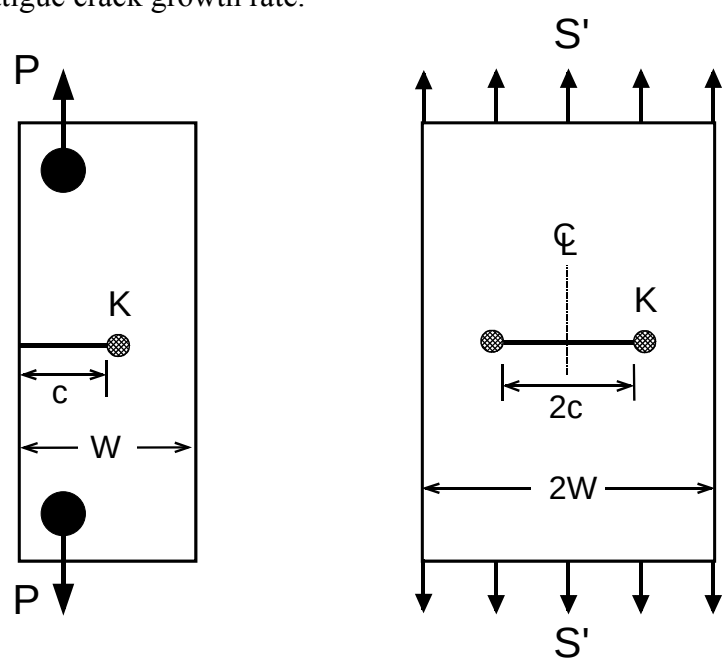

(a) Crack Configuration (b) FASTRAN Model

Figure C-3. General Crack Configuration and Loading Applied to Model to Determine Crack-Opening Stress

For through cracks emanating from a hole (NTYP = negative value), the second model in FASTRAN (NTYP = -4)—two symmetric cracks emanating from a circular hole in a finite-width plate—is used to calculate the crack-opening stress for the general crack configuration.

For 3-D crack configurations, such as a surface crack (figure C-4(a)) and a corner crack emanating from a hole (figure C-4(b)), the highest stress-intensity factor of K_a or K_c is used in the two respective models to calculate crack-opening stress. A surface crack uses the first model (NTYP = 1) and the corner crack at a hole uses the second model (NTYP = -4).

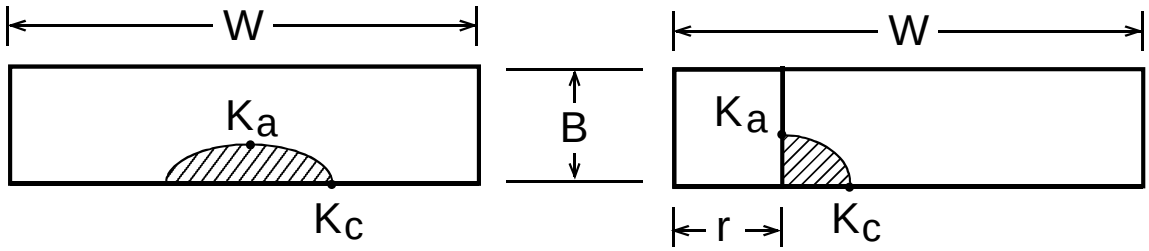

(a) Surface Crack (b) Corner Crack at Hole

Figure C-4. Three-Dimensional Crack Configurations Modeled in FASTRAN

C.6 REFERENCES.

1. Newman, J.C., Jr., "FASTRAN II—Fatigue Crack Growth Structural Analysis Program," NASA TM-104159, February 1992.

2. Newman, J.C., Jr., "A Crack-Closure Model for Predicting Fatigue Crack Growth Under Aircraft Spectrum Loading," *Methods and Models for Predicting Fatigue Crack Growth under Random Load*, ASTM STP 748, 1981, pp. 53-84.

3. Newman, J.C., Jr., "Prediction of Fatigue Crack Growth Under Variable Amplitude and Spectrum Loading Using a Closure Model," *Design of Fatigue and Fracture Resistant Structures*, ASTM STP 761, 1982, pp. 255-277.

4. Newman, J.C., Jr., "A Crack Opening Stress Equation for Fatigue Crack Growth," *International Journal of Fracture*, Vol. 24, 1984, pp. R131-Rl35.